

NUMERICAL HEAT TRANSFER STUDY IN A DUCT EQUIPPED WITH
OBLIQUE BAFFLES

SOMBAT TAMNA

A THESIS SUBMITTED IN PARTIAL FULFILLMENT
OF THE REQUIREMENT FOR THE DEGREE OF
DOCTOR OF ENGINEERING IN MECHANICAL ENGINEERING
FACULTY OF ENGINEERING
KING MONGKUT'S INSTITUTE OF TECHNOLOGY LADKRABANG

2015

KMITL-2015-EN-D-058-180

NUMERICAL HEAT TRANSFER STUDY IN A DUCT EQUIPPED WITH
OBLIQUE BAFFLES

SOMBAT TAMNA

A THESIS SUBMITTED IN PARTIAL FULFILLMENT
OF THE REQUIREMENT FOR THE DEGREE OF
DOCTOR OF ENGINEERING IN MECHANICAL ENGINEERING
FACULTY OF ENGINEERING
KING MONGKUT'S INSTITUTE OF TECHNOLOGY LADKRABANG
2015
KMITL-2015-EN-D-058-180

COPYRIGHT 2015

FACULTY OF ENGINEERING

KING MONGKUT'S INSTITUTE OF TECHNOLOGY LADKRABANG

หัวข้อวิทยานิพนธ์	การศึกษาการถ่ายเทความร้อนเชิงตัวเลขในท่อที่ใส่แผ่นกั้นวางเอียง
นักศึกษา	นายสมบัติ ทำนา
รหัสนักศึกษา	53610201
ปริญญา	วิศวกรรมศาสตรดุษฎีบัณฑิต
สาขาวิชา	วิศวกรรมเครื่องกล
พ.ศ.	2558
อาจารย์ที่ปรึกษาวิทยานิพนธ์	รศ.ดร.ชินรัชช์ เขียรพงษ์
อาจารย์ที่ปรึกษาวิทยานิพนธ์ร่วม	รศ.ดร.พงษ์เจต พรหมวงศ์

บทคัดย่อ

วิทยานิพนธ์นี้นำเสนอการจำลองเชิงตัวเลขสามมิติของการไหลแบบปั่นป่วนที่มีลักษณะการไหลแบบพัฒนาอย่างสมบูรณ์และช้าเป็นช่วง เพื่อศึกษาพฤติกรรมของการไหลแบบอัดตัวไม่ได้และการถ่ายเทความร้อนในช่องการไหลแบบต่างๆ โดยช่องการไหลทดสอบแรกคือช่องการไหลหน้าตัดสี่เหลี่ยมผืนผ้าที่ให้ความร้อนแบบฟลักซ์ความร้อนคงที่บริเวณผนังด้านบนเพียงด้านเดียว ติดแผ่นกั้นรูปตัววีหลายตัวที่ทำมุมปะทะ 45° โดยจัดเรียงแผ่นกั้นรูปตัววีด้านบน-ล่างในแนวตรงกัน แนวเอียงกัน และติดที่ผนังด้านบนด้านเดียว ทำการศึกษาผลกระทบของระยะห่างระหว่างแผ่นกั้น และลักษณะการจัดเรียงแผ่นกั้นที่มีต่อการสูญเสียความดัน การถ่ายเทความร้อน และตัวประกอบสมรรถนะเชิงความร้อน ช่องการไหลต่อมาเป็นท่อสี่เหลี่ยมจัตุรัสที่ให้ความร้อนผนังทุกด้านของท่อแบบฟลักซ์ความร้อนคงที่ โดยสอดใส่แผ่นกั้นรูปตัวยูวางเอียงมุมปะทะ 30° ช่องการไหลทดสอบสุดท้ายคือท่อกลมที่ให้ความร้อนผนังท่อแบบฟลักซ์ความร้อนคงที่ มีการสอดใส่แผ่นกั้นรูปวงแหวนวางเอียงมุมปะทะ 30° โดยทั้งแผ่นกั้นรูปตัวยูและวงแหวนที่ใส่ในช่องการไหล เพื่อศึกษาผลกระทบของมุมปะทะ ความสูง และระยะห่างระหว่างแผ่นกั้นที่มีต่อการสูญเสียความดัน การถ่ายเทความร้อน และตัวประกอบสมรรถนะเชิงความร้อน(η) ตามลำดับ ในการคำนวณเชิงตัวเลขใช้ระเบียบวิธีปริมาตรสี่เหลี่ยม การคู่ควบของความเร็วและความดันใช้วิธีแบบ SIMPLE และใช้แบบจำลองความปั่นป่วนแบบ RNG k- ϵ โดยใช้แบบแผนการคำนวณแบบ QUICK และใช้อากาศเป็นของไหลทดสอบ เลขเรย์โนลด์ส์ที่ศึกษาอยู่ในช่วง 3000 ถึง 20,000

จากการตรวจสอบแบบจำลองกับสมการสหสัมพันธ์จากบทความที่เคยตีพิมพ์ ผลที่ได้มีความสอดคล้องกันดี ผลจากการศึกษาเชิงตัวเลขพบว่า เมื่อเลขเรย์โนลด์ส์เพิ่มขึ้นค่าตัวประกอบความเสียดทานมีแนวโน้มลดลง ความสูงแผ่นกั้นที่เพิ่มขึ้นส่งผลให้ค่าเลขนัสเซิลท์เพิ่มขึ้นแต่ค่าตัวประกอบความเสียดทานก็เพิ่มขึ้นด้วย ค่า η ลดลงเมื่อเลขเรย์โนลด์ส์เพิ่มขึ้น เมื่อเพิ่มระยะห่างระหว่างแผ่นกั้นจะให้ค่าตัวประกอบความเสียดทานลดลง จากผลการคำนวณพบว่าช่องการไหลสี่เหลี่ยมผืนผ้า สี่เหลี่ยมจัตุรัส และท่อกลม ให้ค่า η สูงสุดเท่ากับ 1.83, 1.61 และ 1.54 ตามลำดับ ที่ค่าเลขเรย์โนลด์ส์ต่ำสุดที่ทำการทดสอบ ต่อมาทำการปรับปรุงแผ่นกั้นรูปตัววี แผ่นกั้นรูปตัวยู และแผ่นกั้นวงแหวนวางเอียงเป็นแผ่นกั้นรูปเกือกม้าวางเอียงและแผ่นกั้นเกือกม้ารูปตัววีใส่ในท่อกลม ผลการคำนวณเชิงตัวเลขพบว่าค่าตัวประกอบความเสียดทานลดลงซึ่งส่งผลให้ค่า η เพิ่มขึ้น โดยแผ่นกั้นรูปเกือกม้าวางเอียงให้ค่า η สูงสุดถึง 2.48 ที่ $PR=0.3$, $BR=0.1375$ และ $Re=3000$ แผ่นกั้นเกือกม้ารูปตัววีให้ค่า η สูงกว่าแผ่นกั้นรูปเกือกม้าวางเอียง ซึ่งมีค่า η สูงสุดเท่ากับ 2.76 ที่ $PR=0.35$, $BR=0.085$ และ $Re=3000$

Thesis Title	Numerical Heat Transfer Study in a Duct Equipped with Oblique Baffles
Student	Mr.Sombat Tamna
Student ID	53610201
Degree	Doctor of Engineering
Program	Mechanical Engineering
Year	2015
Thesis Advisor	Assoc.Prof.Dr. Chinaruk Thianpong
Thesis Co-Advisor	Assoc.Prof.Dr. Pongjet Promvonge

ABSTRACT

The thesis presents a 3D numerical simulation of turbulent tube/channel flow through oblique baffles. Three flow simulations were developed under a steady, three-dimensional, periodical, incompressible turbulent flow condition. Firstly, airflow and heat transfer behaviors in a rectangular channel fitted with 45° multiple V-baffles (VB) were examined under a constant heat-flux on the top wall or absorber plate only. The VBs were placed in a single baffle, inline and staggered baffle arrangements on the top and bottom walls. Secondly, effects of 30° inclined U-baffles (UB) mounted in a constant heat-fluxed square channel on the heat transfer rate are investigated. Thirdly, influences of insertion of 30° inclined vortex rings (VR) into a circular tube on thermal performance (η) are examined. Effects of relative VB/UB/VR height and pitch on heat transfer characteristics are also studied. The RNG k - ϵ turbulence model and the finite volume method with the QUICK scheme for handling the pressure-velocity coupling were used to solve the governing RANS equations. The air was used as working fluid for Reynolds numbers (Re) from 3000 to 20,000.

The simulation models were validated and verified with data from published correlations. The numerical studies revealed that the friction factor slightly decreased with increasing Re. The increment of BR significantly increased the Nusselt number and friction factor. The η decreased as Re increases. The numerical results show that the highest η values were 1.83, 1.61, and 1.54 at the lowest Re for the VB channel, UB square-channel and VR tube, respectively. In addition, in order to improve η , two types of baffles; the inclined horseshoe baffles (HB) and the V-shaped horseshoe baffles (VHB) that were the modification by integrating the VB, UB and VR merits were introduced and applied to the corresponding circular tube. The numerical result revealed that the friction factor for the HB/VHB was significantly reduced in comparison with that for the VR. The highest η for the HB was up to 2.48 at PR=0.3, BR=0.1375 and Re=3000. The VHB provided higher η than the HB and its maximum η was about 2.76 at PR=0.35, BR=0.085 and Re=3000.

ACKNOWLEDGEMENT

I would like to express my deepest gratitude to my thesis advisors, Assoc.Prof.Dr.Chinaruk Thianpong and Assoc.Prof.Dr.Pongjet Promvong, for the valuable advices, enlightening, and encouragement.

I would like to give my gratitude to Dr.Watcharin Noothong and Asst.Prof.Dr.Somchai Sripattanapipat for the suggestions and discussions on the heat transfer and computational fluid dynamics.

I extend my sincere thanks to Dr.Sompol Skullong, Dr.Suriya Chokphoemphun, Dr.Supattarachai Suwannapan, Mr.Chitakorn Khanoknaiyakarn, Mr.Prathan Srichai and other member staffs at the Thermo-Fluid and CFD Laboratory, Department of Mechanical Engineering, Faculty of Engineering, King Mongkut's Institute of Technology Ladkrabang, and my appreciation to my colleagues at Thai-Nichi Institute of Technology.

I gratefully acknowledge the Thailand Research Fund (TRF) for the financial support through the Royal Golden Jubilee Ph.D. program (Grant No. PhD/0218/2552).

My most sincere and very deepest thanks are to my parents, and my family for continuous encouragements and supports.

Sombat Tamna

CONTENTS

	Page
THAI ABSTRACT	I
ENGLISH ABSTRACT	II
ACKNOWLEDGEMENTS	III
CONTENTS	IV
LIST OF TABLES	VIII
LIST OF FIGURES	IX
NOMENCLATURE	XIII
CHAPTER 1 INTRODUCTION	1
1.1 The Motivation of the Research	1
1.2 Objectives of the Research	1
1.3 Thesis Outline	2
CHAPTER 2 LITERATURE REVIEW	4
2.1 Application of vortex flow devices in channel heat exchangers	4
2.1.1 Groove/Dimple	4
2.1.2 Ribs/Fins/Baffles/Winglets	5
2.2 Application of vortex flow devices in tubular heat exchangers	15
2.2.1 Wire coil inserts	15
2.2.2 Twisted tape inserts	16
2.2.3 Other vortex-flow devices	18
2.3 Concept of the research	25
CHAPTER 3 MATHEMATICAL FOUNDATION	27
3.1 Governing Equations	27
3.1.1 Equation of continuity	27
3.1.2 Equation of momentum	28
3.1.3 Equation of energy	28
3.2 Turbulence Modeling	29
3.2.1 Reynolds-averaged Navier-Stokes (RANS)	30
3.2.2 RNG $k - \varepsilon$ model	31
3.3 Finite Volume Method	32
3.4 Boundary Conditions	36
3.4.1 Wall boundary condition	36
3.4.2 Periodicity	37

CONTENTS (CONT'D)

	Page
3.5 Solution Algorithm.....	37
3.5.1 Pressure-velocity coupling with SIMPLE algorithm.....	37
3.5.2 Solution procedure.....	38
3.5.3 Key quantifying thermal enhancement factors.....	38
3.6 Flow Topology and Coherent Structure.....	40
3.6.1 Flow topology.....	40
3.6.2 Coherent structure.....	40
3.6.3 Q-criterion.....	41
CHAPTER 4 NUMERICAL SOLUTION PROCEDURE.....	42
4.1 Computational details of tube/channel flows.....	42
4.1.1 Baffle geometry and arrangement for numerical simulation.....	42
4.1.2 Computational domains.....	44
4.1.3 Grid generation.....	47
4.1.4 Boundary conditions.....	48
4.1.5 Computational schemes and convergence criteria.....	49
4.2 Verification of numerical simulation.....	50
4.2.1 Grid independence.....	50
4.2.2 Grid convergence index.....	50
4.2.3 Verification of smooth channel.....	51
CHAPTER 5 VALIDATION OF NUMERICAL SIMULATION.....	52
5.1 Verification of numerical simulation.....	52
5.1.1 Grid independence study.....	52
5.1.2 Verification of smooth tube.....	53
5.2 Validation of numerical simulation.....	54
5.2.1 Validation of VB/UB-channel flow models.....	54
5.2.2 Validation of HB-tube flow model.....	56
CHAPTER 6 TURBULATORS.....	59
6.1 Multiple V-baffles.....	59
6.1.1 Effects on heat transfer.....	59
6.1.2 Effects on friction factor.....	62
6.1.3 Effects on thermal enhancement factor.....	64

CONTENTS (CONT'D)

	Page
6.1.4 Flow and heat topologies for multiple V-baffles	65
6.2 Inclined U-baffles	72
6.2.1 Effects on heat transfer	72
6.2.2 Effects on friction factor	75
6.2.3 Effects on thermal enhancement factor	77
6.2.4 Flow and heat topologies for inclined U-baffles	78
6.3 Inclined Vortex Rings	82
6.3.1 Effects on heat transfer	82
6.3.2 Effects on friction factor	84
6.3.3 Effects on thermal enhancement factor	87
6.3.4 Flow and heat topologies for vortex rings	88
6.4 Conclusions	92
CHAPTER 7 HORSESHOE BAFFLES	94
7.1 Inclined horseshoe baffles	94
7.1.1 Effects on heat transfer	94
7.1.2 Effects on friction factor	97
7.1.3 Effects on thermal enhancement factor	99
7.1.4 Optimization for inclined horseshoe baffles	102
7.1.5 Flow and heat topologies for inclined horseshoe baffles	104
7.2 V-shaped horseshoe baffles	111
7.2.1 Effects on heat transfer	111
7.2.2 Effects on friction factor	112
7.2.3 Effects on thermal enhancement factor	113
7.2.4 Optimization for V-shaped horseshoe baffles	114
7.2.5 Flow and heat topologies for V-shaped horseshoe baffles	115
7.3 Empirical correlations	119
7.4 Conclusions	120
CHAPTER 8 CONCLUSIONS	122
8.1 Conclusions	122
8.2 Suggestions for future work	123

CONTENTS (CONT'D)

	Page
REFERENCES	124
APPENDIX	133
Author publications.....	134
AUTHOR BIOGRAPHY	137

LIST OF TABLES

Table	Page
2.1 Application of vortex flow devices in channel heat exchangers	7
2.2 Application of vortex flow devices in tube heat exchangers	19
3.1 Central coefficient and neighbor coefficients for the QUICK scheme	36
4.1 Numerical scheme/method used in the computation	49
4.2 Residual monitors and convergence criteria	49
5.1 Grid independence study of 30°HB , $\text{BR}=0.1$, $\text{PR}=1.0$ at $\text{Re}=3,000$	52

LIST OF FIGURES

Figure	Page
3.1 A typical velocity of one-dimensional turbulent flow at a point.....	30
3.2 A control volume around general node P	33
3.3 Quadratic profiles used in QUICK scheme.....	35
4.1 Channel geometry of periodic flow for VB.....	43
4.2 Duct geometry of periodic flow for UB	43
4.3 Tube geometry of periodic flow for VR.....	44
4.4 Tube geometry of periodic flow for HB	44
4.5 Tube geometry of periodic flow for VHB.....	44
4.6 Computational domain for VB module.....	45
4.7 Computational domain for UB module	46
4.8 Computational domain for VR module.....	46
4.9 Computational domain for HB module	46
4.10 Computational domain for VHB module.....	46
4.11 Hexahedral grid structure for VB module simulation.....	47
4.12 Hexahedral grid structure for UB module simulation	47
4.13 Hexahedral grid structure for VR module simulation.....	48
4.14 Hexahedral grid structure for HB module simulation	48
4.15 Hexahedral grid structure for VHB module simulation	48
5.1 Verification of predicted f_0 for smooth circular tube.....	53
5.2 Verification of predicted Nu_0 for smooth circular tube	54
5.3 Comparison of predicted f with measurement for VB-channel flow.....	55
5.4 Comparison of predicted Nu with measurement for VB-channel flow.....	55
5.5 Comparison of predicted f with measurement for UB-channel flow	56
5.6 Comparison of predicted Nu with measurement for UB-channel flow	56
5.7 Comparison of predicted f with measurement for HB-tube flow.....	57
5.8 Comparison of predicted Nu with measurement for HB-tube flow.....	57
6.1 Variation of Nu with Re for VB.....	60
6.2 Variation of Nu with PR for VB.....	60
6.3 Variation of Nu/Nu_0 with Re for VB	61
6.4 Variation of Nu/Nu_0 with PR for VB	61
6.5 Variation of f with Re for VB	62
6.6 Variation of f with PR for VB	63
6.7 Variation of f/f_0 with Re for VB.....	63
6.8 Variation of f/f_0 with PR for VB.....	64
6.9 Variation of η with Re for VB.....	65

LIST OF FIGURES (CONT'D)

Figure	Page
6.10 Variation of η with PR for VB	65
6.11(a) Streamlines in transverse planes for single VB at Re=8000 and PR=0.5	66
6.11(b) Streamlines in transverse planes for inline VB at Re=8000 and PR=0.5	67
6.11(c) Streamlines in transverse planes for staggered VB at Re=8000 and PR=0.5	67
6.12 Pressure contours in transverse planes for VB at Re=8000 and PR=0.5	68
6.13 Q isosurface of Q=200 for difference VB arrangement at PR=0.5 and Re=8,000	69
6.14 Temperature contours in transverse planes for VB at Re=8000 and PR=0.5	70
6.15 Local Nu_x contours on upper wall for (a) smooth channel (b) single VB (c) inline and (d) staggered VB arrays at Re=8000, PR=0.5	71
6.16 Streamlines and Nu_x contours on upper wall for inline VB at Re=8000 and PR=0.5	72
6.17 Variation of Nu with Re for UB	73
6.18 Variation of Nu with BR for UB	73
6.19 Variation of Nu/Nu_0 with Re for UB	74
6.20 Variation of Nu/Nu_0 with BR for UB	74
6.21 Variation of f with Re for UB	75
6.22 Variation of f with BR for UB	76
6.23 Variation of f/f_0 with Re for UB	77
6.24 Variation of f/f_0 with BR for UB	77
6.25 Variation of η with Re for UB	78
6.26 Variation of η with BR for UB	78
6.27 Streamline in transverse planes for UB at BR=0.2 and PR=2.0	79
6.28 Pressure contours in transverse plane for UB at BR=0.2 and PR=2.0	79
6.29 Q-isosurfaces of Q=200 for UB with various PRs at BR=0.2 and Re=8,000	80
6.30 Temperature contours in transvers plane of UB at BR=0.2 and PR=2.0	81
6.31 Local Nusselt number contours on the wall for UB at BR=0.2 and PR=2.0	81
6.32 Streamlines and Nu_x contours on the wall for UB at BR=0.2 and PR=2.0	81
6.33 Variation of Nu with Re for VR	83
6.34 Variation of Nu with BR for VR	83
6.35 Variation of Nu/Nu_0 with Re for VR	84
6.36 Variation of Nu/Nu_0 with BR for VR	84
6.37 Variation of f with Re for VR	85
6.38 Variation of f with BR for VR	85

LIST OF FIGURES (CONT'D)

Figure	Page
6.39 Variation of f/f_0 with Re for VR.....	86
6.40 Variation of f/f_0 with BR for VR.....	86
6.41 Variation of η with Re for VR	87
6.42 Variation of η with BR for VR	87
6.43 Streamline in transverse planes of VR at PR=2.0, BR=0.1, and Re=8,000.....	88
6.44 Pressure contour in transverse planes of VR for varied BR at Re=8,000	89
6.45 Pressure contour in transverse planes of VR for varied PR at Re=8,000	89
6.46 Q-isosurfaces of Q=200 for VR with various BR at PR=1.0 and Re=8000	90
6.47 Temperature contour in transverse planes of VR for varied BR at Re=8,000.....	91
6.48 Temperature contours in transverse planes for VR at Re=8000	91
6.49 Local Nu_x contours on the wall for VR at BR=0.1, PR=2.0, and Re=8000	92
7.1 Variation of Nu/Nu_0 with Re for 20° HB.....	95
7.2 Variation of Nu/Nu_0 with Re for 30° HB.....	96
7.3 Variation of Nu/Nu_0 with Re for 45° HB.....	96
7.4 Variation of Nu/Nu_0 with α for HB.....	97
7.5 Variation of f/f_0 with Re for 20° HB.....	98
7.6 Variation of f/f_0 with Re for 30° HB.....	98
7.7 Variation of f/f_0 with Re for 45° HB.....	99
7.8 Variation of f/f_0 with α for HB	99
7.9 Variation of η with Re for 20° HB	100
7.10 Variation of η with Re for 30° HB	100
7.11 Variation of η with Re for 45° HB	101
7.12 Variation of η with α for HB	102
7.13 Variation of Nu/Nu_0 with BR for various PR values.....	103
7.14 Variation of f/f_0 with BR for various PR values	103
7.15 Variation of η with BR for various PR values	104
7.16 Streamlines in transverse planes for 30° HB at Re=8,000, PR=2.0 and BR=0.1	105
7.17 Pressure contours in transverse planes for 30° HB at Re=8000	105
7.18 Pressure contours in transverse planes for 30° HB with various PR at Re=8000.....	106
7.19 Pressure contour in transverse planes for HB with various α at Re=8000	107
7.20 Q-isosurfaces of Q=200 for 30° HB with various BR at Re=8000, PR=1.0	108

LIST OF FIGURES (CONT'D)

Figure	Page
7.21(a) Temperature contours in transverse planes for 30° HB with PR=1.0, BR=0.15 and Re=8000	108
7.21(b) Temperature contours in transverse planes for 30° HB with PR=1.0, BR=0.2 and Re=8000.....	109
7.22(a) Temperature contours in transverse planes for 30° HB with BR=0.10, PR=0.5 and Re=8000.....	109
7.22(b) Temperature contours in transverse planes for 30° HB with BR=0.10, PR=1.0 and Re=8000.....	109
7.22(c) Temperature contours in transverse planes for 30° HB with BR=0.1, PR=2.0 and Re=8000.....	110
7.23(a) Temperature contours in transverse planes for 20°HB at Re=8000.....	110
7.23(b) Temperature contours in transverse planes for 45° HB at Re=8000	110
7.24 Local Nu_x contours on the wall for 30° HB with BR=0.10, PR=2.0 and Re=8000.....	111
7.25 Variation of Nu/Nu_0 with Re	111
7.26 Variation of Nu/Nu_0 with α	112
7.27 Variation of f/f_0 with Re.....	112
7.28 Variation of f/f_0 with α	113
7.29 Variation of η with Re.....	113
7.30 Variation of η with α	114
7.31 Variation of Nu/Nu_0 with BR for various PR values.....	114
7.32 Variation of f/f_0 with BR for various PR values	115
7.33 Variation of η with BR for various PR values	115
7.34 Streamlines in transverse planes for 30° VHB with PR=1.0 and BR=0.10 at Re=8,000.....	116
7.35(a) Pressure contours in transverse planes for 30° VHB at Re=8000	116
7.35(b) Pressure contours in transverse planes for 30° VHB at Re=8000.....	116
7.36 Q-isosurfaces of Q=200 for 30° VHB at Re=8000, PR=1.0.....	117
7.37 Temperature contours in transverse planes for 30° VHB at Re=8000	118
7.38 Local Nusselt number contours on left-half sidewall for 30° VHB at BR=0.1 and PR=1.0.....	119

NOMENCLATURE

Symbol, definition, SI units

A	Heat transfer area: m^2
b	Baffle height: m
BR	Baffle blockage ratio, (b/H), (b/D)
c_p, c_v	Specific heat capacity at constant pressure, volume: $J/(kg \cdot K)$
D	Tube inside diameter, diameter: m
D_h	Hydraulic diameter: m
f	Friction factor
g	Gravitational acceleration: m/s^2
h	Heat transfer coefficient: $W/(m^2 \cdot K)$
H	Channel height: m
i	Internal energy: m
k	Thermal conductivity: $W/(m \cdot K)$
k	Turbulent kinetic energy
K	Mean kinetic energy
L	Length: m
\dot{m}	Mass flow rate: kg/s
Nu	Nusselt number
p_l	Longitudinal pitch: m
p_t	Transverse pitch: m
P	Pressure: Pa, N/m^2
Pr	Prandtl number
PR	Pitch or spacing ratio, (L/H)
ΔP	Pressure drop: Pa, N/m^2
q	Heat transfer rate: W
q_s	Surface heat flux: W/m^2
Q	Heat transfer rate: W or Second scalar invariant of the velocity gradient tensor
T	Temperature: $^{\circ}C$, K
ΔT	Temperature difference: $^{\circ}C$, K
t	Time: s
u, v, w	Velocity component in x, y, z directions in rectangular coordinates: m/s
U	Velocity vector: m/s
W	Channel width: m
x, y, z	Rectangular Cartesian coordinates: m

NOMENCLATURE (CONT'D)

Greek

δ	Boundary layer thickness: m
Γ	thermal diffusivity
Ω_{ij}	vorticity tensor
α	baffle inclination angle or angle of attack, degree
ε	Viscous dissipation
η	Thermal enhancement factor(= $(Nu/Nu_0)/(f/f_0)^{1/3}$)
μ	Dynamic viscosity: Pa·s
ν	Kinematic viscosity: m^2/s
ρ	Fluid density: kg/m^3
τ	shear stress: Pa, N/m^2
Φ	Viscous dissipation function

Subscripts

b	Bulk mean
eff	Effective
i, j, k	Cartesian indices
in	Inlet
m	Mean value
out	Outlet
ref	Reference
s	Surface value
x, y, z	The x, y, z components
w	Wall value
0	Smooth channel

Superscripts

+	Sublayer-scaled value
'	Fluctuating quantity

Mathematical operation symbols

d/dx	Derivative with respect to x: m^{-1}
$\partial/\partial t$	Partial time derivative operator: s^{-1}

CHAPTER 1

INTRODUCTION

1.1 The Motivation of the Research

In recent years, many techniques have been proposed for enhancement of the heat-transfer rate in a tube/channel. These can be classified into two main groups:

- Passive technique requiring no additional power source
- Active technique requiring additional external power inputs

In the case of the passive technique, convection heat transfer from surfaces by attachments of different solid shapes with different geometries, such as baffles, fins, ribs, blocks and winglets, have been widely exploited. Heat transfer augmentation with such arrangements can be achieved by the increase in the surface area (surface extension) and also by the high turbulence intensity (mixing) generated due to the attachments of those vortex-flow devices. This type of forced convection heat transfer is encountered in much process equipment such as heat exchangers, nuclear reactor fuel elements, turbine blades, electronic boards and components etc. Improved heat-transfer rates are normally accompanied by the increase in pressure drop in the flow over such surfaces. Thus the main target is to design the attachments in such a way and the geometry that they will yield the maximum enhancement in the heat-transfer rate with minimum increase in pressure drop or minimum decrease in the flow rate.

As mentioned earlier, the heat transfer enhancement is achieved at the expense of an increased pressure drop. Energy loss due to the pressure drop may sometimes exceed that gained due to the heat-transfer enhancement. For many practical applications, it may thus be necessary to determine the net economic benefit due to the heat-transfer enhancement.

1.2 Objectives of the Research

The primary objective of the research is to study numerically the heat transfer enhancement in a baffled channel/tube in order to understand the physical phenomena of heat transfer enhancement and flow characteristics. In the present study, numerical computations are carried out using a well-known commercial program, ANSYS FLUENT 14.5 that is suitable for the complex vortex flow.

The main research objectives are as follows:

1. To obtain numerical solutions for fluid flow in a heat exchanger tube/channel with angled/inclined baffles to allow studying the effect of baffle height, baffle pitch length, angle of attack and orientation on heat transfer enhancement.

2. To try to explain the mechanism of heat transfer augmentation in a heat exchanger tube from the results of the numerical computations
3. To evaluate the optimum thermal performance of the baffled tube using air as a working fluid.

1.3 Thesis Outline

The thesis consists of 8 chapters, the contents of which are briefly described below:

Chapter 1 introduces the motivation of the research and the objectives of the study.

Chapter 2 starts with the literature survey in experimental and computational research work on baffled channels/tube and flow topology.

Chapter 3 provides the mathematical foundations employed as the governing equations in the numerical simulation. The turbulence model is introduced to represent the physics of fluid flow. The finite volume method is briefly described to solve the algebraic equations discretized from the governing equations. The solution algorithm, the solution procedure, and the boundary conditions are explained. The key quantifying performance parameters are defined to evaluate the thermal performance.

Chapter 4 describes the numerical flow model and the computational details to represent the computational domain of interest. The geometries and arrangements of the baffles placed in the channel/tube are prescribed. The grid generation, the boundary conditions, and the computational schemes are presented. The validation methods are described and discussed.

Chapter 5 presents the validation of the numerical flow model. For validation purpose, the comparisons of numerical solutions with experimental data are described and discussed.

Chapter 6 deals with the numerical solutions of the multiple V-baffles, inclined U-baffles and inclined vortex rings in a channel/tube. The flow topology and coherent structures of the air flow and mechanism of heat transfer enhancement using the baffles are described and discussed. The effects of the baffle geometries and arrangements on the pressure loss, heat transfer and thermal performance are reported and discussed.

Chapter 7 explains the numerical results of the modified vortex rings in the form of the inclined horseshoe baffles and V-shaped horseshoe baffles inserted into a circular tube. The flow topology and coherent structures of the air flow and details of heat transfer enhancement by both the horseshoe baffle inserts are described and discussed. Influents of attack angle, blockage ratios and pitch ratios on heat transfer

are examined. The optimum geometrical configuration of the baffles that provides the highest thermal performance is also presented.

Chapter 8 summaries the main conclusions of the thesis and makes suggestions for future work.

CHAPTER 2

LITERATURE REVIEW

The heat transfer enhancement (HTE) methods in a heat exchanger system are needed for engineering and industrial work. In general, the HTE methods can be divided into two groups which are the passive and the active methods [1,2]. The passive HTE without stimulation by external power, such as a rough surfaces, extended surfaces, swirl/vortex flow devices, surface tension devices, etc. The active HTE, which requires extra external power sources, such as mechanical aids, swirl flow-turbulator devices, flow-induced vibration, surface-fluid vibration, injection and suction of the fluid, jet impingement. The vortex/swirl flow devices have been commonly used passive HTE methods in single-phase internal flows in a tube/duct/channel heat exchanger by placing or inserting the rib, fin, baffle, winglet, wire coils, helical/twisted tapes, vortex rings and conical into the tube/duct/channel to enhance heat transfer rate in the system.

Since the present study relates to heat transfer enhancement using a vortex flow devices with the air and water, therefore, the following literature reviews are focused mainly on relevant passive HTE methods for the air. The reviews are divided into two parts for both experimental and numerical work. First, the articles of duct/channel heat exchanger researches are surveyed due to the extensive studies in the field of HTE. Second, the articles of convective heat transfer enhancement of circular tube heat exchangers are reviewed and discussed.

2.1 Application of vortex flow devices in channel heat exchangers

Many research used passive HTE method to enhance the thermal performance of duct/channel heat exchangers such as insertion of vortex flow devices, artificial roughness on a surface with vortex flow devices (grooves/ribs/fins/baffles/winglets), dimpled surface and so on. The development of thermal boundary layer or the laminar sub layer near the wall can be reduce by using such method. The literature survey of various vortex flow devices used in channel heat exchangers is presented in Table 2.1.

2.1.1 Groove/Dimple

Earlier studies carried out on vortex flow in channel utilized different geometries to enhance the thermal performance. For groove and dimple applications, Jaurker et al. [3] studied experimentally the heat transfer and friction characteristics of rib-grooved artificial roughness on one broad heated wall. They

found that the heat transfer coefficient for rib-grooved arrangement is higher than that for the transverse ribs as compared to that of rectangular transverse ribs of similar rib height and rib spacing. Jin et al. [4] studied the effects of the pulsating flow agitation on the heat transfer in a triangular grooved channel. Layek et al. [5] carried out studies the effect of repeated integral transverse chamfered rib-groove roughness on one broad wall of rectangular duct. The mass transfer enhancement in grooved channels with different cavity lengths for pulsatile flow were proposed by Nishimura et al. [6] A numerical investigation of turbulent forced convection in a two dimensional channel with periodic transverse grooves by utilizing $k-\epsilon$ turbulence model on the lower channel wall was conducted by Eiamsa-ard and Promvonge [7]. The influence of discrete grooved structures of P, V and W-type grooves on heat transfer enhancement in a narrow channel were studied by Tang et al. [8]. Xia et al. [9] numerically studied the heat transfer enhancement by longitudinal vortex generators in a three-dimensional dimple heat exchangers. The effect of conventional dimpled cavity with secondary hemispherical protrusions on flow characteristics and heat transfer performances of rectangular dimpled channels was numerically investigated by Liu et al. [10]. Skullong et al. [11] investigated experimentally the thermal performance of turbulent flow in a solar air heater channel with combined wavy-rib and groove turbulators. They found that the ribbed-grooved upper wall at PR = 0.5 yields the highest thermal performance.

2.1.2 Ribs/Fins/Baffles/Winglets

Both experimentally and numerically for using ribs/fins/baffles/winglets and combined devices in duct/channel [12–50]. Fiebig [12] studied the effects of embedded vortices in internal flow on heat transfer and pressure loss enhancement. It was concluded that the longitudinal vortex generators generate higher heat transfer enhancement for the same pressure penalty than transverse vortex generators. Numerical simulations of turbulent flows and heat transfer in a rib-roughened channel with longitudinal vortex generatorst were carried out by Zhu et al. [13]. Numerical and experimental determination of flow structure and heat transfer effects of longitudinal vortices in a channel flow was conducted by Biswas et al. [14]. Verma and Prasad [16] investigated the optimal thermohydraulic performance of artificially roughened solar air heaters and the optimal thermohydraulic performance curves are suitable for the practical design of such collectors. Karwa et al. [17] experimentally investigated the thermo-hydraulic performance of solar air heaters having integral chamfered rib roughness on absorber plates, the thermal efficiency (10 to 40%) of solar air heaters with artificially

roughened absorber plate due to the enhancement in the Nusselt number of the order of 50 to 120% over the smooth absorber plate.

An experimental study of heat transfer characteristics of a pair of longitudinal vortices using color capturing technique was conducted by Kim and Yang [18]. Momin et al. [19] experimentally investigated the heat transfer and friction in solar air heater duct with V-shaped rib roughness on absorber plate. It was observed that the maximum enhancement of Nusselt number and friction factor as a result of providing artificial roughness has been found to be respectively 2.30 and 2.83 times that of smooth duct for an angle of attack of 60° . An experimental study heat transfer and friction behaviors in rectangular channels with varying number of ribbed walls was conducted by Chandra et al. [22]. A numerical of laminar flow and heat transfer in the horizontal channel with staggered baffles proposed by Mousavi and Hooman [66]. The correlations for Nusselt number and friction factor for solar air heater with roughened duct having arc-shaped wire as artificial roughness have been developed by Saini and Saini [32]. A numerical study on laminar convection heat transfer in a channel with longitudinal vortex generator were proposed by Wu and Tao [36, 37]. Chu et al. [40] numerically explored the three-dimensional numerical study on fin-and-oval-tube heat exchanger with longitudinal vortex generators (LVGs). They pointed out that the LVGs with placement of downstream, angles of attack $\alpha = 30^\circ$ and minimum tube-row number provide the best heat transfer performance. The effects of combined ribs and winglet type vortex generators (WVGs) on forced convection heat transfer and fluid friction behaviors in a triangular ribbed channel was investigated experimentally by Promvong et al. [42]. A numerical study of laminar flow and heat transfer in square channel with different baffle were reported by Promvong et al. [44, 45] and Promvong and Kwankaomeng [46]. The effect of Z-shaped baffle placed on the absorber plate at three blockage ratios and pitch ratios on heat transfer augmentation in a rectangular channel was investigated experimentally and numerically by Sriromreun et al. [47]. Tamna et al [50] investigated experimentally and numerically the turbulent flow and heat transfer in a three-dimensional solar air heater channel with multiple V-baffle vortex generators BVG. They found that the single BVG with PR = 0.5 yields the highest thermal performance.

Table 2.1 Application of vortex flow devices in channel heat exchangers

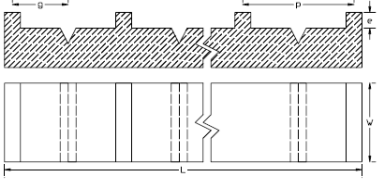
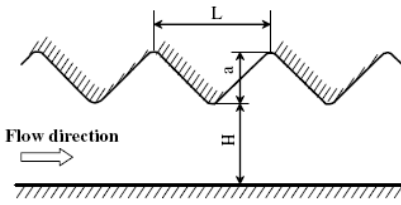
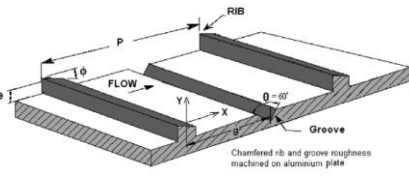
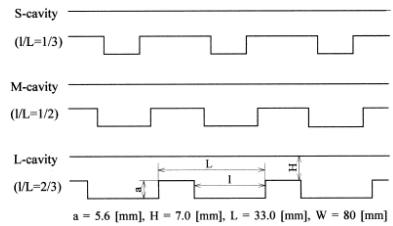
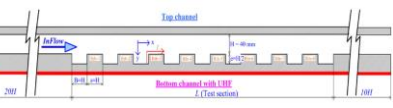
Authors and configuration	Conditions	Results
<p>Jaurker et al. [3]</p> 	<p>Re=3000–21,000, V-shaped rib with relative roughness height of 0.02–0.034 and angle of attack of flow of 30°–90°</p>	<p>Maximum Nu = 160 Maximum f = 0.04 Maximum η = 1.8</p>
<p>Jin et al. [4]</p> 	<p>Re=270–910, Pulsating flow in a triangular grooved channel with PIV system</p>	<p>Maximum of 350% of heat transfer enhancement is achieved compared to the steady flow case</p>
<p>Layek et al. [5]</p> 	<p>Re=3000–21,000, Transverse chamfered rib-groove with $e/D_h=0.022-0.04$, $P/e=4.5-10$, $g/P=0.3-0.6$ and $\phi = 5-30^\circ$</p>	<p>Maximum Nu = 180 Maximum f = 0.033</p>
<p>Nishimura et al. [6]</p> 	<p>Re=40–1400, Grooved channels for pulsatile flow</p>	<p>The enhancement at intermediate Strouhal numbers, depending on the cavity length and Reynolds number</p>
<p>Eiamsa-ard and Promvonge [7]</p> 	<p>Re=6000–18,000, Transverse grooves with the groove-width to channel-height ratio, $B/H = 0.5 - 1.75$, groove pitch ratio = 2 and depth ratio = 0.5.</p>	<p>Maximum Nu = 63 Maximum f = 0.04 Maximum η = 1.33</p>

Table 2.1 (cont'd)

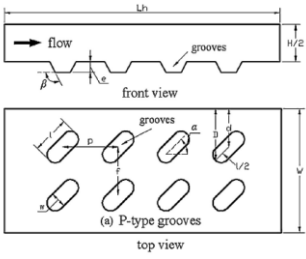
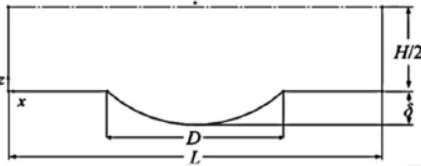
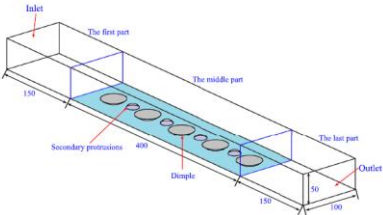
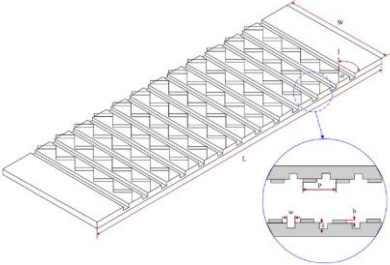
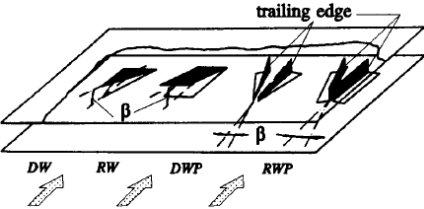
Authors and configuration	Conditions	Results
<p>Tang et al. [8]</p>  <p>(a) P-type grooves</p>	<p>Re=4016–10,709, P, V and W-type grooves</p>	<p>$Nu/Nu_0 = 1.6-1.9$ $f/f_0 = 2.0-2.3$ $\eta = 1.25-1.48$</p>
<p>Xia et al. [9]</p> 	<p>Re=400–1200, Dimples and grooved crescent- shape protrusion added surface</p>	<p>$Nu/Nu_0 = 1.15-1.6$ $f/f_0^{1/3} = 0.9-1.15$ $\eta = 1.4$</p>
<p>Liu et al. [10]</p> 	<p>Re=5000–25,000, Primary dimples, primary dimple with secondary protrusion and primary dimple with two secondary protrusions</p>	<p>$Nu/Nu_0 = 1.52-1.82$ $f/f_0 = 1.64-1.98$ $\eta = 1.28-1.46$</p>
<p>Skullong et al. [11]</p> 	<p>Re=4000–21,000, Wavy-rib and groove</p>	<p>$Nu/Nu_0 = 4.4-7.69$ $f/f_0 = 14-134$ $\eta = 1.1-1.75$</p>
<p>Fiebig [12]</p> 	<p>Re=350–300,000, Winglets and wing-type vortex generators</p>	<p>longitudinal vortex generators generate higher heat transfer enhancement for the same pressure penalty than transverse vortex generators.</p>

Table 2.1 (cont'd)

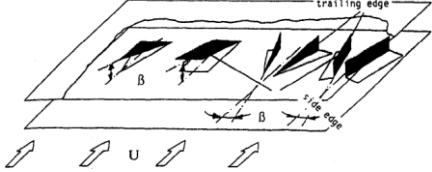
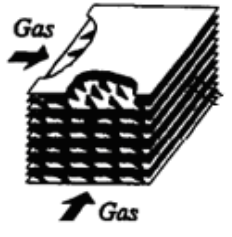
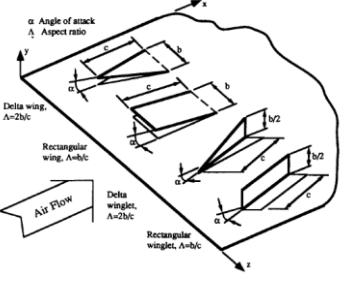
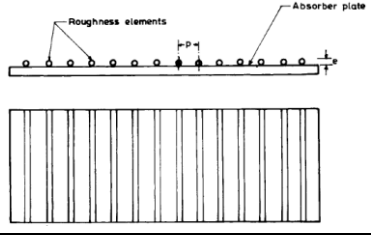
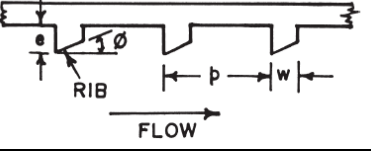

Authors and configuration	Conditions	Results
Zhu et al. [13] 	$Re=300,000$, Delta wing, rectangular wing, delta winglet pair and rectangular winglet pair	$Nu/Nu_0 = 2.1$ $f/f_0 = 3.59$ $\eta = 1.25-1.48$
Biswas et al. [14] 	$Re=1580$, Winglet	$Nu_{sa} = 50$
Gentry and Jacobi [15] 	$Re=600-1000$, Delta-Wing	$Sh_e/Sh_0 = 1.48-1.60$
Vermaa and Prasad [16] 	$Re=5000-20,000$, Small diameter wires	$Nu/Nu_0 = 1.29-2.08$ $f/f_0 = 14-134$ $\eta = 1.1-1.75$
Karwa et al. [17] 	$Re=3750-16,350$, Rib roughness on absorber plates	$Nu/Nu_0 = 1.44-2.2$ $f/f_0 = 1.8-3.8$
Kim and Yang [18] 	$\beta = -20-45^\circ$, $X = 5, 10, 20$ and 35	$St = 6.0-8.7$

Table 2.1 (cont'd)

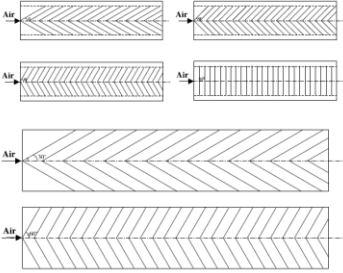
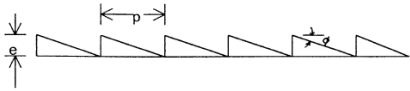
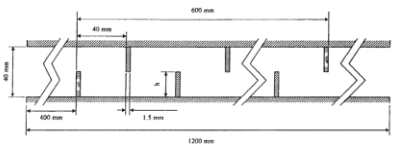
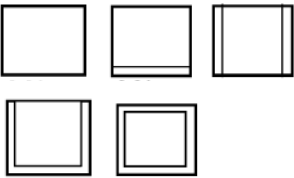
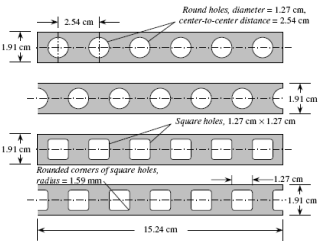
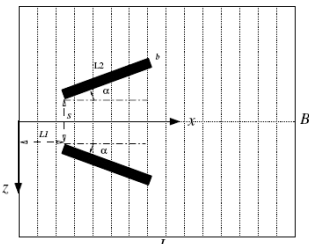
Authors and configuration	Conditions	Results
<p>Malik et al. [19]</p> 	<p>Re=2500–18000, V-shaped rib</p>	<p>Maximum Nu = 69 Maximum $f = 0.033$ Maximum $\eta = 1.8$</p>
<p>Bhagoria et al. [20]</p> 	<p>Re=3000–18000, Transverse wedge shaped rib</p>	<p>Maximum Nu = 110 Maximum $f = 0.040$</p>
<p>Yang and Hwang [21]</p> 	<p>Re=10,000–50,000, Porous-baffle</p>	<p>Nu/Nu₀ = 10–80</p>
<p>Chandra et al. [22]</p> 	<p>Re=10,000–80,000, Varying number of ribbed walls</p>	<p>Nu/Nu₀ = 1.0–5.0 $f/f_0 = 1.2–12$ $\eta = 1.0–1.8$</p>
<p>Lau et al. [23]</p> 	<p>Re=7000–28,000, Round and square holes in a wide rectangular channel</p>	<p>Nu/Nu₀ = 4.7–6.3 $f/f_0 = 270–490$ $\eta = 0.65–1.1$</p>
<p>Sohankar [24]</p> 	<p>Re=200–2000, vee-shaped rib</p>	<p>$f/J = 5.37–7.7$</p>

Table 2.1 (cont'd)

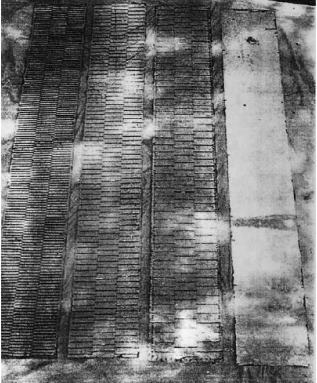
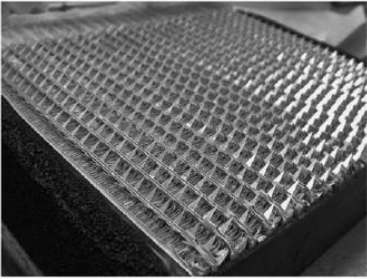
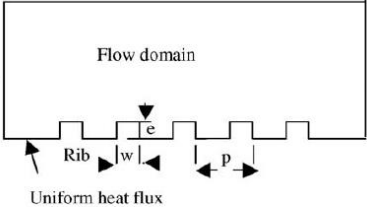
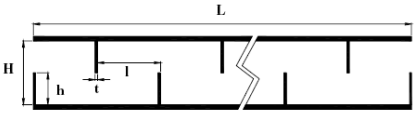
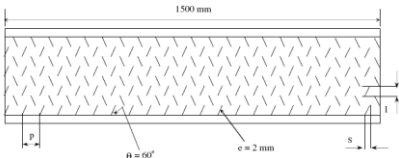
Authors and configuration	Conditions	Results
<p>Sahu and Bhagoria [25]</p> 	<p>Re=3000–12,000, 90° broken transverse ribs</p>	<p>Nu = 9.57–42.73 Thermal efficiency = 51.29–83.15%</p>
<p>Joardar and Jacobi [26]</p> 	<p>Re=200–550, Louver-fin</p>	<p>$h = 32\text{--}140 \text{ W/m}^2 \text{ K}$ $f = 5\text{--}8$</p>
<p>Chaube et al. [27]</p> 	<p>Re=3000–20,000, Rib roughness on absorber plate</p>	<p>Nu = 20–210 $f = 0.02\text{--}0.16$ $\eta = 1.3\text{--}2.15$</p>
<p>Mousavi and Hooman [28]</p> 	<p>Re=50–500, Staggered baffles</p>	<p>$Nu/Nu_0 = 1.0\text{--}3.5$</p>
<p>Karmare and Tikekar [29]</p> 	<p>Re=4000–17,000, Metal grit ribs</p>	<p>Nu = 20–95 $f = 0.01\text{--}0.024$ $\eta = 2\text{--}3$</p>

Table 2.1 (cont'd)

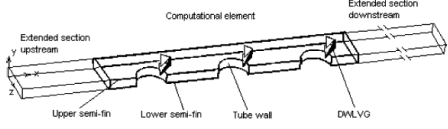
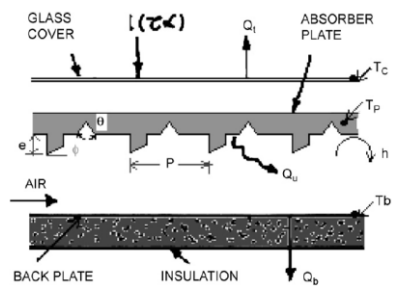
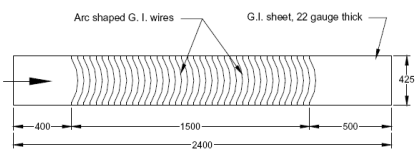
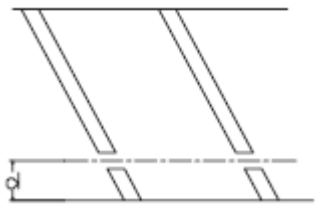
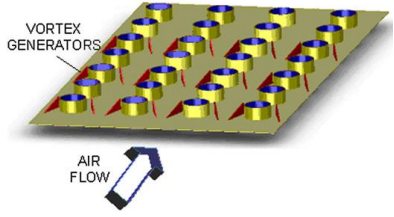
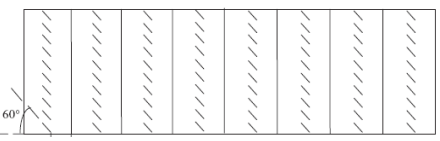
Authors and configuration	Conditions	Results
<p>Wu and Tao [30]</p> 	<p>Re=800–2000, Delta winglet, $\alpha = 30$ and 45°</p>	<p>Nu = 16–30 $\Delta P = 8–38$</p>
<p>Layek et al. [31]</p> 	<p>Re=200–550, Transverse chamfered rib-groove</p>	<p>Augmentation entropy generation number (N_a) = 0.56–1.2</p>
<p>Saini and Saini [32]</p> 	<p>Re=2000–17,000, Arc-shaped wire, $W/H = 12$, $P/e = 10$, $e/d = 0.0213–0.0422$, $\alpha/90 = 0.3333–0.6666$</p>	<p>Nu = 10–130 $f = 0.012–0.18$</p>
<p>Aharwal et al. [33]</p> 	<p>Re=3000–18,000, Inclined continuous rib with gap, $P/e = 10$, $e/Dh = 0.0377$, $\alpha = 60^\circ$, $g/e = 0.5–2$ and $d/W = 0.1667–0.667$</p>	<p>$Nu/Nu_0 = 1.5–2.6$ $f/f_0 = 2.0–2.9$ $\eta = 1.0–1.85$</p>
<p>Joardar and Jacobi [34]</p> 	<p>Re=220–9600, Winglet-type vortex generator arrays in compact plain-fin- and-tube</p>	<p>$J/f = 0.15–0.375$ $Z = 9–25 \text{ W/m K}$</p>
<p>Varun et al. [35]</p> 	<p>Re=2000–14,000, Transverse element- rib</p>	<p>Nu = 4–59 $f = 0.03–0.08$ $\eta = 0.11–0.79$</p>

Table 2.1 (cont'd)

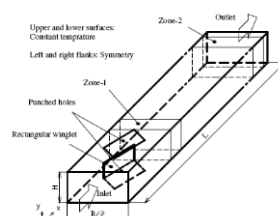
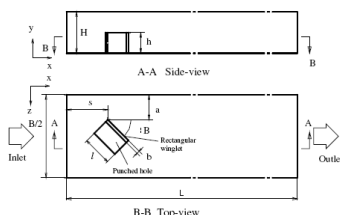
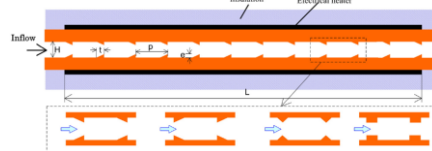
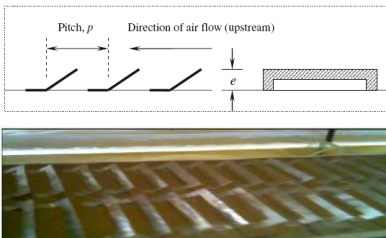
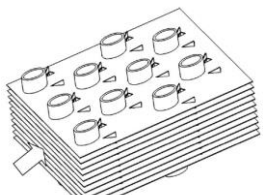
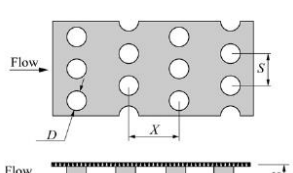
Authors and configuration	Conditions	Results
<p>Wu and Tao [36]</p> 	<p>Re=1600, Rectangular winglet, $\alpha = 30-45^\circ$</p>	<p>$Nu/Nu_0 = 1.132-1.289$ $f/f_0 = 1.18-1.68$</p>
<p>Wu and Tao [37]</p> 	<p>Re=800-3000, Rectangular winglet, $\alpha = 15-90^\circ$</p>	<p>$Nu/Nu_0 = 1.05-1.23$ $f/f_0 = 1.1-2.3$</p>
<p>Promvongse and Thianpong [38]</p> 	<p>Re=4000-16,000, Wedge (right-triangular) and rectangular shapes rib</p>	<p>$Nu/Nu_0 = 2.6-4.4$ $f/f_0 = 10-170$ $\eta = 0.8-1.1$</p>
<p>Bopche and Tandale [39]</p> 	<p>Re=3800-18,000, U-shaped, $P/e = 6.67-57.14$</p>	<p>$Nu/Nu_0 = 1.4-2.28$ $f/f_0 = 1.5-1.98$ $\eta = 1.3-1.82$</p>
<p>Chu et al. [40]</p> 	<p>Re=500-2500, Delta winglet</p>	<p>$Nu = 0.3-0.8$ $f = 8.5-14.5$</p>
<p>Yu et al. [41]</p> 	<p>Re=1678-8500, Stagger-arrayed short pin fins</p>	<p>$Nu = 8-130$ $f = 0.03-7$ $\eta = 1.06-1.82$</p>

Table 2.1 (cont'd)

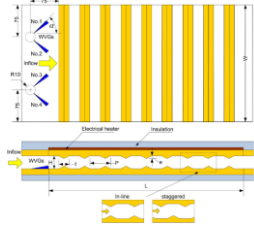
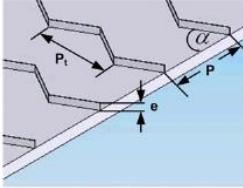
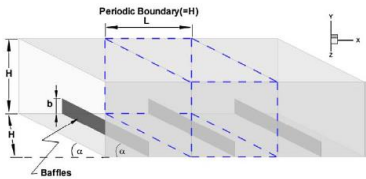
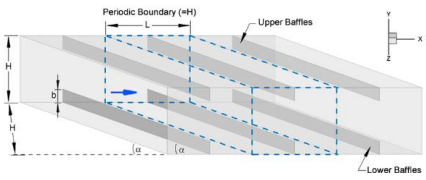
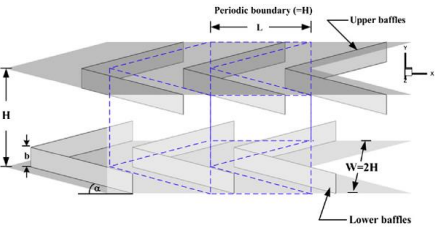
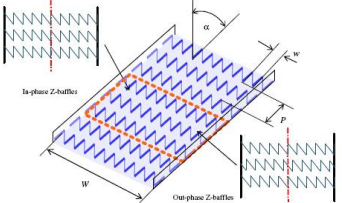
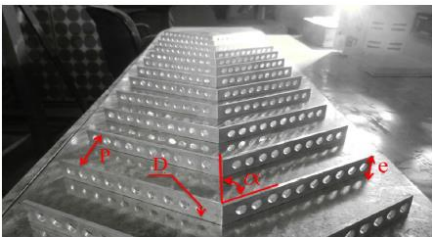
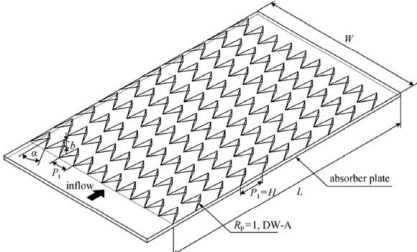
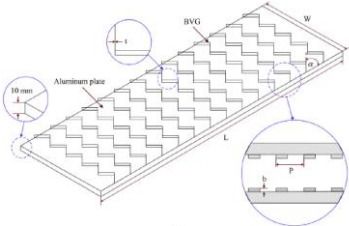
Authors and configuration	Conditions	Results
Promvonge et al. [42] 	$Re=5000-22,000$, Triangular rib and winglet	$Nu/Nu_0 = 2.2-2.6$ $f/f_0 = 2.2-5.5$ $\eta = 0.9-1.65$
Promvonge [43] 	$Re=5000-25,000$, Multiple 60° V-baffles	$Nu/Nu_0 = 2.6-5.8$ $f/f_0 = 5-38$ $\eta = 1.47-1.87$
Promvonge et al. [44] 	$Re=100-1200$, 45° inclined baffles on one wall	$Nu/Nu_0 = 1.5-8.7$ $f/f_0 = 2-70$ $\eta = 0.5-2.2$
Promvonge et al. [45] 	$Re=100-2000$, 30° in-line angled baffle on two opposite channel walls	$Nu/Nu_0 = 0.9-16$ $f/f_0 = 1-54$ $\eta = 1-4$
Promvonge and Kwankaomeng [46] 	$Re=100-1200$, 45° staggered V-baffles	$Nu/Nu_0 = 0.9-11$ $f/f_0 = 1-90$ $\eta = 0.9-2.8$
Sriromreun et al. [47] 	$Re=4400-20,400$, Z-shaped baffles	$Nu/Nu_0 = 4.3-6.7$ $f/f_0 = 6.5-36$ $\eta = 1.4-2.2$

Table 2.1 (cont'd)

Authors and configuration	Conditions	Results
<p>Alam et al. [48]</p> 	<p>Re=2000–20,000, V blocks with relative blockage height of 0.4–1.0, relative pitch ratio of 4–12 and open area ratio of 5–25%</p>	<p>$Nu/Nu_0 = 6.76$ $f/f_0 = 28.84$ $\eta = 2.5–3.0$</p>
<p>Skullong and Promvonge [49]</p> 	<p>Re=5000–24,000, Delta-winglet,</p>	<p>$Nu/Nu_0 = 1.5–1.61$ $f/f_0 = 2.1–3.5$ $\eta = 2.15$</p>
<p>Tamna et al. [50]</p> 	<p>Re=4000–21,000, 45° multiple V-baffle</p>	<p>$Nu/Nu_0 = 3.91–7.53$ $f/f_0 = 12.5–129.6$ $\eta = 1.83$</p>

2.2 Application of vortex flow devices in tubular heat exchangers

For enhancement of heat transfer in a tubular heat exchanger, the wire coils, helical/twisted tapes, vortex rings and conical turbulators have been widely used. The literature survey on different types of vortex flow devices used in tubular heat exchangers is presented in Table 2.2.

2.2.1 Wire coil inserts

Wire-coil inserts is one of the HTE methods and put into the flow tube/duct to improve the energy transport at the heated surface indirectly that helps improve fluid mixing between the core and the near-wall flow regions, thus the heat transfer is enhanced by fast fluid mixing. Promvonge [51] investigated and compared the results between the effects of square cross-sectional and circular cross-sectional coil-wires on the heat transfer and flow friction characteristics in a tube having a uniform wall heat-flux and also, studied the wire coil insert in conjunction with a snail-type

swirl generator mounted at the tube entrance as reported in Ref. [52]. Promvonge [53] investigated the effect of combined wire coil and twisted tape on heat transfer and turbulent flow friction characteristics in a uniform heat-fluxed tube. The twisted tape was inserted into the wire coil, both wire coil and twisted tape was placed inside the test tube to create a continuous impinging swirl flow along the tube wall.

Gunes et al. [54] investigated the equilateral triangle cross-sectioned coiled-wire inserted with three pitch ratios and two different ratio of equilateral triangle length side to tube diameter heat transfer enhancement and pressure drop of airflow in a tube heat exchanger. Gunes et al. [55] again studied experimentally on heat transfer and pressure drop in a heat exchanger tube with coiled-wire inserts placed separately from the tube wall with three pitch ratios ($P/D = 1$, $P/D = 2$ and $P/D = 3$) and two different distances ($s = 1$ mm, $s = 2$ mm) in turbulent flow regime ($Re = 4105$ to $26\,400$). The combined devices with non-uniform wire coil and twisted tape inserts on thermal performance characteristics in a tube were studied by Eiamsa-ard et al. [56]. The optimum values of the design parameters, the ratio of the distance between the coiled wire and test tube wall to tube diameter (s/D), pitch ratio (P/D), ratio of the side length of equilateral triangle to tube diameter (a/D) of equilateral triangular cross-sectioned coiled wire inserts in a tube were studied by Gunes et al. [57]. Nasr et al. [58] presented an application of artificial neural networks (ANNs) to characterize thermo-hydraulic behavior of helical wire coil inserts inside tube with four types of wire coils which were tested within a geometrical range with helical pitch $0.156 < p/d_h < 0.354$ and wire diameter $0.027 < e/d_h < 0.094$.

2.2.2 Twisted tape inserts

Earlier studies of passive HTE with swirl flow devices, the twisted-tape inserts have been extensively investigated both experimentally and numerically for augmentation of the heat transfer rate in tube heat exchangers.

The insertion of twisted tapes is widely employed in heat transfer engineering applications for enhancing the heat transfer rate in a heat exchanger system. In general, the twisted tape is can be divided into two groups: typical and modified twisted-tapes. Both typical and modified twisted-tapes have been made by focusing on the effect of geometry and twist ratio on heat transfer and flow friction in tubes. For typical twisted tape is to create swirl generator that help to increase turbulence levels resulting in improved heat transfer rate, albeit with a minimal pressure loss penalty. Eiamsa-ard et al. [59] studied the effects of the short-length typical twisted tapes with various tape-length ratios on heat transfer, friction factor and thermal performance characteristics. Eiamsa-ard et al. [60] again investigated the thermal characteristics in a heat exchanger tube with dual twisted tape elements in tandem.

Bas and Ozceyhan [61] experimentally investigated on heat transfer enhancement in a tube with twisted tape inserts placed separately from the tube wall with five twist ratios ($y/D = 2, 2.5, 3, 3.5$ and 4) and two clearance ratios ($c/D = 0.0178$ and 0.0357). Bhuiya et al. [62] experimentally studied the effects of triple twisted tape inserts with four different twist ratios ($y = 1.92, 2.88, 4.81$ and 6.79) on heat transfer rate, friction factor and thermal enhancement efficiency. Bhuiya et al. [63] again presented the experimental results of the heat transfer and fluid friction characteristics in a heat exchanger tube with double counter twisted tape inserts. The regularly-spaced twisted tape elements with two twisted ratios ($y=6.0$ and 8.0) and three space ratios ($S=1.0, 2.0,$ and 3.0) on heat transfer and pressure loss in a double pipe heat exchanger were reported by Eiamsa-ard et al. [64].

On the other hand, modifications of twisted tapes were made with a view to the increase in heat transfer rate rather than the reduction of friction loss. These can be divided into several categories such as tape-edge modification [65–67], tape-surface modification [68, 69], helical left–right screw tapes [70–72], alternate-axes twisted-tapes [73, 74] and twisted tapes with wings [75–77]. The effect of twisted tape with serrated-edge insert on heat transfer and pressure loss behaviors for turbulent flow Reynolds numbers from 4000 to 20,000 was carried out by Eiamsa-ard and Promvong [65]. Influences of using the serrated twisted tape on heat transfer enhancement in a tube were also reported by Chang et al. [68]. Sivashanmugam and Suresh [70] conducted an experimental work on heat transfer and friction factor of circular tube fitted with full-length helical screw element of different twist ratio, and helical screw inserts with spacer length 100, 200, 300, and 400 mm. Eiamsa-ard and Promvong [73] examined the heat transfer and flow friction characteristics in a circular tube equipped with two types of twisted tapes: (1) typical twisted tapes and (2) alternate clockwise and counterclockwise twisted tapes (C–CC twisted tapes). They found that the C–CC twisted-tapes provided higher heat transfer rate, friction factor and heat transfer enhancement index than the typical twisted-tapes. The modifications of twisted tapes were used for heat transfer augmentation by numerical researchers. Guo et al. [78] conducted a numerical investigation on heat transfer and friction factor characteristics in a circular tube fitted with center-cleared twisted tape. The results showed that the thermal performance factor of the tube with center-cleared twisted tape can be enhanced by 7–20% as compared with the tube with conventional twisted tape. Li et al. [79] numerically investigated heat transfer enhancement characteristics of tube inserted with centrally hollow narrow twisted tape.

2.2.3 Other vortex-flow devices

Apart from twisted tapes and wire coils, various styles of vortex flow devices have been applied in order to improve the heat transfer rate in tube heat exchangers. The effects of the regularly spaced helical screw-tape on the heat transfer enhancement and thermal performance in laminar and turbulent regions were also reported by Sivashanmugam and Suresh [80]. Promvonge et al. [81] reported the effect of inclined vortex rings (VR) on thermal performance enhancement in a heat exchanger tube. The study showed that the VR at BR = 0.1 and PR = 0.5 yields the best thermal performance. The influence of inclined horseshoes baffles in a tubular heat exchanger on heat transfer rate, friction factor and thermal enhancement factor was studied by Promvonge et al. [82]. Tandiroglu [83] studied the effect of flow geometry parameters on transient heat transfer for turbulent flow ($3000 \leq Re \leq 20,000$) in a circular tube with baffle inserts. The effect of V-nozzle inserts with different pitch ratios (PR = 2.0, 4.0 and 7.0) on heat transfer and flow friction characteristics were studied by Eiamsa-ard and Promvonge [84]. Promvonge [85] experimentally investigated the effect of conical ring inserts with three different ring diameter ratios ($d/D = 0.5, 0.6$ and 0.7) and for each ratio, the rings were placed with three different arrangements (converging conical ring, referred to as CR array, diverging conical ring, DR array and converging–diverging conical ring, CDR array) on heat transfer and friction factor in a tube. The influences of propeller type swirl generators on turbulent convection in round tube has been presented by Eiamsa-ard et al. [86]. They found that the increase in heat transfer over the plain tube is about 2.07 to 2.18 times for PR=5, blade angles $\theta=60^\circ$ and N=8.

Table 2.2 Application of vortex flow devices in tube heat exchangers

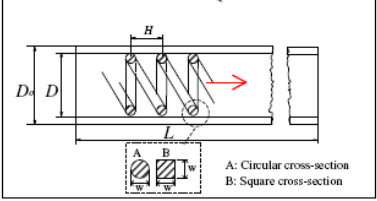
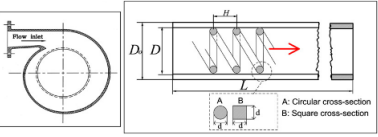
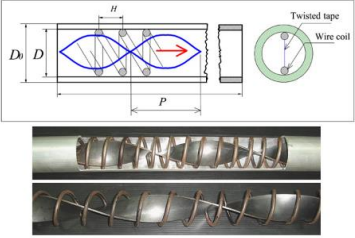
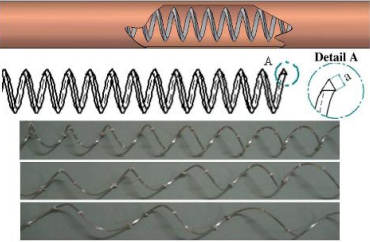
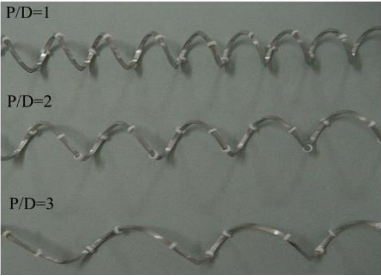
Authors and configuration	Conditions	Results
<p>Promvonge [51]</p> 	<p>Re=5000–25,000, Wires coil with two different spring coiled wire pitches</p>	<p>$Nu/Nu_0 = 1.8-2.6$ $f/f_0 = 5-9$ $\eta = 1.1-1.3$</p>
<p>Promvonge [52]</p> 	<p>Re=5000–25,000, Square cross section wires coil with a snail- type swirl generator</p>	<p>$Nu/Nu_0 = 3.4-3.9$ $f/f_0 = 42-50$ $\eta = 0.9-1.1$</p>
<p>Promvonge [53]</p> 	<p>Re=3000–18,000, Wire coils with different coil pitch in conjunction with twisted tapes</p>	<p>$Nu/Nu_0 = 3.0-6.5$ $f/f_0 = 27-75$ $\eta = 0.85-1.53$</p>
<p>Ozceyhan and Buyukalaca [54]</p> 	<p>Re=3500–27,000, Equilateral triangular coiled wire</p>	<p>$Nu/Nu_0 = 1.27-2.5$ $f/f_0 = 3-6$ $\eta = 0.88-1.36$</p>
<p>Ozceyhan and Buyukalaca [55]</p> 	<p>Re=4105–26,400, Coiled wire with three different pitch ratios and two different distances from tube wall</p>	<p>$Nu/Nu_0 = 1.6-3.1$ $f/f_0 = 5-8$ $\eta = 1-1.5$</p>

Table 2.2 (cont'd)

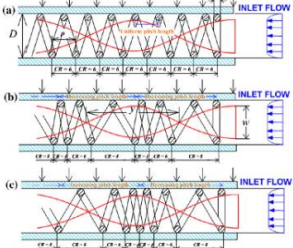
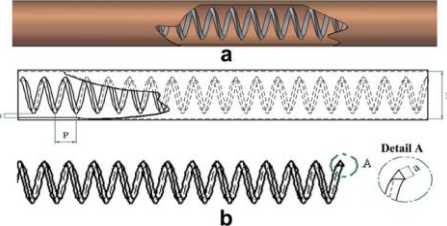
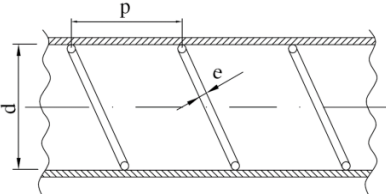
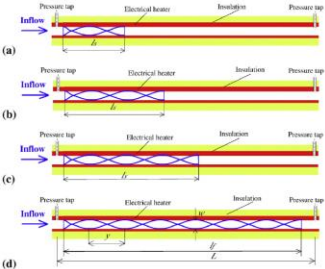
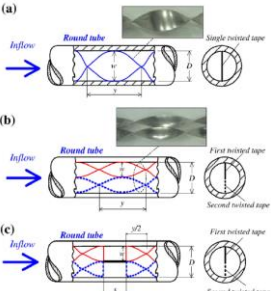
Authors and configuration	Conditions	Results
<p>Eiamsa-ard et al. [56]</p> 	<p>Re=4600–20,000, Non-uniform wire coil and twisted</p>	<p>$Nu/Nu_0 = 2.3-3.7$ $f/f_0 = 8-27$ $\eta = 0.97-1.2$</p>
<p>Gunes et al. [57]</p> 	<p>Re=13,200–19,800, Optimization of design parameters in a tube with coiled wire inserts by Taguchi method</p>	<p>$Nu = 133.14$ $f = 0.18$</p>
<p>Nasr et al. [58]</p> 	<p>Re=4200–49,000, Wire coils with helical pitch in rang 0:156– 0:354 and wire diameter in rang 0:027–0:094</p>	<p>$Nu = 233$ $f = 0.0419$</p>
<p>Eiamsa-ard et al. [59]</p> 	<p>Re=4000–20,000, Short-length twisted tape</p>	<p>$Nu/Nu_0 = 1.1-1.45$ $f/f_0 = 1.53-2.4$ $\eta = 0.8-1.05$</p>
<p>Eiamsa-ard et al. [60]</p> 	<p>Re=4000–19,000, Dual twisted tape elements</p>	<p>$\eta = 1-1.1$</p>

Table 2.2 (cont'd)

Authors and configuration	Conditions	Results
<p>Bas and Ozceyhan [61]</p> 	<p>Re=5132–24,989, Twisted tape with twist ratio of 2, 2.5, 3, 3.5 and 4 and clearance ratios of 0.0178 and 0.0357</p>	<p>$Nu/Nu_0 = 1.36\text{--}2.75$ $f/f_0 = 2.2\text{--}4.0$ $\eta = 1.18\text{--}1.76$</p>
<p>Bhuiya et al. [62]</p> 	<p>Re=7200–50,050, Perforated twisted tape with different porosities of 1.6, 4.5, 8.9 and 14.7%</p>	<p>$Nu/Nu_0 = 2.1\text{--}4.4$ $f/f_0 = 2.1\text{--}4.6$ $\eta = 1.28\text{--}1.59$</p>
<p>Bhuiya et al. [63]</p> 	<p>Re=6950–49,000, double counter twisted tape</p>	<p>$Nu/Nu_0 = 1.3\text{--}3.4$ $f/f_0 = 1.8\text{--}3.8$ $\eta = 1.0\text{--}1.35$</p>
<p>Eiamsa-ard et al. [64]</p> 	<p>Re=2000–12,000, Regularly spaced twisted tape</p>	<p>$Nu/Nu_0 = 2.21\text{--}2.79$ $f/f_0 = 1.94\text{--}4.26$ $\eta = 0.63\text{--}1.05$</p>
<p>Eiamsa-ard and Promvonge [65]</p> 	<p>Re=4000–20,000, serrated twisted tape</p>	<p>$\eta = 1.17$</p>
<p>Murugesan et al. [66]</p> 	<p>Re=2000–12,000, Square-cut twisted tape</p>	<p>$Nu/Nu_0 = 1.05\text{--}1.81$ $f/f_0 = 2.45\text{--}3.81$ $\eta = 0.98\text{--}1.27$</p>

Table 2.2 (cont'd)

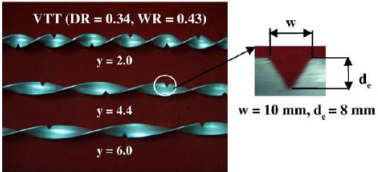
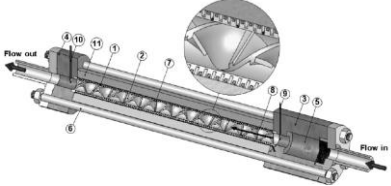

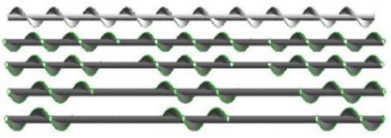
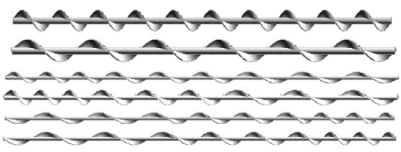
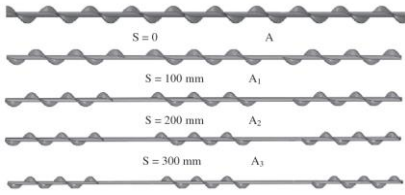
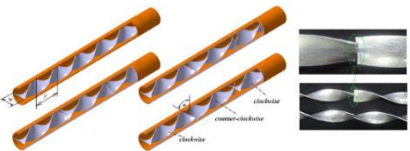
Authors and configuration	Conditions	Results
<p>Murugesan et al. [67]</p> 	<p>Re=2000–12,000, V-cut twisted tape</p>	<p>$\eta = 1.02\text{--}1.27$</p>
<p>Chang et al. [68]</p> 	<p>Re=5000–25,000, Serrated twisted tape</p>	<p>$Nu/Nu_0 = 1\text{--}5$ $f/f_0 = 2\text{--}80$ $\eta = 0.7\text{--}1.6$</p>
<p>Bhuiya et al. [69]</p> 	<p>Re=7200–49,800, Perforated twisted tape</p>	<p>$Nu/Nu_0 = 2.1\text{--}4.4$ $f/f_0 = 2.1\text{--}4.6$ $\eta = 1.28\text{--}1.59$</p>
<p>Sivashanmugam and Suresh [70]</p> 	<p>Re=6000–14,000, Helical screw with spacer length 100, 200, 300, and 400 mm</p>	<p>$Nu = 170$ $f = 0.12$</p>
<p>Sivashanmugam and Suresh [71]</p> 	<p>Re=2700–13,500, Helical screw-tape</p>	<p>$Nu = 180$ $f = 0.2$</p>
<p>Ibrahim [72]</p> 	<p>Re=570–1310, Helical screw-tape</p>	<p>$Nu = 19$ $f = 0.18$</p>
<p>Eiamsa-ard and Promvonge [73]</p> 	<p>Re=3000–27,000, Typical, alternate clockwise and counterclockwise twisted</p>	<p>$Nu/Nu_0 = 1.27\text{--}1.91$ $f/f_0 = 3.42\text{--}5.1$ $\eta = 0.96\text{--}1.4$</p>

Table 2.2 (cont'd)

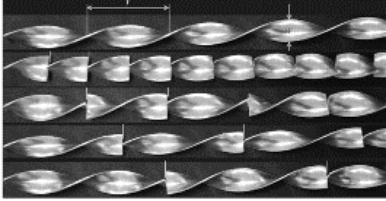
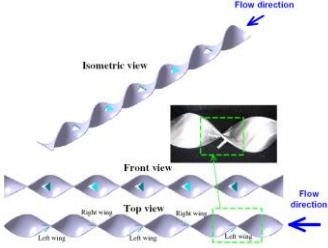
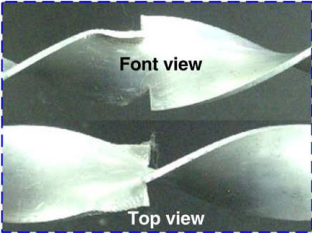

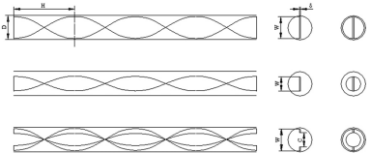
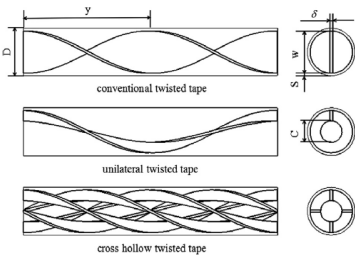
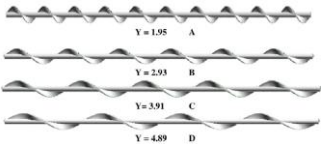
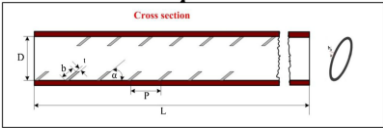
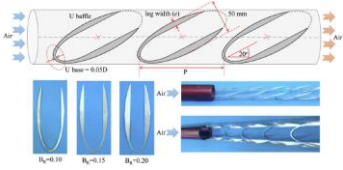
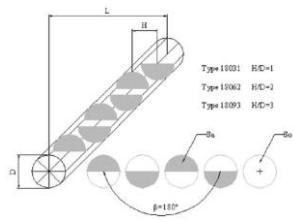
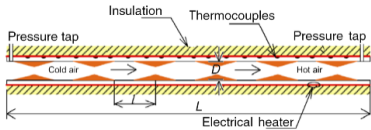
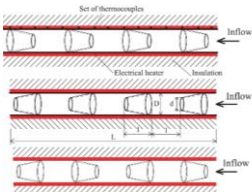
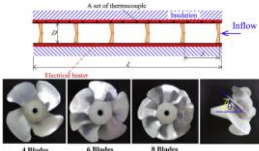
Authors and configuration	Conditions	Results
<p>Eiamsa-ard et al. [74]</p> 	<p>Re=5000–21,500, Uniform/non-uniform twisted tape</p>	<p>$Nu/Nu_0 = 1.25\text{--}2.95$ $f/f_0 = 3.3\text{--}10$ $\eta = 0.89\text{--}1.38$</p>
<p>Eiamsa-ard et al. [75]</p> 	<p>Re=5200–22,000, Twisted tapes consisting of centre wings and alternate-axes</p>	<p>$Nu/Nu_0 = 1.5\text{--}2.9$ $f/f_0 = 4.5\text{--}8.5$ $\eta = 0.9\text{--}1.4$</p>
<p>Wongcharee and Eiamsa-ard [76]</p> 	<p>Re=3000–27,000, Delta-winglet twisted tape</p>	<p>$\eta = 0.9\text{--}1.25$</p>
<p>Wongcharee and Eiamsa-ard [77]</p> 	<p>Re=5500–20,200, Trapezoidal wings</p>	<p>$Nu/Nu_0 = 1.4\text{--}2.8$ $f/f_0 = 3.5\text{--}8.2$ $\eta = 0.7\text{--}1.45$</p>
<p>Guo et al. [78]</p> 	<p>Re=500–1750, Center-cleared twisted tape</p>	<p>$\eta = 2.5\text{--}5.5$</p>
<p>Li et al. [79]</p> 	<p>Re=400–1200, Centrally hollow narrow twisted tapes</p>	<p>$\eta = 2.6\text{--}5.6$</p>

Table 2.2 (cont'd)

Authors and configuration	Conditions	Results
Sivashanmugam and Suresh [80] 	Re=200–3000, Regularly spaced helical screw-tape	$Nu = 70$ $f = 0.3$
Promvonge et al. [81] 	Re=5000–26,000, Inclined vortex rings	$Nu/Nu_0 = 3.6-4.3$ $f/f_0 = 35.1-36.5$ $\eta = 1.1-1.4$
Promvonge et al. [82] 	Re=5300–24,000, Inclined horseshoe baffles	$Nu/Nu_0 = 2-3.9$ $f/f_0 = 3-19$ $\eta = 1.3-1.88$
Tandiroglu [83] 	Re=3000–20,000, Baffle inserts	$Nu = 110$ $f = 0.046$
Eiamsa-ard and Promvonge [84] 	Re=8000–18,000, V-nozzle arrangements with different pitch ratios of 2.0–7.0	$Nu/Nu_0 = 3.16-3.70$ $\eta = 0.85-1.19$
Promvonge [85] 	Re=6000–26,000, Conical ring	$Nu/Nu_0 = 1.91-4.33$ $\eta = 0.9-1.8$
Eiamsa-ard et al. [86] 	Re=4000–21,000, Propeller type swirl generators	$Nu/Nu_0 = 1.6-2.3$ $\eta = 0.82-1.19$

2.3 Concept of the research

According to the literature review above, various turbulence promoter devices have been used in the thermal systems both tubular and flat-surface duct/channel heat exchangers for heat transfer enhancement. Each turbulator is suitable for different applications indicating its advantages and disadvantages. Among turbulators, the winglet turbulator demonstrates the superiority of thermal performance in a duct/channel heat exchanger. This superiority lies in the ability of providing the heat transfer rate at lower flow resistance. The purpose of the present research is therefore to develop and modify the turbulator for use in a channel/tube heat exchanger. The present research can be divided into 2 sections.

Section I: Turbulators

First, presents a numerical study on heat transfer augmentation in a solar air heater channel fitted with multiple V-baffle (VB) turbulators. During the test air was passed through the test channel under a uniform wall heat-flux of the absorber plate. The fluid flow and heat transfer characteristics are presented for Reynolds numbers based on the channel hydraulic diameter ranging from 4000 to 20,000. The VBs are applied at a relative baffle height (in terms of blockage ratio, $BR=b/H=0.25$) and attack angle of 45° with respect to the main flow direction. The use of the VBs is to generate multiple longitudinal vortex flows through the test channel to increase turbulence intensity and stronger mixing of fluid between the core and the near-wall flow. Influences of three different baffle pitch to channel-height ratios ($PR=P/H=0.5, 1$ and 2) on heat transfer and pressure drop in terms of respective Nusselt number and friction factor (or energy loss for propelling air through the channel) are examined. Three VB arrangements, namely, one VB wall (or single VB), in-line and staggered VBs on two opposite walls are also investigated.

Next, presents a numerical analysis of turbulent periodic flow and heat transfer behaviors in an isothermal-fluxed square channel fitted with inclined U-baffles (UB). Five baffle blockage ratios, ($BR=b/H=0.05, 0.1, 0.15, 0.2$ and 0.25), at three pitch spacing ratio, $p/H=PR=0.5, 1.0$ and 2.0 and an attack angle, $\alpha=30^\circ$ are introduced in the present study. The UBs are mounted repeatedly on the channel walls to create longitudinal vortex flows through the test channel. The computations based on the finite volume method and coupling the pressure-velocity with the SIMPLE algorithm have been conducted for the airflow in the form of Reynolds numbers ranging from 4000 to 20,000. Influences of five baffle-to-duct height or blockage ratios ($b/H=BR=0.05, 0.1, 0.15, 0.2$ and 0.25) on the heat transfer in terms of Nusselt number and the pressure loss in the form of friction factor are compared between the inserted channel and the smooth channel.

Finally, presents a numerical investigation of the influence of inclined vortex rings (VR) on heat transfer augmentation in a uniform heat-fluxed tube has been investigated numerically. In the present work, the 30° inclined VRs were mounted repeatedly in the tube with various geometry parameters of the VR, four relative ring heights ($BR=b/D=0.05, 0.1, 0.15$ and 0.2) and three relative ring pitches ($PR=P/D=1.0, 1.5$ and 2.0). Air was employed as the test fluid in the tube for the Re from 4000 to 20,000. The aim at using the VR is to create counter-rotating vortices inside the tube to help increase the turbulence intensity as well as to convey the colder fluid from the core regime to the heated-wall region. To find an optimum thermal performance condition, the effect of BR and PR values on the heat transfer and pressure loss in the tube is examined.

Section II: Horseshoe baffles

In this section, investigations have been conducted to examine the effect of relative baffle pitch lengths and widths of the inclined horseshoe baffles (HB) and V-shaped horseshoe baffles (VHB) insert on heat transfer rate and flow friction characteristics in a uniform heat-fluxed tube using air as the test fluid for the turbulent regime, $Re=3000-20,000$. The HB and VHB are the modification of the VB, UB and VR by integrating their merits of those turbulators. The application of the HB and VHB is expected to be a promising insert device for improvement of thermal systems in industrial applications.

CHAPTER 3

MATHEMATICAL FOUNDATION

The chapter deals with the governing mathematical equations of fluid flow and heat transfer used for mathematical modelling, numerical procedure and solution. The governing Navier-Stokes equations derived from the three basic conservation laws are first proposed including the Reynolds average Navier-Stokes equations for turbulent flows. The appearance of Reynolds stresses obtained from the time-averaged momentum equations leads to turbulence model used in the computation to represent the characteristics of the turbulent flow. Then, the finite volume approach is employed in solving the algebraic governing equations discretized by a second-order differencing scheme. The boundary conditions of the flow model are prescribed. Next, details of the solution algorithm and procedure employed in the present study are also explained. To evaluate the thermal performances, the key pertinent parameters are offered.

3.1 Governing Equations

The governing equations for a numerical simulation of the fluid flow and heat transfer problem are introduced. The equations represent the mathematical foundation of the principle conservation laws of physics. For an incompressible viscous fluid, the governing equations were derived from the conservations of mass, momentum and energy.

In the present study, a numerical model of fluid flow and heat transfer in a tube/duct/channel was developed under the following major assumptions:

- Steady three-dimensional fluid flow and heat transfer.
- Turbulent and incompressible flow.
- Negligible body forces, viscous dissipation and radiation heat transfer.

3.1.1 Equation of continuity

The continuity equation was derived by the conservation of mass using a mass balance of a fluid element flowing in and out a control volume in a flow field. From the principle that the mass of a fluid must be conserved and it cannot be created or destroyed. The net rate of change of a mass entering and exiting a differential control volume must equal zero. For a steady, three-dimensional incompressible fluid flow, the conservation of mass equation can be derived to

$$\text{div}(\mathbf{U})=0 \quad (3.1)$$

where \mathbf{U} is the velocity vector has the velocity components of u , v , and w in x , y , and z directions, respectively.

3.1.2 Equation of momentum

The momentum equations were derived by the conservation of momentum using Newton's second law of motion. This law states that external forces acting on a body in a given direction is equal to the net rate of change of velocity times mass (momentum) in the same direction. The external forces are classified as surface and body forces. The surface forces are from the pressures and stresses acting on the control volume surface. The body forces include only gravitational forces but neglecting magnetic and electric fields acting on the body of fluid. For a steady, three-dimensional and incompressible fluid flow, the momentum equations in terms of velocity gradients can be derived to each direction as following equations.

x-momentum:

$$\text{div}(\rho u \mathbf{U}) = -\frac{\partial P}{\partial x} + \text{div}(\mu \text{grad } u) \quad (3.2a)$$

y-momentum:

$$\text{div}(\rho v \mathbf{U}) = -\frac{\partial P}{\partial y} + \text{div}(\mu \text{grad } v) \quad (3.2b)$$

z-momentum:

$$\text{div}(\rho w \mathbf{U}) = -\frac{\partial P}{\partial z} + \text{div}(\mu \text{grad } w) \quad (3.2c)$$

The terms on the left-hand side of the conservation of momentum equations are the rates of change of momentum. The first term on the right-hand side is the pressure force and the second term within the bracket is the viscous forces. For the present study, the body force acting on the fluid element was negligible and excluded from the above equation.

3.1.3 Equation of energy

The energy equation can be derived by the conservation of energy using the first law of thermodynamics for a differential control volume in a flow field. This law expresses that the net rate of change of energy is equal to the sum of the rate of heat addition to and the rate of work done on a fluid particle. For a steady, three-dimensional and incompressible fluid flow, the conservation of energy equation can be derived to

$$\text{div}(\rho i \mathbf{U}) = \text{div}(k \text{ grad } T) + \Phi \quad (3.3)$$

where i is the internal energy of the control volume ($i = c_v T$). The viscous dissipation (Φ) was defined as

$$\Phi = \mu \left\{ 2 \left[\left(\frac{\partial u}{\partial x} \right)^2 + \left(\frac{\partial v}{\partial y} \right)^2 + \left(\frac{\partial w}{\partial z} \right)^2 \right] + \left(\frac{\partial u}{\partial y} + \frac{\partial v}{\partial x} \right)^2 + \left(\frac{\partial u}{\partial z} + \frac{\partial w}{\partial x} \right)^2 + \left(\frac{\partial v}{\partial z} + \frac{\partial w}{\partial y} \right)^2 \right\} \quad (3.4)$$

The term on the left-hand side of the energy equation is the convective rate of change of heat transfer. The first term on the right-hand side represents the rate of change of conductive heat transfer while the second term is the viscous dissipation owing to friction in the fluid which may usually be neglected except in systems with large velocity gradients [1]. Therefore, the energy equation can be written as

$$\text{div}(\rho i \mathbf{U}) = \text{div}(k \text{ grad } T) \quad (3.5)$$

In numerical simulation, these partial differential equations as the governing equations were integrated over all of the control volumes in the region of interest or the computational domain. This is equivalent to applying the three fundamental conservation laws to each control volume. The discretization approach is described in subsequent section of the finite volume method.

3.2 Turbulence Modeling

At a low flow rate or low Reynolds number, the fluid flow is regarded as a laminar flow when at a high Reynolds number, the flow is viewed to be turbulent. The turbulent flow is characterized by a highly unsteady and random state of three-dimensional motion which the velocity and pressure change continuously on a broad range of time and length scales [87]. A typical one-dimensional velocity of turbulent flow at a point can be displayed in Figure 3.1. The term $u(t)$ is the instantaneous velocity at time t while $u'(t)$ and U are fluctuating velocity an averaged flow velocity over a time, respectively. Thus, $u(t) = U + u'(t)$.

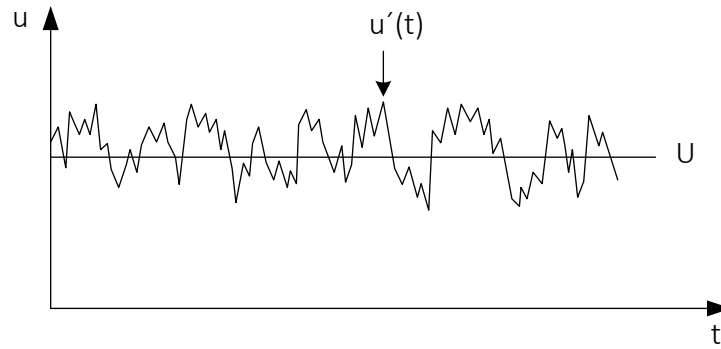


Figure 3.1 A typical velocity of one-dimensional turbulent flow at a point.

There are several approaches in numerical prediction of the turbulent flows such as Reynolds-averaged Navier-Stokes (RANS), direct numerical simulation (DNS), and large eddy simulation (LES). Each method requires different computational efforts and time. In the present study, the RANS approach was applied in simulation of the turbulent flow model.

3.2.1 Reynolds-averaged Navier-Stokes (RANS)

Turbulent flow models can be simulated by an approximation method. This method is based on time-averaging the equations of motion over a time interval assuming that the flow is statistically steady. By averaging, all of unsteadiness in the flow is regarded as a part of the turbulence. This approach results in a set of partial differential equations which are called the Reynolds-averaged Navier-Stokes (RANS) equations. In a statistically steady flow, every variable can be written as the sum of a time-averaged component, $\bar{\varphi}$ and a fluctuating component, $\varphi'(t)$ with zero mean value as expressed in the following equation.

$$\varphi(t) = \bar{\varphi} + \varphi'(t) \quad (3.6)$$

The time-averaged component is defined as

$$\bar{\varphi} = \lim_{T \rightarrow \infty} \frac{1}{T} \int_0^T \varphi(t) dt \quad (3.7)$$

Here t is time and T is the averaging time interval. This interval must be large enough compared to the typical time scale of the fluctuations. Therefore, the component $\bar{\varphi}$ is free from the time that the averaging is started. In the present work,

the flow is steady and thus, the Reynolds-averaged Navier-Stokes (RANS) equations are required.

The tube/channel flow is governed by the Reynolds averaged Navier-Stokes (RANS) equations and the energy equation. In the Cartesian tensor system these equations can be written as follows:

Continuity equation:

$$\frac{\partial}{\partial x_i}(\rho u_i) = 0 \quad (3.8)$$

Momentum equation:

$$\frac{\partial}{\partial x_j}(\rho u_i u_j) = -\frac{\partial p}{\partial x_i} + \frac{\partial}{\partial x_j} \left[\mu \left(\frac{\partial u_i}{\partial x_j} + \frac{\partial u_j}{\partial x_i} \right) - \overline{\rho u'_i u'_j} \right] \quad (3.9)$$

where ρ is the density of fluid, and u_i is a mean component of velocity in the direction x_i , p is the pressure, μ is the dynamic viscosity, and u' is a fluctuating component of velocity. Repeated indices indicate summation from one to three for 3-dimensional problems.

Energy equation:

$$\frac{\partial}{\partial x_j}(\rho u_i T) = \frac{\partial}{\partial x_j} \left((\Gamma + \Gamma_t) \frac{\partial T}{\partial x_j} \right) \quad (3.10)$$

where Γ and Γ_t are molecular thermal diffusivity and turbulent thermal diffusivity, respectively and are given by

$$\Gamma = \frac{\mu}{Pr}, \text{ and } \Gamma_t = \frac{\mu_t}{Pr_t} \quad (3.11)$$

3.2.2 RNG $k - \varepsilon$ model

The Reynolds-averaged approach to turbulence modeling requires that the Reynolds stresses, $-\overline{\rho u'_i u'_j}$ in Eq. (3.9) needs to be modeled. The Boussinesq hypothesis relates the Reynolds stresses to the mean velocity gradients as seen in the equation below:

$$-\rho \overline{u'_i u'_j} = \mu_t \left(\frac{\partial u_i}{\partial x_j} + \frac{\partial u_j}{\partial x_i} \right) - \frac{2}{3} \left(\rho k + \mu_t \frac{\partial u_i}{\partial x_i} \right) \delta_{ij} \quad (3.12)$$

where k is the turbulent kinetic energy, defined by $k = 1/2 \cdot \overline{u'_i u'_i}$ and δ_{ij} is a Kronecker delta. The merit of the Boussinesq approach is the relatively low computational cost associated with the computation of the turbulent viscosity, μ_t given as $\mu_t = \rho C_\mu k^2 / \varepsilon$. The RNG $k-\varepsilon$ model is one of the two-equation models that employ the Boussinesq hypothesis.

The steady state transport equations are expressed as:

$$\frac{\partial}{\partial x_i} (\rho k u_i) = \frac{\partial}{\partial x_j} \left(\alpha_k \mu_{eff} \frac{\partial k}{\partial x_j} \right) + G_k - \rho \varepsilon \quad (3.13)$$

$$\frac{\partial}{\partial x_i} (\rho \varepsilon u_i) = \frac{\partial}{\partial x_j} \left(\alpha_\varepsilon \mu_{eff} \frac{\partial \varepsilon}{\partial x_j} \right) + C_{1\varepsilon} \frac{\varepsilon}{k} G_k - C_{2\varepsilon} \rho \frac{\varepsilon^2}{k} - R_\varepsilon \quad (3.14)$$

In the above equations, α_k and α_ε are the inverse effective Prandtl numbers for k and ε , respectively. $\alpha_k = \alpha_\varepsilon = 1.39$, $C_{1\varepsilon}^* = 1.42$, $C_{2\varepsilon} = 1.68$, respectively. The effective viscosity μ_{eff} is written by

$$\mu_{eff} = \mu + \mu_t = \mu + \rho C_\mu \frac{k^2}{\varepsilon} \quad (3.15)$$

where C_μ is a constant and set to 0.0845, derived using the ‘‘renormalization group’’ (RNG) method.

The first term on the left-hand side of the RNG $k-\varepsilon$ model equations is the convective rate of change of k or ε . The right-hand side of the equations includes the transport of k or ε by diffusion, rate of k or ε production, and rate of k or ε destruction, respectively.

3.3 Finite Volume Method

The governing RANS equations in terms of partial differential equations are transformed into discrete algebraic equations. The solution of the discretized equations produces a set of values corresponding to the solution of the original

equations. The discretization process can be divided into two steps which are the discretization of the solution domain and the discretization of the governing equation.

The discretization of the solution domain generates a numerical description of the computational domain. This process is also known as grid generation. The space is divided into a finite number of discrete regions which called control volumes (CVs) or cells. The discretization of the governing RANS equations together with the domain discretization produces an appropriate transformation of the RANS equations into a system of discrete algebraic equations. Then, the set of algebraic equations is solved simultaneously using any direct or iterative method.

The generic conservation equation for an arbitrary quantity (ϕ) can be written in the vector form as follows:

$$\text{div}(\rho u \phi) = \text{div}(\Gamma \text{grad } \phi) + S_\phi \quad (3.16)$$

The left-hand side of the equation is the convective term. The right-hand sides are the diffusive term and the source term, respectively. The finite volume method uses the integral form of the conservation equation as the starting point. Therefore, formal integration over a control volume gives

$$\int_V (\rho \phi u) \cdot n dA = \int_V (\Gamma \text{grad } \phi) \cdot n dA + \int_{CV} S_\phi dV \quad (3.17)$$

The integral equation represents the flux balance in a control volume. The left-hand side yields the net convective flux. The right-hand side includes the net diffusive flux and the production and destruction of the quantity ϕ within the control volume, respectively. The integral conservation equation is applied to each control volume and to the entire solution domain. The integral conservation equations for all control volumes are summed to obtain the global conservation equations.

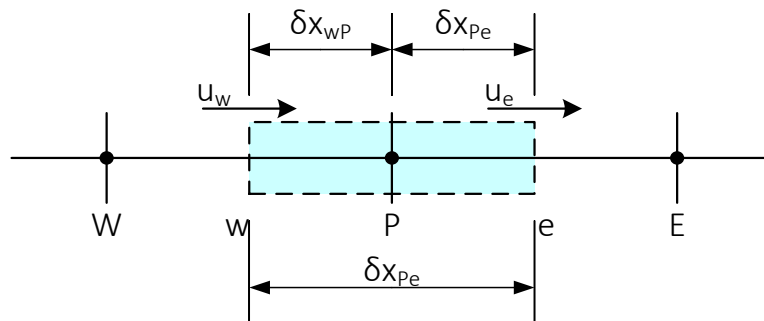


Figure 3.2 A control volume around general node P

For simplicity, the one-dimensional control volume is illustrated in Figure 3.2. Focusing on general node P, the neighboring nodes are identified by W and E nodes. The control volume faces are identified by w and e faces.

Integration of transport equation (Equation 3.16) over the control volume gives

$$(\rho u A \phi)_e - (\rho u A \phi)_w = \left(\Gamma A \frac{d\phi}{dx} \right)_e - \left(\Gamma A \frac{d\phi}{dx} \right)_w \quad (3.18)$$

Integration of continuity equation (3.1) yields

$$(\rho u A \phi)_e - (\rho u A \phi)_w = 0 \quad (3.19)$$

The variables $F = \rho u$ and $D = \Gamma/\delta x$ are defined to represent the convective mass flux per unit area and diffusion conductance at the cell faces, respectively. Assuming that the face area, $A_w = A_e = A$, the integrated convection-diffusion equation (Equation 3.18) can be written as

$$F_e \phi_e - F_w \phi_w = D_e (\phi_E - \phi_P) - D_w (\phi_P - \phi_W) \quad (3.20)$$

The integrated continuity equation (3.19) can be expressed as

$$F_e - F_w = 0 \quad (3.21)$$

Assuming that the velocity field is known and the quantity ϕ at the e and w faces can be calculated, therefore the integrated convection-diffusion equation (Equation 3.20) can be solved.

QUICK numerical scheme

The quadratic upstream interpolation for convective kinetics (QUICK) scheme introduced by Leonard in 1979 [91] was employed in the present study. The QUICK scheme uses a three-point upstream-weighted quadratic interpolation for cell face values. The quantity ϕ can be obtained from a quadratic function passing through two bracketing nodes on each side of the face and a node on the upstream side. For a uniform grid, the value of quantity ϕ at the cell faces between two bracketing nodes i and $i-1$, and upstream node $i-2$ can be estimated by

$$\phi_{face} = \frac{6}{8}\phi_{i-1} + \frac{3}{8}\phi_i - \frac{1}{8}\phi_{i-2} \quad (3.22)$$

For demonstration, the QUICK scheme for one-dimensional convection-diffusion problem for a general node P is illustrated in Figure 3.3. For positive flow, $F_w > 0$ ($u_w > 0$), the quantity ϕ at the w face is

$$\phi_w = \frac{6}{8}\phi_W + \frac{3}{8}\phi_P - \frac{1}{8}\phi_{WW} \quad (3.23)$$

When $F_e > 0$ ($u_e > 0$), the quantity ϕ at the e face is

$$\phi_e = \frac{6}{8}\phi_P + \frac{3}{8}\phi_E - \frac{1}{8}\phi_W \quad (3.34)$$

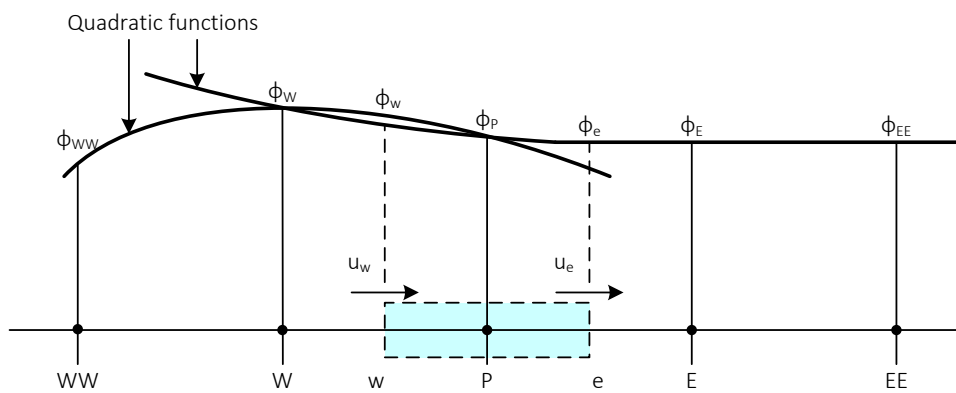


Figure 3.3 Quadratic profiles used in QUICK scheme.

Equations 3.23 and 3.24 were substituted in the discretized convection-diffusion equation (Equation 3.20) and solved for central and neighboring coefficients. Moreover, the quantity ϕ for negative flow directions can be obtained using the same sequence. Therefore, the QUICK scheme for one-dimensional convection-diffusion problem can be expressed as

$$a_P\phi_P = a_W\phi_W + a_E\phi_E + a_{WW}\phi_{WW} + a_{EE}\phi_{EE} \quad (3.25)$$

The central and neighbor coefficients in equation 3.25 can be identified using the expressions in Table 3.1.

Table 3.1 Central coefficient and neighbor coefficients for the QUICK scheme

Central coefficient	Formula
a_P	$a_W + a_E + a_{WW} + a_{EE} + (F_e - F_w)$
Neighbor coefficients	Formula
a_W	$D_w + \frac{6}{8}\alpha_w F_w + \frac{1}{8}\alpha_e F_e + \frac{3}{8}(1-\alpha_w)F_w$
a_{WW}	$-\frac{1}{8}\alpha_w F_w$
a_E	$D_e - \frac{3}{8}\alpha_e F_e - \frac{6}{8}(1-\alpha_e)F_e - \frac{1}{8}(1-\alpha_w)F_w$
a_{EE}	$\frac{1}{8}(1-\alpha_e)F_e$
Note:	$\alpha_w = 1$ for $F_w > 0$ and $\alpha_e = 1$ for $F_e > 0$ $\alpha_w = 0$ for $F_w < 0$ and $\alpha_e = 0$ for $F_e < 0$

For the QUICK scheme, the cell face values of fluxes are always calculated by quadratic interpolation between the two bracketing nodes and an upstream node. Since the scheme is based on a quadratic function, its accuracy in terms of Taylor series truncation error is third-order on a uniform mesh. The QUICK scheme has greater accuracy than the central differencing or hybrid schemes. Furthermore, the QUICK scheme is also suitable for quadrilateral and hexahedral meshes aligned with the flow direction.

3.4 Boundary Conditions

3.4.1 Wall boundary condition

The boundary conditions appropriate to a solid wall boundary must be specified for velocity and turbulence parameters. The wall boundary condition is treated between the fluid and solid regions. Since the viscous sublayer and buffer layer are extremely thin, the wall function which is a set of semi-empirical formulas must be used along with finer grid at the near-wall region [88]. In the present study, the no-slip condition was applied at the solid wall. The fluid velocity at the wall is equal to zero. For the RNG $k - \varepsilon$ model, enhanced wall treatment method which combines the standard two-layer model with the enhanced wall function was also suggested to bridge the viscosity affected between the near-wall and the fully-turbulent regions.

3.4.2 Periodicity

The flow becomes periodically fully-developed in repetitive geometries. Since the geometry and arrangement of the baffled tube/channel was successively repetitive, the flow became periodic far from the entrance region, mostly for the distance of about 10 hydraulic diameters from the inlet. The periodic boundary conditions were advisably applied for a large number of repetitive modules. By using the periodic flow condition, the time and cost consumption can be substantially reduced for the computation of self-repeating modules. Therefore, the periodic module was used as the computational domain.

3.5 Solution Algorithm

3.5.1 Pressure-velocity coupling with SIMPLE algorithm

The pressure-based solver uses a solution algorithm to solve the governing equations. Since the governing equations are non-linear and coupled, the solution loop must be employed iteratively in order to obtain a converged numerical solution. The pressure-based segregated algorithm solves the individual governing equations sequentially for the solution variables as reported in [91]. Since the governing equations are solved in separated manner, the segregated algorithm is memory efficient. The discretized equations are stored in the memory one at a time.

The iteration procedure of the pressure-based segregated algorithm consists of the following steps.

1. Update fluid properties such as density, viscosity, specific heat, turbulent viscosity based on the current solution.
2. Sequentially solve the momentum equations using the recently updated values of pressure and face mass fluxes.
3. Solve the pressure correction equation using the recently obtained velocity field and the mass flux.
4. Correct the face mass fluxes, pressure, and the velocity field using the pressure correction obtained from step 3.
5. Solve the equations for additional scalars such as turbulent quantities and energy using the current values of the solution variables.
6. Check for the convergence of the governing equations.

These steps are continued until the convergence criteria are satisfied.

The pressure-velocity coupling solver was employed with the SIMPLE (Semi-Implicit Method for Pressure Linked Equations) algorithm. The SIMPLE algorithm is a segregated algorithm that uses a relationship between velocity and pressure

corrections to enforce the mass conservation and to obtain the pressure. The SIMPLE algorithm field as seen in [91] can be described as the following sequence.

1. Guess the pressure field.
 2. Solve the momentum equations to obtain the velocity field.
 3. Solve the pressure correction equation.
 4. Calculate the new pressure from the pressure correction value.
 5. Calculate the velocity field from their corrected values using the velocity correction formula. The corrected velocity field exactly satisfies the continuity equation.
 6. Solve the discretization equation for other variables such as temperature and turbulence quantities if they influence the fluid properties.
- Treat the corrected pressure as a new guessed pressure. Return to step 2 and repeat the whole procedure until the convergence criteria is satisfied.

3.5.2 Solution procedure

In the present study, the ANSYS Workbench was employed to numerically investigate the effects of baffles on the heat transfer and fluid flow characteristics in a channel. First, the problem of interest and the assumptions were defined. Then, the computational domain and the boundary conditions were determined. The solid geometry of computational domain was constructed using the DesignModeler application. Next, the computational grid was generated using the Mesh application in the ANSYS Workbench. The turbulence model and the solution methods were established using the FLUENT application in the ANSYS Workbench. The flow and thermal boundary conditions were applied. The convergence criteria were specified. After that, the computations were performed. Finally, the numerical solutions were examined and discussed. The flow topology and coherent structure were also introduced to visualize the fluid flow and heat transfer behaviors.

3.5.3 Key quantifying thermal enhancement factors

The key quantifying thermal enhancement factors were Reynolds number, the friction factor, Nusselt number and the thermo-hydraulic performance.

The Reynolds number is defined as a ratio of inertia to viscous forces and is derived as

$$\text{Re} = \frac{\rho U_m D_h}{\mu} \quad (3.26)$$

where ρ , μ , and U_m are the fluid density, dynamic viscosity, and mean velocity, respectively. The hydraulic diameter (D_h) for the rectangular channel, square channel and circular tube is defined as $D_h = 4WH/2(W + H)$, H and D , respectively.

The friction factor is defined as the dimensionless pressure drop for internal flow. The friction factor can be calculated by evaluating the pressure drop (ΔP) across the length of periodic module (L) for the numerical model. The friction factor is expressed as

$$f = \frac{(\Delta P/L)D_h}{(\rho U_m^2/2)} \quad (3.27)$$

From the Newton's law of cooling, the local convective heat transfer coefficient (h_x) is defined as

$$h_x = \frac{q_s}{(T_s - T_b)} \quad (3.28)$$

where q_s is surface heat flux, T_s is surface temperature, and T_b is bulk fluid temperature.

The local Nusselt number is defined as a ratio of convective heat transfer to conduction in a fluid and is expressed as

$$\text{Nu}_x = \frac{h_x D_h}{k} \quad (3.29)$$

where k is the thermal conductivity of the fluid.

The area-weighted average Nusselt number is defined as

$$\text{Nu} = \frac{1}{A} \int_A \frac{h_x D_h}{k} dA \quad (3.30)$$

To compare the key quantifying thermal enhancement factors of the baffled tube/channel with based values of the smooth tube/channel, the relative friction factor and the Relative Nusselt number are introduced. The relative friction factor is expressed as f/f_0 while the relative Nusselt number is given by Nu/Nu_0 . The f , Nu and f_0 , Nu_0 are the friction factor and Nusselt number for the baffled tube/channel and the smooth tube/channel, respectively.

To evaluate the thermal performance of the baffled tube/channel, the thermo-hydraulic performance is introduced. The thermo-hydraulic performance is

defined as the ratio of the heat transfer coefficient of an augmented surface (h) to the smooth surface (h_0) at the same pumping power criterion. The thermo-hydraulic performance (η) is derived as

$$\eta = \frac{h}{h_0} \Big|_{pp} = \frac{Nu}{Nu_0} \Big|_{pp} = \frac{(Nu/Nu_0)}{(f/f_0)^{1/3}} \quad (3.31)$$

where f , Nu and f_0 , Nu_0 stand for the friction factor and Nusselt number for the baffled tube/channel and the smooth tube/channel, respectively.

3.6 Flow Topology and Coherent Structure

3.6.1 Flow topology

The topology in the case of periodic incompressible flow can be described by the two dimensional streamlines. The definitions of streamline, streamsurface, and isosurface or vortex core are summarized in the following:

- Streamline is a tool for visualizing the vector fields is to plot the location of streamlines, which are lines tangential to the vector field of the velocity vector field. The projection of streamlines to solid walls is very useful. The plotting is done using wall shear stress vectors, and their corresponding wall streamlines.
- Streamsurface is a set of streamlines passing through a fixed curve inside the flow field. This streamsurface is tangential to the velocity vector field. The streamsurface is very useful for the flow visualization.
- Vortex is a region of the flow where streamlines are closed and approximately circular.

3.6.2 Coherent structure

By definition, a coherent structure is a three-dimensional region of the flow over which at least one fundamental flow variable (e.g. velocity component, temperature, etc.) exhibits significant correlation with itself or with another variable over a range of space and/or time that is significantly larger than the smallest local scale of the flow.

After the Reynolds decomposition, the fluctuating part is decomposed into the coherent motion and to the turbulent background. The coherent part has important impact on the dynamics of the flow that provides a depth insight and mechanism of heat transfer inside tube/channel heat exchangers.

3.6.3 Q-criterion

The Q is a fundamental variable that is able to detect a vortex. The Q is the second scalar invariant of the velocity gradient tensor and can be expressed for fluids with constant density as follows:

$$Q = \frac{1}{2}(\Omega_{ij}\Omega_{ji} - S_{ij}S_{ji}) \quad (3.32)$$

where Ω_{ij} is the anti-symmetrical part of the velocity gradient tensor, $\partial_j u_i$ or the vorticity tensor, which is expressed as

$$\Omega_{ij} = \frac{1}{2}(\partial_i u_j - \partial_j u_i) \quad (3.33)$$

where S_{ij} is the symmetrical part of the velocity gradient tensor, $\partial_j u_i$ or the rate of strain tensor, which is expressed as

$$S_{ij} = \frac{1}{2}(\partial_i u_j + \partial_j u_i) \quad (3.34)$$

Equation 3.32 shows that the Q is the indicator of vorticity dominance over strain. The results of the flow topology and coherent structure for the flow are presented in chapter 6 and chapter 7.

The next chapter offers the structure of numerical model and the computational details to represent the given problem of interest. The geometries and arrangements of the baffles are also described. The numerical model was verified and validated. Thereafter, the effects of various configurations of tube/channel flows on the prescribed key quantifying thermal enhancement factors are presented and discussed in chapter 6.

CHAPTER 4

NUMERICAL SOLUTION PROCEDURE

The chapter describes the numerical simulation algorithm, the numerical verification and validation procedures. The computational detail of the baffle geometry and arrangement used in the tube/channel is first introduced and then, it follows with the computational domain and the grid generation including the boundary conditions. Next, the numerical schemes and methods used in the present computation are presented, apart from the convergence criteria. Finally, the verification and validation methods are also provided.

4.1 Computational details of tube/channel flows

This section describes the computational detail on tube/channel flows through various types of baffles to represent the tube/channel flow problems of interest. First, the baffle's geometry and its arrangement in the tube/channel were defined, apart from the computational domain and grid structure. The boundary conditions based on prescribed major assumptions were described including the computational schemes and the convergence criteria.

4.1.1 Baffle geometry and arrangement for numerical simulation

Figure 4.1 depicts a rectangular channel fitted with multiple V-baffles (VB) repeatedly placed on the channel wall. The full-length channel was divided into 3 parts: entry, test section and exit. The detail of the full-length channel mounted with the VB on the channel wall and a module/period of one periodic flow, computational domain and baffle arrangement are also shown in Figure 4.1. The periodic flow channel attains a periodically fully developed flow and thermal condition where the velocity field and heat transfer pattern repeats itself from one module to another. The concept of periodically fully developed flow and its solution procedure has been first introduced by Patankar et al. [88]. In the periodic flow module, air flows through the channel at an inlet temperature (T_i) and flows over a VBs. The longitudinal pitch spacing (P_l) is a distance between the VB cells, in which P_l/H is defined as the pitch ratio (PR) while the transverse pitch spacing (P_t) is a distance between the VB cells in transverse direction. To investigate the flow structure and heat transfer mechanism, the module with three VB arrangements (single VB; inline and staggered VB placed on two opposite walls) is simulated and their numerical results are validated with the measurement in the current work.

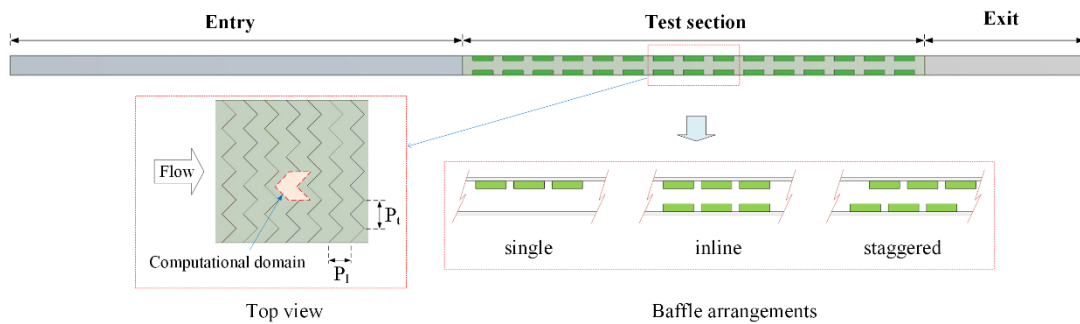


Figure 4.1 Channel geometry of periodic flow for VB.

Figure 4.2 displays a square channel inserted with inclined U-baffles (UB). The full-length of the test duct was also divided into 3 parts: entry, test section and exit. The pitch spacing, p is a distance between the neighboring baffle cells/modules. Periodic boundaries are used for the inlet and outlet of the flow domain. The concept of periodically fully developed flow and its solution procedure has been described in Ref. [88]. Constant mass flow rate of air at 300 K is assumed due to periodically fully developed flow conditions. The physical properties of the air have been assumed to remain constant at mean bulk temperature. Impermeable boundary and no-slip wall conditions have been implemented over the walls of square channel as well as the UBs. The uniform heat-flux of the square channel walls is maintained at 600 W/m^2 while the baffle is assumed at adiabatic wall conditions.

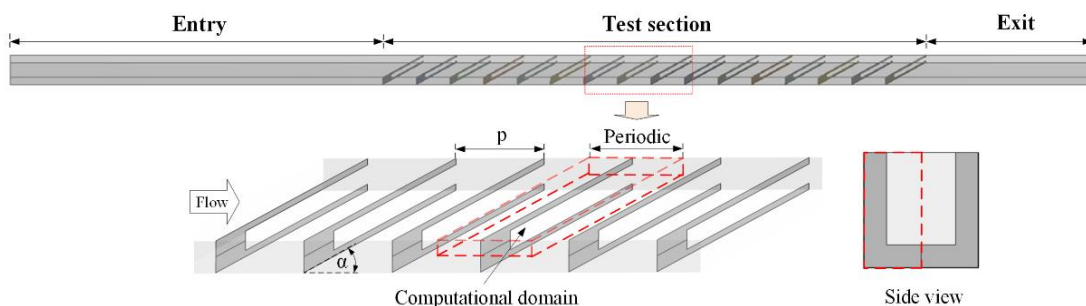


Figure 4.2 Duct geometry of periodic flow for UB.

Figures 4.3, 4.4 and 4.5 show a circular tube fitted with vortex rings (VR), Inclined Horseshoe baffles (HB) and V-shaped Horseshoe baffles (VHB), respectively. The full-length of the test tube was also divided into 3 parts: entry, test section and exit. For a periodic flow module, the flow under consideration is expected to attain a periodic flow condition in which the velocity field repeats itself from one cell/module to another. The concept of periodically fully developed flow and its

solution procedure has been described in Ref. [88]. The air enters the test tube at an inlet temperature, T_{in} , and flows over the different types of VR/baffles. The pitch spacing, p is a distance between the neighboring baffle cells/modules.

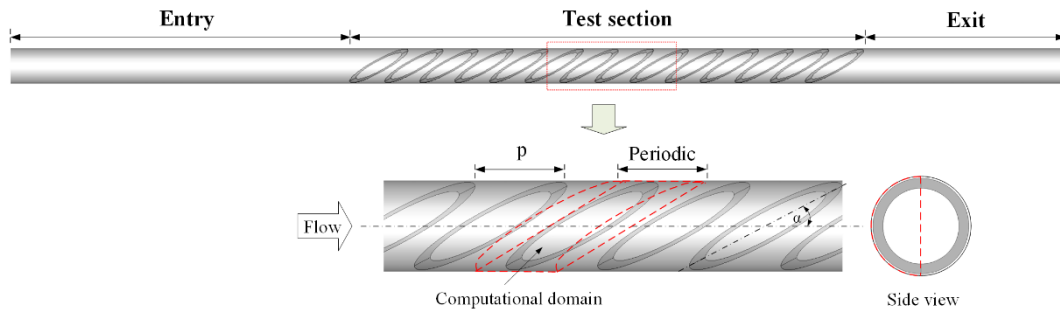


Figure 4.3 Tube geometry of periodic flow for VR.

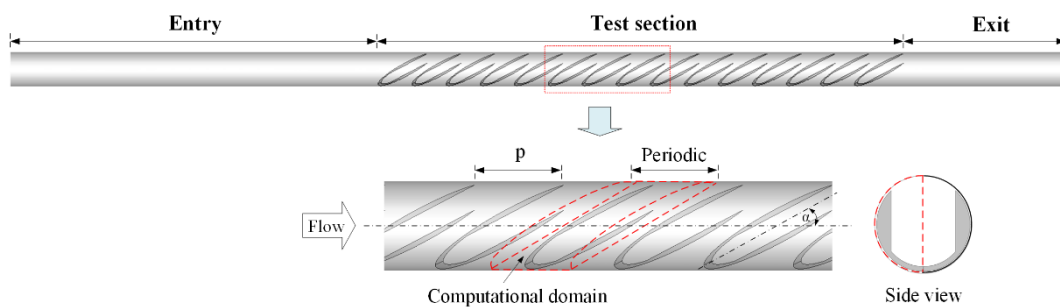


Figure 4.4 Tube geometry of periodic flow for HB.

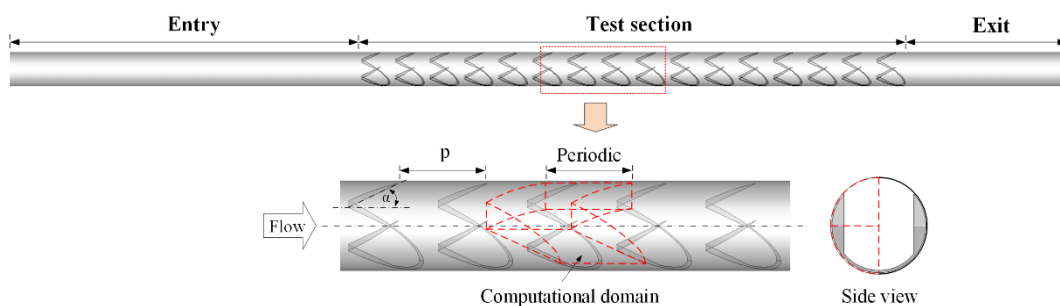


Figure 4.5 Tube geometry of periodic flow for VHB.

4.1.2 Computational domains

Using a periodicity characteristic of the given problems, the computational domains for the VB, UB, VR, HB and VHB modules are depicted in Figures 4.6, 4.7, 4.8, 4.9 and 4.10, respectively. In Figure 4.6, a constant surface heat-flux condition was applied at the top wall only. The inlet and outlet planes were specified as periodic

boundaries. The sidewalls were also assigned as symmetry planes. For the UB module in Figure 4.7, a constant heat-flux value was applied on all walls while similar uniform heat-flux was used for the tube flow modules fitted with VR, HB and VHB as shown in Figures 4.8, 4.9 and 4.10, respectively. In fact, Nu is free from heat-flux boundary conditions and thus, any of heat-flux value can be applied on the tube/channel wall. In the present work, these tube/channel walls are heating at a constant heat flux of 600W/m^2 . The symmetry geometry was assigned as symmetry plane in the periodic flow modules.

For the 30° UB periodic channel flow module in Figure 4.7, the channel height, H was set to 45 mm while the baffle blockage ratio ($BR=b/H$) is varied in a range of $BR=0.05-0.25$ with the pitch spacing ratio, $s=p/H=0.5-2.0$ in the present investigation. Periodic boundaries are used for the inlet and outlet of the flow domain. Constant mass flow rate of air with 300K ($Pr=0.707$) is assumed due to periodically fully-developed flow conditions.

For the periodic tube flow modules for VR, HB and VHB baffles as shown in Figures 4.8, 4.9 and 4.10, the air enters the tube at an inlet temperature, T_{in} , and flows over the 45° VR, HB and VHB baffles where b is the baffle height, $D=0.05$ m, is the tube diameter and b/D is known as the blockage ratio, $BR=0.05-0.20$. The axial pitch, L is a distance between the baffle modules in which L/D is defined as the pitch ratio, PR having a value in the range of 0.5–2.0.

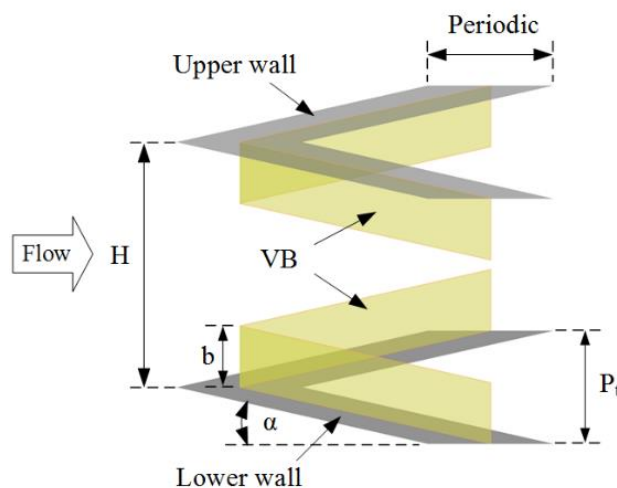


Figure 4.6 Computational domain for VB module.

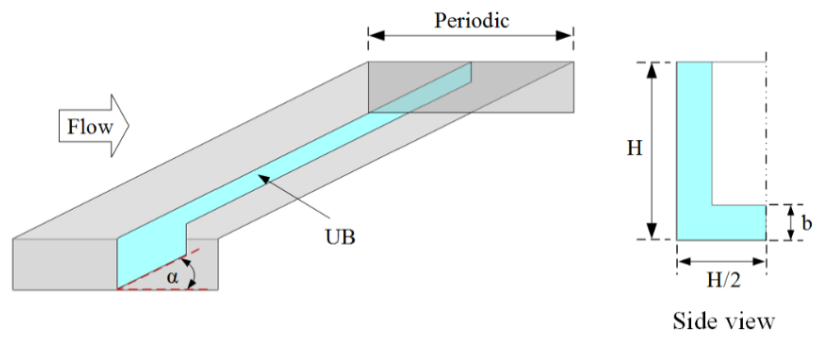


Figure 4.7 Computational domain for UB module.

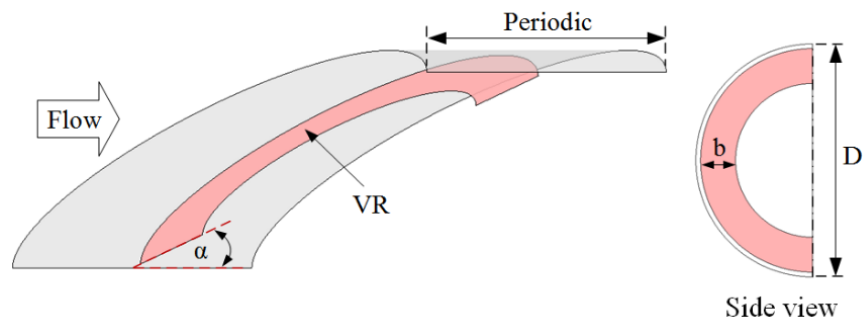


Figure 4.8 Computational domain for VR module.

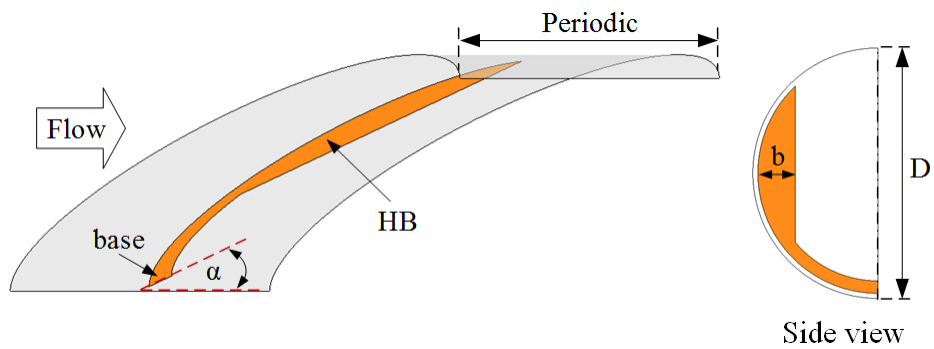


Figure 4.9 Computational domain for HB module

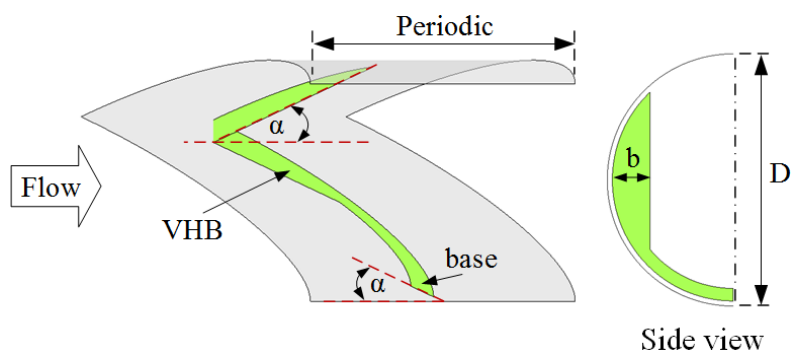


Figure 4.10 Computational domain for VHB module.

4.1.3 Grid generation

The numerical solution of the RANS and energy equations requires an arrangement of a discrete set of grids or meshes in the flow field. These equations are approximated by a set of algebraic equations on the discretized equations with defined grids. Then, the system of algebraic equations can be solved to obtain a set of discrete values which is an approximated solution of the RANS and energy equations. The determination of grids for a given body is known as grid generation.

The grid structure in the current study was generated by the Meshing application in the ANSYS Workbench. The computational domain created in previous section was meshed with quadrilateral-faced hexahedral elements.

Samples of hexahedral grid structure used for each case of the computation are presented in Figures 4.11 to 4.15. The grid structure was designed to be non-uniform for effective computation. As a matter of fact, a fine grid was required where high gradient area of variable solutions was expected. Therefore, the grid structure was intentionally densely packed around the baffles, at the wall boundaries, and at the periodic boundaries.

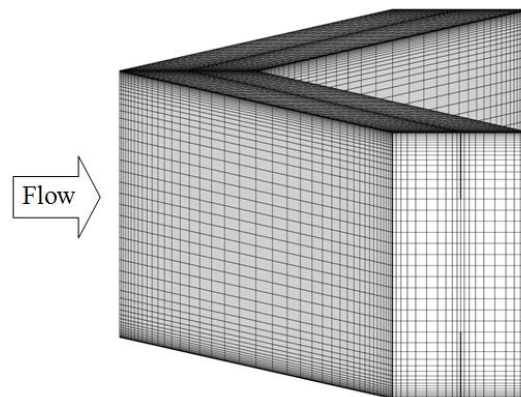


Figure 4.11 Hexahedral grid structure for VB module simulation.

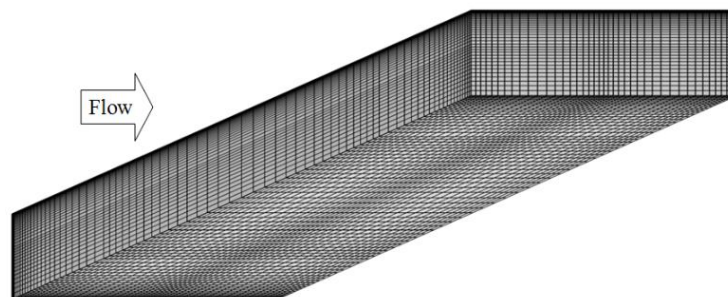


Figure 4.12 Hexahedral grid structure for UB module simulation.

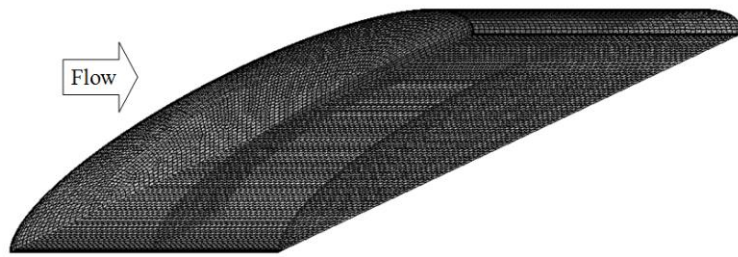


Figure 4.13 Hexahedral grid structure for VR module simulation

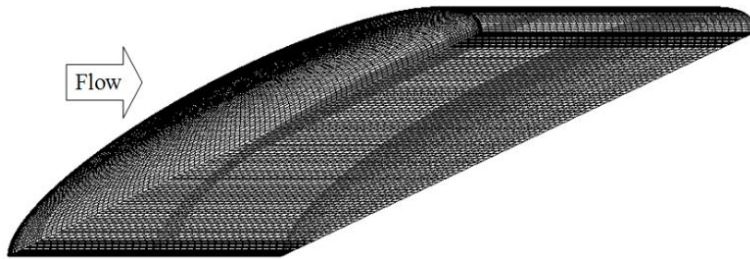


Figure 4.14 Hexahedral grid structure for HB module simulation

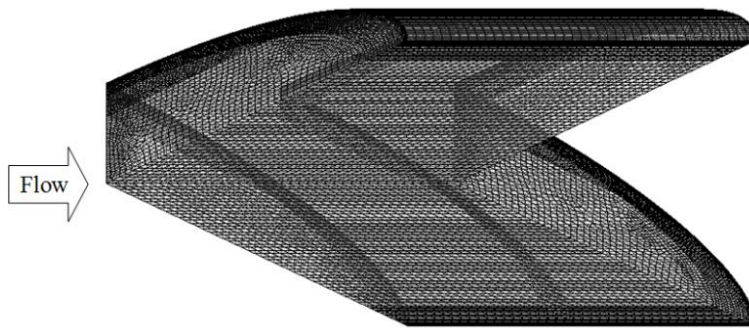


Figure 4.15 Hexahedral grid structure for VHB module simulation.

4.1.4 Boundary conditions

The following boundary conditions were imposed for the computations.

- Periodic boundary conditions were applied at the inlet and outlet of each periodic module while symmetry planes were used for symmetric geometry.
- No-slip boundary conditions were imposed along the stationary solid wall of the channel.
- The top wall of the channel was assumed to be at a constant surface heat flux while all walls were set to a constant heat-flux for the square channel and the round tube.
- The upstream bulk temperature of the fluid was specified to be 300K.

4.1.5 Computational schemes and convergence criteria

Since the algebraic equations for steady flow were non-linear, an iteration scheme was used to solve the equations. The algebraic equations had to be modified using linearization process. Then, the linear systems could be solved by iteration techniques. The numerical schemes or methods employed in the present study are presented in Table 4.1.

Table 4.1 Numerical scheme/method used in the computation

Spatial discretization	Numerical scheme/method
Pressure-velocity coupling	SIMPLE
Gradient	Least squares cell based
Pressure	Standard
Momentum	QUICK
Turbulent Kinetic Energy (k)	QUICK
Turbulent Dissipation Rate (ε)	QUICK
Energy	QUICK

For the iteration method, the convergence criteria had to be determined to terminate the iteration process. The residual was used as an indicator for the iterative convergence. The residual of the algebraic equation is the change in the equation over each step of iteration. It is usually scaled or normalized to eliminate the effect of magnitude of the flow variable. In order to minimize the iteration error, the normalized residual should be reduced until the first two or three most significant digits of the general flow variable will not change in further iterations.

Table 4.2 Residual monitors and convergence criteria

Residual monitor	Absolute criteria
Continuity	1×10^{-6}
x-velocity	1×10^{-6}
y-velocity	1×10^{-6}
z-velocity	1×10^{-6}
Turbulent Kinetic Energy (k)	1×10^{-6}
Turbulent Dissipation Rate (ε)	1×10^{-6}
Energy	1×10^{-9}

The computations for each steady-state simulation were considered to have converged when the monitoring residuals for all variables less than 1×10^{-6} except for the energy equation, the convergence criterion was set to less than 1×10^{-9} . The monitoring residuals and their convergence criteria are also listed in Table 4.2.

4.2 Verification of numerical simulation

The verification is a process of determining that a computational model accurately represents the conceptual description of the domain of interest. This section presents the verification methods used to estimate the errors in the numerical model.

4.2.1 Grid independence

The quality of a numerical solution depends highly on the quality of generated grid. A high quality grid is critical to reliability and accuracy of the numerical solution. A low quality grid may lead to an incorrect solution. Therefore, it is important to test if the attained solution is grid independent. A simple method to test for the grid independence is to refine the resolution of the numerical model and repeat the simulation. If the results do not change significantly, the successive refined grid is probably adequate. If there are significant differences between two solutions, the successive grid is likely an inadequate. This method is often called a grid refinement study. For the present study, the grid refinement study was performed for various grid resolutions. The observed key parameters for the test of grid independence were the friction factor, the average Nusselt number, and the averaged y^+ values. The settings and results of the grid refinement study are presented in the next chapter.

4.2.2 Grid convergence index

The other method to examine the numerical error in a numerical solution is to determine the grid convergence index (GCI). This approach was originally proposed by Roached [89] for reporting the grid refinement study. The GCI is based on generalized Richardson extrapolation involving comparison of discrete solutions at two different grid sizes [90]. The objective is to provide a measure of uncertainty of the grid convergence. The GCI indicates how much the numerical solution would change with a further grid refinement. A small value of GCI indicates that the computation is within the asymptotic range of convergence. The GCI on the fine grid is defined as per [91]

4.2.3 Verification of smooth channel

To verify the numerical model, at preliminary stage, computational experiments were repeatedly performed to quantify the average friction factor (f_0) and average Nusselt number (Nu_0) for smooth tube/channel at a given Reynolds number ranging from 4000 to 20,000. Then, the calculated Nu_0 and f_0 were qualified with prominent classical correlations at the same given Reynolds numbers.

The average friction factor for smooth tube/channel was compared with Blasius correlation [92] and Petukhov correlation [92] for fully developed turbulent flow in tubes/ducts.

The Blasius correlation is expressed as

$$f = 0.316 \text{Re}^{-1/4} \quad \text{for } \text{Re} \leq 2 \times 10^4 \quad (4.1)$$

The Petukhov correlation is given by

$$f = (0.790 \ln \text{Re} - 1.64)^{-2} \quad \text{for } 3,000 \leq \text{Re} \leq 5 \times 10^6 \quad (4.2)$$

The average Nusselt number for smooth channel was compared with Dittus-Boelter correlation [93] and Gnielinski correlation [92] for fully developed turbulent flow in tubes/ducts.

The Dittus-Boelter correlation is expressed as

$$\text{Nu} = 0.023 \text{Re}^{4/5} \text{Pr}^{2/5} \quad \text{for } 0.6 \leq \text{Pr} \leq 160, \text{Re} \geq 1 \times 10^4 \quad (4.3)$$

The Gnielinski correlation is given by

$$\text{Nu} = \frac{(f/8)(\text{Re} - 1000)\text{Pr}}{1 + 12.7(f/8)^{1/2}(\text{Pr}^{2/3} - 1)} \quad \text{for } 0.5 \leq \text{Pr} \leq 2,000, \text{Re} \geq 1 \times 10^4 \quad (4.4)$$

The numerical result was verified with the classical correlations and available experimental data for different geometric parameters and arrangements of baffled tubes/channels. The next chapter presents the results of preliminary numerical verification, and validation of numerical simulation with available experimental data.

CHAPTER 5

VALIDATION OF NUMERICAL SIMULATION

This chapter describes the verification and validation numerical results obtained from the procedures introduced in the previous chapter. First, the verification of numerical solutions is reported. Then, grid independence was tested. The numerical data of smooth tube/channel were validated with the published classical correlations. Finally, to validate the periodic flow models as given in chapter 4, comparison between numerical results and available experimental data is reported.

5.1 Verification of numerical simulation

5.1.1 Grid independence study

The grid density used in the numerical flow models was based on successive grid refinement experiments. The vital parameter specified the grid resolution of the numerical flow model was the edge size of following geometries: the V-baffle's curve, baffle's height, baffle's longitudinal pitch, and the deducted tube/channel's height. To test for grid independence solution, first, the grid density was refined from 50,000 (coarse) to 800,000 (fine) elements by adjusting the edge size of the geometries. Next, numerical simulations of the baffled tube were conducted at a prescribed Reynolds number of 3000 using those refined grid models. Then, the numerical solutions compiled from the grid refinement study were determined and reported in Table 5.1.

Table 5.1 Grid independence study of 30°HB, BR=0.1, PR=1.0 at Re=3,000

case	No. of Elements	Nu	f	%Error Nu	%Error f
1	49952	34.61	0.1891	-	-
2	107040	35.02	0.1916	1.18	1.28
3	203376	35.13	0.1903	0.30	0.64
4	402250	35.12	0.1908	0.03	0.23
5	808010	35.12	0.1906	0.01	0.10

The absolute errors of predicted friction factor and Nusselt number compared to each other. The errors are also presented in Table 5.1. Regarding the grid density studied, the friction factor and Nusselt number values for cases: 3, 4, and 5 were marginal to each other. Therefore, the grid densities for cases 3, 4, and 5 were regarded as grid independence solutions. Hence, to reduce the computational efforts, the grid density of case no. 3 (203,376 elements) was deliberately selected for meshing the numerical model. Corresponding to the errors obtained from the refinement, the

selected grid density was sufficiently fine for achieving the desired computational accuracy. If the PR increases more than PR=1.0, more grid mesh is needed to keep grid density constant along the tube/channel model.

5.1.2 Verification of smooth tube

To verify the numerical flow model for smooth tube, the computations were performed to quantify the friction factor (f_0) and Nusselt number (Nu_0) for numerical smooth tube flows at Reynolds number (Re) ranging from 4000 to 20,000. Then, the predicted f_0 and Nu_0 values for the tube flows are qualified with the data from the published classical correlations as expressed in previous chapter at similar Reynolds numbers. The predicted f_0 are compared with the Blasius and Petukhov correlations while the predicted Nu_0 are compared with the Dittus-Boelter and Gnielinski correlations for the tube flow model.

Comparisons of predicted and correlation values of the friction factor and Nusselt number for a tube flow model are depicted in Figures 5.1 and 5.2, respectively. In the figures, the predicted values for numerical smooth tube are in reasonably agreement with the correlation data. The predicted friction factor is within 6.8% and 3.82% compared to the Blasius and Petukhov correlations, respectively. For Nusselt number, the maximum deviation of the predicted is within 5.03% and 18.25% compared to data from Dittus-Boelter and Gnielinski correlations, respectively. Also, experimental data of f_0 and Nu_0 taken from Ref. [82] are included in the figures. A careful consideration indicates that the numerical solutions based on the verification results are reliable.

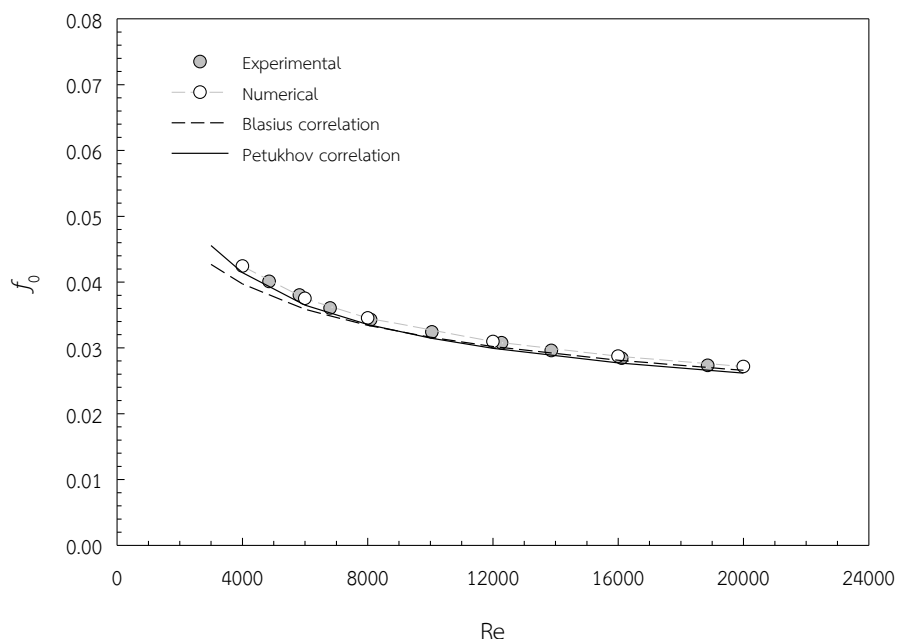


Figure 5.1 Verification of predicted f_0 for smooth circular tube.

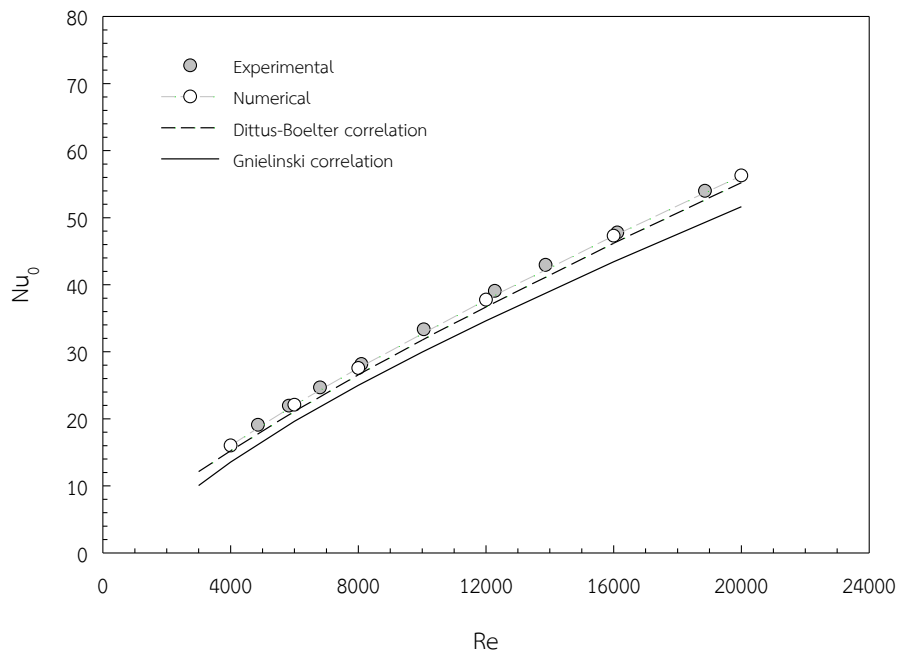


Figure 5.2 Verification of predicted Nu_0 for smooth circular tube.

5.2 Validation of numerical simulation

To validate the three numerical flow models, the experimental data were needed for comparison. Therefore, available experimental data were used to compare with the predicted values from the numerical flow simulations. Firstly, the numerical simulation of a baffled-channel flow as mentioned earlier in chapter 4 was carried out under the same condition of a constant surface heat flux on the top channel wall or the absorber wall. Secondly, the numerical flow model of a U-baffled square channel was conducted and the numerical results were validated with available measurements [82]. Finally, the numerical flow simulation in a HB-baffled tube was performed and the result was validated with measurements of the HB-baffled tube [82].

5.2.1 Validation of VB/UB-channel flow models

The comparisons of predicted friction factor and Nusselt number with experimental data are presented in Figures 5.3 and 5.4 for the channel fitted with multiple V-baffles or the VB-channel flow model. The comparisons are made for the characteristics of V-baffles with $BR = 0.25$, $PR = 0.5$, and $\alpha = 45^\circ$ and there are three types of V-baffle arrangements: single V-baffles on absorber plate only, inline V-baffles and staggered V-baffles on lower and upper walls. In Figure 5.3, the predicted f from the numerical flow model is in good agreement with measurements for the three arrangements. The maximum deviation of the predicted f is within $\pm 8.36\%$ for each arrangement. Figure 5.4 displays a comparison between the predicted Nu and available measurement for the three arrangements of the VB-channel flows. It is noted that the predicted Nu tending to increase with the rise of Re is in good agreement with the

measured Nu for all the three cases. The deviation of the predicted Nu is within $\pm 8.1\%$ for each arrangement. This validation makes high confidence for using the simulation of the VB-channel flow model with the turbulence model and numerical schemes mentioned earlier in previous chapter.

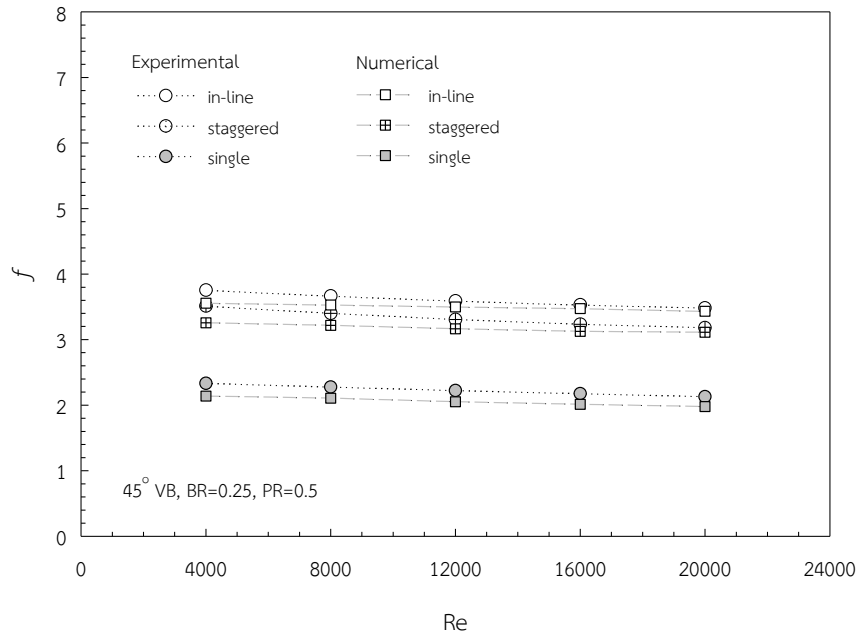


Figure 5.3 Comparison of predicted f with measurement for VB-channel flow.

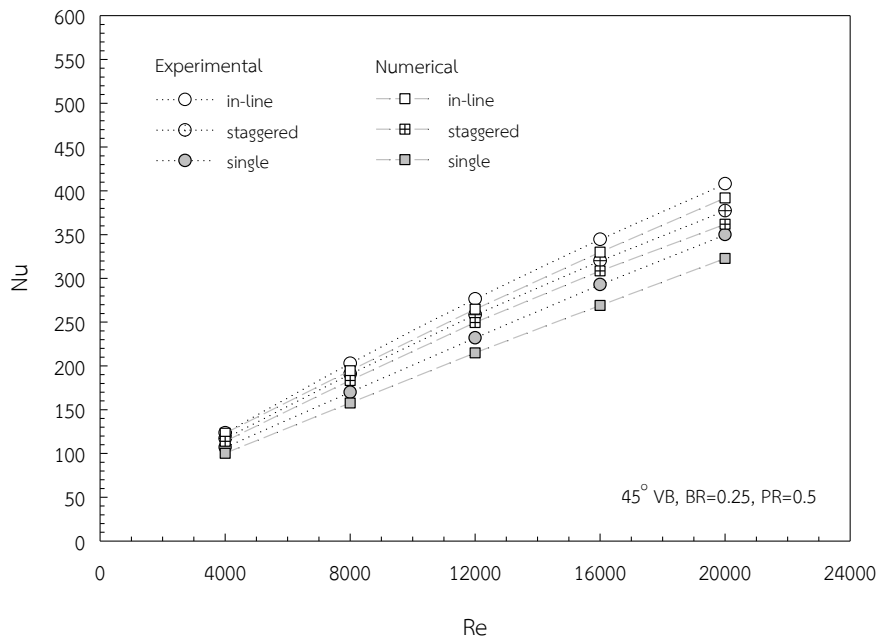


Figure 5.4 Comparison of predicted Nu with measurement for VB-channel flow.

Figures 5.5 and 5.6 depict, respectively, the comparison between the predicted data of f and Nu from the simulation of a square channel inserted with inclined U-baffles or UB-channel flow and measured data. The simulation was performed for the

U-baffled channel with $BR = 0.2$, $\alpha = 30^\circ$ and three values of PR (PR = 0.5, 1.0 and 2.0) as reported earlier in chapter 4. As can be seen in Figure 5.5, the predicted f agrees very well with available measurements for the three PR cases. The predicted f and Nu are within $\pm 11.01\%$ deviation with measured data for each PR.

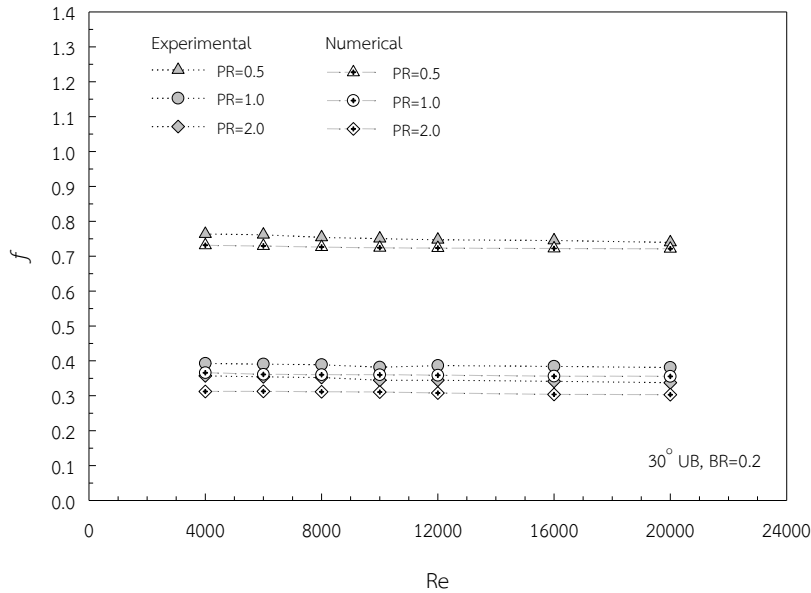


Figure 5.5 Comparison of predicted f with measurement for UB-channel flow.

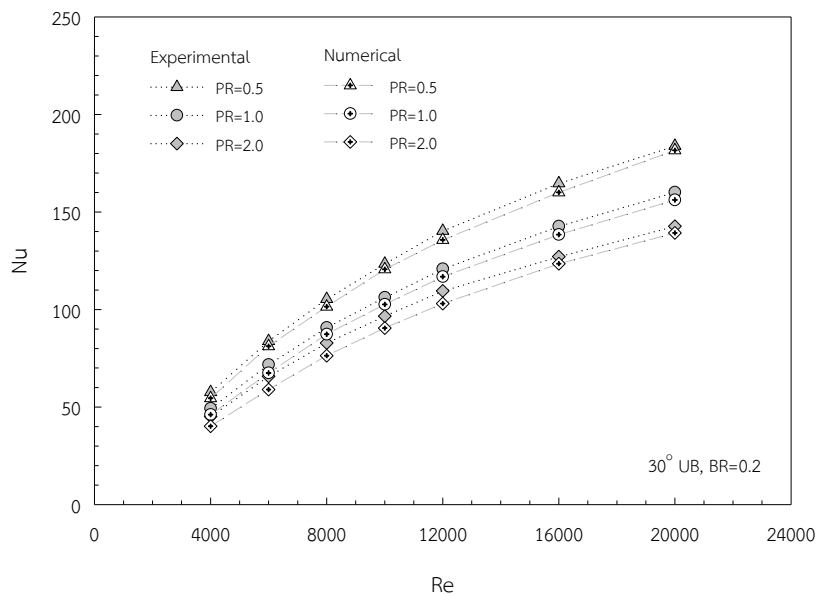


Figure 5.6 Comparison of predicted Nu with measurement for UB-channel flow.

5.2.2 Validation of HB-tube flow model

Comparisons of the predicted f and Nu for turbulent tube flow through an inclined horseshoe baffles (HB) or the HB-tube flow model with available measurements are presented in Figures 5.7 and 5.8, respectively. The parameters of

the HBs used in the simulation are $BR = 0.2$, $PR = 0.5$, and $\alpha = 20^\circ$ and the measured data at these HB parameters are taken from Ref. [82] for comparison. It is visible in Figure 5.7 that the predicted f agrees fairly well with measured data and is within $\pm 8.16\%$. Also, it is interesting to note that the predicted Nu for the HB-tube flow is in good agreement with measurement and an excellent agreement can be observed at higher Re . The maximum deviation of the predicted Nu is within $\pm 12.45\%$. As a result, the numerical solutions based on the validation results are regarded to be acceptable.

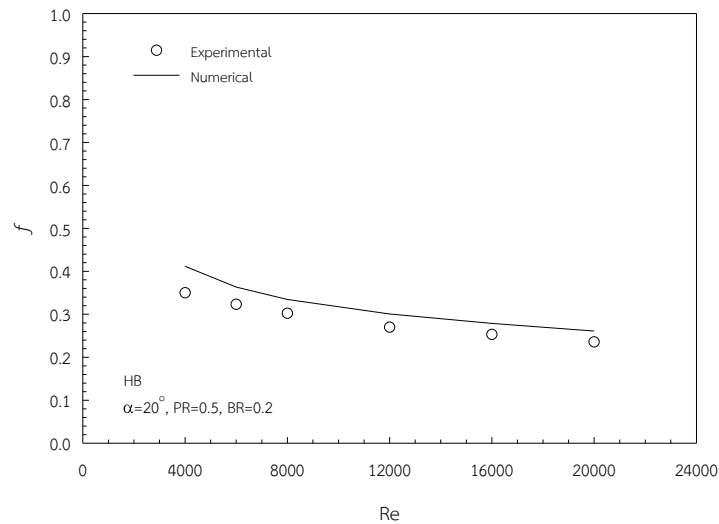


Figure 5.7 Comparison of predicted f with measurement for HB-tube flow.

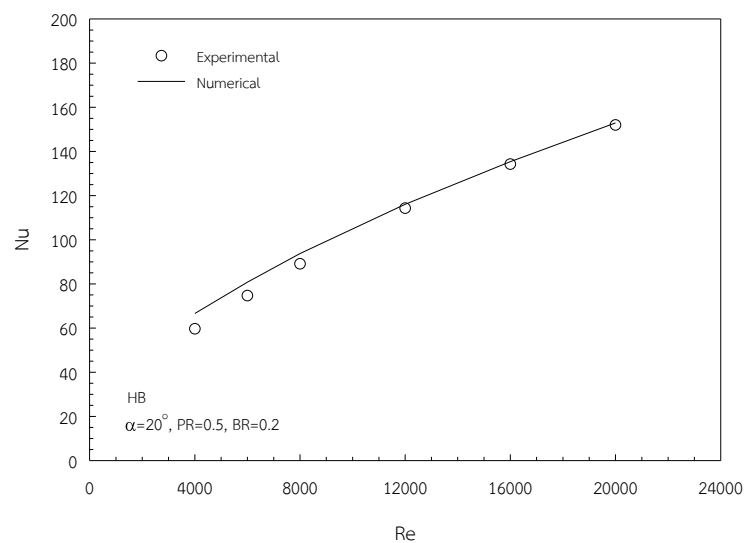


Figure 5.8 Comparison of predicted Nu with measurement for HB-tube flow.

The constructed numerical flow models for various baffle types are entirely verified and validated. The flow model can be used to represent the specified flow problem of interest. Next, the numerical computations with several airflow rates and different geometric parameters of various baffle types are performed to investigate the

fluid flow and heat transfer characteristics in a baffled tube/channel and presented in the next chapter. Chapter 6 presents and discusses the numerical results of various arrangements of various baffles mounted in the tube/channel using air as a working fluid.

CHAPTER 6

TURBULATORS

This chapter presents numerical investigations on heat transfer enhancement and pressure loss using proposed turbulators inserted into a rectangular channel, a square channel and a circular tube. All channels and tube were studied under a uniform surface heat-flux condition. The investigations were conducted with different blockage ratios (BR) and pitch ratios (PR) for Reynolds number (Re) ranging from 4000 to 20,000. The numerical results for each channel/tube were calculated and presented in terms of Nusselt number (Nu), friction factor (f), and thermal enhancement factor (η).

Three different turbulators were used for each channel and tube. First, the multiple V-baffles (VB) were placed in a rectangular channel with three arrangements: VBs mounted on a single wall, on inline and on staggered opposite walls. Second, the inclined U-baffles (UB) were inserted into a square channel while finally, the inclined vortex-ring baffles (VR) were inserted into a circular tube.

6.1 Multiple V-baffles

6.1.1 Effects on heat transfer

The numerical results on heat transfer under uniform heat flux condition in a rectangular channel fitted repeatedly with V-baffles were calculated and presented in the terms of Nusselt number (Nu). The V-baffles were arranged in a single wall of the absorber plate, inline and staggered arrays on the top and bottom walls. The variations of predicted Nu obtained under a range of Reynolds number and various pitch ratio values are presented in Figures 6.1 and 6.2, respectively. In Figure 6.1, it is found that the V-baffles yielded substantial heat transfer enhancement with a similar trend in comparison with the smooth channel. The Nu values increased with the increment of Re. The inline array gave higher Nu than the others. This is because the inline arrangement caused the flow recirculation and separation that provided the increment in turbulence intensity. At PR=0.5, comparing with the smooth channel, the Nu values for the in-line, staggered, and single wall arrangements were in the range of 728-763%, 652-719%, and 614-660%, respectively. This indicates that the inline arrangement gives higher heat transfer than the staggered and the single wall arrangements around 6-12% and 16-18%, respectively. Moreover, at PR=2, the V-baffles with inline, staggered, and single wall arrangements provided the Nu in a range of 453-490%, 431-460%, and 398-415% higher than the smooth channel. The inline arrangement performed better than the staggered and single wall arrangements at about 8-11% and 19-20%,

respectively. In Figure 6.2, the Nu reduced with the increment of PR. This is because the smaller PR provided more interruption of the boundary layer and also provided stronger vortex strength which leads to higher heat transfer rate. Therefore, the vortex flows created by the V-baffles could induce the impingement flow along the channel wall, especially behind the V-tip of baffles.

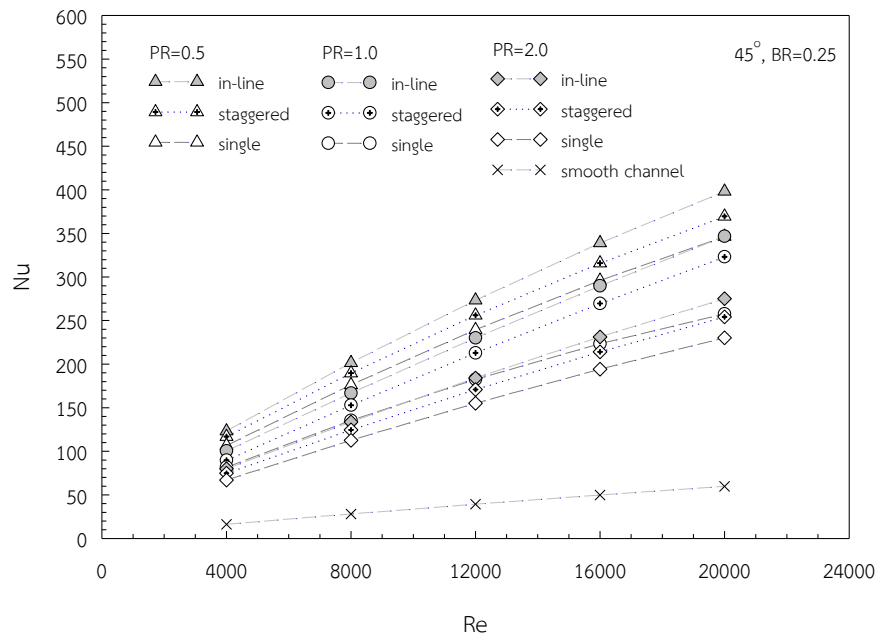


Figure 6.1 Variation of Nu with Re for VB.

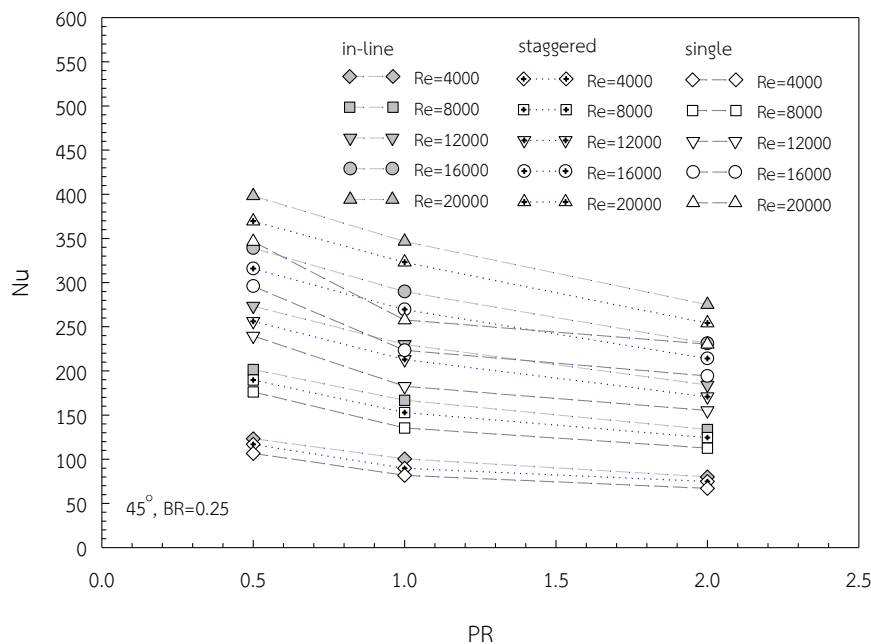


Figure 6.2 Variation of Nu with PR for VB.

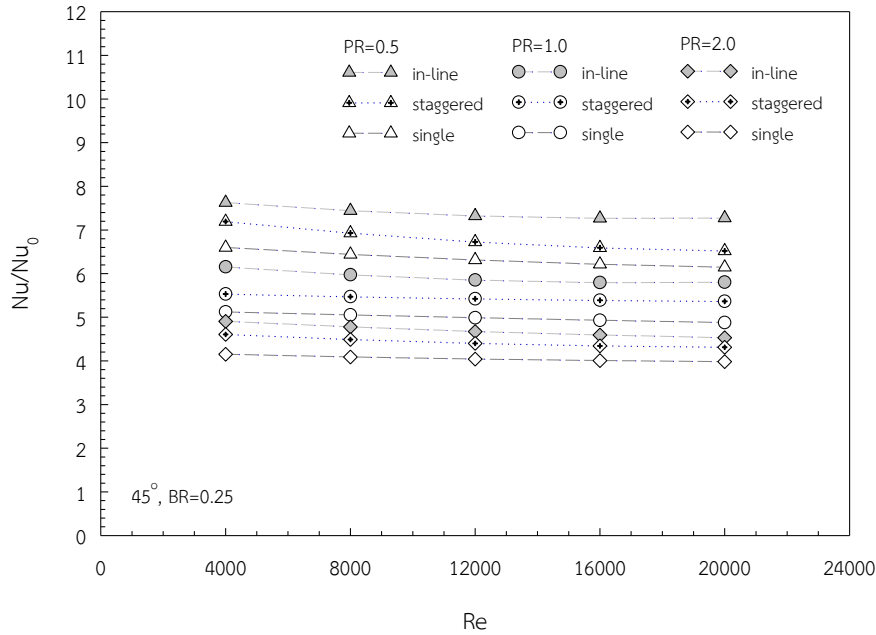


Figure 6.3 Variation of Nu/Nu_0 with Re for VB.

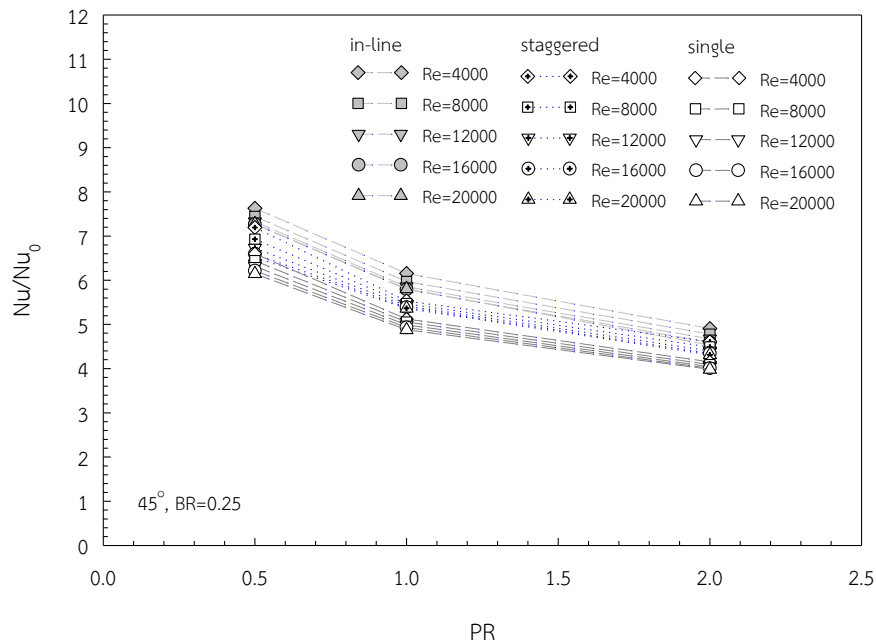


Figure 6.4 Variation of Nu/Nu_0 with PR for VB.

The relative Nusselt number defined as a ratio of augmented Nu to smooth channel's Nu , Nu/Nu_0 . The relative Nusselt numbers plotted against Re and PR were depicted in Figures 6.3 and 6.4, respectively. In Figure 6.3, the Nu/Nu_0 decreased slightly with increasing Re for all cases. The Nu/Nu_0 for the in-line arrangement was higher than that for the staggered and single wall arrangements. The higher flow blockage and stronger swirl/vortex flow from the in-line arrangement lead to better fluid mixing between the core and near-wall regions. A further investigation revealed that, for the

inline arrangement, the Nu/Nu_0 at $PR=0.5$ was also higher than that at $PR=1$ and 2 . The staggered and single wall arrangements also gave the similar trends. At $PR=0.5$, 1 and 2 , the increases in Nu/Nu_0 for the inline, staggered, and single wall arrangements were approximately in the range of $7.28-7.63$, $6.52-7.19$ and $6.15-6.6$; $5.81-6.16$, $5.37-5.53$ and $4.88-5.12$; and $4.53-4.9$, $4.31-4.61$ and $3.98-4.15$ times, respectively. In Figure 6.4, the Nu/Nu_0 was found to reduce steeply from $PR=0.5$ to $PR=1$ and then decrease gradually to $PR=2$ for each Re .

6.1.2 Effects on friction factor

The effects of V-baffles on the isothermal pressure drop across the rectangular channel are presented in this section. The variations of the pressure drop in terms of friction factor (f) with Reynolds number (Re) and Pitch ratio (PR) were showed in Figures 6.5 and 6.6, respectively. In Figure 6.5, it was apparent that the use of V-baffles leads to a large increase in f over the smooth channel. As expected, the obtained f from the V-baffles with inline arrangement was considerably higher than the staggered and single wall arrangements. The average increase in f was in a range of $12.5-139.7$ times above the smooth channel. At $PR=0.5$, the f with the inline array was around 8 and 38 times higher than the staggered and single wall arrays, respectively. The pressure losses may come from higher rotating flow and increasing surface area due to the presence of the V-baffles as can be seen in Figure 6.6.

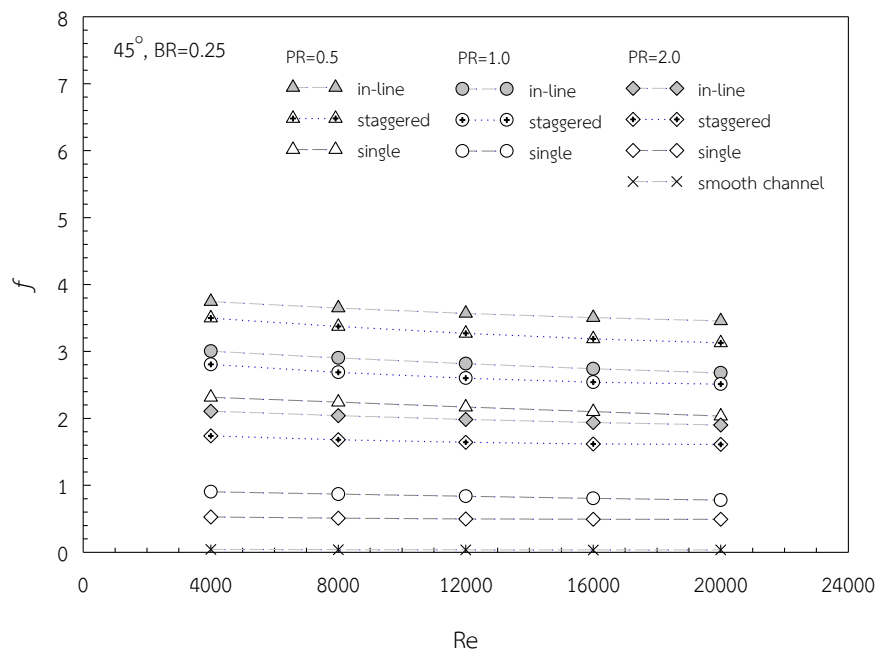


Figure 6.5 Variation of f with Re for VB.

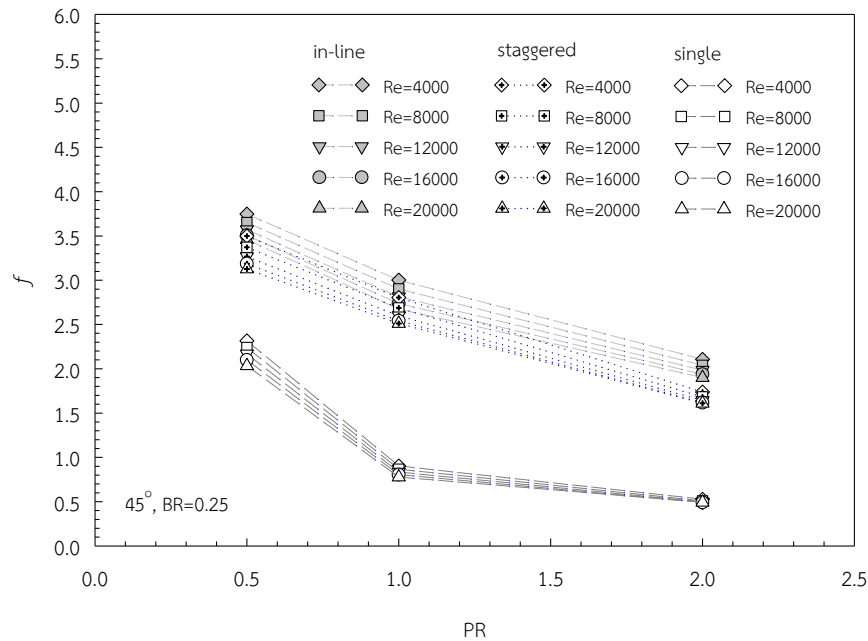


Figure 6.6 Variation of f with PR for VB.

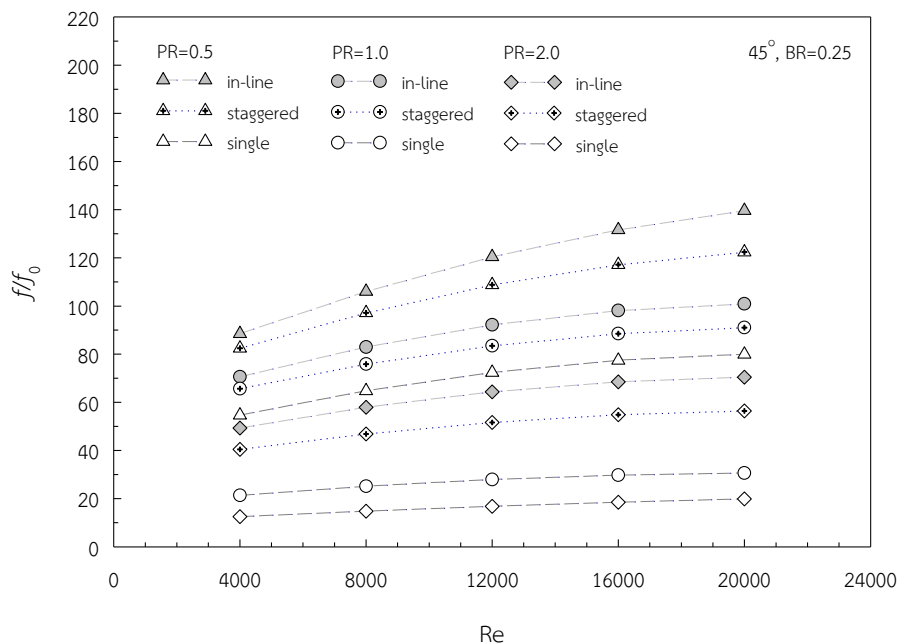


Figure 6.7 Variation of f/f_0 with Re for VB.

The effects of V-baffles on the isothermal friction factor ratio, f/f_0 , with Re and PR values were depicted in Figures 6.7 and 6.8, respectively. In Figure 6.7, the V-baffles provided a considerable increase in f/f_0 with the increment of Re. This can be due to higher flow blockage, larger surface area, and the reverse flow. The f/f_0 for the inline array was much higher than that for the staggered and single wall arrays at a similar flow condition. The variations of f/f_0 with PR for various arrangements were presented in Figure 6.8. In the figure, the f/f_0 was nearly independent from Re values and tended to decrease with the increment of PR. At PR=0.5, 1 and 2, the f/f_0 were in the range of

88.45-139.65, 82.42-122.42 and 54.62-79.9; 70.53-100.93, 65.7-90.8 and 21.36-30.63; and 49.3-70.41, 40.44-56.44 and 12.5-19.87 times for the inline, staggered, and single wall arrangement, respectively. For the single wall arrangement, the increment of PR from 0.5 to 1 reduced the friction loss significantly as shown in Figure 6.8.

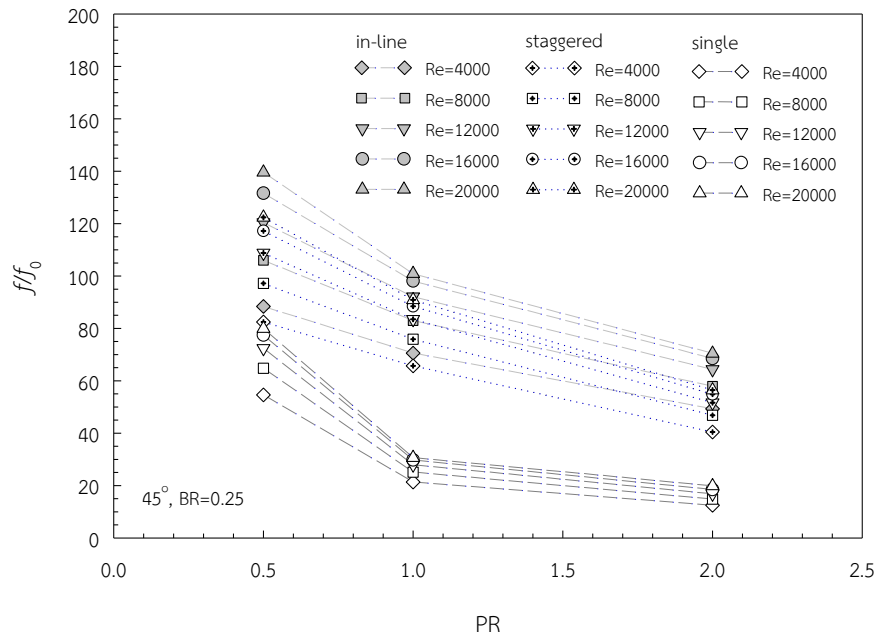


Figure 6.8 Variation of f/f_0 with PR for VB.

6.1.3 Effect on thermal enhancement factor

The variations of thermal enhancement factor (η) with Re and PR values were depicted in Figures 6.9 and 6.10, respectively. The data of Nu and f were compared at an identical pumping power condition. In Figure 6.9, the η showed the downtrend with increasing Re for all cases. The V-baffle with a single wall arrangement having PR=0.5 gave the highest η at the lowest Re. This is because of lowest flow blockage. The inline and staggered arrangements provided lower η because of their higher friction factor values. For the single wall VB, at PR=0.5, 1 and 2, the maximum η were about 1.83, 1.77 and 1.75, respectively. At a given PR, the single wall VB yielded the η around 9-21% and 12-27% higher than the inline and the staggered, respectively.

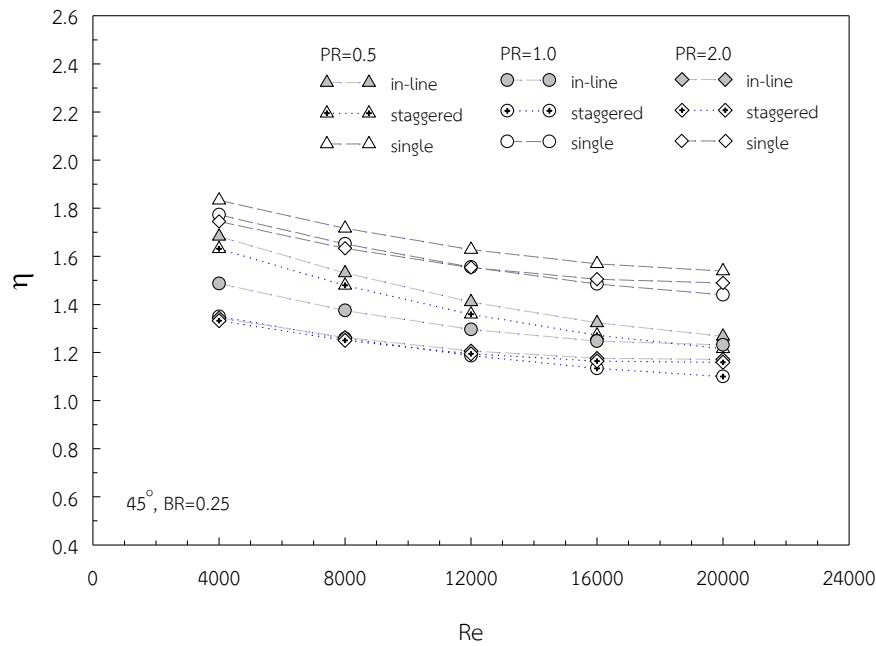


Figure 6.9 Variation of η with Re for VB.

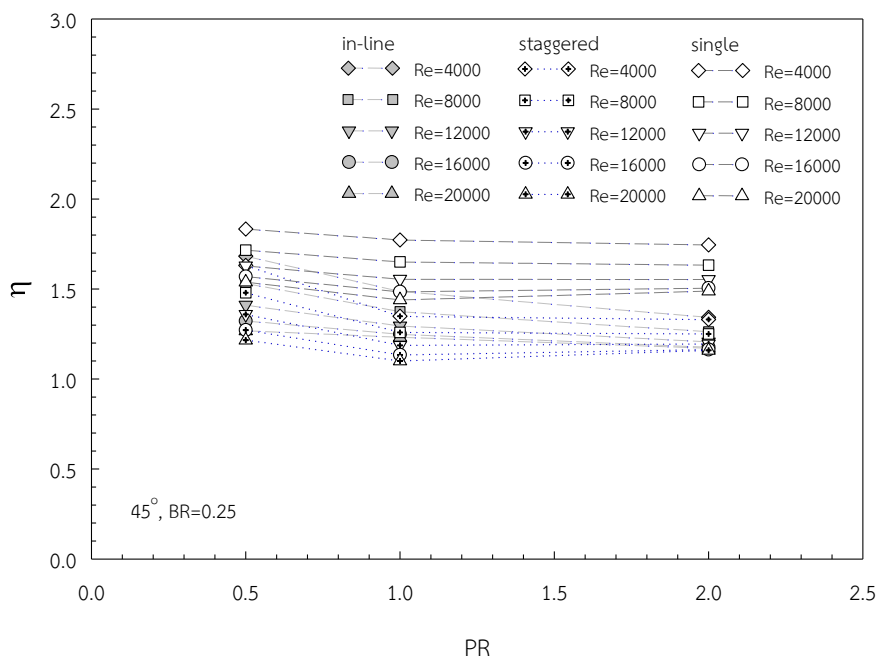


Figure 6.10 Variation of η with PR for VB.

6.1.4 Flow and heat topologies for multiple V-baffles

The flow and vortex coherent structures of different V-baffle arrangements in a rectangular channel can be presented using streamlines plotted on transverse planes at various locations. The distance between each transverse plane was 0.2 times PR. Figure 6.11 (a), (b), and (c) presents streamlines at locations $x/P=0$ to $x/P=1$ for V-baffles with single array, inline, and staggered arrays, respectively. In Figure 6.11 (a), a pair of vortex pairs occurred for using the single array. The vortex pairs for downstream V-

baffles were swirling in direction that left the heat surface (called “common-flow-up”). In the meantime, the vortex pairs for upstream V-baffles were swirling in direction toward the heat surface (called “common-flow-down”). For inline array, the vortex pairs induced by the V-baffles occurred symmetrically on top and bottom walls as shown in Figure 6.11 (b). However, for staggered array, the vortex pairs occurred on top and bottom walls were not symmetrical. As a result, the inline array produced more intensity of vortex strength than the other arrangements.

Figure 6.12 (a), (b), and (c) presents pressure distributions for different V-baffle arrangements on transverse planes at location $x/P=0$ to $x/P=1$ for single VB, inline VB, and staggered VB arrays, respectively. Considering the upward V-baffles, for all arrangements, the pressures in front of the tip area of V-baffles were high while the pressures behind the tip region of V-baffles were low. This behavior induced the flow to be swirled and become vortex flow behind the V-baffles. The highest pressure drops was seen in the sequence of the inline, the staggered, and the single VB arrays.

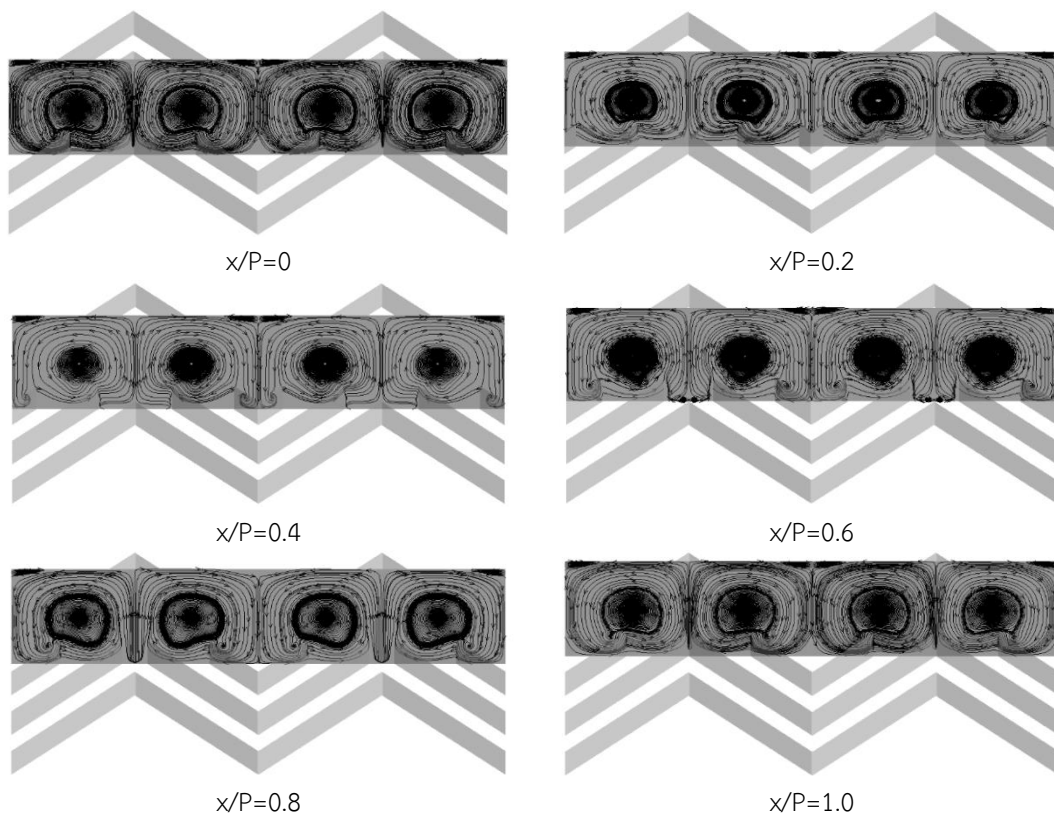


Figure 6.11(a) Streamlines in transverse planes for single VB at $Re=8000$ and $PR=0.5$.

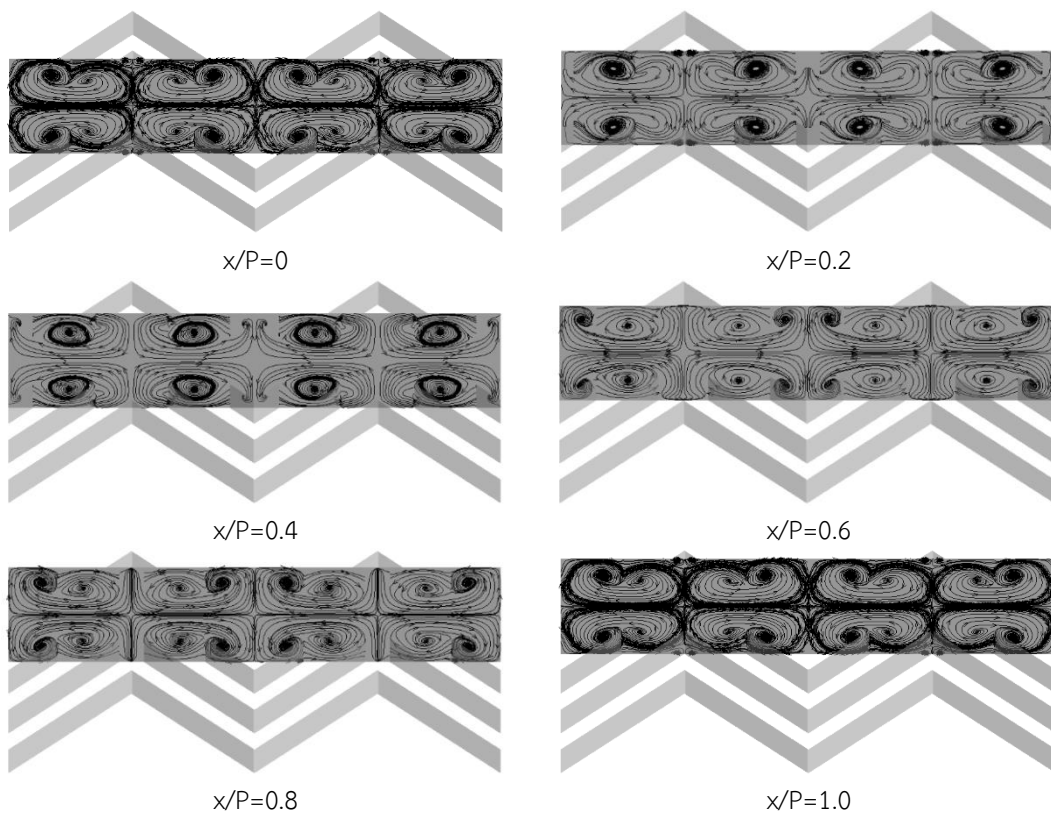


Figure 6.11(b) Streamlines in transverse planes for inline VB at $Re=8000$ and $PR=0.5$.

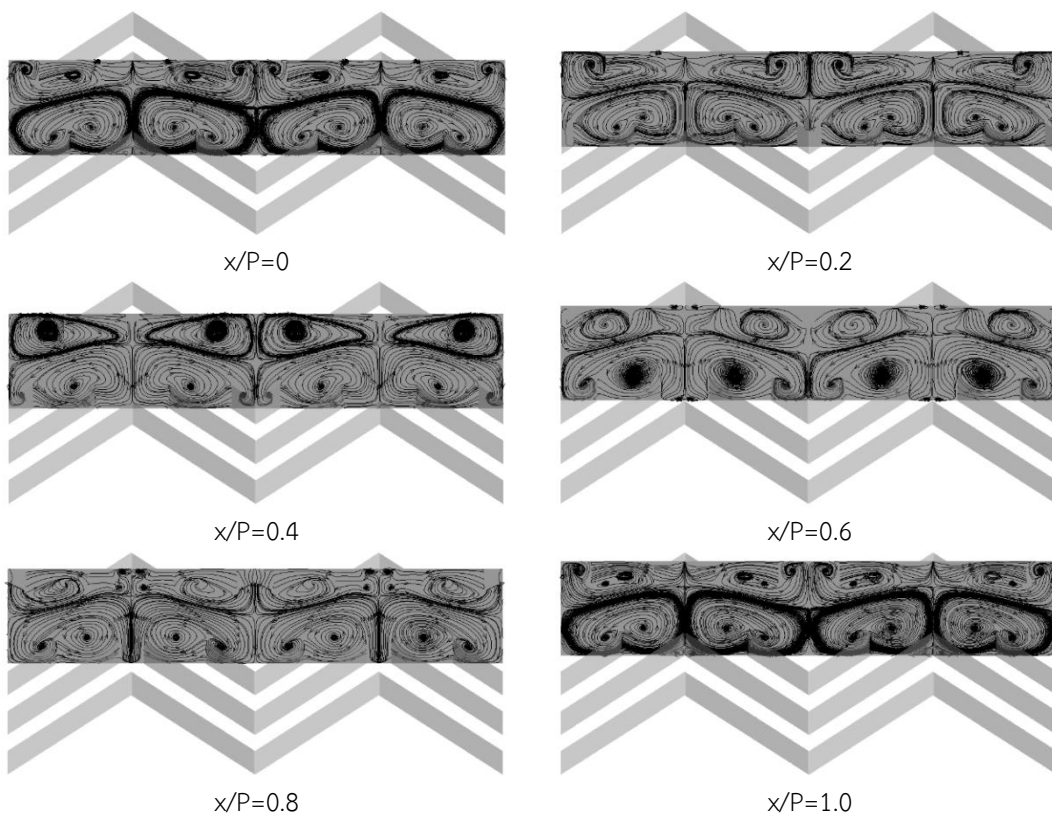


Figure 6.11(c) Streamlines in transverse planes for staggered VB at $Re=8000$ and $PR=0.5$.

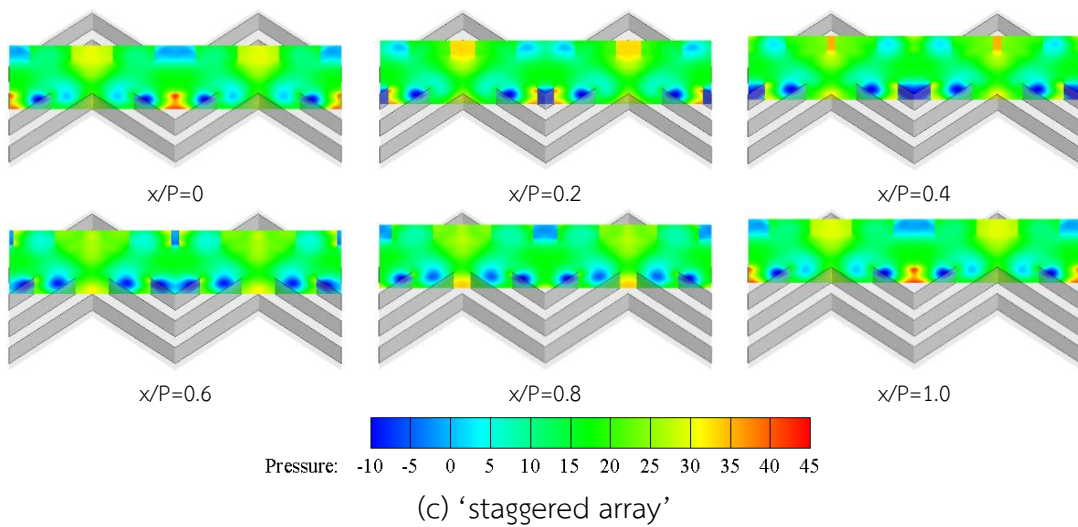
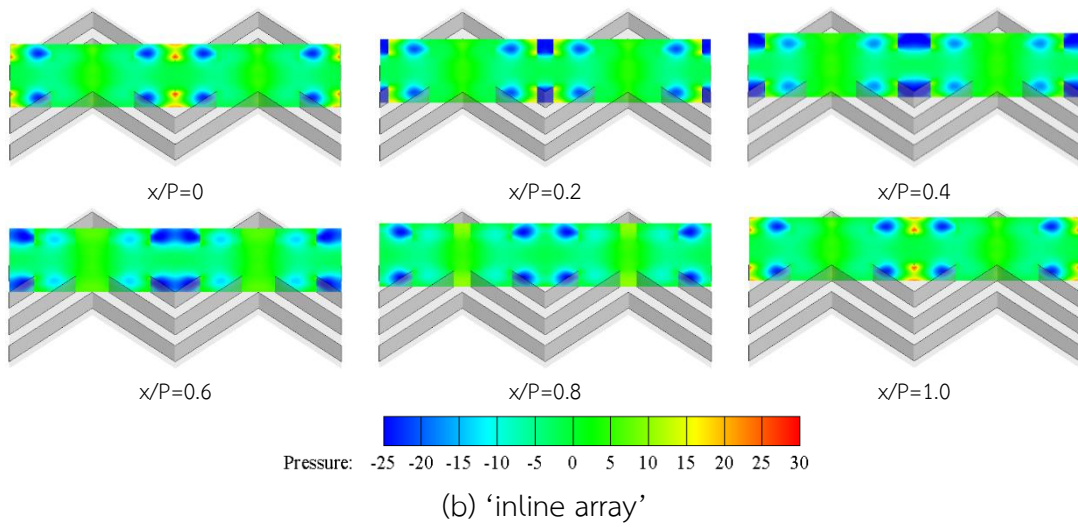
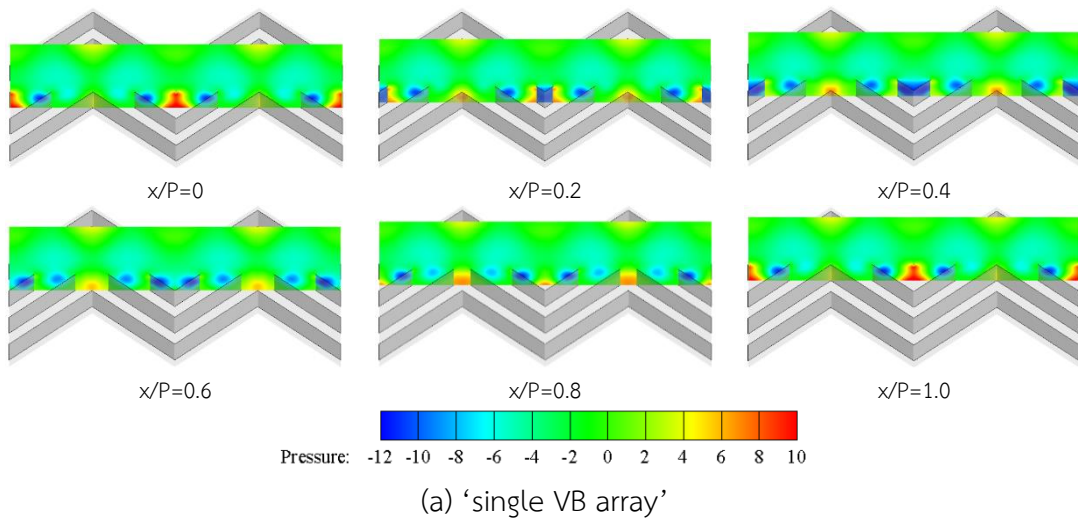


Figure 6.12 Pressure contours in transverse planes for VB at $Re=8000$ and $PR=0.5$.

The Q isosurfaces of the flows through V-baffles with single, inline, and staggered VB arrangements were presented in Figure 6.13 (a), (b), and (c), respectively. For all, the Q isosurfaces occurred behind the baffles and along the flow streamlines. The Q isosurfaces exposed only on the heat surface with the V-baffles for the single VB array as depicted in Figure 6.13 (a). The core flows for the inline array were largest and strongest as shown in Figure 6.13 (b).

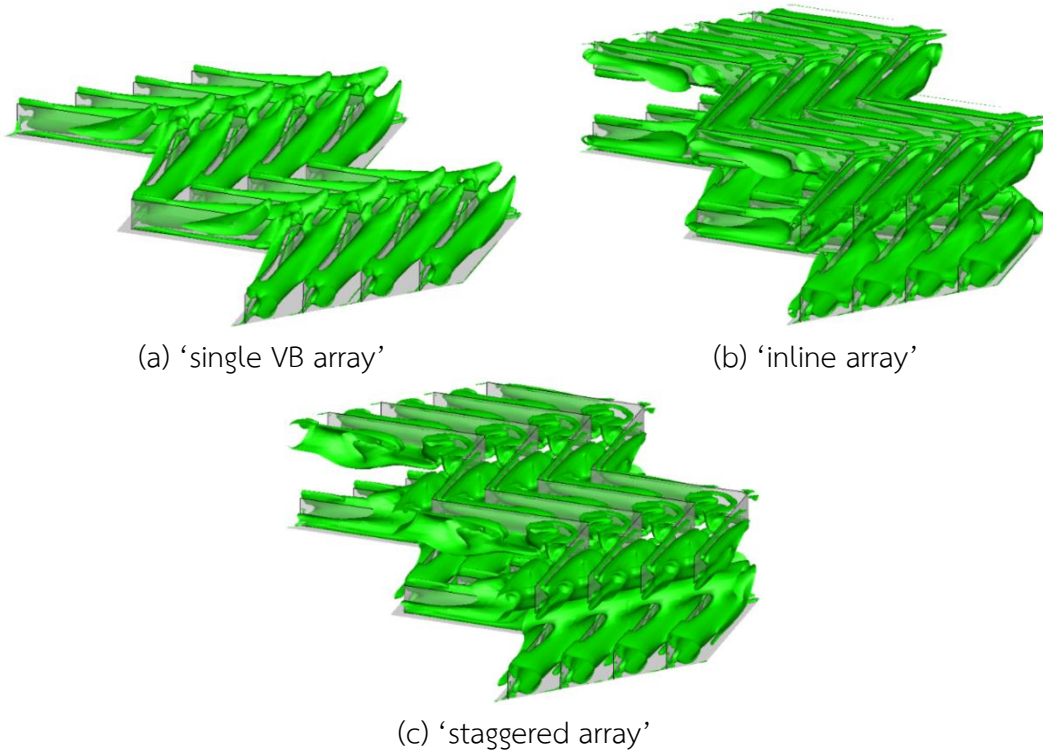
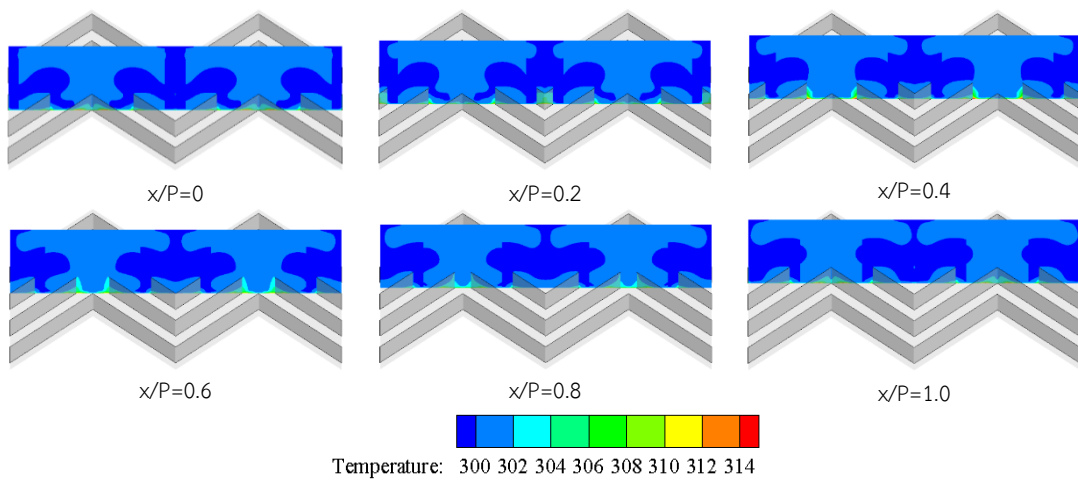
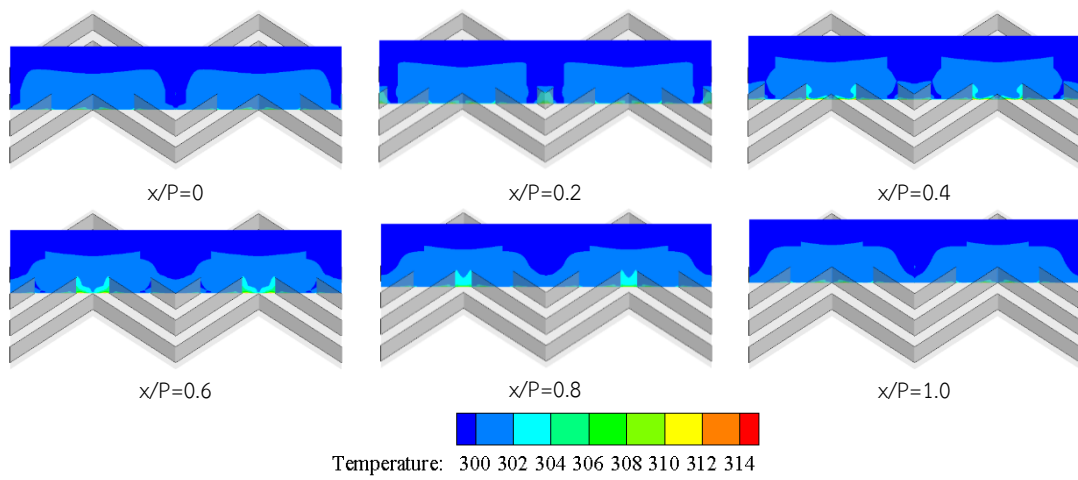


Figure 6.13 Q isosurface of $Q=200$ for different VB arrangement at $PR=0.5$ and $Re=8,000$.

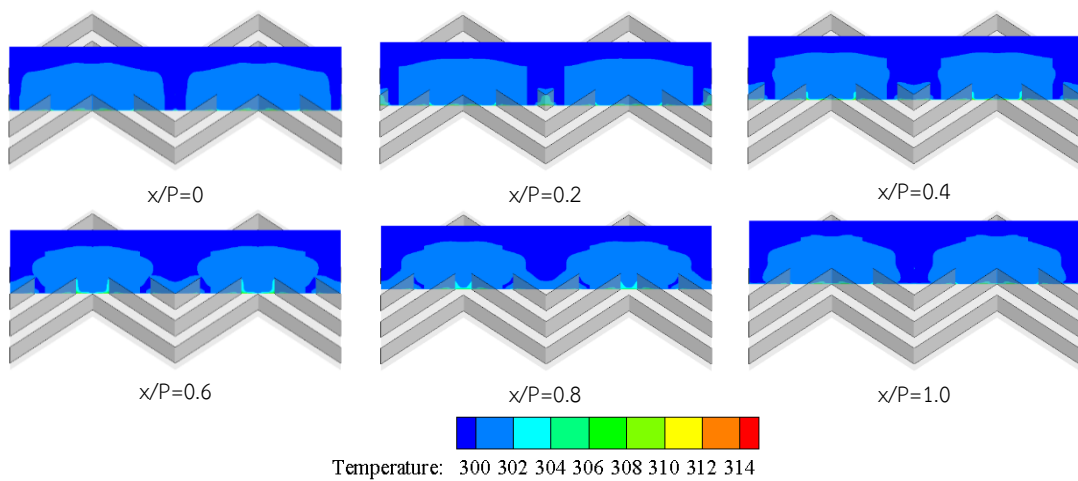
The temperature distributions of V-baffles with single, inline, and staggered VB arrangements on transverse planes at location $x/P=0$ to $x/P=1$ were presented in Figure 6.14 (a), (b), and (c), respectively. As a result, for all arrangements, the air with lower temperature was induced toward the heat surface behind the upstream V-baffles to exchange the heat.



(a) 'single VB arrays'



(b) 'in-line arrays'



(c) 'staggered arrays'

Figure 6.14 Temperature contours in transverse planes for VB at $Re=8000$ and $PR=0.5$.

The local Nusselt number contours on the upper wall of smooth channel, single, inline, and staggered VB arrangements were depicted in Figure 6.15 (a), (b), (c), and (d), respectively. For comparison, these local Nusselt numbers were calculated at Reynolds number of 8,000 and pitch ratio of 0.5. The channel with V-baffles produced high local Nusselt numbers in the area behind the tip of upward V-baffles which were the reattachment area of the flow. The inline array gave the highest averaged local Nusselt number. The smooth channel gave lowest heat transfer rate because of no reattachment flow.

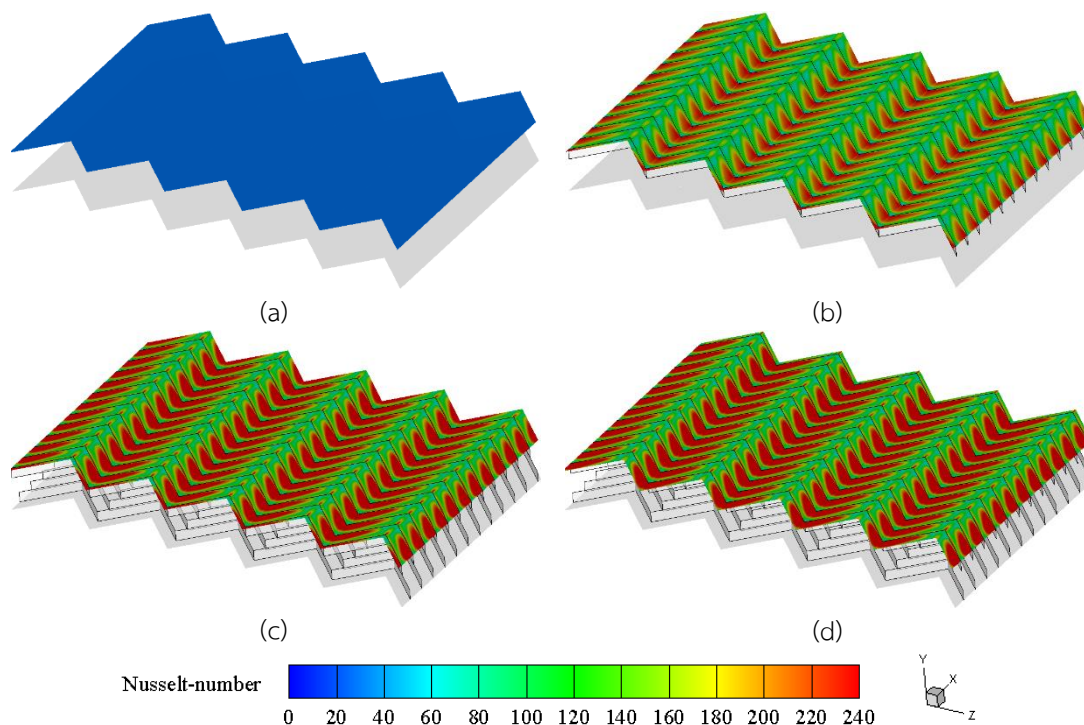


Figure 6.15 Local Nu_x contours on upper wall for (a) smooth channel (b) single VB (c) inline and (d) staggered VB arrays at $Re=8000$, $PR=0.5$.

The local Nusselt number (Nu_x) contour including the streamlines showing the impingement flow on the upper wall of the tested channel with inline VB arrays at $Re=8000$, $PR=0.5$ was presented in Figure 6.16. It is apparent from the figure that the high Nu values for the multiple V-baffles were in large areas over the channel wall. The peaks could be observed on the channel wall area around the upstream of V-tip where the red area showed the impingement flow region of the secondary flow providing higher heat transfer rate than other areas. The vortex-induced impingement flow was responsible to heat transfer enhancement in the channel, apart from fast fluid mixing between the core and the near-wall regions.

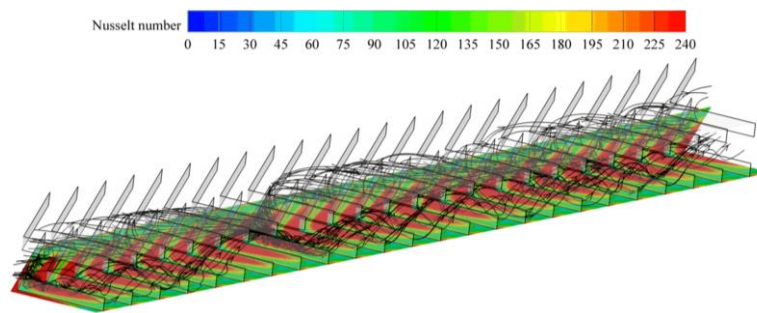


Figure 6.16 Streamlines and Nu_x contours on upper wall for inline VB at $Re=8000$ and $PR=0.5$.

6.2 Inclined U-baffles

6.2.1 Effects on heat transfer

The numerical results on heat transfer in a square channel fitted repeatedly with U-baffles under a uniform surface heat-flux condition are presented in this section. The U-baffles had 5 baffle-to-duct heights or blockage ratios ($BR=0.05, 0.1, 0.15, 0.2,$ and 0.25). The heat transfer coefficient was calculated and presented in the form of Nusselt number (Nu). The variations of Nu with Re and BR values are displayed in Figures 6.17 and 6.18, respectively. In Figure 6.17, the Nu increased with increasing BR and Re . The higher Nu could be obtained at the larger BR . This is because the larger BR produced flow recirculation and separation which gave better increase in the turbulence intensity of the flow than the smaller one. Depending on Reynolds number, for U-baffles at $PR=0.5$, the Nu values for the $BR=0.05, 0.1, 0.15, 0.2,$ and 0.25 were in the range of 244-282%, 271-313%, 304-346%, 337-389%, and 356-404% above the smooth channel, respectively. This indicated that the use of U-baffles with $BR=0.25$ yielded higher heat transfer than that with $BR=0.2, 0.15, 0.1$ and 0.05 around 4-6%, 16-17%, 29-31%, and 43-46%, respectively. At $PR=1$ and 2 , the $BR=0.05, 0.1, 0.15, 0.2,$ and 0.25 also provided Nu in the range of 211-240%, 230-266%, 261-301%, 298-333%, and 308-351%; and 177-204%, 204-232%, 236-273%, 266-307%, and 278-321% higher than the smooth channel, respectively. At $BR=0.25$, the U-baffle with $PR=0.5$ performed better than the one with $PR=1$ and 2 approximately 15% and 26%, respectively. Figure 6.18 showed that the Nu tends to increase with the increment of BR . This is because the U-baffles generated longitudinal vortex flows which can help increase the flow turbulence degree and also transport the central core flow to the near-wall regions. Thus, the merit of the U-baffle was that the created vortex flows could induce impingement flow over the duct heated walls (called vortex-induced impingement). Also, the vortex flows could wash up the flow trapped in the channel corner regions which normally acted as ineffectively heat transfer areas. This phenomenon led to higher heat transfer rate in the square channel.

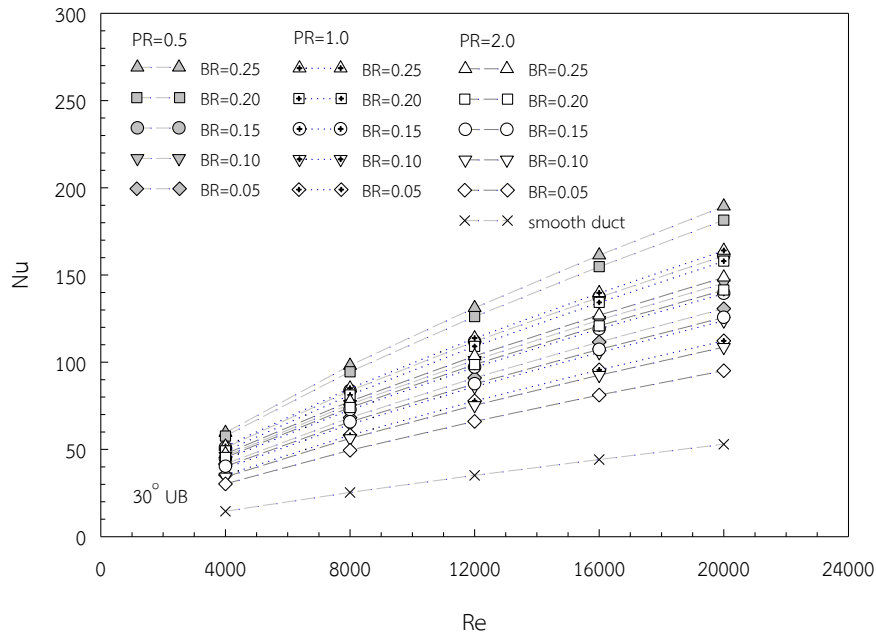


Figure 6.17 Variation of Nu with Re for UB.

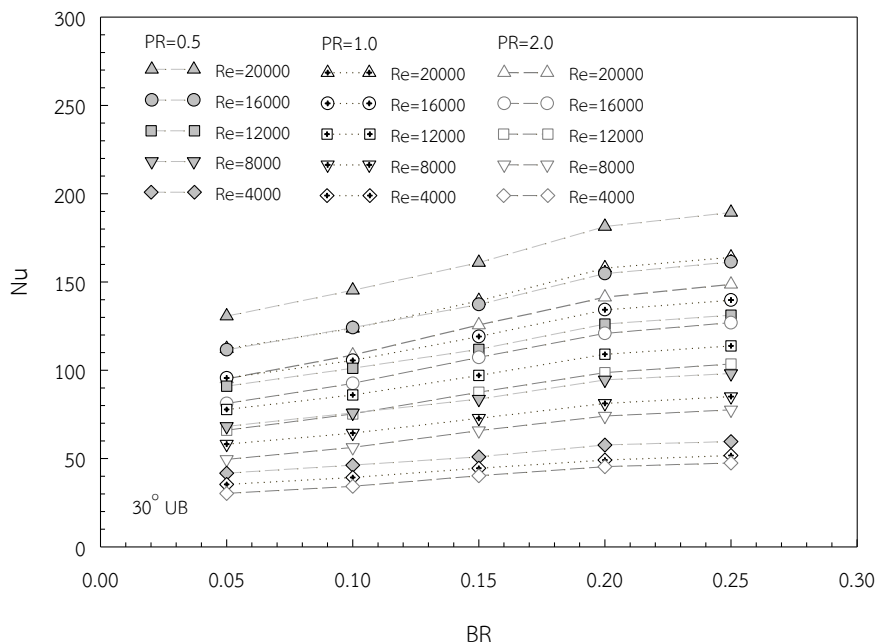


Figure 6.18 Variation of Nu with BR for UB.

The relative Nusselt numbers (Nu/Nu_0) plotted against Re and BR were depicted in Figures 6.19 and 6.20, respectively. In Figure 6.19, the Nu/Nu_0 tended to decrease with the increase in Re for all cases. The BR=0.25 provided the highest Nu/Nu_0 due to higher flow blockage and more frequent interruption of the flow leading to stronger swirl/vortex strength. Depending on Re, the BR=0.25, 0.2, 0.15, 0.1, and 0.05 yielded the Nu/Nu_0 values around 3.56-4.04, 3.37-3.89, 3.04-3.46, 2.71-3.13, and 2.44-2.82; 3.08-3.51, 2.98-3.33, 2.61-3.01, 2.30-2.66, and 2.11-2.40; and 2.78-3.21, 2.66-3.07, 2.36-2.73, 2.04-2.32, and 1.77-2.04 times for PR=0.5, 1, and 2, respectively. It was noted that the

Nu/Nu_0 of the U-baffles with BR=0.2 and PR=1 was two times higher than that of the full-length coil insert. In Figure 6.20, the Nu/Nu_0 showed a steeper increase at the beginning with the rise of BR value but gave a slower increase for $BR \geq 0.2$. The PR=0.5 provided higher Nu/Nu_0 than the PR=1 and 2 at a given BR value. A close inspection revealed that at similar BR value, the PR=0.5 yielded the Nu/Nu_0 approximately 17-27% higher than the PR=1 and 2.

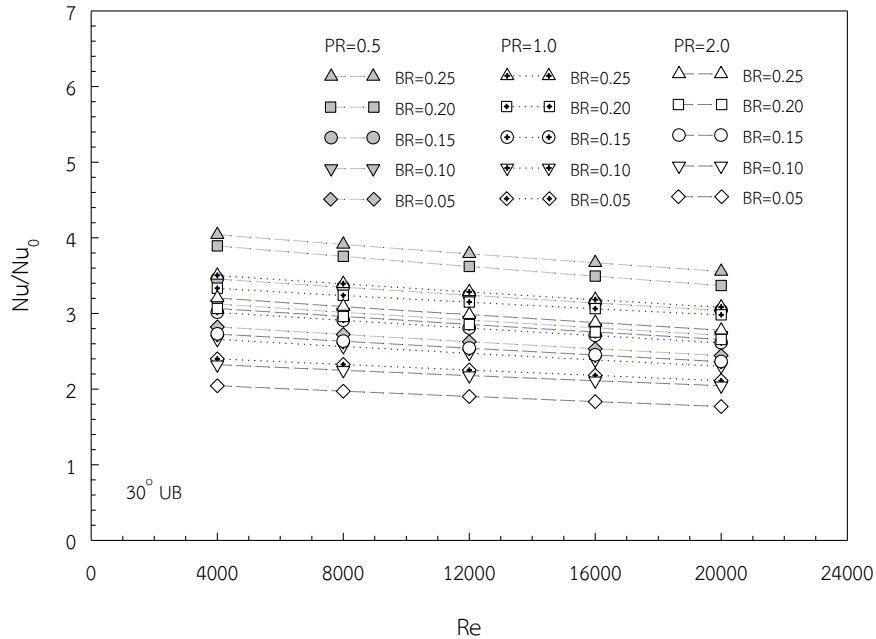


Figure 6.19 Variation of Nu/Nu_0 with Re for UB.

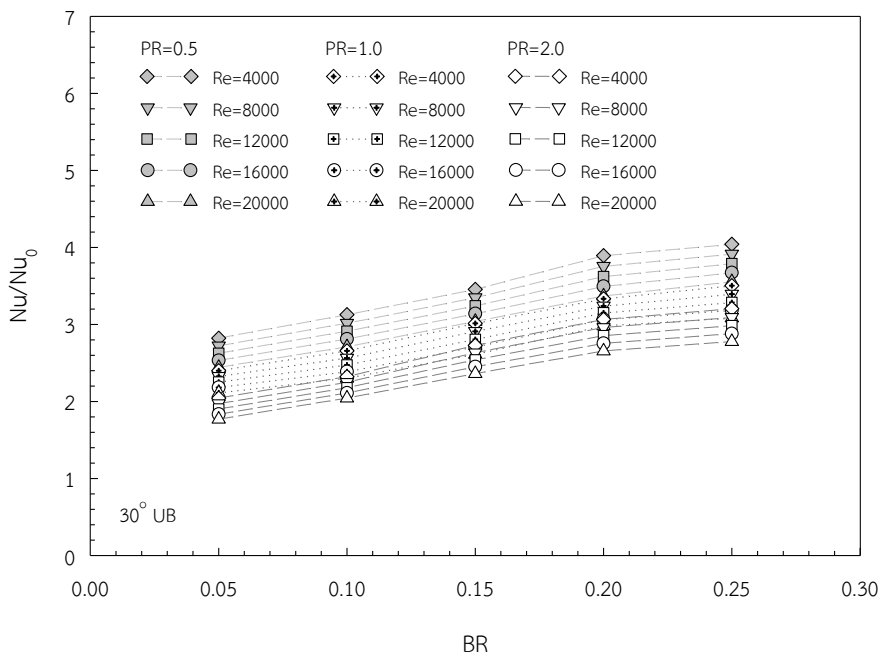


Figure 6.20 Variation of Nu/Nu_0 with BR for UB.

6.2.2 Effects on friction factor

The effects of the U-baffle inserts on the isothermal pressure drop across the square channel are depicted in Figure 6.21. The variations of the pressure drop in the form of f with Re and BR values are presented in Figures 6.21 and 6.22, respectively. In Figure 6.21, the use of U-baffles led to a substantial increase in the f over the smooth channel. As expected, the f for the U-baffles with $BR=0.25$ was substantially higher than that with smaller BR . The average increase in f was in a range of 3.8 to 41.7 times over the smooth channel. At $PR=0.5$, the f value for $BR=0.25$ was found to be around 30, 41, 45, and 58 times higher than that for $BR=0.2$, 0.15, 0.1, and 0.05, respectively. However, the f tended to increase with raising the BR and showed the steeper increase for $BR \geq 0.2$ as displayed in Figure 6.22. This could be due to the higher flow blockage, the larger surface area, and the reverse flow. The pressure losses were mainly due to high viscous losses near the wall, the extra forces exerted by reversing flow, and also the high flow blockage from the presence of the U-baffles.

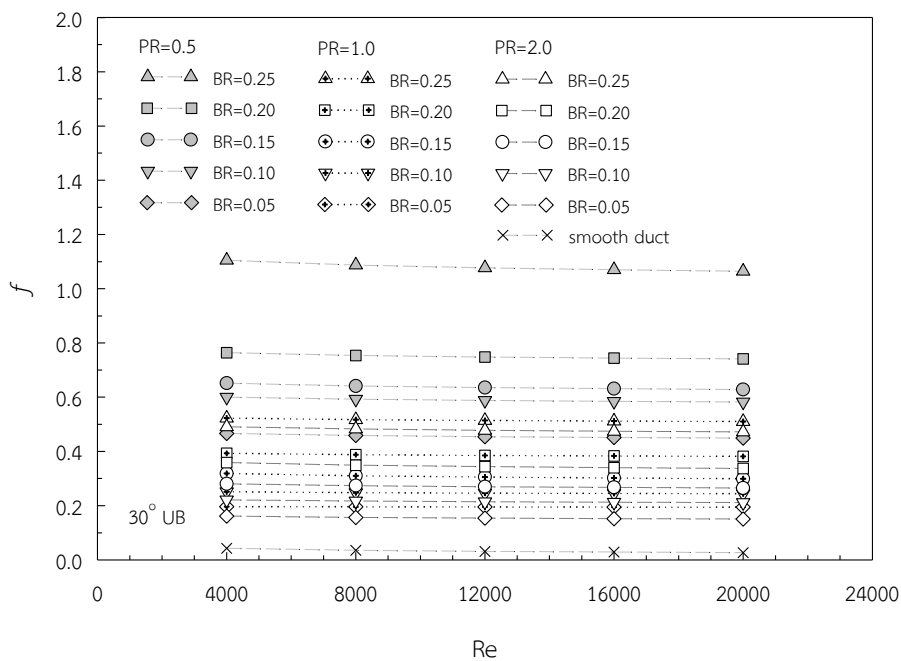


Figure 6.21 Variation of f with Re for UB.

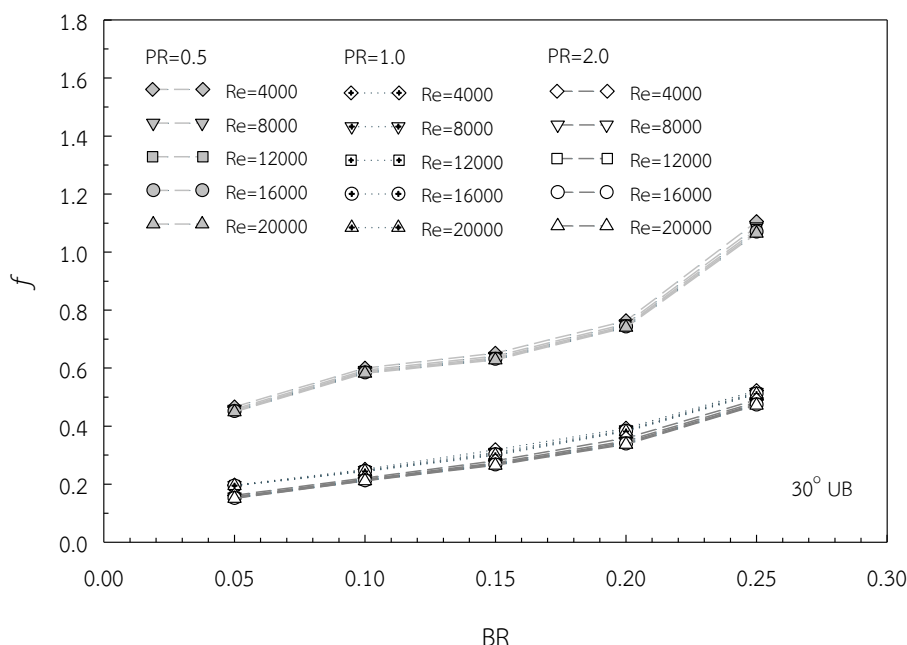


Figure 6.22 Variation of f with BR for UB.

Effects of U-baffle inserts on the isothermal friction factor ratio (f/f_0) with Re and BR values are depicted in Figures 6.23 and 6.24, respectively. In Figure 6.23, it is visible that the application of U-baffles leads to a substantial increase in f/f_0 with the rise of Re. As expected, the f/f_0 for BR=0.25 was much higher than that for BR=0.2, 0.15, 0.1, and 0.05 at a similar operating condition. For BR=0.25, 0.2, 0.15, 0.1, and 0.05, the increases in f/f_0 values at PR=0.5, 1, and 2 were about 25.7-41.7, 17.9-29.1, 15.2-24.5, 14.1-22.9, and 10.9-17.7; 12.2-20, 9.2-15, 7.4-11.7, 5.9-9.5, and 4.6-7.5; and 11.4-18.3, 8.4-13.1, 6.5-10.3, 5.2-8.3, and 3.8-5.8 times, respectively. The U-baffles at BR=0.15 and PR=2 also provided slightly higher f/f_0 than the full-length coil insert. Thus the flow blockage due to the presence of the U-baffles was a key factor that gave a high pressure drop in the channel. In Figure 6.24, the f/f_0 was found to increase with the rise in Re and BR values. It is visible that the UB inserts provided a substantial increase in the f/f_0 at about 3.8-41.7 times, depending on BR, PR and Re values. The BR=0.25 provided the largest f/f_0 of about 35.7, 17.04, and 15.8 times for using the PR=0.5, 1, and 2, respectively. This indicates that at a very high BR, the increment of PR was less effective to reduce significantly the friction loss in the channel.

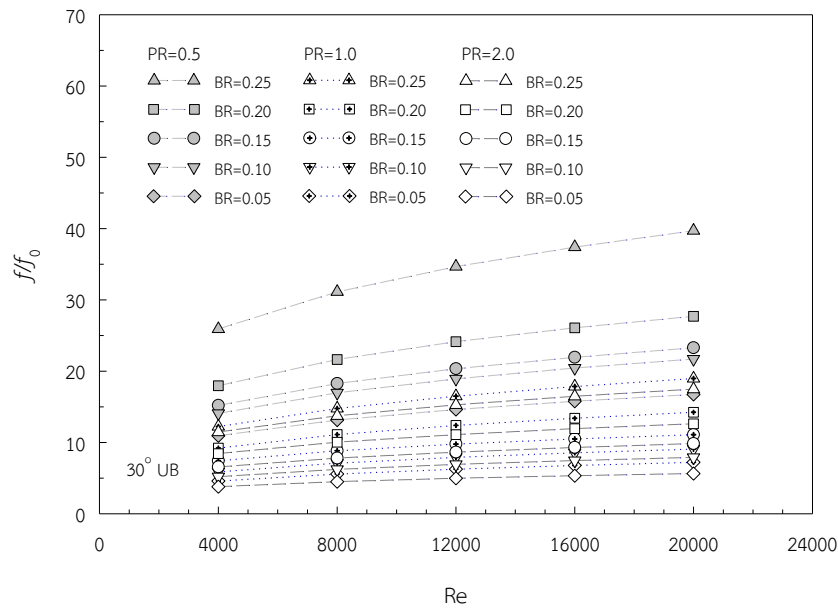


Figure 6.23 Variation of f/f_0 with Re for UB.

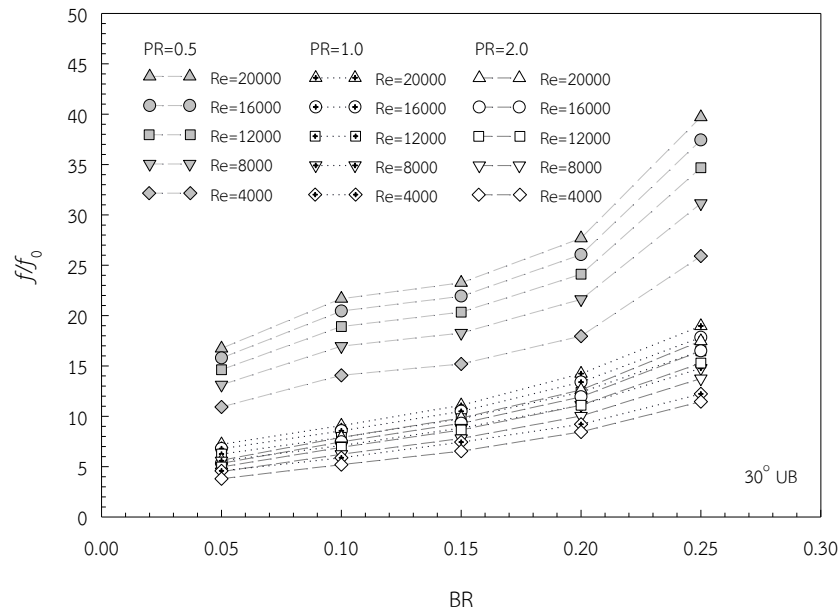


Figure 6.24 Variation of f/f_0 with BR for UB.

6.2.3 Effects on thermal enhancement factor

The variations of the thermal enhancement factor (η) with Re and BR values are depicted in Figures 6.25 and 6.26, respectively. The Nu/Nu_0 and f/f_0 were compared at an identical pumping power condition. In Figure 6.25, the η tended to reduce with the increase in Re for all cases. It is seen that the UB at BR=0.2 and PR=1 gives the highest η at the lowest Re. At PR=1, the maximum η were about 1.45, 1.48, 1.55, 1.6, and 1.53 for BR=0.05, 0.1, 0.15, 0.2, and 0.25, respectively. The maximum η was at BR=0.2, PR=1, and Re=4000.

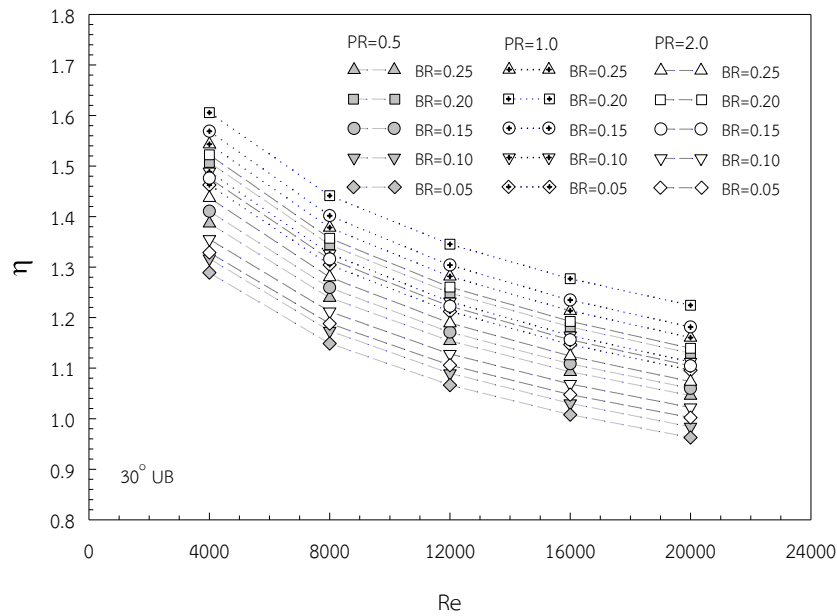


Figure 6.25 Variation of η with Re for UB.

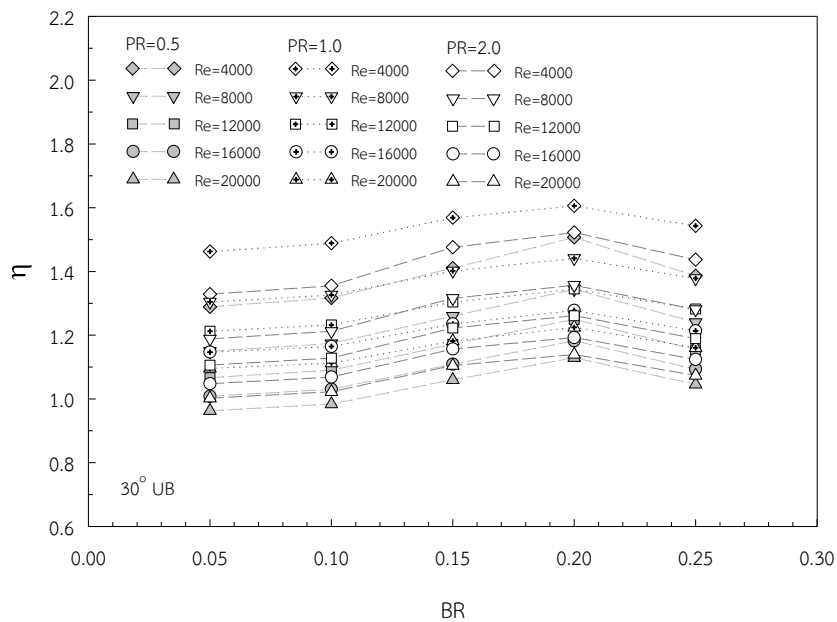


Figure 6.26 Variation of η with BR for UB.

6.2.4 Flow and heat topologies for inclined U-baffles

The flow and vortex coherent structures of the flow in a square channel fitted with inclined U-baffles (UB) can be described by plotting streamlines on transverse planes at each observed location. Each position was located at a distance of $0.2 \times PR$. Figure 6.27 presents the streamlines of the UB with $\alpha=30^\circ$, $BR=0.2$, and $PR=2.0$ in transverse planes at $x/P=0$ to $x/P=1$. From the figure, a longitudinal vortex pair occurred along the channel. The vortex pairs were induced toward the bottom wall. The longitudinal vortex pair also reduced with reducing PR .

The pressure distributions of the UB at $BR=0.2$ and $PR=2.0$ in transverse planes at $x/P=0$ to $x/P=1$ are presented in Figure 6.28. The high pressure region was in front of the UB while the low one was behind the UB. This behavior induced the longitudinal vortex flows and also the secondary vortex flows behind the UBs. The pressure drop also increased with reducing the PR.

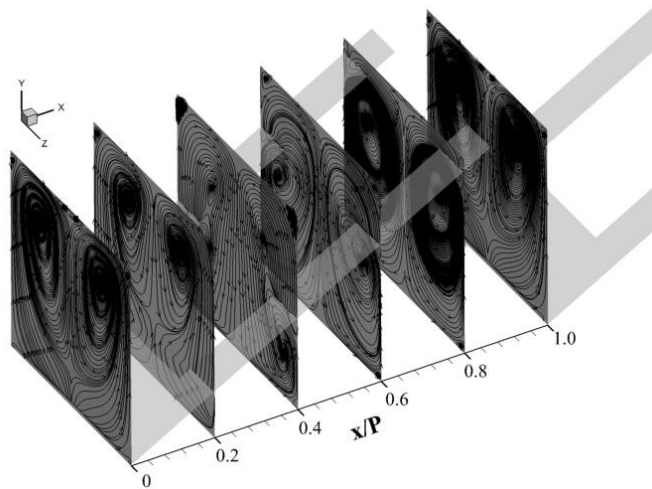


Figure 6.27 Streamline in transverse planes for UB at $BR=0.2$ and $PR=2.0$.

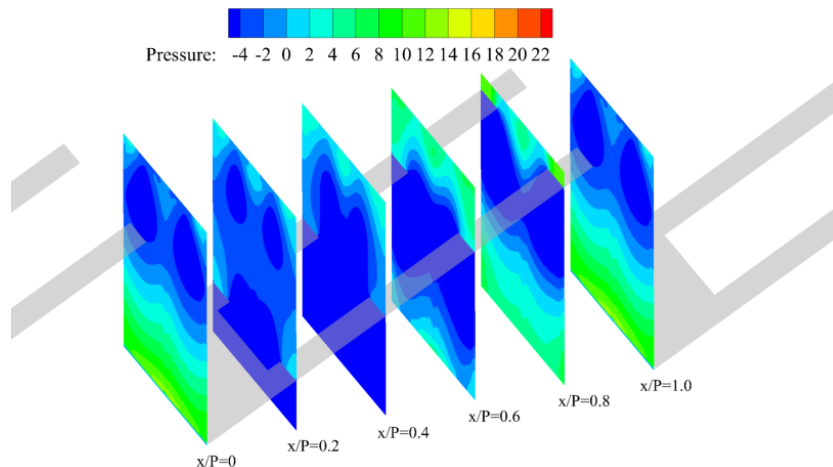


Figure 6.28 Pressure contours in transverse plane for UB at $BR=0.2$ and $PR=2.0$.

The Q-isosurfaces of the UBs (half left) with $\alpha=30^\circ$, $BR=0.2$, and various PRs at $Re=8,000$ are presented in Figure 6.29. The main vortex core flow occurred along the top wall of the channel. The smaller core flows also occurred behind the UBs. These smaller core flows also joined the main core flow. The shorter PR produced larger and stronger core flows than the longer PR.

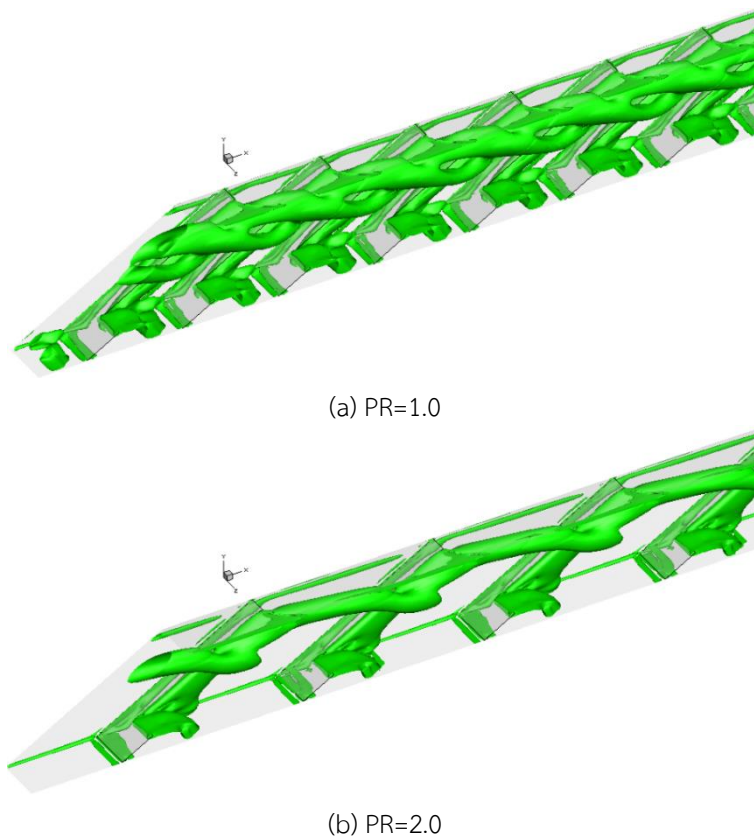


Figure 6.29 Q-isosurfaces of $Q=200$ for UB with various PRs at $BR=0.2$ and $Re=8,000$.

The temperature distribution contours of the inclined U-baffles at $BR=0.2$ and $PR=2.0$ on transverse planes at $x/P=0$ to $x/P=1$ are presented in Figure 6.30. The flow with lower temperature was induced toward the sidewalls and bottom wall which increased the heat transfer rate. However, in the zone behind the UB, there was no air mixing between lower and higher temperatures. Therefore, heat transfer rate in this zone was low. When the PR was reduced, the near wall boundary layer also reduced and the temperature gradient at the wall increased, leading to the enhancement of heat transfer rate.

The local Nusselt number for the UBs at $BR=0.2$ and $PR=2.0$ on the square channel's walls is presented in Figure 6.31. The higher local Nusselt numbers were at the wall area between the baffles. The corner, the middle top, and the wall area behind the baffles produced the low local Nusselt numbers. The smaller PR also gave the higher average local Nusselt numbers than the larger PR.

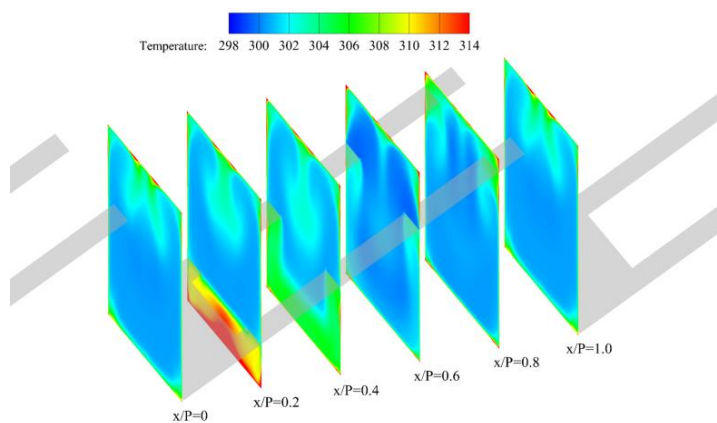


Figure 6.30 Temperature contours in transversal plane of UB at BR=0.2 and PR=2.0.

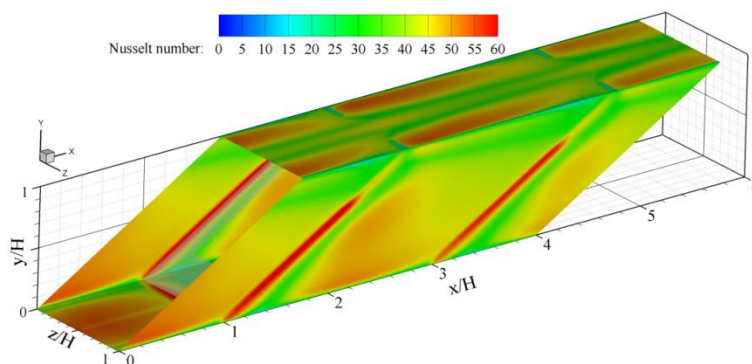


Figure 6.31 Local Nusselt number contours on the wall for UB at BR=0.2 and PR=2.0.

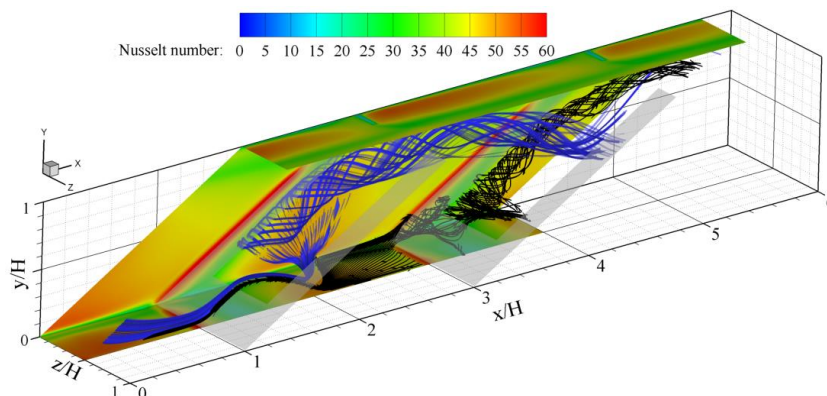


Figure 6.32 Streamlines and Nu_x contours on the wall for UB at BR=0.2 and PR=2.0.

Figure 6.32 presents the local Nusselt number and the streamlines of the UBs at BR=0.2 and PR=2.0. The UBs produced the longitudinal vortex pairs and also induced the impinging flow toward the heat surface. This phenomenon enhanced the heat transfer rate. The shorter pitch also gave more flow reattachment than the longer pitch.

6.3 Inclined Vortex Rings

6.3.1 Effects on heat transfer

The numerical results on heat and flow characteristics of inclined vortex rings (VR) having four ring-to-tube heights or blockage ratios (BR=0.05, 0.1, 0.15, and 0.2) are displayed in Figures 6.33 and 6.34, respectively. In Figure 6.33, it is found that the Nusselt number increased with increasing the BR, apart from the Re. The higher Nu was seen at the largest BR which gives rise to flow recirculation and separation and provides higher turbulence intensity than the smaller. At PR=0.5, the Nu values for BR=0.1, 0.15 and 0.2 were in the ranges of 260–297%, 330–387%, and 354–435% above that for the smooth tube, respectively. The VR at BR=0.2 gave higher heat transfer than that at BR=0.15 and 0.1 around 9-12% and 41-46%, respectively. At PR=2.0, the BR=0.1, 0.15, and 0.2 provided the Nu in a range of 191–222%, 214–253%, and 224–271% higher than the smooth tube, respectively. At PR=2.0, the VR with BR=0.2 performed better than the one with BR=0.15 and 0.1 at about 1-3% and 17-22%, respectively. Figure 6.34 shows the variation of Nu with PR values. In the figure, the Nu tended to reduce with the increment of PR. This is because the VR insert could generate two main longitudinal vortex flows that can help to increase the flow turbulence degree and to transport the core flow to the near-wall regions. Thus, the created vortex flows can induce impingement flow over the tube wall (called vortex-induced impingement).

In Figure 6.33, it is visible that the Nu increased with reducing the PR. This is because the VRs with smaller PR interrupted the development of the boundary layer of the fluid flow and also increased the turbulence intensity of the flow. The VRs at BR=0.2 and PR=0.5 showed higher heat transfer rate than the one at PR=1.0, 1.5, and 2.0 around 20%, 28%, and 38%, respectively.

The relative Nusselt numbers (Nu/Nu_0) plotted against Re and BR values are presented in Figures 6.35 and 6.36, respectively. In Figure 6.35, the Nu/Nu_0 tended to slightly decrease with the rise of Re for all cases. Note that the Nu/Nu_0 for BR=0.2 was higher than that for BR=0.15 and 0.1. This is due to higher flow blockage of using BR=0.2 interrupted the flow and to stronger swirl/vortex flow strength, leading to promoting the high levels of air mixing over the others. Depending on Re, the PR=0.5, 1.0, 1.5, and 2.0, provided the Nu/Nu_0 in a range of 3.61–4.35, 2.87–3.47, 2.56–3.09, and 2.24–2.71; 3.31–3.87, 2.78–3.25, 2.45–2.87, and 2.23–2.63; and 2.55–2.97, 2.21–2.57, 2.03–2.36, and 1.91–2.22 times for BR=0.2, 0.15, and 0.1, respectively. In Figure 6.36, it can be observed that the Nu/Nu_0 showed a steeper decrease at the beginning with the rise of PR but gave a slower increase for $PR \geq 0.1$. The VR at PR=0.5 provided the highest Nu/Nu_0 at a given BR value.

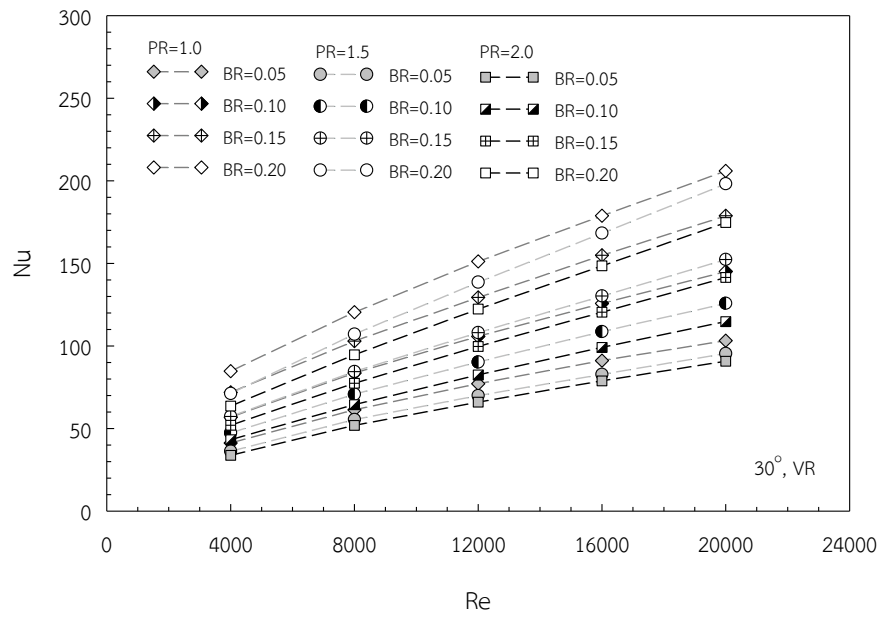


Figure 6.33 Variation of Nu with Re for VR.

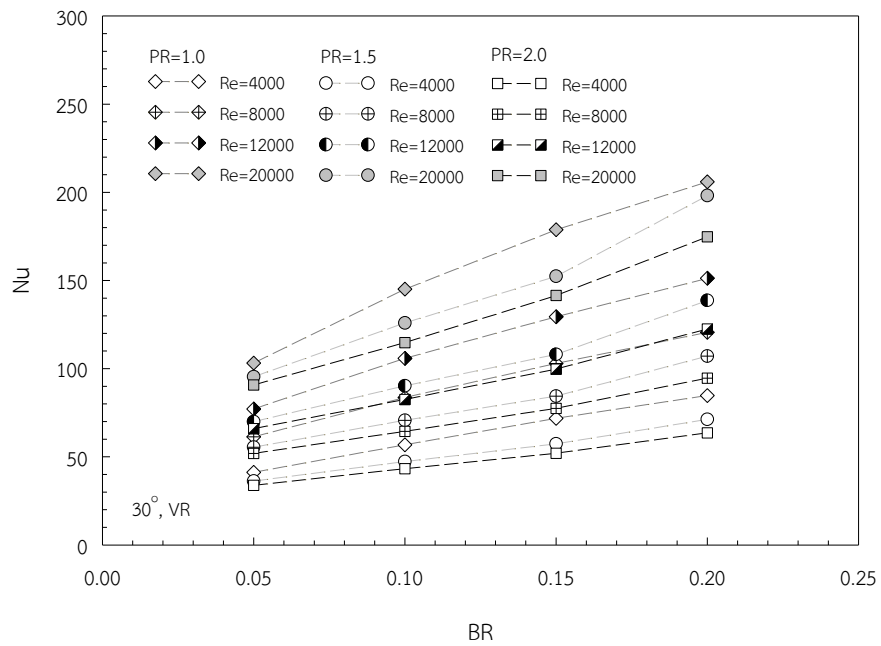


Figure 6.34 Variation of Nu with BR for VR.

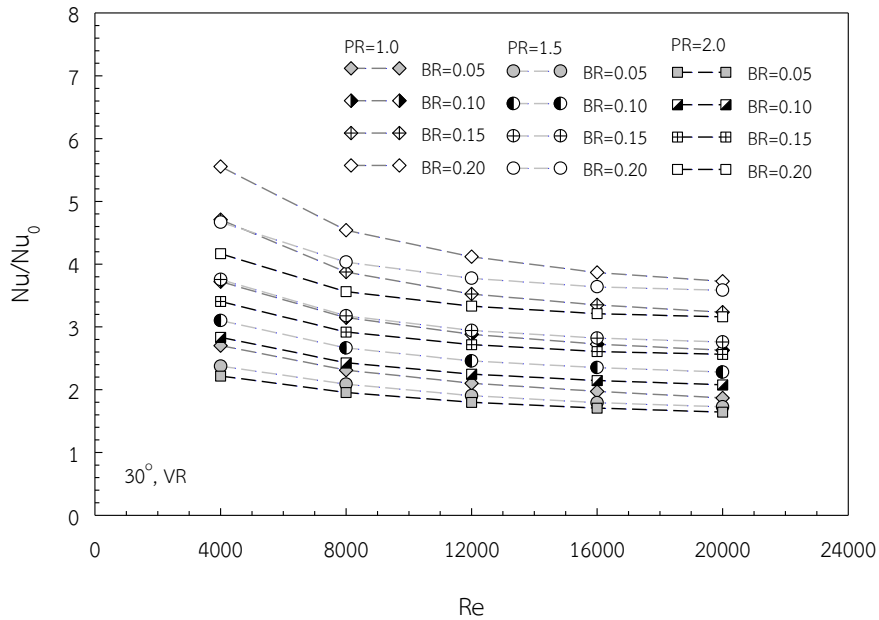


Figure 6.35 Variation of Nu/Nu_0 with Re for VR.

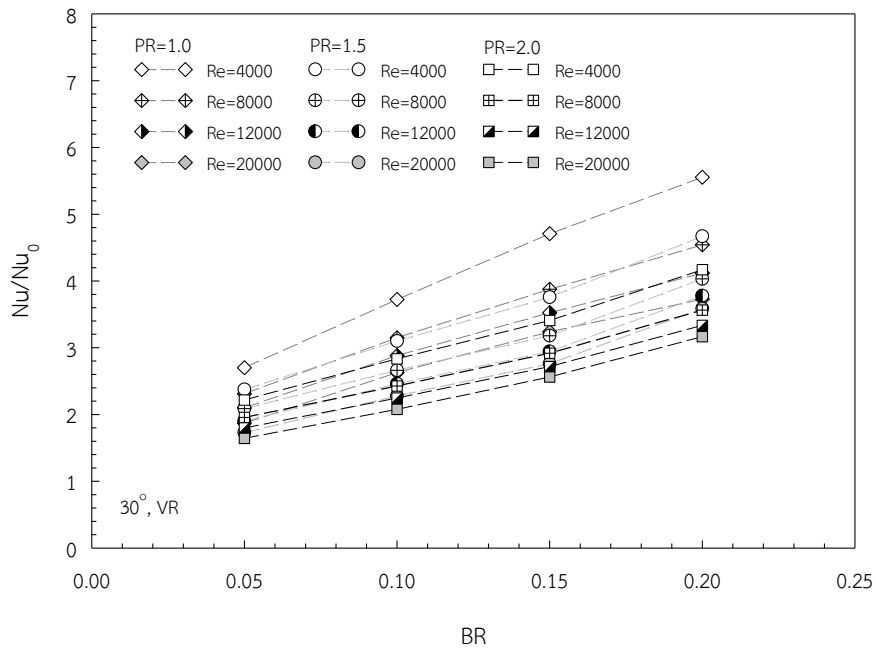


Figure 6.36 Variation of Nu/Nu_0 with BR for VR.

6.3.2 Effects on friction factor

The effect of the vortex rings (VR) on the isothermal pressure drop across the circular tube is reported. The variations of the pressure drop in the form of friction factor (f) with Re and BR are presented in Figures 6.37 and 6.38, respectively. In Figure 6.37, it is apparent that the VR yields a substantial increase in f over the smooth tube. As expected, the f for the VR with $BR=0.2$ was substantially higher than that with smaller BR . The average increase in f was in a range of 4.8 to 35 times over the smooth tube. The f of the VR at $PR=0.5$ and $BR=0.2$ was found to be around 13 and 25 times

above that at BR=0.15 and 0.1, respectively. This was due to higher flow blockage, larger surface area, and reversing flow. The pressure losses were mainly due to high viscous losses near the wall, the extra forces exerted by the reverse flow, and the high flow blockage. In Figure 6.38, the f for larger BR (=0.2) was much higher than that for smaller BR. The f tended to increase with the increment of BR and also decreased significantly from PR=0.5 to PR=2.0, especially for lower BR, as shown in Figure 6.38. At BR=0.2, the f for PR=0.5 was found to be around 46%, 61%, and 73% higher than that for PR=1.0, 1.5, and 2.0, respectively.

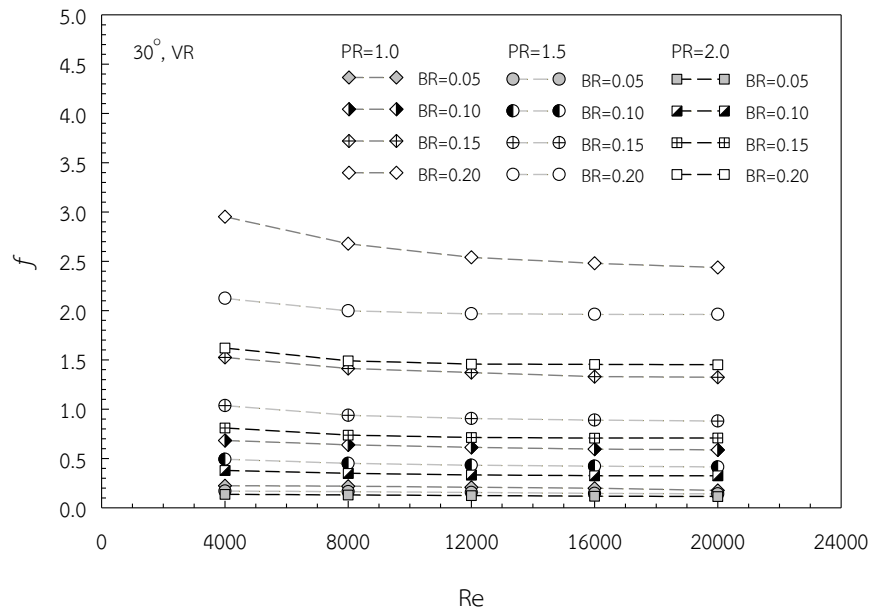


Figure 6.37 Variation of f with Re for VR.

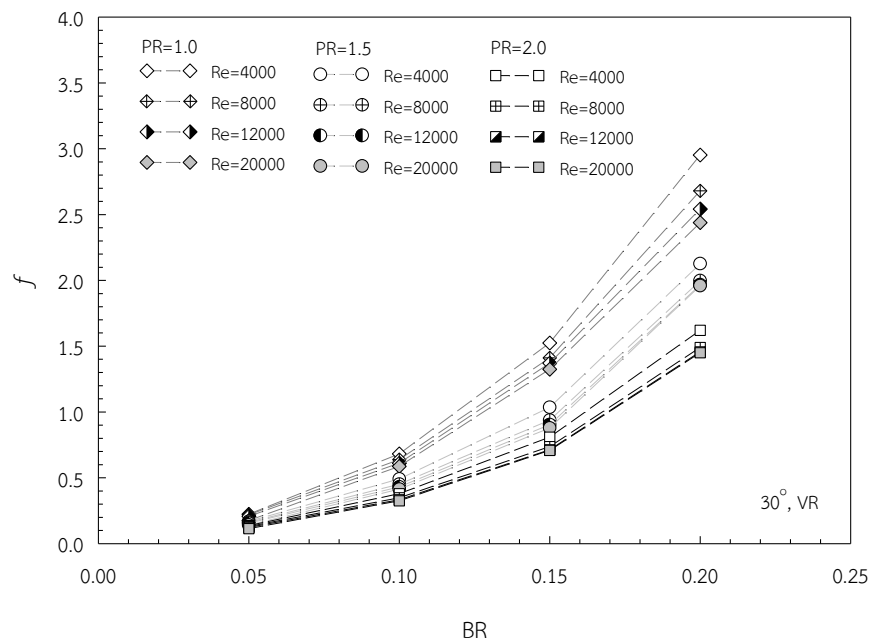


Figure 6.38 Variation of f with BR for VR.

The effects of the VR inserts on the isothermal friction factor ratio (f/f_0) plotted against Re and PR values are presented in Figures 6.39 and 6.40, respectively. In Figure 6.39, the VRs yielded a substantial increase in f/f_0 with the rise of Re. This is due to the flow blockage, the larger surface area, and the reverse flow. The f/f_0 at BR=0.2 was much higher than that at BR=0.15 and 0.1 at a similar operating condition. At PR=0.5, 1.0, 1.5, and 2.0, the increases in f/f_0 were about 35.1–36.5, 19–19.8, 13.8–14.4, and 9.5–10; 21.7–23.1, 13.9–14.8, 9.7–10.3, and 8.1–8.6; and 9.8–11, 6.8–7.7, 5.5–6.2, and 4.9–5.5 times for BR=0.2, 0.15, and 0.1, respectively. The variation of f/f_0 with PR values is presented in Figure 6.40. In the figure, the f/f_0 was independent from Re and tended to decrease with the rise of PR. This means that at a high BR, increasing the PR was less effective to reduce significantly the friction loss in the tube.

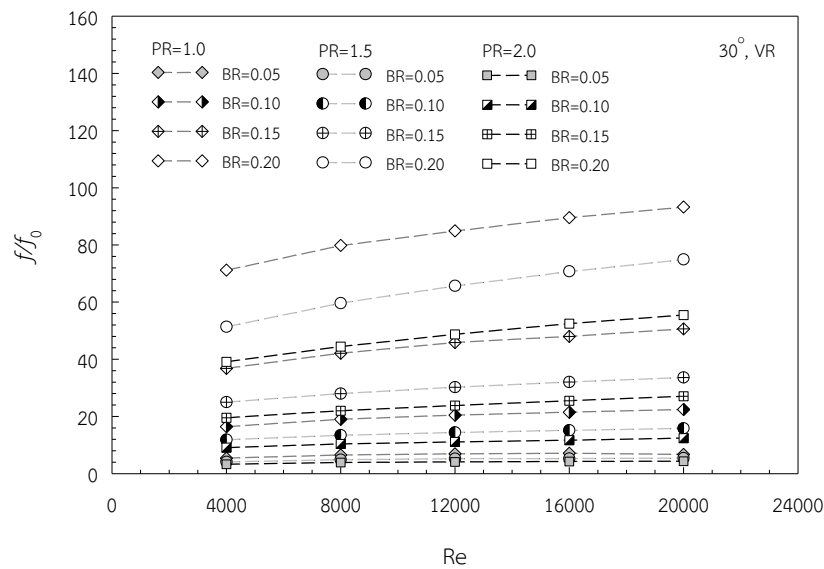


Figure 6.39 Variation of f/f_0 with Re for VR.

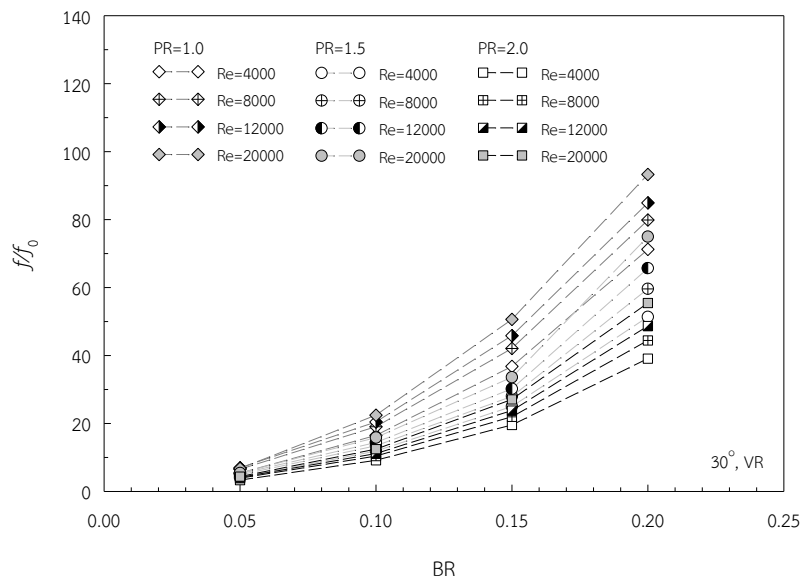


Figure 6.40 Variation of f/f_0 with BR for VR.

6.3.3 Effects on thermal enhancement factor

Figure 6.41 shows the variation of the thermal enhancement factor (η) with a given range of Re. The Nu/Nu_0 and f/f_0 were compared at an identical pumping power condition. The η showed the downtrend with the increase in Re for all cases. It is seen that the VR at BR=0.1 and PR=0.5 gives the highest η at the lowest Re. At BR=0.1, the maximum η were, respectively, about 1.4, 1.35, 1.34, and 1.31 for PR=0.5, 1.0, 1.5, and 2.0. At a given BR, the PR=0.5 yielded the η around 3%, 4%, and 6% higher than the PR=1, 1.5, and 2, respectively.

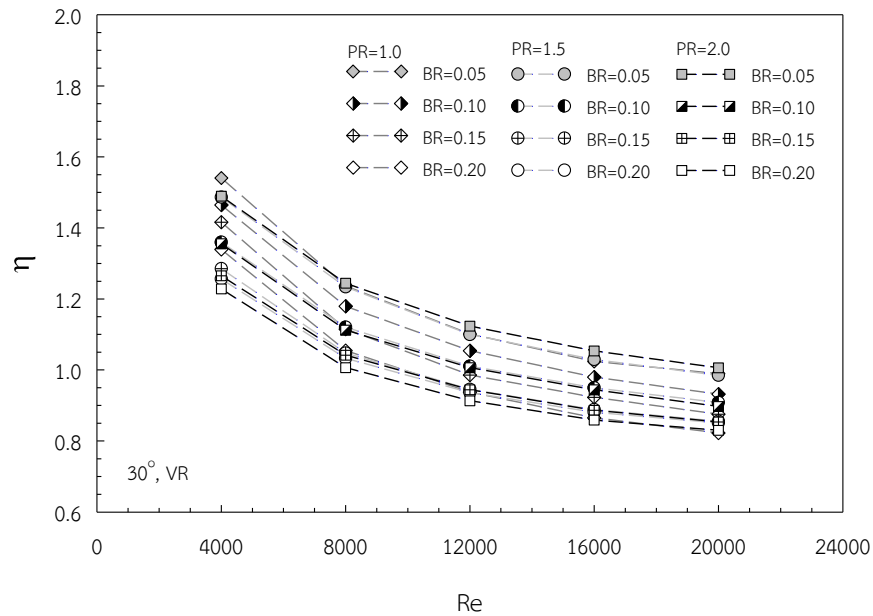


Figure 6.41 Variation of η with Re for VR.

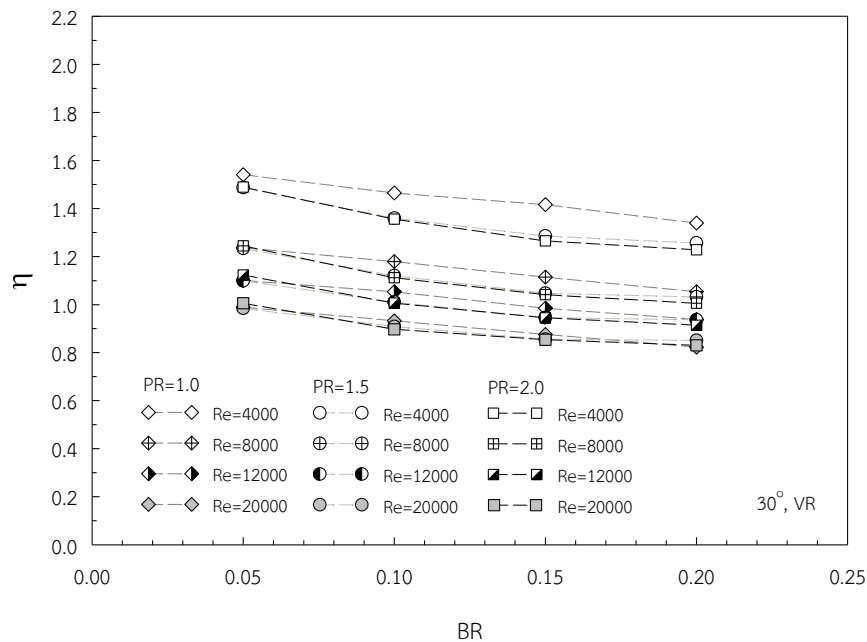


Figure 6.42 Variation of η with BR for VR.

6.3.4 Flow and heat topologies for vortex rings

The flow and vortex coherent structure of the VR in a circular tube can be described by plotting the streamlines in the transverse planes as shown in Figure 6.43. The distance for each transverse plane in a flow module (from a VR to another) was set to $0.2PR$ in the range of $x/P=0$ to $x/P=1$ for VR at $\alpha=30^\circ$, $PR=2.0$, and $BR=0.1$. From the figure, a longitudinal vortex pair appeared along the tube and the vortex pairs were induced toward the bottom wall. The size of the longitudinal vortex pair also reduced with reducing the PR .

The pressure distribution contours displayed in transverse planes at $x/P=0$ to $x/P=1$ are presented in Figure 6.44 (a) and (b). The high pressure regions were in front of the VRs on both top and bottom walls. The highest pressure appeared in front of the VR on the top wall area. The lowest pressure occurred behind the vortex rings at the bottom wall area. This phenomenon led to the induction of the vortex flows. The pressure drop increased with increasing the BR due to higher flow blockage. The pressure drop also reduced with increasing the PR .

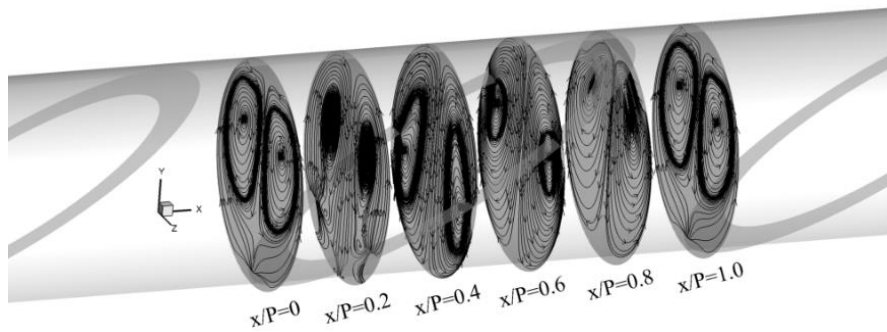
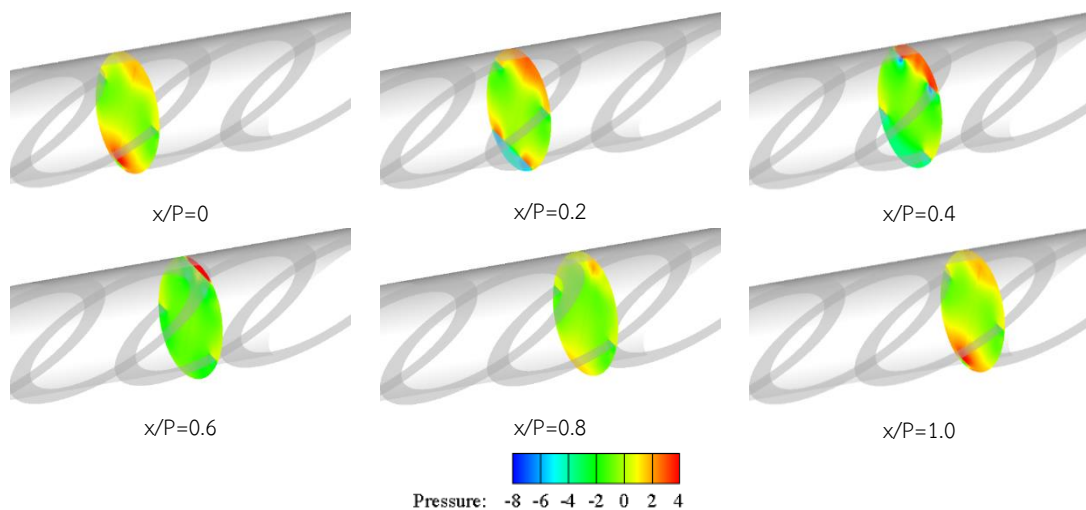


Figure 6.43 Streamlines in transverse planes for VR at $PR=2.0$, $BR=0.1$, and $Re=8,000$.



(a) $PR=1.0$ and $BR=0.1$

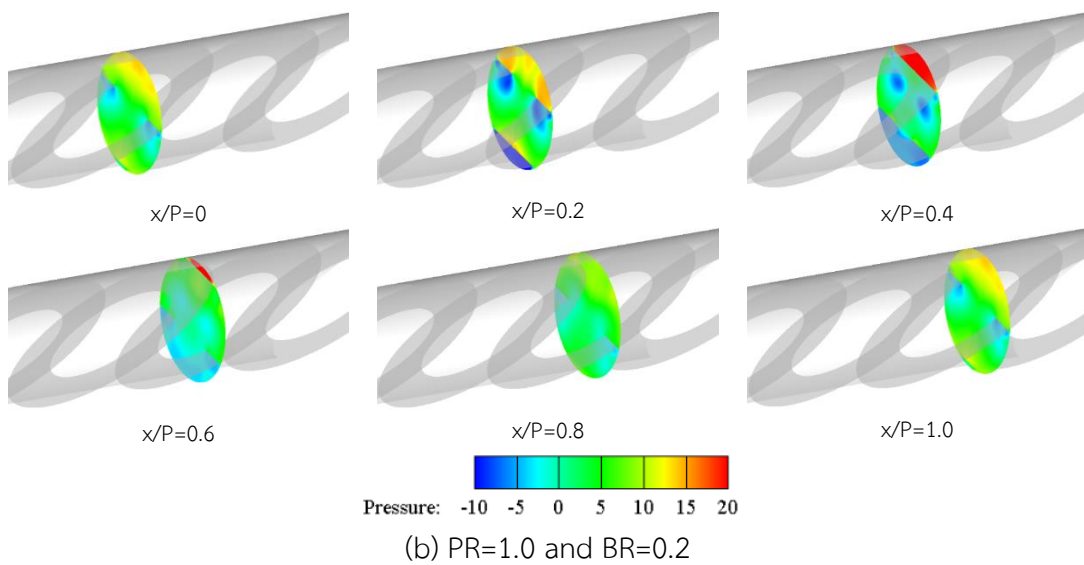


Figure 6.44 Pressure contours in transverse planes for VR with various BR at Re=8000.

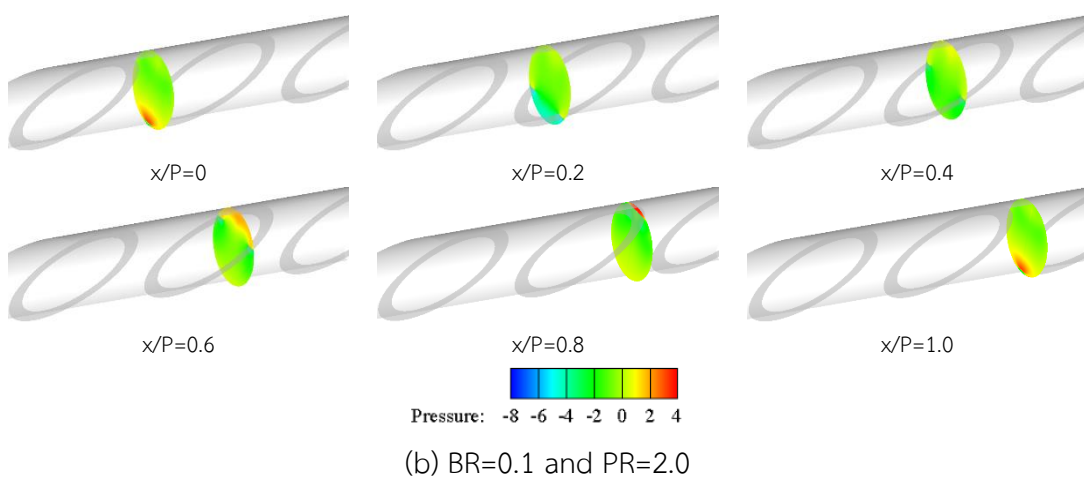
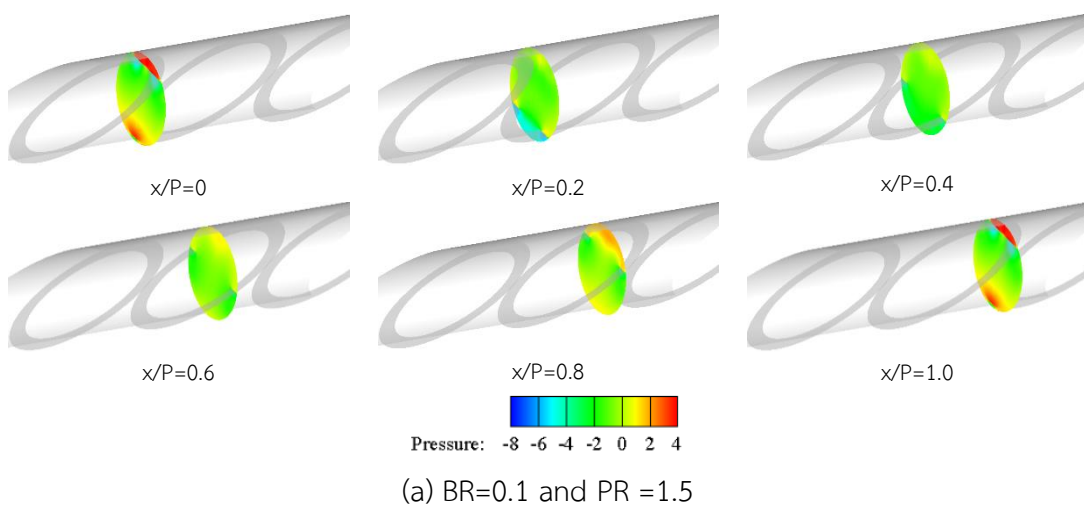


Figure 6.45 Pressure contours in transverse planes for VR with various PR at Re=8000.

The Q-isosurface (half left) of the VR turbulators at $Re=8000$ and $PR=1.0$ are presented in Figure 6.46. The vortex core flows appeared along the tube and behind the VRs. The higher BR produced larger and stronger vortex core flows than the lower one.

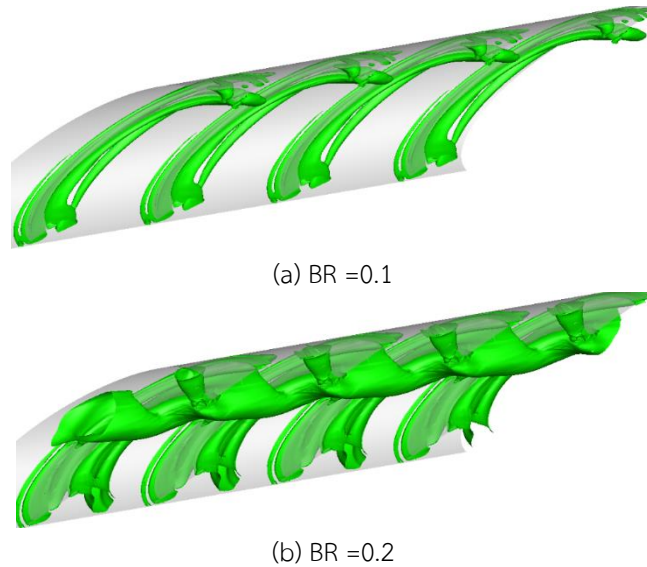
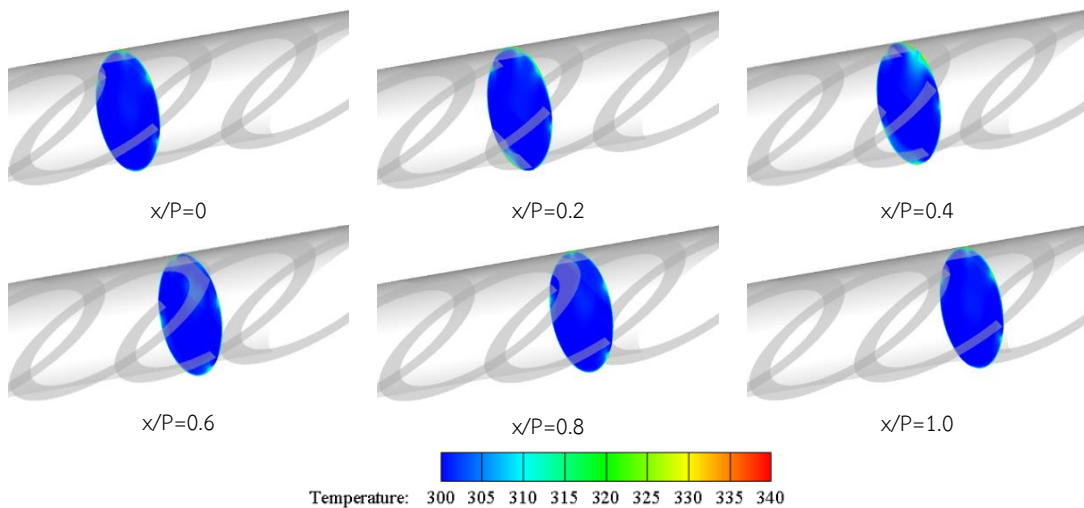
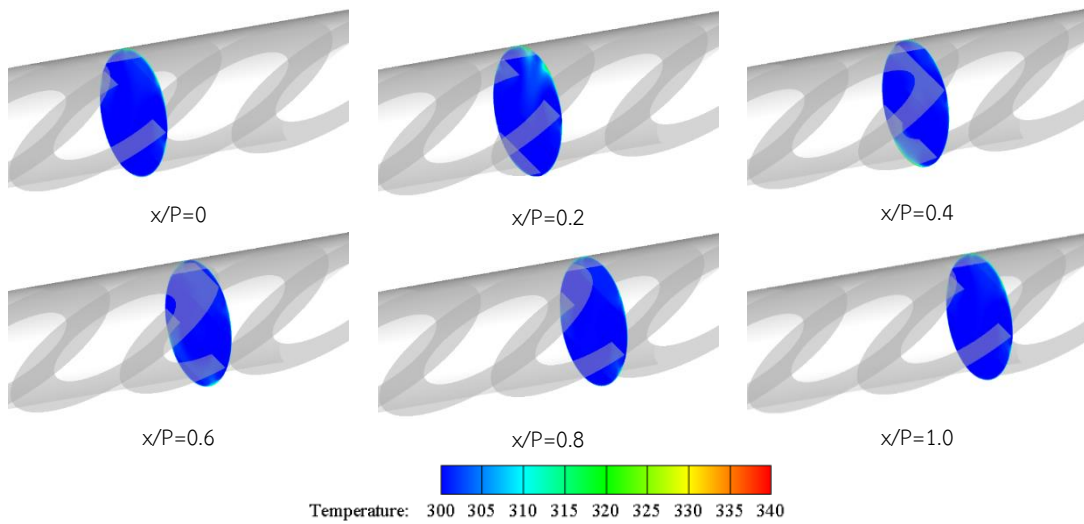


Figure 6.46 Q-isosurfaces of $Q=200$ for VR with various BR at $PR=1.0$ and $Re=8000$.

The temperature distribution contours of the VR with various BR in transverse planes at $x/P=0$ to $x/P=1$ are presented in Figure 6.47 (a) and (b). The lower air temperature was induced from the top wall toward the other walls which can enhance the heat transfer rate. When the BR was increased, the near wall boundary layer was reduced but the temperature gradient at the wall was increased leading to enhancement of the heat transfer rate. When the pitch was longer (larger PR), the heat transfer rate also reduced as shown in Figure 6.48 (a) and (b).

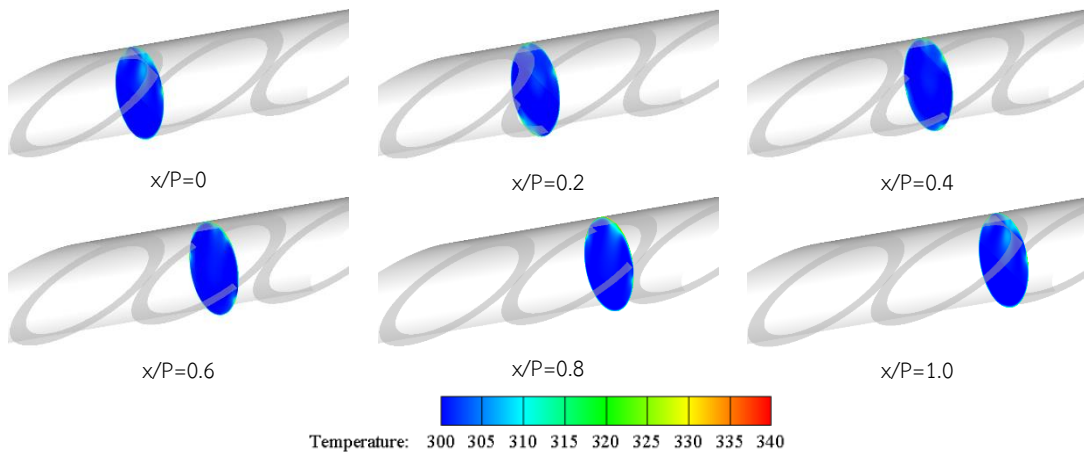


(a) $PR=1.0$ and $BR=0.10$

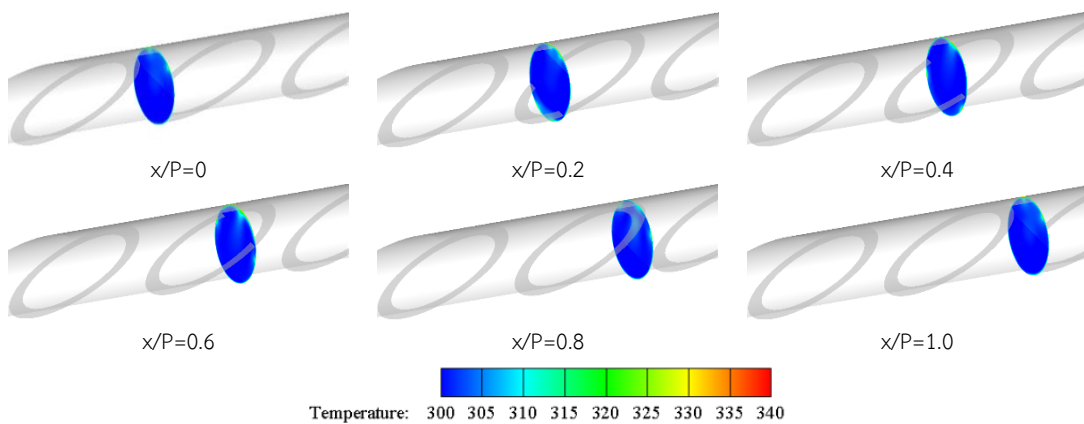


(b) PR=1.0 and BR=0.20

Figure 6.47 Temperature contour in transverse planes of VR for varied BR at $Re=8,000$.



(a) BR=0.10 and PR=1.5



(b) BR=0.10 and PR=2.0

Figure 6.48 Temperature contours in transverse planes for VR at $Re=8000$.

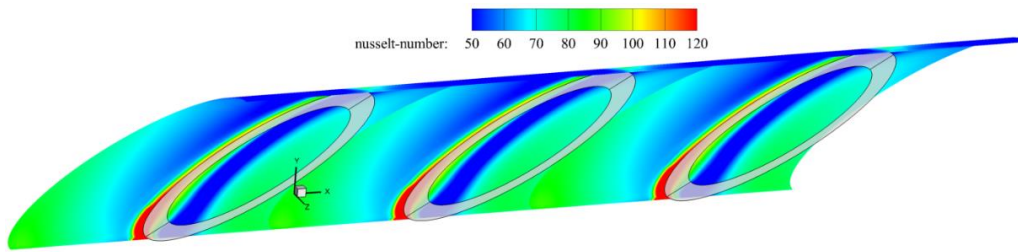


Figure 6.49 Local Nu_x contours on the wall for VR at $BR=0.1$, $PR=2.0$, and $Re=8000$.

The plot of local Nusselt number contours of a circular tube fitted with VRs is presented in Figure 6.49. The high local Nusselt number areas were at the wall between the VRs. However, at the vicinity of the VR and the middle on the top wall, the local Nusselt numbers were low, except for some wall area below the VR. The shorter pitch gave higher local Nusselt number than the longer pitch.

6.4 Conclusions

Numerical studies have been conducted to investigate the air flow characteristics, pressure losses, and heat transfer rates in a rectangular channel, a square channel, and a circular tube, respectively. The turbulators inserted into those passages were multiple V-baffles (VB), inclined U-baffles (UB), and vortex ring baffles (VR). The studied parameters were pitch ratios (PR) and blockage ratios (BR) for a given range of Reynolds number from 4000 to 20,000. A uniform surface heat-flux condition was applied as a thermal condition. From the numerical results of the present study, the following conclusions can be drawn.

For the case of VBs, the inline array at $PR=0.5$ provided highest pressure drop ($f/f_0=12.51-139.65$) but also yielded a considerable heat transfer augmentation ($Nu/Nu_0=3.98-7.63$) depending on Re . The Nu/Nu_0 augmentation tended to slightly decrease with the rise in Re . However, the VB with a single wall arrangement at smaller PR should be applied to obtain higher thermal enhancement factor. The best operating condition for using the VB was obtained at smallest PR at the lowest Re . The single VB arrangement at $PR=0.5$ yielded the highest η of 1.83 at $Re=4000$.

For the case of UBs, the counter-rotating vortex flows created by the UB could help to induce impingement flows on the walls which led to drastic increase in heat transfer rate in the square channel. The enhancement for Nu was about 2-4 times above the smooth channel at $PR=0.5-2.0$ and $BR=0.05-0.25$. However, the increase in f was in a range of about 4-40 times above the smooth channel, depending on BR and Re . The η for the UB was higher than unity (indicating higher performance over the smooth channel) and its maximum value was about 1.6 at $PR=1.0$, $BR=0.2$, and $Re=4000$.

For the case of VRs, the VR could create two main counter-rotating vortex flows along the tube that helped induce impingement flows over the lower tube wall leading to greater increase in heat transfer. The VRs at PR=1.0 and BR=0.2 caused a high pressure drop ($f/f_0=71.25-93.29$) but also provided a considerable heat transfer augmentation in the tube ($Nu/Nu_0=3.73-5.56$). The Nu of the VR showed the increasing trend with the rise in BR and Re values but with the reduction of PR. The η of the VR was above unity and tended to decrease with the increment in Re, BR, and PR values. The VR at PR=1.0 and BR=0.05 yielded the highest η of 1.54 at the lowest Re.

CHAPTER 7

HORSESHOE BAFFLES

This chapter presents numerical results on heat transfer enhancement and pressure loss using inclined horseshoe baffles (HB) and V-shaped Horseshoe baffles (VHB) inserted into a circular tube. The numerical investigations were carried out by varying the air flowrate for Re ranging from 3000 to 20,000. A uniform surface heat flux was applied as the thermal boundary condition. The HBs were mounted periodically in the tube with different attack angles ($\alpha=20^\circ$, 30° , and 45°), various PRs (PR=0.25–2.00), and blockage ratios (BR=0.075–0.2). Similarly, the VHBs were also mounted repeatedly in the tube with the same geometry parameters as the HBs.

The numerical results of heat transfer coefficient, pressure drop, and thermal performance were calculated and presented in terms of relative Nusselt number (Nu/Nu_0), relative friction factor (f/f_0), and thermal enhancement factor (η), respectively. The optimal baffle geometry characteristics that provide the maximum η were further investigated to study the flow structure and heat transfer mechanisms. Moreover, the optimization analysis for the HBs and VHBs cases was also performed to obtain the optimal thermal performance of each case. Finally, the empirical correlations for Nusselt number (Nu) and friction factor (f) for both the HB and VHB were also determined.

7.1 Inclined horseshoe baffles

7.1.1 Effects on heat transfer

The effects of three PRs (PR=0.5, 1, and 2) and BRs (BR=0.1, 0.15, and 0.2) on the heat transfer coefficients were examined and presented in the form of Nu/Nu_0 . The variations of Nu/Nu_0 with Re are presented in Figures 7.1, 7.2, and 7.3 for the HBs at $\alpha=20^\circ$, 30° , and 45° , respectively. In the figures, the Nu/Nu_0 values tend to decrease slightly with the increase of Re for all cases. The Nu/Nu_0 for the HBs is obviously greater than that for the smooth tube because the baffles give a stronger air mixing and turbulence intensity leading to the destruction of thermal boundary layer. The vortex flows also contributes to better air mixing between fluids at the core and the wall regions. The flow behaviors promote an increase in the tangential and radial turbulent fluctuation or the turbulence intensity, thinning the boundary layer, and enhanced the heat transfer rate inside the tube.

The heat transfer coefficients show the upward trend with reducing PR or increasing BR. This is due to the higher turbulence intensity that imparts to the flow between the baffles and gives a result in higher temperature gradients near the tube's

wall. The variation of Nu/Nu_0 with different attack angles (α) is depicted in Figure 7.4 for HBs at $PR=1.0$ and $BR=0.1$. The Nu/Nu_0 tends to increase slightly with the increment of α for all Re values. This is because the larger α can generate stronger vortex flow and give higher turbulence intensity and better fluid mixing leading to higher heat transfer rate than the smaller one.

For the 20° HB at $PR=0.5, 1, \text{ and } 2$, the Nu/Nu_0 values for $BR=0.1, 0.15, \text{ and } 0.2$ were in a range of 2.59-3.87, 2.78-4.36, and 2.77-4.37; 1.88-2.85, 2.04-3.15, and 2.16-3.39; and 1.63-2.28, 1.80-2.52, and 1.85-2.67 times, respectively, depending on Re .

For the 30° HB at $PR=0.5, 1, \text{ and } 2$, the Nu/Nu_0 values for $BR=0.1, 0.15, \text{ and } 0.2$ were in a range of 2.65-4.06, 2.83-4.60, and 2.91-4.77; 1.96-2.91, 2.10-3.24, and 2.31-3.53; and 1.74-2.42, 1.89-2.71, and 2.06-2.95 times, respectively.

For the 45° HB at $PR=0.5, 1, \text{ and } 2$, the Nu/Nu_0 values for $BR=0.1, 0.15, \text{ and } 0.2$ were in a range of 2.72-4.20, 2.86-4.64, and 3.16-5.12; 2.16-3.11, 2.45-3.56, and 2.73-3.95; and 1.88-2.51, 2.12-2.92, and 2.36-3.23 times, respectively. The maximum Nu/Nu_0 was found to be about 5.12 at $\alpha=45^\circ, PR=0.5, BR=0.2, \text{ and } Re=3000$.

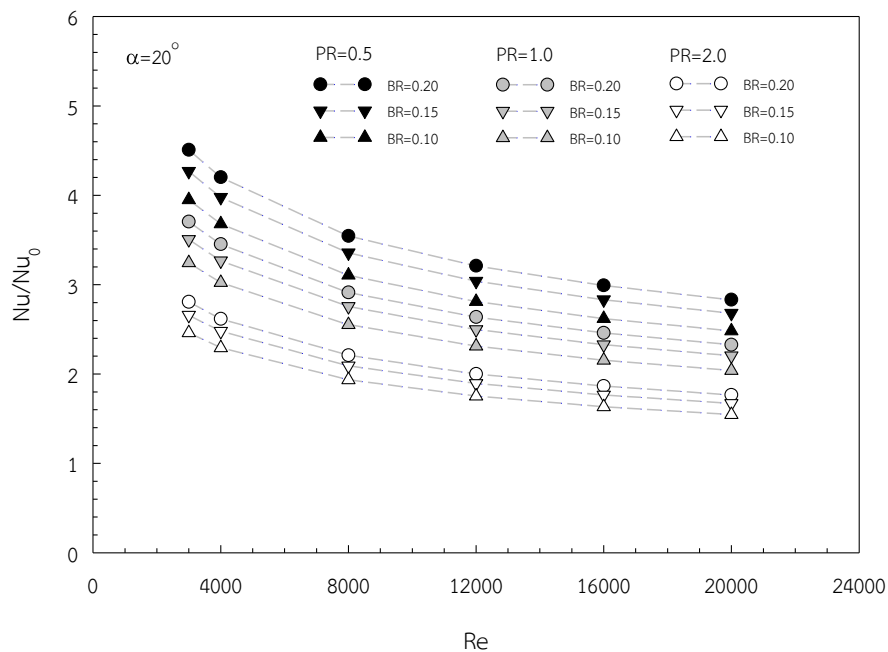


Figure 7.1 Variation of Nu/Nu_0 with Re for 20° HB.

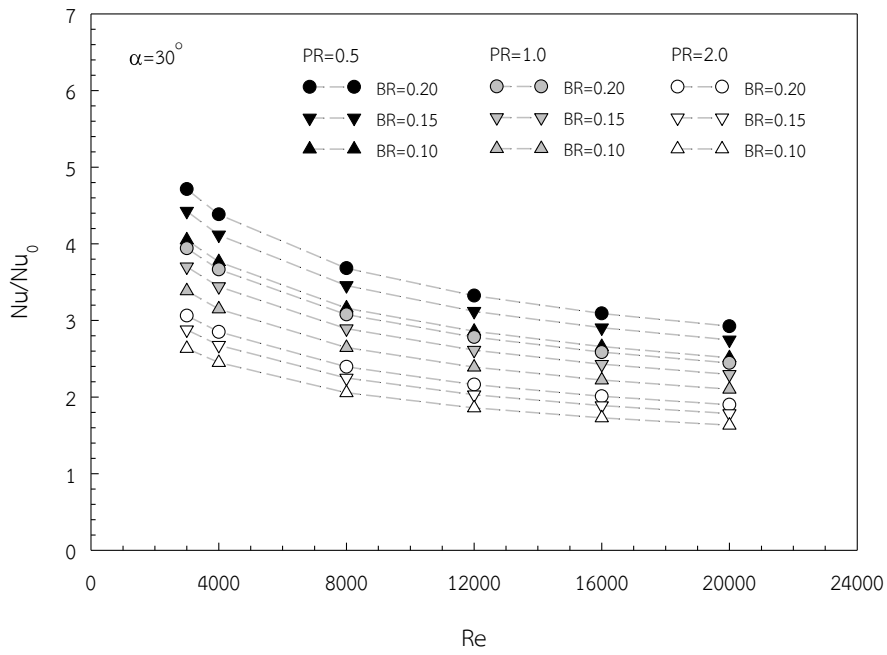


Figure 7.2 Variation of Nu/Nu_0 with Re for 30° HB.

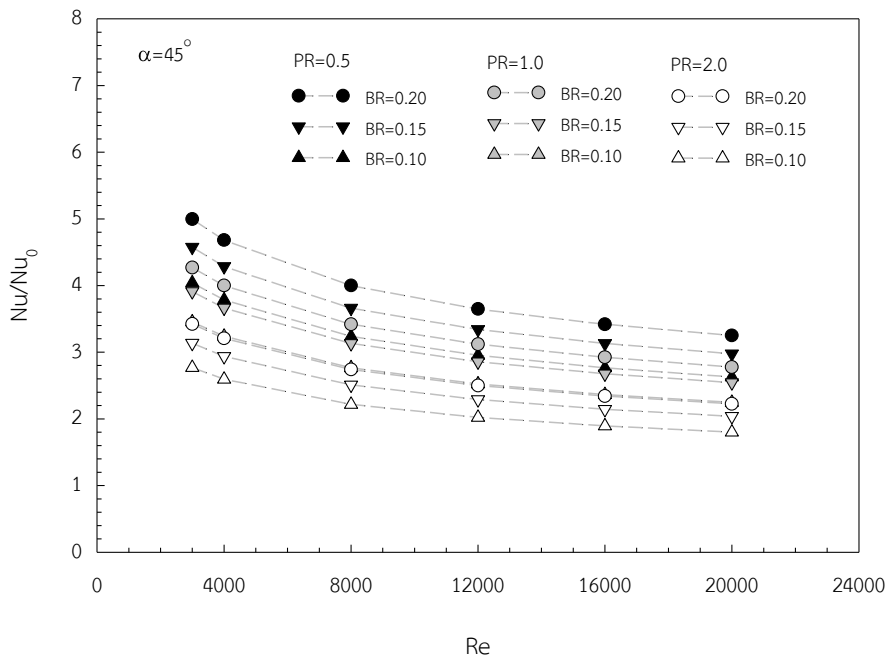


Figure 7.3 Variation of Nu/Nu_0 with Re for 45° HB.

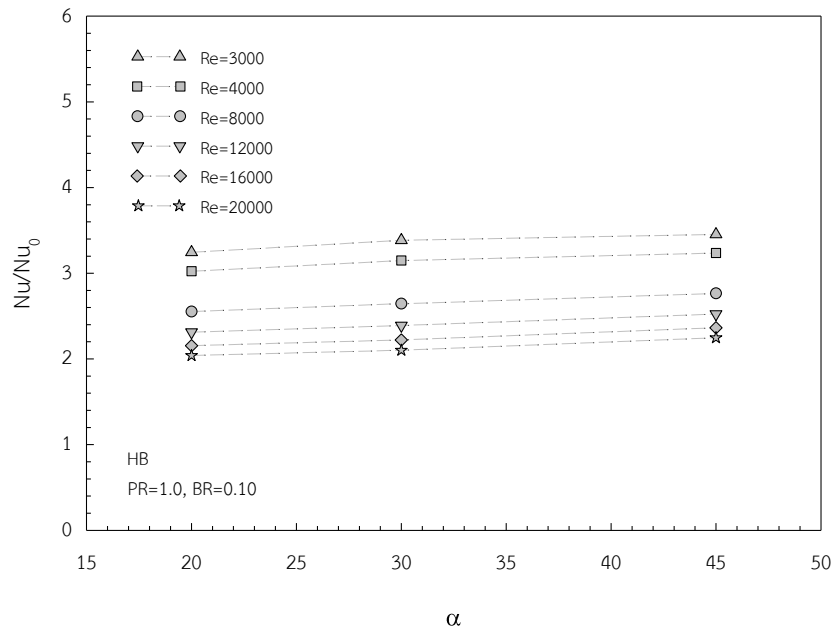


Figure 7.4 Variation of Nu/Nu_0 with α for HB.

7.1.2 Effects on friction factor

Figures 7.5, 7.6, and 7.7 present the variations of f/f_0 with Re for HBs with $\alpha=20^\circ$, 30° and 45° , respectively. In the figures, the f/f_0 values tend to increase slightly with the increment of Re for all cases. The HBs provided a substantial increase in f/f_0 . This could be attributed to the dissipation of dynamic pressure of the fluid due to higher surface area and also the swirl flows. The f/f_0 values obtained from three PRs were in a similar trend pattern. The f/f_0 increased with decreasing PR. The variation of f/f_0 with different α values is displayed in Figure 7.8 for PR=1.0 and BR=0.1. In the figure, the f/f_0 tended to increase sharply with the increment of α .

Depending on Re, for 20° HB at PR=0.5, 1, and 2, the f/f_0 values for BR=0.1, 0.15, and 0.2 were in a range of 5.17-5.74, 7.41-7.40, and 9.93-9.98; 4.14-4.09, 5.48-5.22, and 6.98-6.65; and 2.96-2.99, 3.89-3.72, and 5.07-4.80, respectively.

For 30° HB at PR=0.5, 1, and 2, the f/f_0 values for BR=0.1, 0.15, and 0.2 were in a range of 7.29-7.70, 10.71-11.02, and 14.72-15.40; 5.47-5.85, 7.95-8.02, and 11.08-11.39; and 3.65-4.05, 5.38-5.65, and 7.75-8.46 times, respectively.

For 45° HB at PR=0.5, 1, and 2, the f/f_0 values for BR=0.1, 0.15, and 0.2 were in a range of 12.32-13.32, 19.08-21.21, and 30.05-35.90; 7.89-10.08, 13.36-16.62, and 21.13-27.23; and 4.83-6.44, 8.21-10.61, and 13.30-17.40 times, respectively.

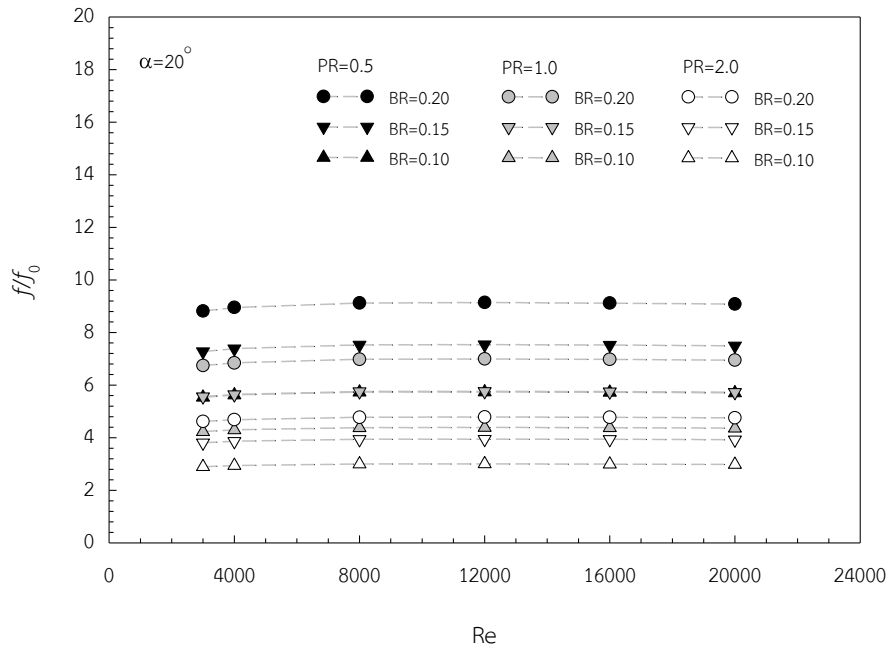


Figure 7.5 Variation of f/f_0 with Re for 20° HB.

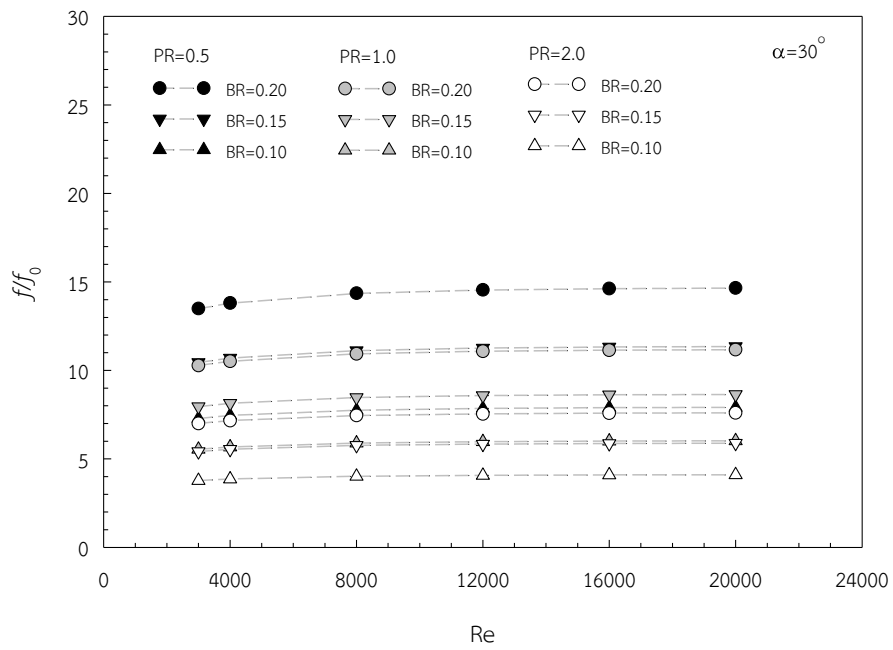


Figure 7.6 Variation of f/f_0 with Re for 30° HB.

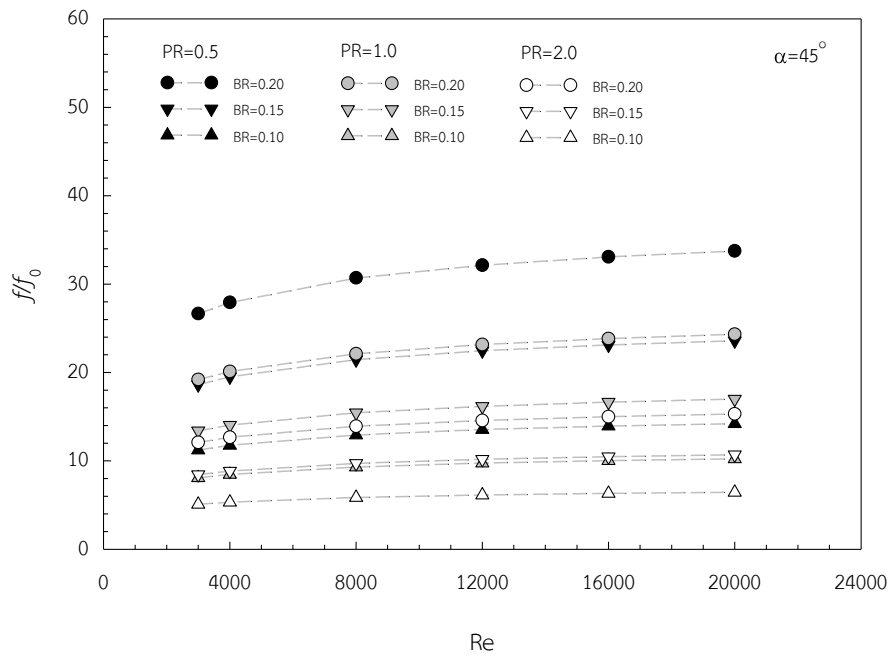


Figure 7.7 Variation of f/f_0 with Re for 45° HB.

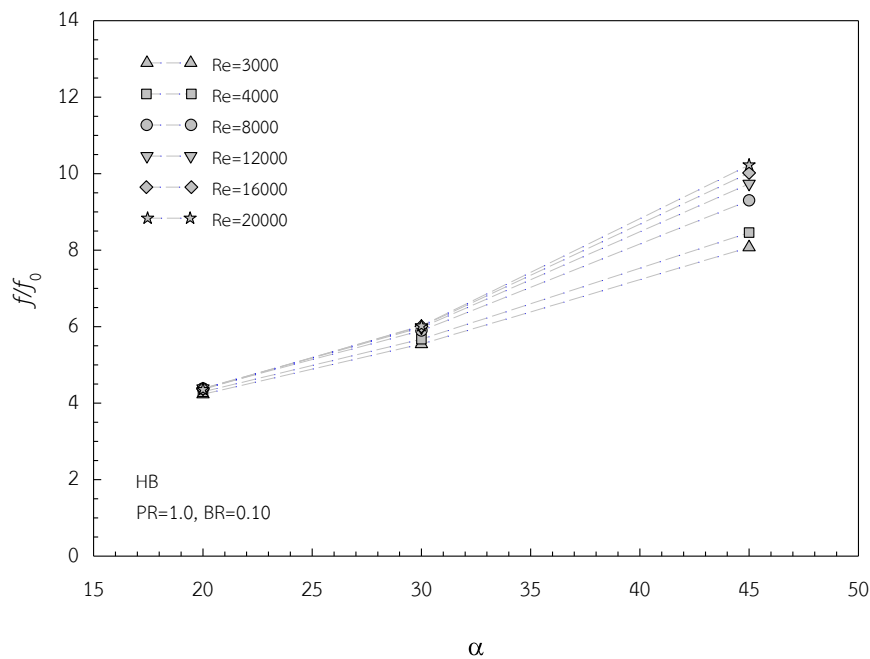


Figure 7.8 Variation of f/f_0 with α for HB.

7.1.3 Effects on thermal enhancement factor

In thermal performance evaluation, the thermal enhancement factor (η) under a constant pumping power was taken into account by using Eq. (3.31). The variations of η with Re are depicted in Figures 7.9, 7.10 and 7.11 for HB with $\alpha=20^\circ$, 30° and 45° , respectively. Most of η values were above unity except for the HB with $\alpha=45^\circ$, PR=2.0 at which the η values were below unity at higher Re . The η showed the downward trend with increasing Re . The variation of η with different attack angles is portrayed in

Figure 7.12 for HB at PR=1.0 and BR=0.1. The η tended to increase with reducing α for all cases.

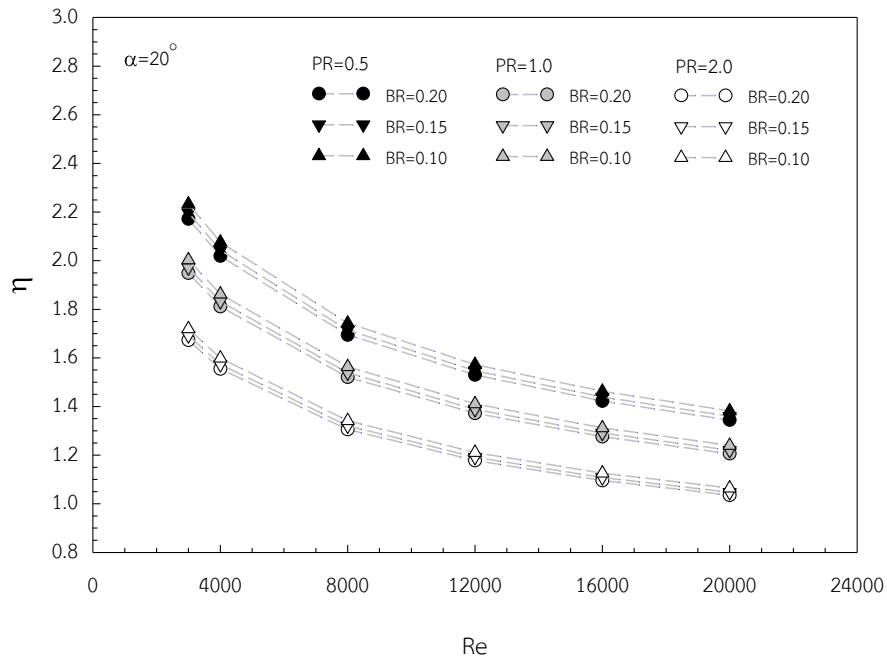


Figure 7.9 Variation of η with Re for 20° HB.

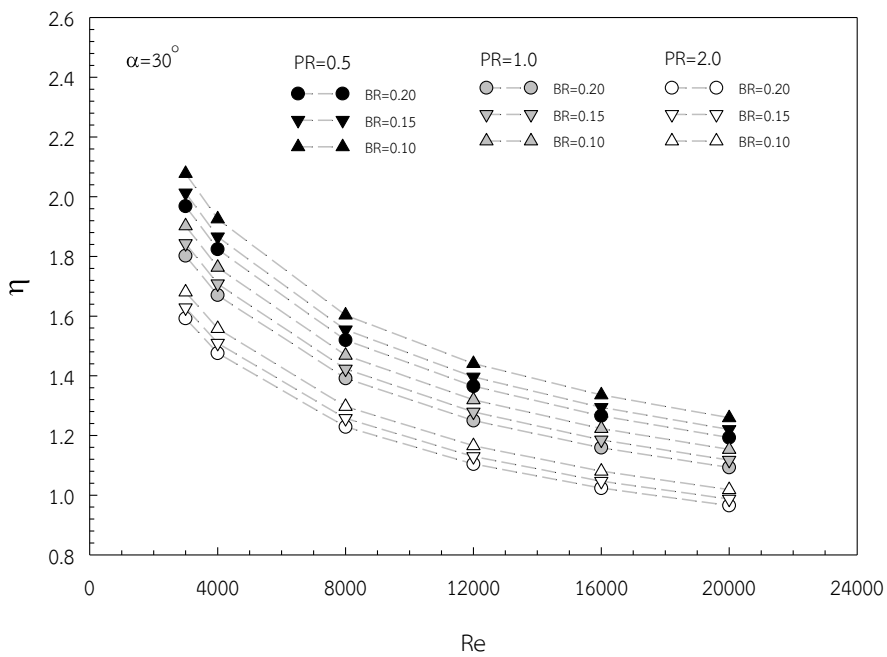


Figure 7.10 Variation of η with Re for 30° HB.

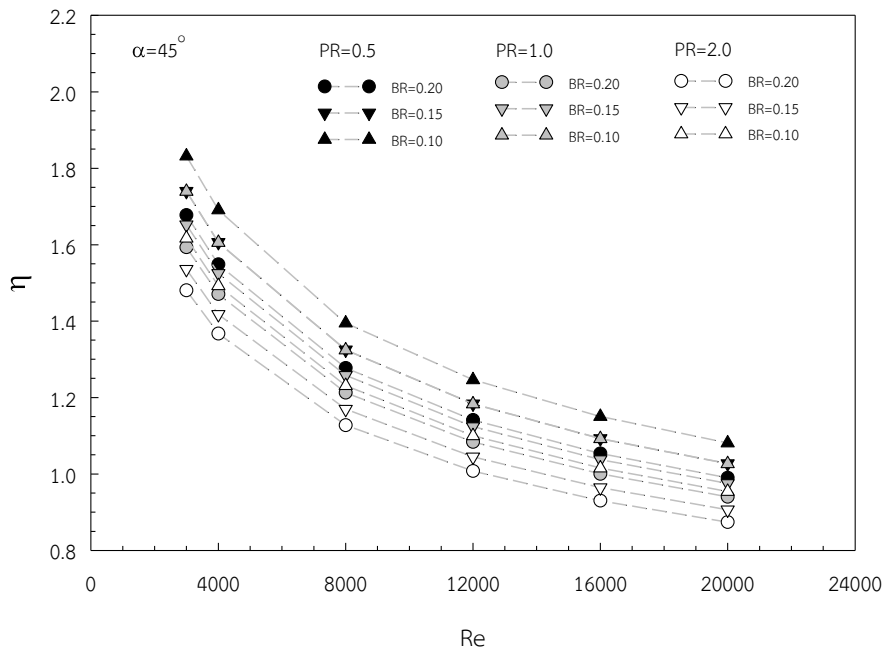


Figure 7.11 Variation of η with Re for 45° HB.

Depending on Re , for 20° HB, the maximum η was in a range of 1.45–2.25 at $BR=0.1$ and $PR=0.5$ while the minimum was in a range of 0.9–1.55 at $BR=0.2$ and $PR=2.0$. The η values for $BR=0.1$, 0.15, and 0.2 were approximately 1.45–2.23, 1.43–2.21, and 1.29–2.03, respectively. At a given BR , the HB at $PR=0.5$ yielded the maximum η while the lowest η was found at $PR=2.0$. The highest η was found to be 2.25 for $BR=0.1$ and $PR=0.5$ at the lowest Re .

For 30° HB, the maximum η was in a range of 1.34–2.13 at $BR=0.1$ and $PR=0.5$ whereas the minimum was in a range of 0.95–1.42 at $BR=0.2$ and $PR=2.0$. The η values for $BR=0.1$, 0.15, and 0.2 were about 1.32–2.11, 1.27–2.06, and 1.17–1.95, respectively. The $PR=0.5$ yielded the optimum η while the $PR=2.0$ gave the lowest η . The highest η was found to be 2.13 for $BR=0.1$ and $PR=0.5$.

For 45° HB, the maximum η was in a range of 1.15–1.82 at $BR=0.1$ and $PR=0.5$ while the minimum was in a range of 0.88–1.30 at $BR=0.2$ and $PR=2.0$. The η values for $BR=0.1$, 0.15, and 0.2 were around 1.08–1.76, 1.03–1.74, and 0.96–1.65, respectively. At a given BR , the highest η was found at $BR=0.1$ and $PR=0.5$ while the lowest η was found at $PR=2.0$. The highest η was found to be 1.82 at $BR=0.1$ and $PR=0.5$.

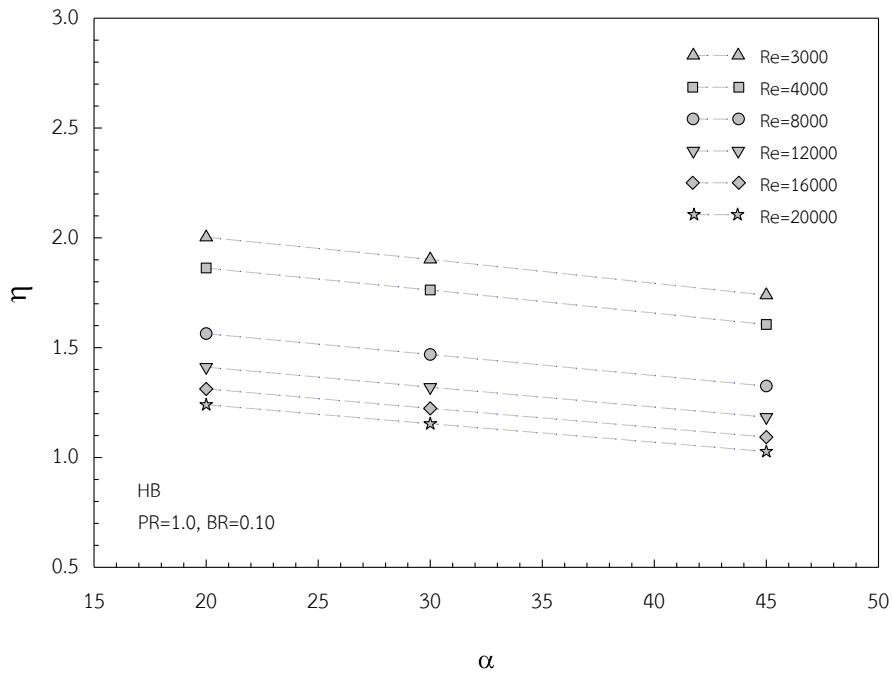


Figure 7.12 Variation of η with α for HB.

7.1.4 Optimization for inclined horseshoe baffles

In the present optimization, only the 30° HB was chosen to find the optimum configuration parameters of the BR and PR at Re=3000. The reason is that the 30° HB case provided higher Nu/Nu_0 while its η was slightly lower than the 20° HB case. In this study, the PR was varied from 0.25 to 1.25 but the BR from 0.075 to 0.175. The variations of Nu/Nu_0 , f/f_0 , and η are depicted in Figures 7.13 to 7.15. Depending on Re, the Nu/Nu_0 was ranging from 2.47-5.56 while the f/f_0 was ranging from 2.95-13.95. The η increased with decreasing PR from PR=1.25 to PR=0.30 but decreased with PR=0.25 as shown in Figure 7.15. The maximum η factor was found to be 2.48 at PR = 0.3 and BR = 0.1375 and these PR and BR values are regarded as the optimal parameters to obtain the highest η for using the 30° HB.

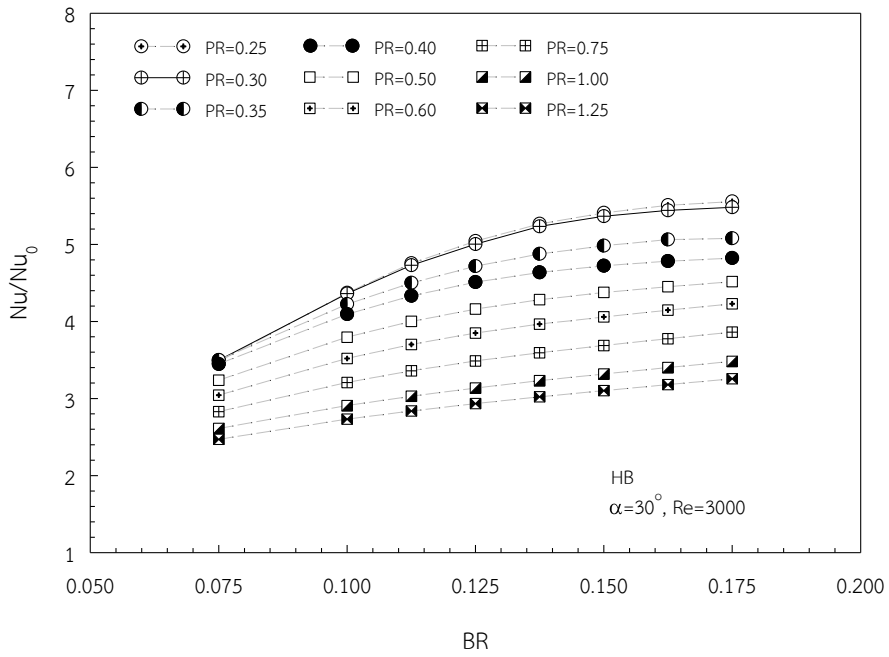


Figure 7.13 Variation of Nu/Nu_0 with BR for various PR values.

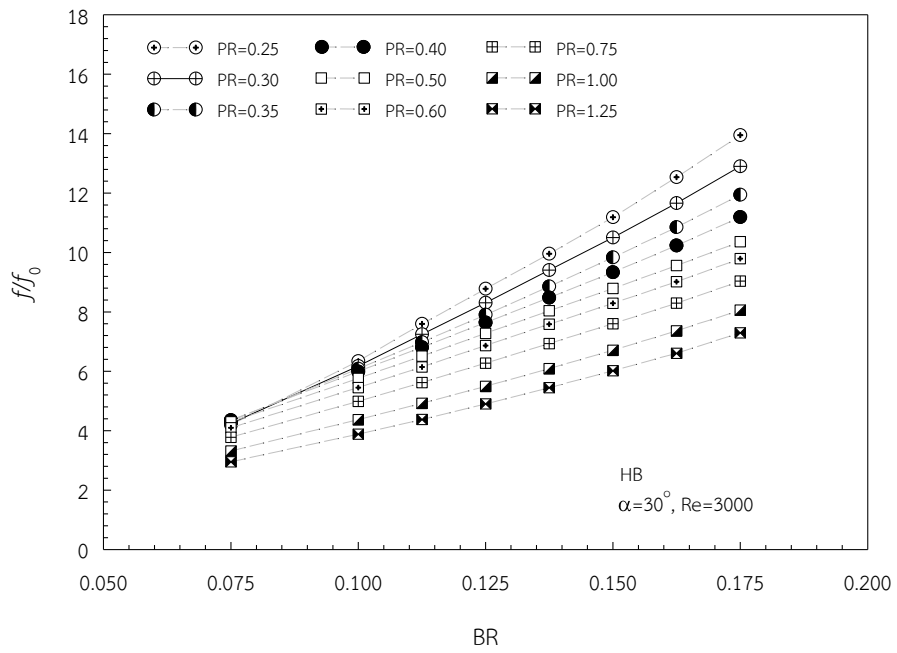


Figure 7.14 Variation of f/f_0 with BR for various PR values.

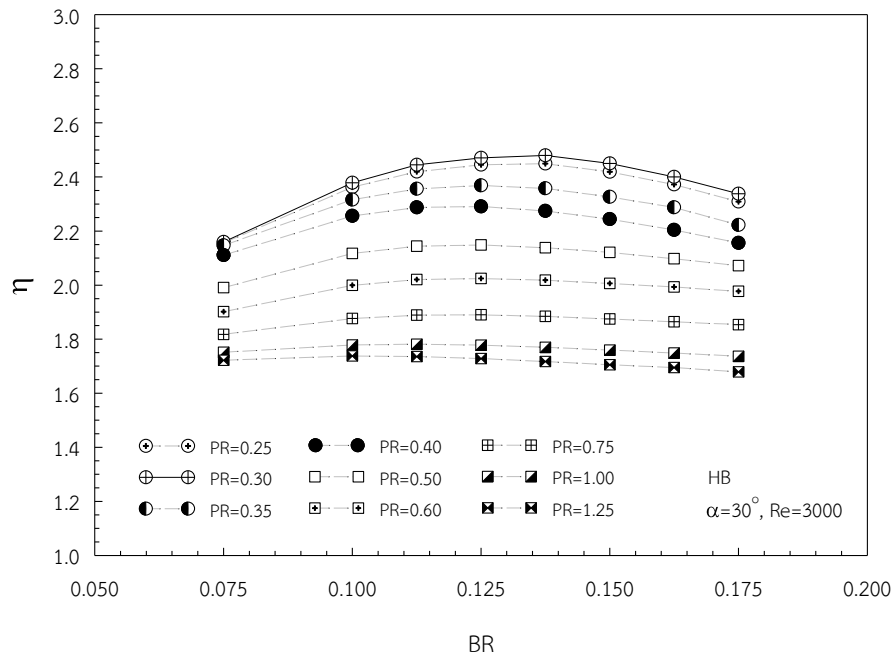


Figure 7.15 Variation of η with BR for various PR values.

7.1.5 Flow and heat topologies for inclined horseshoe baffles

The flow and coherent structure of the HB inserted tube could be described using streamlines plotted on transverse planes as shown in Figure 7.16. Each transverse plane was located from $x/P=0$ to $x/P=1$ in a step of $0.2PR$ for the 30° HB with $PR=2.0$, and $BR=0.1$. The vortex pairs appeared along the tube in a direction that induced the flow toward the bottom wall. When the PR reduced, longitudinal vortex flow was stronger.

The pressure distribution contours of the HBs plotted in transverse planes at $x/P=0$ to $x/P=1$ with different BRs were presented in Figure 7.17 (a) and (b). The high pressure area occurred in front of the base of the horseshoe baffle. The low pressure distribution occurred behind the base of the HB. This pressure difference induced the vortex pairs along the tube. Increasing the BR also increased the pressure drop. The larger PR also reduced the pressure drop as shown in Figure 7.18. Moreover, increasing the angle of attack also led to an increase in pressure loss due to its higher pressure drag as shown in Figure 7.19.

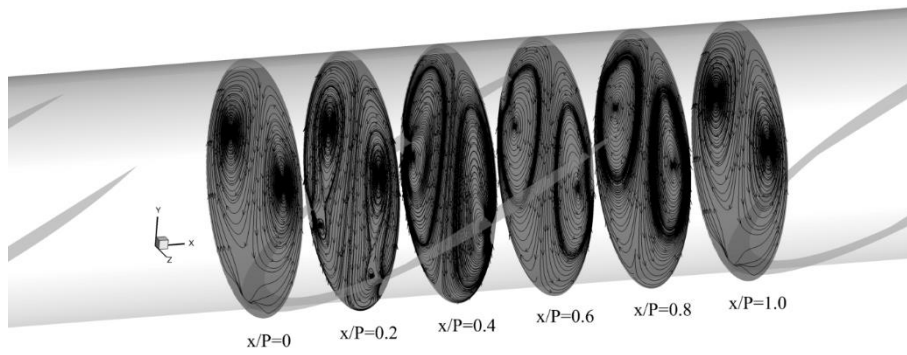
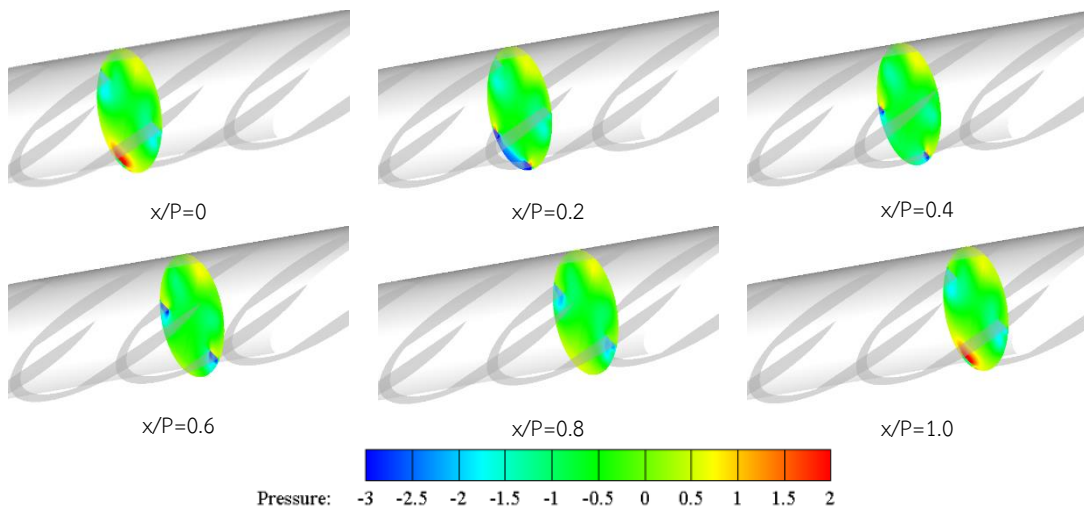
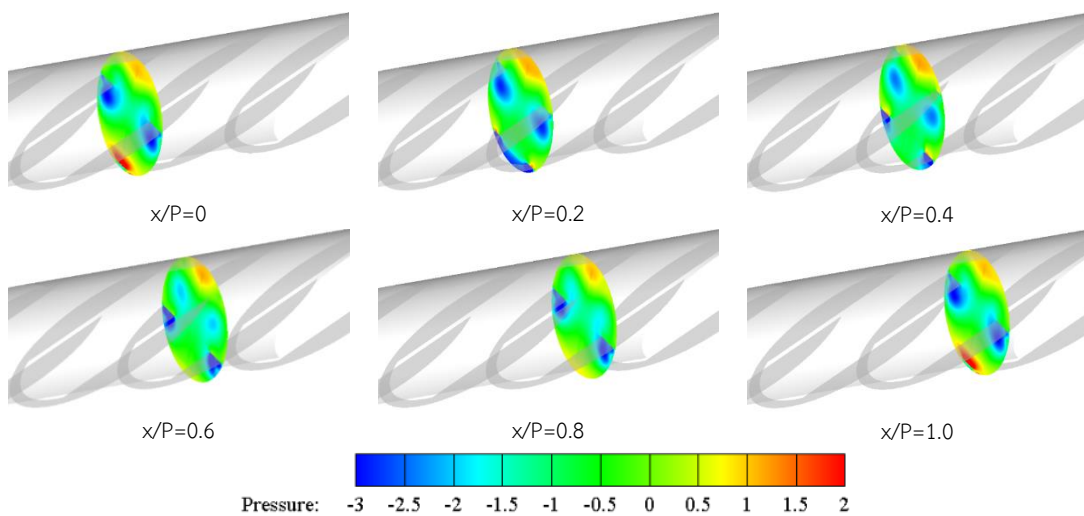


Figure 7.16 Streamlines in transverse planes for 30° HB at $Re=8,000$, $PR=2.0$ and $BR=0.1$.

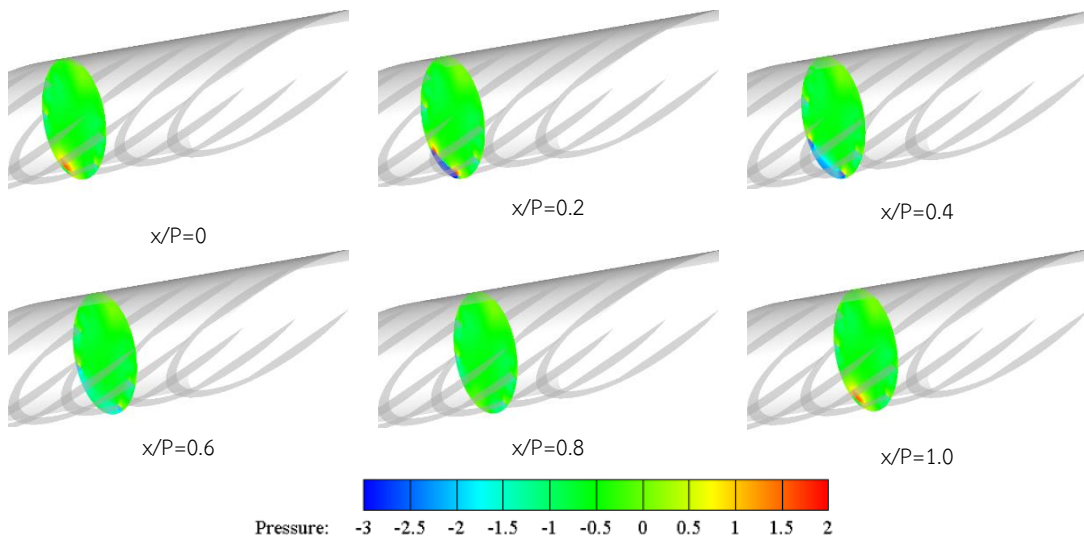


(a) $PR=1.0$ and $BR=0.15$

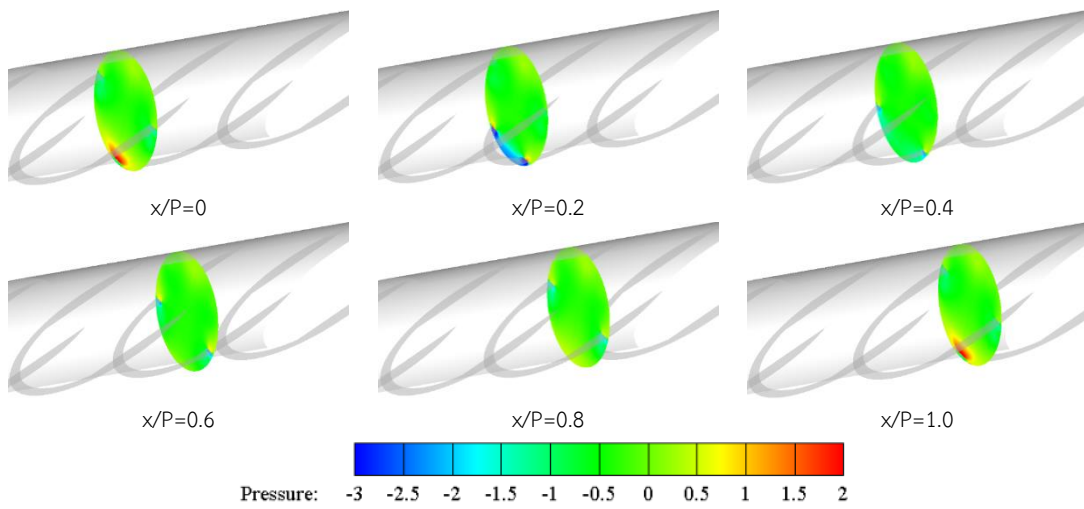


(b) $PR=1.0$ and $BR=0.20$

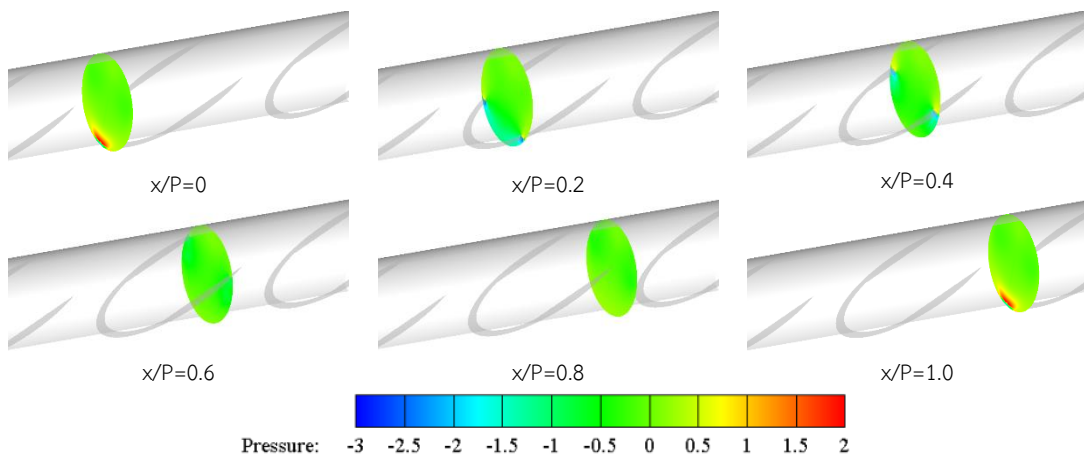
Figure 7.17 Pressure contours in transverse planes for 30° HB at $Re=8000$.



(a) BR=0.1 and PR=0.5



(b) BR=0.1 and PR=1.0



(c) BR=0.1 and PR=2.0

Figure 7.18 Pressure contours in transverse planes for 30° HB with various PR at $Re=8000$.

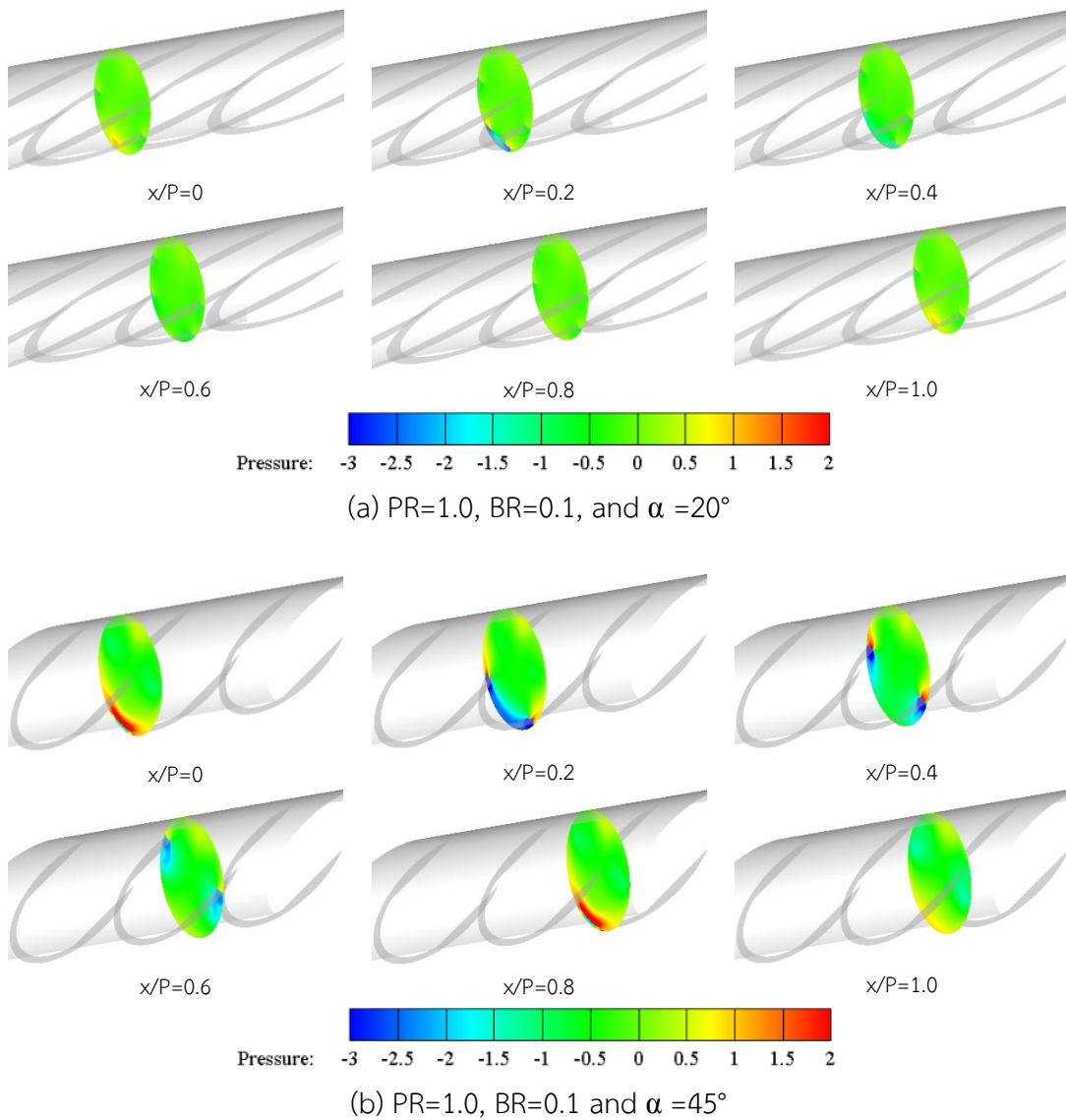


Figure 7.19 Pressure contour in transverse planes for HB with various α at $Re=8000$.

The plot of Q-isosurfaces of HBs at $Re=8000$ and $PR=1.0$ is shown in Figure 7.20. The longitudinal vortex core flow which was the main vortex core appeared along the top wall of the tube. The vortex-core flows also occurred behind the HBs and joined with the main core flow. The higher BR produced larger and stronger vortex core flow than the lower BR.

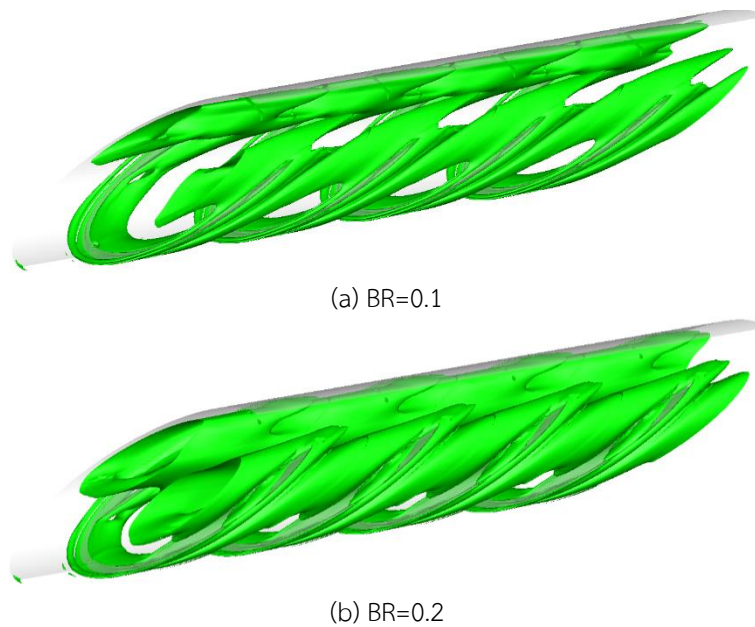


Figure 7.20 Q-isosurfaces of $Q=200$ for 30° HB with various BR at $Re=8000$, $PR=1.0$.

The temperature contours of HBs in a tube are presented in Figure 7.21. The contours were plotted on transverse planes at $x/P=0$ to $x/P=1$. The lower air temperature from the top wall of the tube was induced to the other walls. This behavior increased the heat transfer rate. However, the heat transfer rate was low at the area behind the horseshoe baffles. When the baffle height was increased, the near wall boundary layer also decreased which enhanced the heat transfer rate. When the PR was reduced, the heat transfer rate also increased as shown in Figure 7.22. Moreover, when the angle of attack was increased, the heat transfer rate also increased as shown in Figure 7.23.

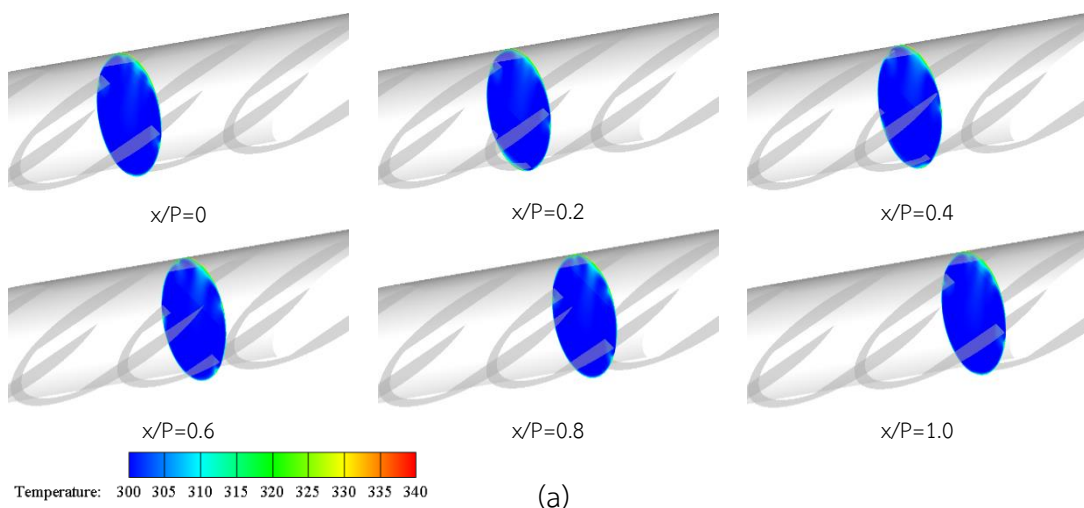


Figure 7.21(a) Temperature contours in transverse planes for 30° HB with $PR=1.0$, $BR=0.15$ and $Re=8000$.

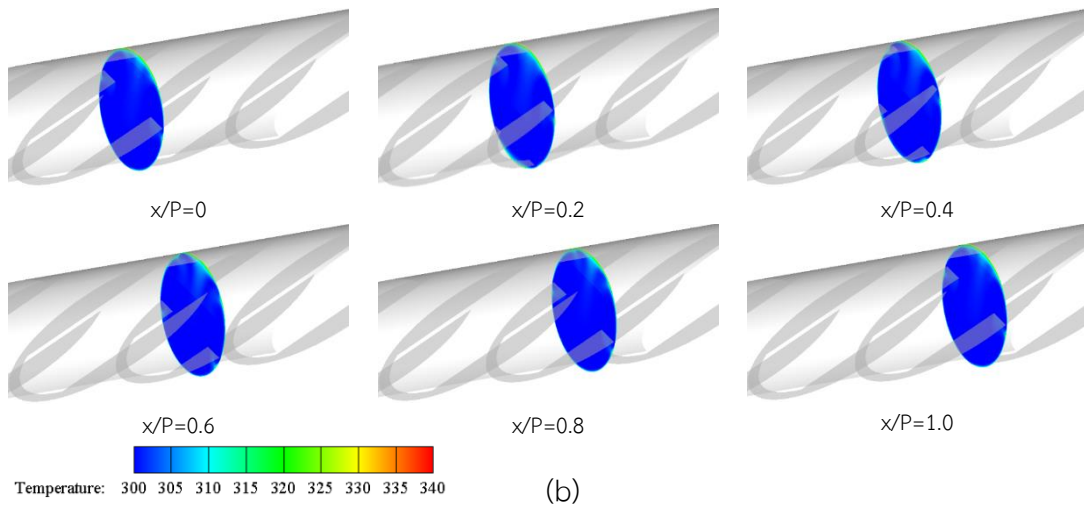


Figure 7.21(b) Temperature contours in transverse planes for 30° HB with PR=1.0, BR=0.2 and Re=8000.

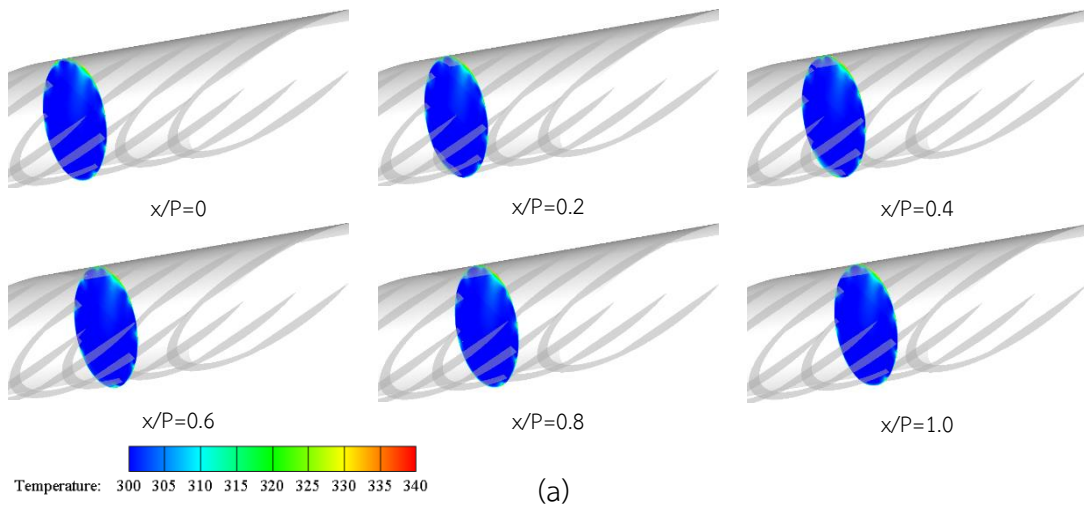


Figure 7.22(a) Temperature contours in transverse planes for 30° HB with BR=0.10, PR=0.5 and Re=8000.

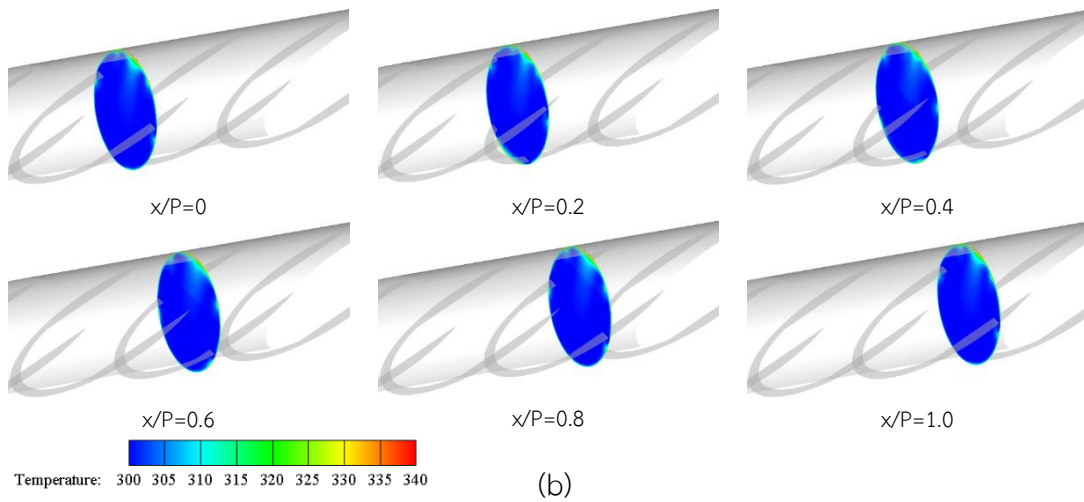


Figure 7.22(b) Temperature contours in transverse planes for 30° HB with BR=0.10, PR=1.0 and Re=8000.

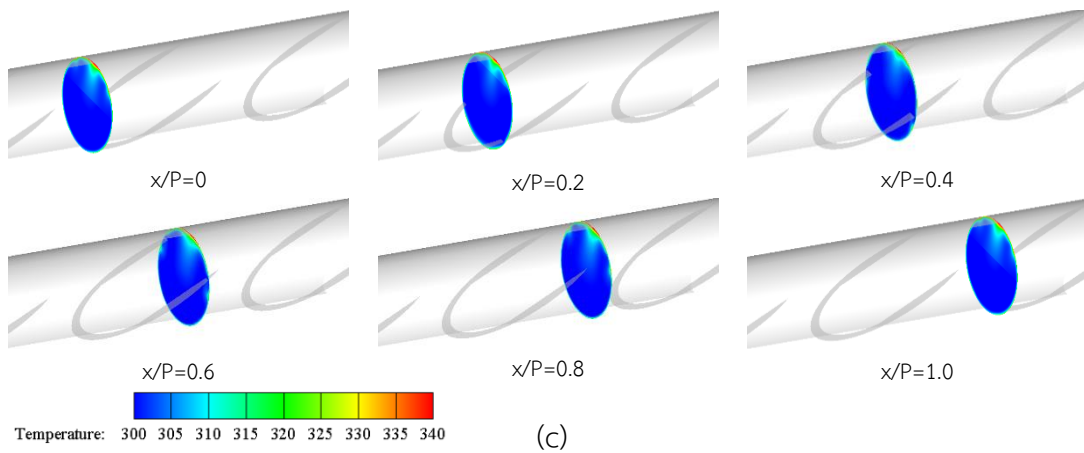


Figure 7.22(c) Temperature contours in transverse planes for 30° HB with BR=0.1, PR=2.0 and Re=8000.

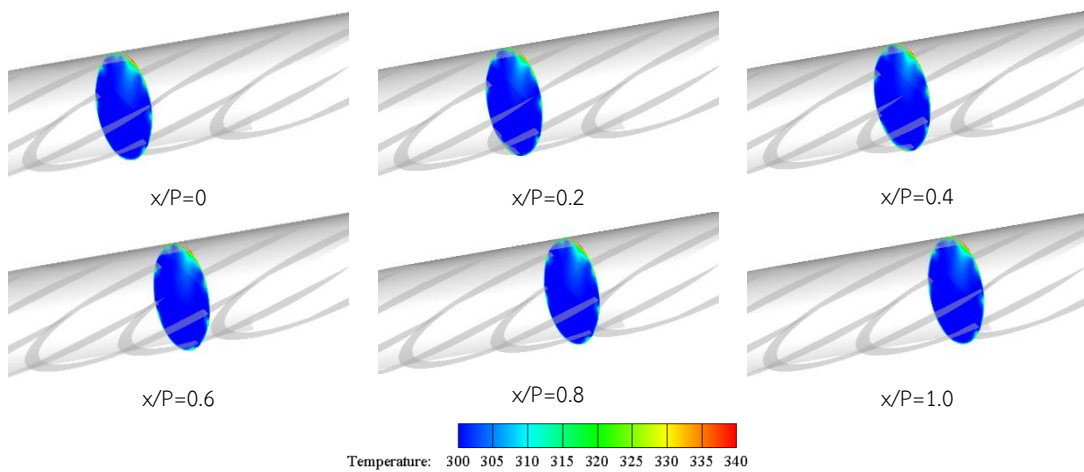


Figure 7.23(a) Temperature contours in transverse planes for 20° HB at Re=8000.

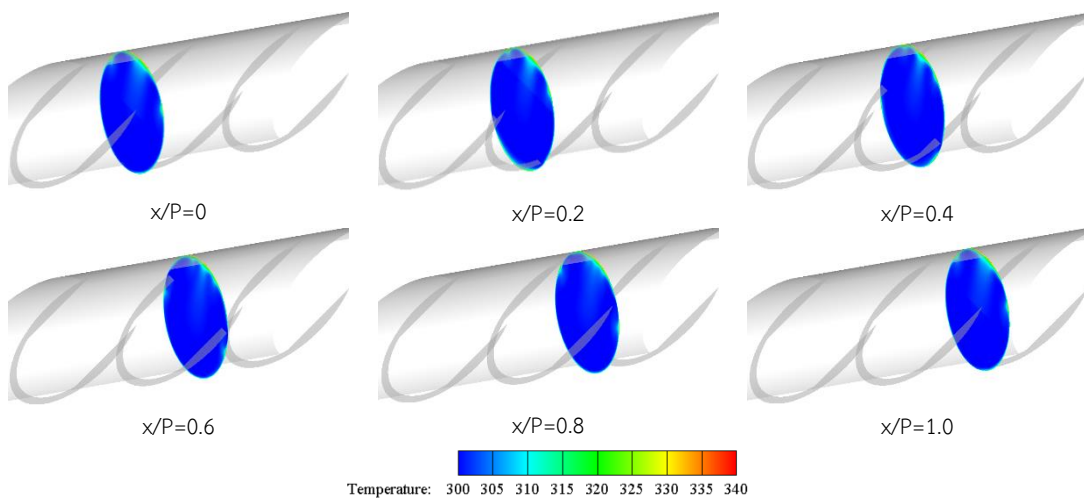


Figure 7.23(b) Temperature contours in transverse planes for 45° HB at Re=8000.

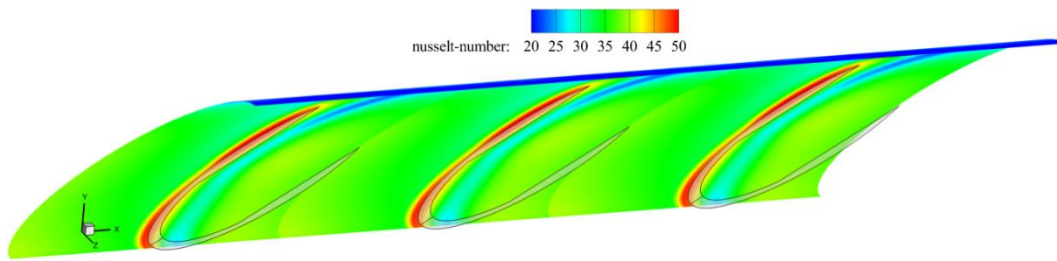


Figure 7.24 Local Nu_x contours on the wall for 30° HB with $BR=0.10$, $PR=2.0$ and $Re=8000$.

The local Nusselt number contour plot of a 30° HB inserted tube with $BR=0.1$, and $PR=2.0$ is displayed in Figure 7.24. The local Nusselt numbers were high at the area between the HBs. However, the area near the HB and at the middle of top wall gave low local Nusselt numbers. When the PR reduced, the averaged local Nusselt number was also increased.

7.2 V-shaped horseshoe baffles

7.2.1 Effects on heat transfer

The variations of Nu/Nu_0 with Re and α values for using the VHB are presented in Figures 7.25 and 7.26, respectively. The VHBs gave the heat transfer coefficient much higher than the smooth tube. The Nu/Nu_0 tended to decrease with the increase of Re for all cases. Depending on Re , the Nu/Nu_0 values at $PR=1.0$ were in the range of 1.91-2.66, 2.1-2.95, 2.24-3.16, 2.37-3.42, 2.6-3.72, 2.72-3.98, and 2.89-4.23 times for $BR=0.075$, 0.1, 0.125, 0.15, 0.2, 0.25, and 0.3, respectively.

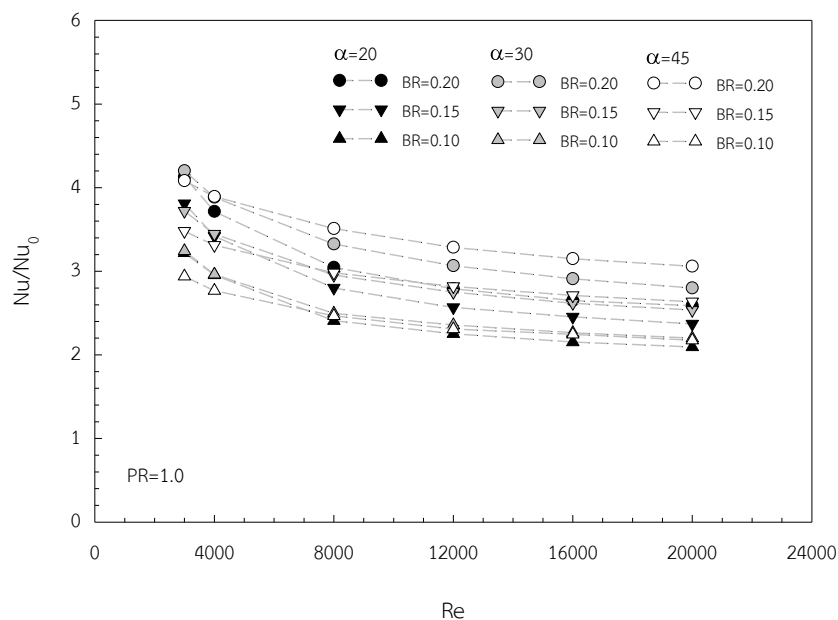


Figure 7.25 Variation of Nu/Nu_0 with Re .

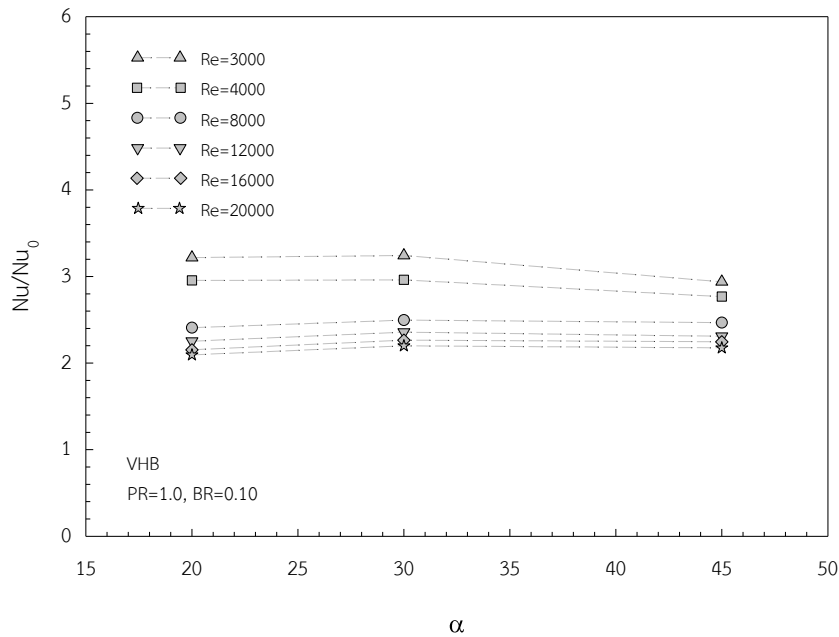


Figure 7.26 Variation of Nu/Nu_0 with α .

7.2.2 Effects on friction factor

Figures 7.27 and 7.28 present the variations of f/f_0 with Re and α for the VHBs, respectively. The f/f_0 showed the downward trend with increasing Re for all cases. The VHB gave a substantial increase in f/f_0 over the smooth tube. The f/f_0 increased with increasing both Re and BR values. Depending on Re , the f/f_0 values at $PR=1.0$ were in a range of 3.86-5.01, 4.75-6.21, 5.89-7.8, 7.5-10.03, 11.43-13.67, 16.9-20.21, and 25.81-32.6 times for $BR=0.075, 0.1, 0.125, 0.15, 0.2, 0.25,$ and 0.3 , respectively.

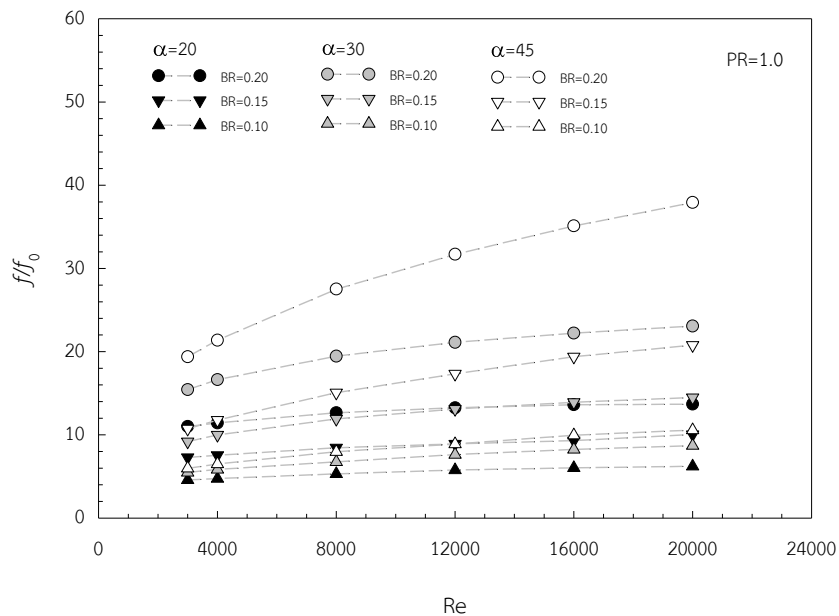


Figure 7.27 Variation of f/f_0 with Re .

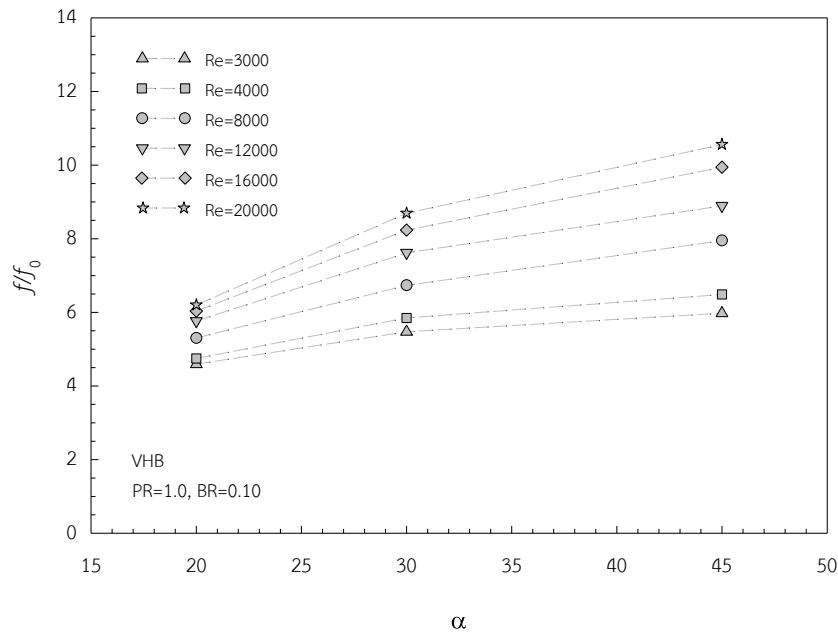


Figure 7.28 Variation of f/f_0 with α .

7.2.3 Effects on thermal enhancement factor

Figures 7.29 and 7.30 depict, respectively, the variations of the thermal enhancement factor (η) with Re and α for the tube inserted with VHBs. In the figure, the η values were above unity indicating that the use of VHBs is better than the smooth tube. Depending on Re, the maximum η was about 1.76 at BR=0.1 and PR=1.0 while the minimum was around 0.9 at BR=0.3 and PR=1.0. The η values were approximately 1.12-1.7, 1.14-1.76, 1.13-1.75, 1.1-1.74, 1.08-1.65, 1.0-1.55, and 0.9-1.43 at BR=0.075, 0.1, 0.125, 0.15, 0.2, 0.25, and 0.3, respectively. The highest η was found to be 1.76 at BR=0.1 and PR=1.0.

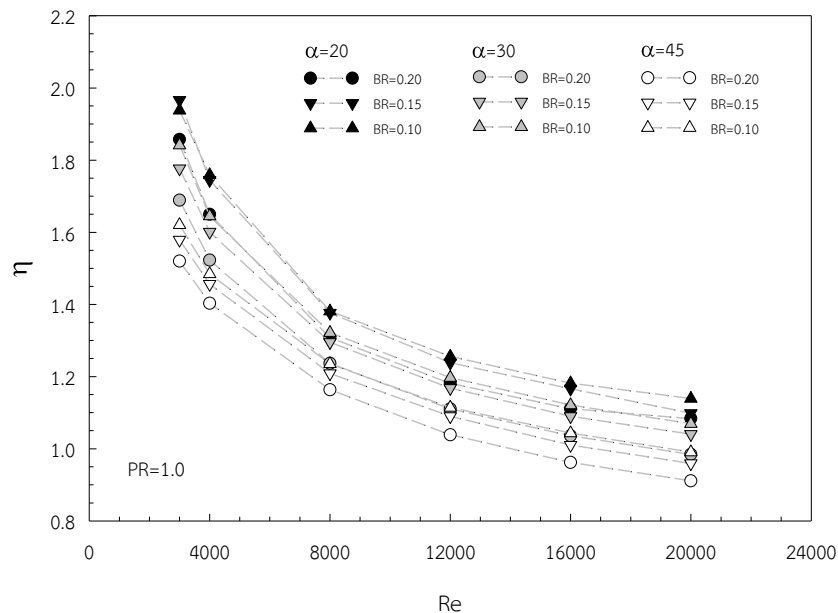


Figure 7.29 Variation of η with Re.

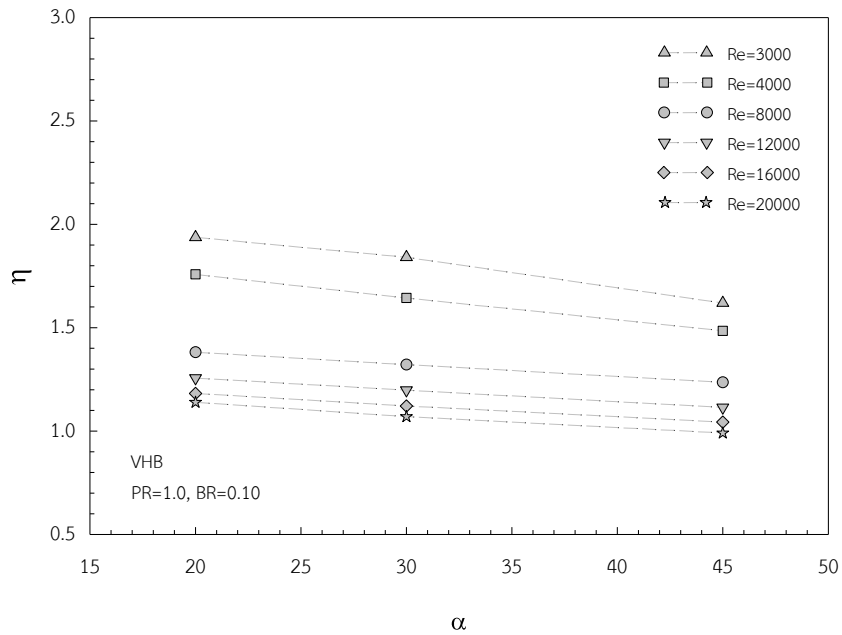


Figure 7.30 Variation of η with α .

7.2.4 Optimization for V-shaped horseshoe baffles

Similar to the 30° HB case, the 30° VHBs was chosen to find the optimum configuration parameters of BR and PR at Re=3000 only. The PR was ranging from 0.30 to 1.50 while the BR was from 0.045 to 0.125. The variations of Nu/Nu_0 , f/f_0 , and η are presented in Figures 7.31 to 7.33. According to the numerical results, depending on Re, the Nu/Nu_0 was in a range of 1.91-5.53 whereas the f/f_0 was from 1.73 - 9.19. The maximum η was found to be 2.76 at PR=0.35 and BR=0.085.

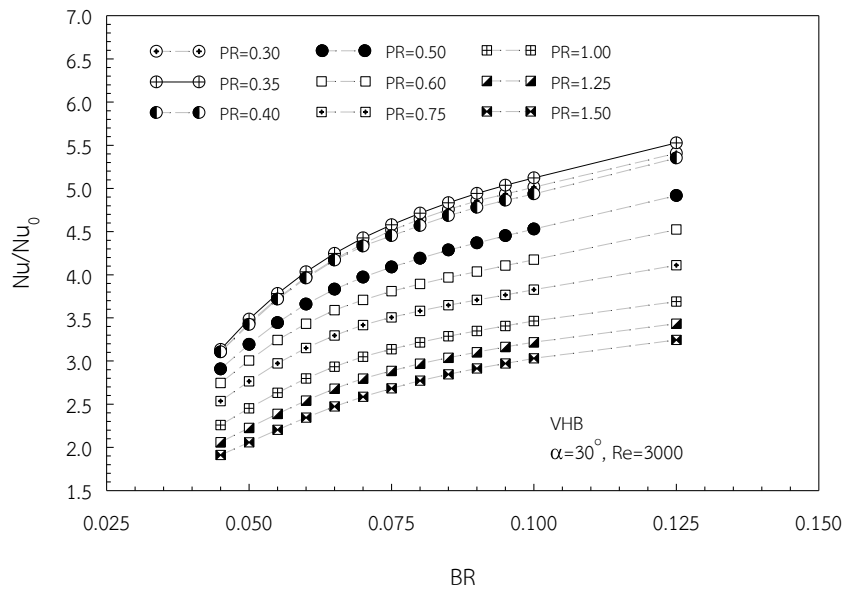


Figure 7.31 Variation of Nu/Nu_0 with BR for various PR values.

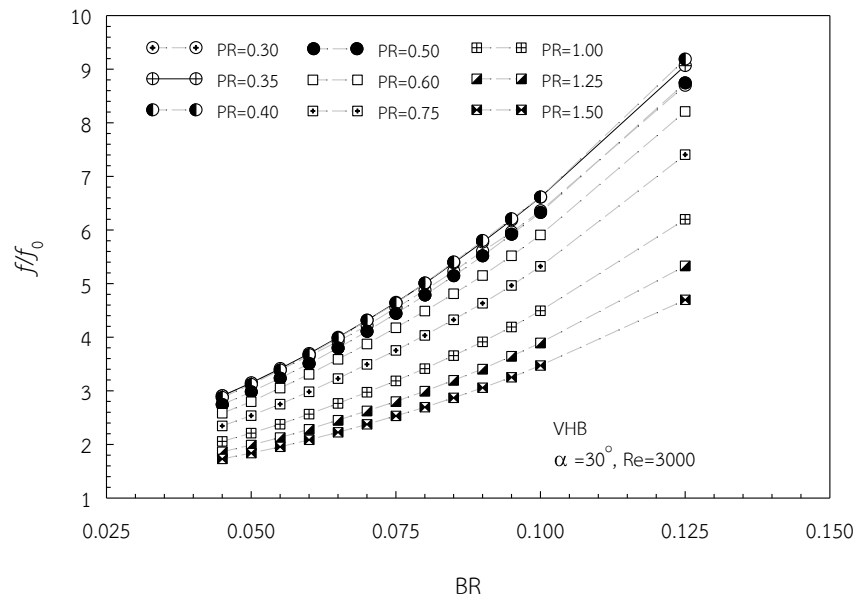


Figure 7.32 Variation of f/f_0 with BR for various PR values.

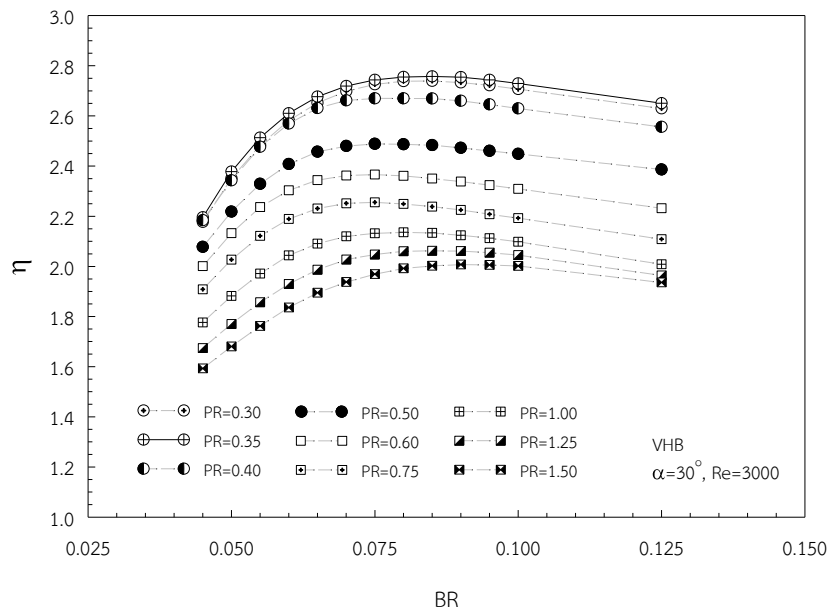


Figure 7.33 Variation of η with BR for various PR values.

7.2.5 Flow and heat topologies for V-shaped horseshoe baffles

The flow and coherent structure of the VHBs could be described by plotting streamlines on the transverse planes. Each transverse plane was located in a step of $0.2PR$ on $x/P=0$ to $x/P=1$ as presented in Figure 7.34 for the VHBs with $\alpha=30^\circ$, $PR=1.0$, and $BR=0.1$. In the figure, the two counter-rotating vortices pairs appeared along the top and bottom halves in the tube. The top vortex pairs were common-flow-down vortices while the bottom vortex pairs were common-flow-up vortices. When the BR increased, the size of vortex pairs also increased which enhanced the air mixing.

The pressure contour plot of the VHBs with $BR=0.1$ and 0.2 on transverse planes from $x/P=0$ to $x/P=1$ is presented in Figure 7.35 (a) and (b), respectively. The high

pressures were in the area in front of the base of the VHB and also at the V-tip of the VHB. The low pressure areas occurred behind the V-tip of the VHB. The increasing BR had blocked the flow which led to an increase in pressure drop.

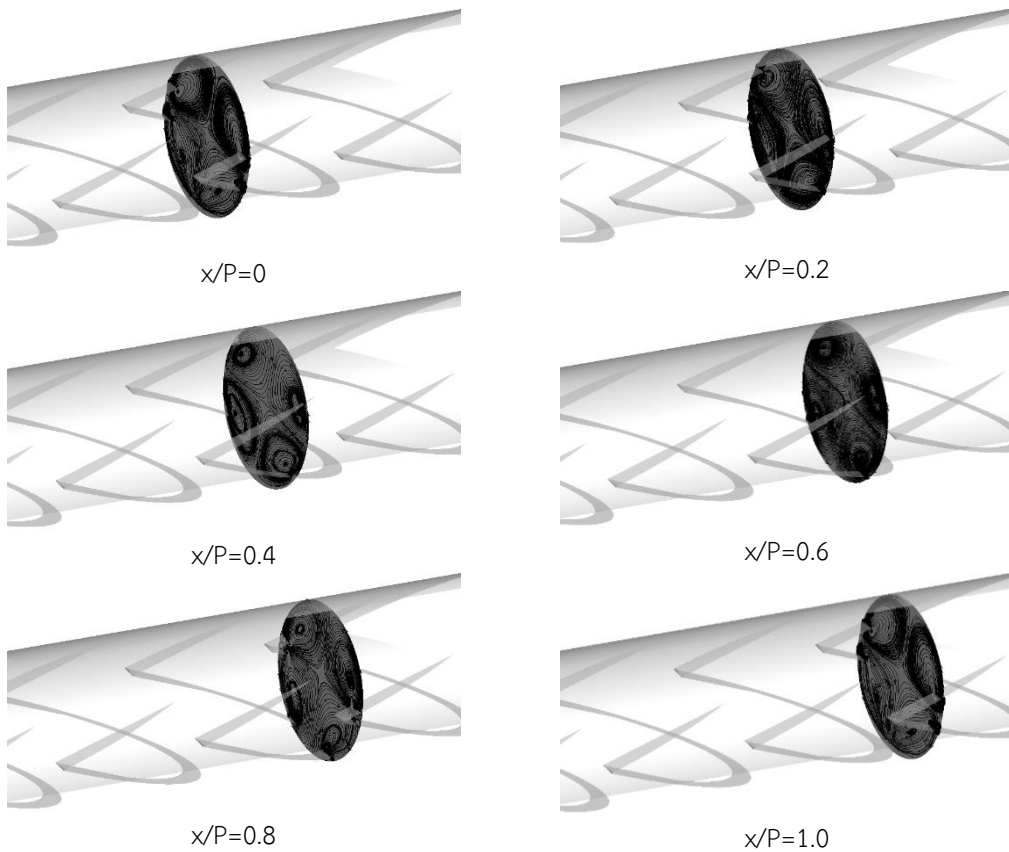
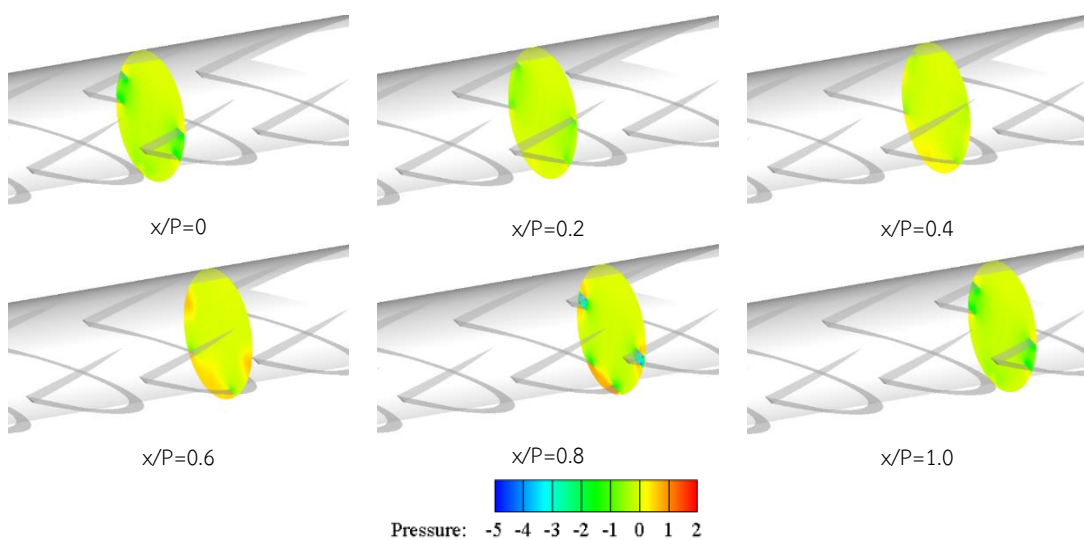


Figure 7.34 Streamlines in transverse planes for 30° VHB with PR=1.0 and BR=0.10 at Re=8,000.



(a) PR=1.0, BR =0.10

Figure 7.35(a) Pressure contours in transverse planes for 30° VHB at Re=8000.

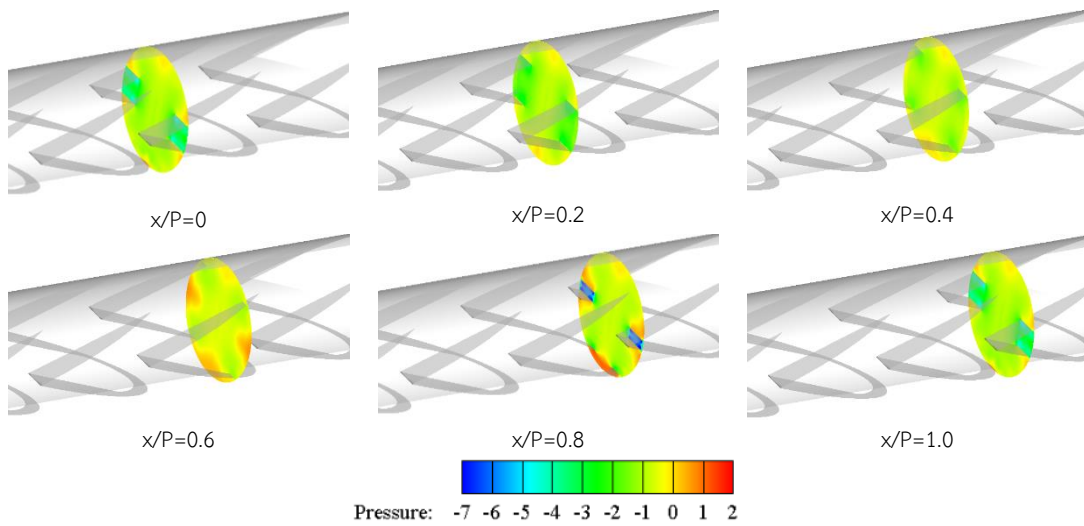
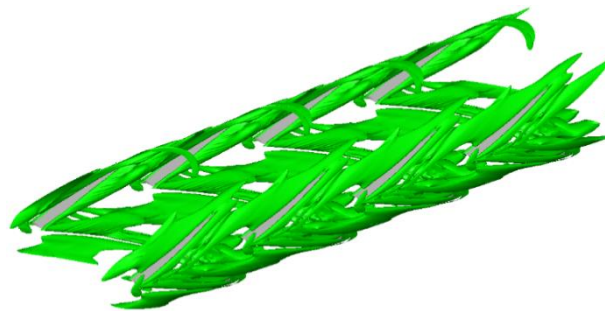
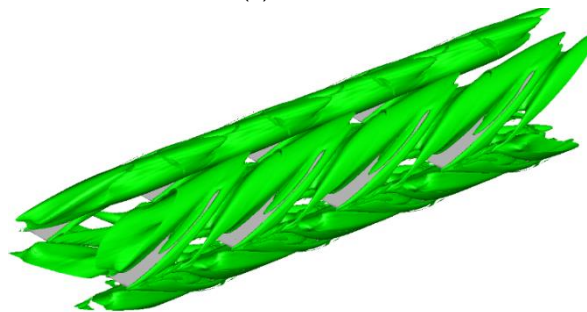


Figure 7.35(b) Pressure contours in transverse planes for 30° VHB at Re=8000.

The plots of Q-isosurfaces of the 30° VHB with BR=0.1 and 0.2 at Re=8000, PR=1.0 are presented in Figure 7.36(a) and (b), respectively. The four main vortex core flows appeared along the tube. These main vortex-core flows also joined at the V-tip of the VHBs. The higher BR also produced the larger and stronger vortex flows.



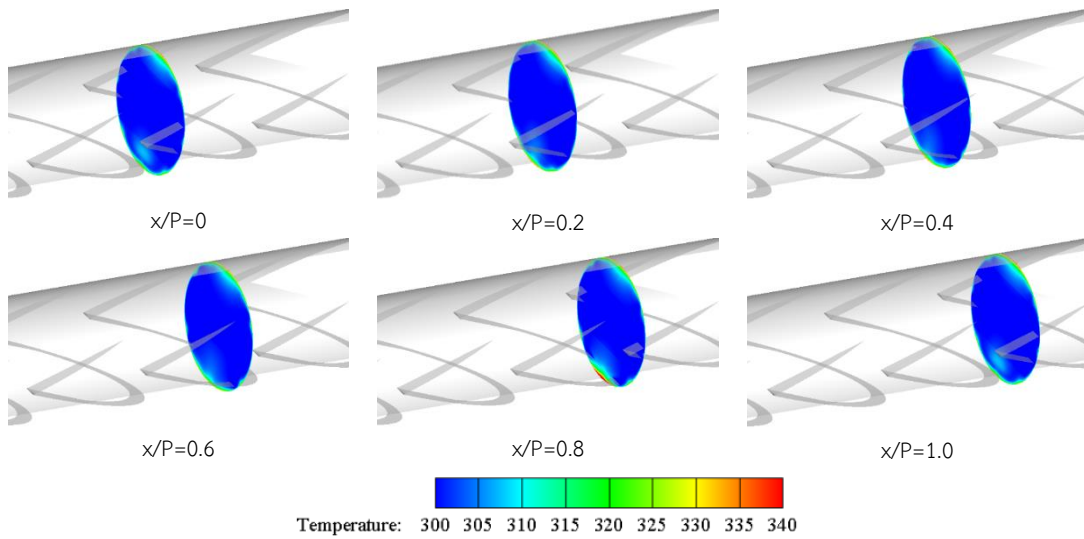
(a) BR =0.1



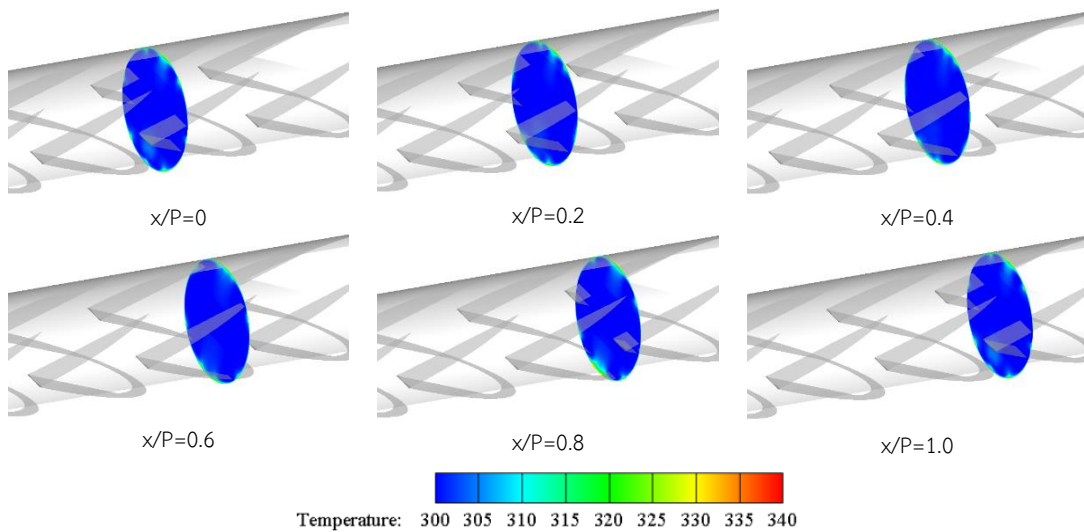
(b) BR =0.2

Figure 7.36 Q-isosurfaces of Q=200 for 30° VHB at Re=8000, PR=1.0.

The temperature contours of the 30°VHBs with BR=0.1 and 0.2 plotted in transverse planes from $x/P=0$ to $x/P=1$ are depicted in Figure 7.37(a) and (b), respectively. The higher temperature areas were found on the upper and lower walls while the lower temperatures regions were on the left and right sidewalls or behind the V-tip of the VHB. When the BR increased, the near-wall boundary layer thickness was also decreased which enhanced the heat transfer rate.



(a) PR=1.0, BR =0.10



(b) PR=1.0, BR =0.20

Figure 7.37 Temperature contours in transverse planes for 30° VHB at $Re=8000$.

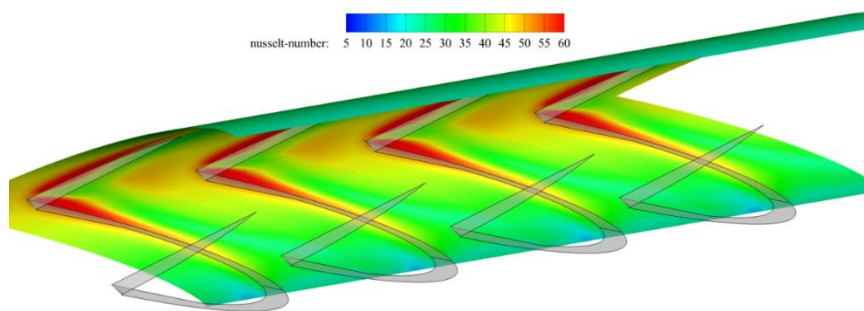


Figure 7.38 Local Nusselt number contours on left-half sidewall for 30° VHB at BR=0.1 and PR=1.0.

The local Nusselt number contour plot of the 30° VHBs at BR=0.1, and PR=0.1 is presented in Figure 7.38. The high local Nusselt number areas were on the sidewalls behind the baffle V-tip at which was the highest Nu_x area. The area on the lower and upper walls had the lowest Nu_x .

7.3 Empirical correlations

The empirical correlations for Nusselt number (Nu), friction factor (f) and thermal enhancement factor (η) for various baffle geometries in the present work are presented in equations (7.1) – (7.18), respectively. The obtained correlations revealed that Nu was related to Re , Prandtl number (Pr), blockage ratio (BR) and pitch ratio (PR) while the f and η were dependent of Re , BR and PR . Obviously, the predicted Nu and f were within ± 10 each under the condition of $Re=3000-20,000$ and $BR=0.075-0.2$.

Correlations for 20° HBs, PR=0.25–2.0.

$$Nu = 1.323Re^{0.555}Pr^{0.4}BR^{0.191}(PR+1)^{-0.683} \quad (7.1)$$

$$f = 15.936Re^{-0.277}BR^{0.673}(PR+1)^{-0.935} \quad (7.2)$$

$$\eta = 17.98Re^{-0.253}BR^{-0.0402}(PR+1)^{-0.377} \quad (7.3)$$

Correlations for 30° HBs, PR=0.25–2.0.

$$Nu = 1.493Re^{0.548}Pr^{0.4}BR^{0.219}(PR+1)^{-0.622} \quad (7.4)$$

$$f = 27.822Re^{-0.249}BR^{0.891}(PR+1)^{-0.948} \quad (7.5)$$

$$\eta = 16.27Re^{-0.264}BR^{-0.078}(PR+1)^{-0.306} \quad (7.6)$$

Correlations for 45° HBs, PR=0.25–2.0.

$$Nu = 1.445Re^{0.573}Pr^{0.4}BR^{0.306}(PR+1)^{-0.546} \quad (7.7)$$

$$f = 55.3\text{Re}^{-0.168}\text{BR}^{1.249}(\text{PR} + 1)^{-1.142} \quad (7.8)$$

$$\eta = 13.622\text{Re}^{-0.278}\text{BR}^{-0.127}(\text{PR} + 1)^{-0.18} \quad (7.9)$$

Correlations for 20° VHBs, PR=0.3–2.0.

$$\text{Nu} = 1.511\text{Re}^{0.56}\text{Pr}^{0.4}(\text{PR} + 1)^{-0.525}\text{BR}^{0.31} \quad (7.10)$$

$$f = 16.86\text{Re}^{-0.131}(\text{PR} + 1)^{-1.167}\text{BR}^{1.084} \quad (7.11)$$

$$\eta = 19.934\text{Re}^{-0.294}(\text{PR} + 1)^{-0.136}\text{BR}^{-0.0512} \quad (7.12)$$

Correlations for 30° VHBs, PR=0.3–2.0.

$$\text{Nu} = 1.494\text{Re}^{0.592}\text{Pr}^{0.4}(\text{PR} + 1)^{-0.621}\text{BR}^{0.38} \quad (7.13)$$

$$f = 18.444\text{Re}^{-0.053}(\text{PR} + 1)^{-1.256}\text{BR}^{1.285} \quad (7.14)$$

$$\eta = 19.129\text{Re}^{-0.287}(\text{PR} + 1)^{-0.203}\text{BR}^{-0.0485} \quad (7.15)$$

Correlations for 45° VHBs, PR=0.3–2.0.

$$\text{Nu} = 1.089\text{Re}^{0.648}\text{Pr}^{0.4}(\text{PR} + 1)^{-0.671}\text{BR}^{0.456} \quad (7.16)$$

$$f = 17.085\text{Re}^{0.022}(\text{PR} + 1)^{-1.256}\text{BR}^{1.479} \quad (7.17)$$

$$\eta = 14.307\text{Re}^{-0.257}(\text{PR} + 1)^{-0.252}\text{BR}^{-0.0374} \quad (7.18)$$

7.4 Conclusions

Numerical studies have been conducted to investigate the air flow characteristics, pressure losses, and heat transfer rates in a tube. The baffles inserted into the tube were HB and VHB. The pertinent parameters were PRs and BRs for a given range of Re from 3000 to 20,000. A uniform surface heat flux was applied as a thermal condition. From the numerical results, the following conclusions can be drawn.

For the case of HBs, the counter-rotating vortices created by the HB could help to induce impingement flows on the walls which led to drastic increase in heat transfer rate in the tube. The order of enhancement for Nu was approximately 2–6 times above the smooth tube at PR=0.5–2.0 and BR=0.075–0.25. However, the increase in f was in a range of around 3–60 times above the smooth tube depending on BR and Re values. The η for the HB was higher than unity (indicating higher thermal performance than the smooth tube) and its maximum was found to be 2.48 at $\alpha=30^\circ$, PR=0.3, BR=0.1375 and Re=3000.

For the case of VHB, the VHBs could create two pairs of main counter-rotating

vortices along the tube that helped to induce impingement flows over the sidewall which led to greater increase in heat transfer. Depending on Re, the VHB at PR=1.0, BR=0.2 caused a high pressure drop ($f/f_0=25.81-32.6$) but also gave a considerable heat transfer augmentation in the tube ($Nu/Nu_0=2.89-4.23$). The Nu of the VHB showed an increasing trend with the rise in BR and Re values. The η of the VHB was above unity and tended to decrease with the increment in Re and BR values. The 30° VHB at PR=0.35 and BR=0.085 yielded the highest η of 2.76 at the lowest Re.

CHAPTER 8

CONCLUSIONS

The main objective of the present study was to investigate the fluid flow and heat transfer characteristics of a channel/tube fitted with various types of baffles using air as the test fluid for Reynolds numbers (Re) from 3000 to 20,000. A steady three-dimensional turbulent flow model was developed with an assumption of periodically fully-developed turbulent flow. A constant surface heat-flux as thermal boundary condition was applied on the top wall of a channel, all walls of a square channel and of a tube. The computational domain was mapped into the physical domain to create the numerical model. Grid structure was specified and generated. The RNG $k-\epsilon$ turbulence model was employed in the numerical simulation. By applying the finite volume method, the numerical simulation was iteratively solved using the QUICK scheme. The numerical solutions were verified with grid refinement study method. The numerical solutions were also compared with the smooth tube correlations. The results from the numerical simulation were validated with available experimental data [50, 82]. The numerical simulations were carried out to investigate the effect of varied geometric parameters of the turbulators and flow conditions on the key quantifying thermal performance factors. In addition, in order to improve the tabulator for use in a round tube, the inclined horseshoe baffles (HB) and the V-shaped horseshoe baffles (VHB) were introduced and applied to the corresponding tube. The numerical result revealed that the friction factor was significantly reduced. The highest thermal performance factor was about 2.76 at $PR=0.35$, $BR=0.085$, $Re=3000$ for the VHB.

8.1 Conclusions

Numerical studies have been conducted to investigate the characteristics of airflow, pressure losses, and heat transfer rates in a rectangular channel, a square channel, and a circular tube, respectively. From the numerical results of the present study, the following conclusions can be drawn.

For the case of multiple V-baffles (VB) placed repeatedly on the channel wall, the in-line array having $PR=0.5$ caused higher pressure drop, but also provided a considerable heat transfer augmentation, depending on Re . The Nu/Nu_0 augmentation tended to slightly decrease with the rise in Re . However, the VB placed on a single wall or the absorber wall at smaller PR should be applied to obtain higher η . The best operating condition for the VBs was obtained at the smallest PR and Re . The single VB wall at $PR=0.5$ yielded the highest η of 1.83 at the lowest Re .

For the case of inclined U-baffles (UB), the counter-rotating vortex flows created by the UB could help to induce impingement flows on the walls resulting in drastic increase in heat transfer rate in the square channel. The η for the UB was higher than unity (indicating higher thermal performance than the smooth channel) and its maximum value was about 1.6 at PR=1.0, BR=0.2 and Re=4000.

For the case of inclined vortex rings (VR) or ring baffles, the VR could create a pair of main counter-rotating vortex flows along the tube that help to induce impingement flows on the lower tube wall leading to greater increase in heat transfer. The η of the VR was also above unity and tended to decrease with the increment in Re, BR, and PR values. The VR at PR=1.0 and BR=0.05 yielded the highest η around 1.54 at lower Re.

For the case of inclined horseshoe baffles (HB), two counter-rotating vortex flows created by the HB could help to induce impingement flows on the tube wall resulting in drastic increase in heat transfer rate. The η for the HB was higher than unity and its maximum was about 2.48 at PR=0.3, BR=0.1375 and Re=3000.

For the case of V-shaped horseshoe baffles (VHB) with V-tip pointing upstream, the VHB could create two pairs of main counter-rotating vortices along the tube that can help induce impingement/reattachment flows on the wall behind the V-tip leading to drastic increase in the heat transfer. All η values for the VHB were above unity and tended to decrease with the increment in Re and BR values. The VHB with $\alpha=30^\circ$, PR=0.35 and BR=0.085 yielded the highest η around 2.76 at Re=3000.

8.2 Suggestions for future work

A numerical investigation of an unsteady flow in a three-dimensional flow model should be introduced to the simulation of the horseshoe baffles which can allow more details or depth insight of the heat transfer mechanism and flow structure to be more accurately observed.

The numerical investigation of the horseshoe baffles should be offered to the numerical simulation of nanofluid flow.

The application of Large Eddy Simulation (LES) or Direct Numerical Simulation (DNS) should also be considered to the numerical simulation of the horseshoe baffles.

REFERENCES

- [1] Warren M. Rohsenow, James P. 1998. Hartnett and Yong I. Cho. **Handbook of Heat Transfer**. 3rd ED. New York : McGraw-Hill, Inc. 1998.
- [2] Liu S. and Sakr M. "A comprehensive review on passive heat transfer enhancements in pipe exchangers." **Renewable and Sustainable Energy Reviews**. vol. 19, 2013. pp. 64–81.
- [3] Jaurker A.R., Saini J.S. and Gandhi B.K. "Heat transfer and friction characteristics of rectangular solar air heater duct using rib-grooved artificial roughness." **Solar Energy**., vol. 80, 2006. pp. 895–907.
- [4] Jin D.X., Lee Y.P. and Lee D.-Y. "Effects of the pulsating flow agitation on the heat transfer in a triangular grooved channel." **International Journal of Heat and Mass Transfer**., vol. 50, 2007. pp. 3062–3071.
- [5] Layek A., Saini J.S. and Solanki S.C. "Heat transfer and friction characteristics for artificially roughened ducts with compound turbulators." **International Journal of Heat and Mass Transfer**., vol. 50, 2007. pp. 4845–4854.
- [6] Nishimura T., Oka N., Yoshinaka Y. and Kunitsugu K. "Influence of imposed oscillatory frequency on mass transfer enhancement of grooved channels for pulsatile flow." **International Journal of Heat and Mass Transfer**., vol. 43, 2000. pp. 2365–2374.
- [7] Eiamsa-ard S. and Promvonge, P. "Numerical Study on Heat Transfer of Turbulent Channel Flow over Periodic Grooves." **International Communications in Heat and Mass Transfer**., vol. 35, 2008. pp. 844–852.
- [8] Tang X.-Y., Jiang, G. and Cao G. "Parameters study and analysis of turbulent flow and heat transfer enhancement in narrow channel with discrete grooved structures." **Chemical Engineering Research and Design**., vol. 93, 2015. pp. 232–250.
- [9] Xia H.H., Tang G.H., Shi Y. and Tao W.Q. "Simulation of heat transfer enhancement by longitudinal vortex generators in dimple heat exchangers." **Energy**., vol. 74, 2014. pp. 27–36.
- [10] Liu J., Song Y., Xie G. and Sunden B. "Numerical modeling flow and heat transfer in dimpled cooling channels with secondary hemispherical protrusions." **Energy**., vol. 79, 2015. pp. 1–19.
- [11] Skullong S., Kwankaomeng S., Thianpong C. and Promvonge P. "Thermal performance of turbulent flow in a solar air heater channel with rib-groove turbulators." **International Communications in Heat and Mass Transfer**., vol. 50, 2014. pp. 34–43.

- [12] Fiebig M. "Embedded vortices in internal flow: heat transfer and pressure loss enhancement." **International Journal of Heat and Fluid Flow**. vol. 16, 1995. pp. 376–388.
- [13] Zhu J.X., Fiebig M. and Mitra N. K. "Numerical investigation of turbulent flows and heat transfer in a rib-roughened channel with longitudinal vortex generatorst." **International Journal of Heat and Mass Transfer**., vol. 38, 1995. pp. 495–501.
- [14] Biswas G., torii K., fuji D. and Nishino K. "Numerical and experimental determination of flow structure and heat transfer effects of longitudinal vortices in a channel flow." **International Journal of Heat and Mass Transfer**., vol. 39, 1996. pp. 3441–3451.
- [15] Gentry M.C. and Jacobi A.M. "Heat transfer enhancement by delta-wing vortex generators on a flat plate: Vortex interactions with the boundary layer." **Experimental Thermal and Fluid Science**., vol. 14, 1997. pp. 231–242.
- [16] Verma S.K. and Prasad B.N. "Investigation for the optimal thermohydraulic performance of artificially roughened solar air heaters." **Renewable Energy**., vol. 20, 2000. pp. 19–36.
- [17] Karwa R., Solanki S.C. and Saini J.S. "Thermo-hydraulic performance of solar air heaters having integral chamfered rib roughness on absorber plates." **Energy**., vol. 26, 2001. pp. 161–176.
- [18] Kim E. and Yang J.S. "An experimental study of heat transfer characteristics of a pair of longitudinal vortices using color capturing technique." **International Journal of Heat and Mass Transfer**., vol. 45, 2002. pp. 3349–3356.
- [19] Momin A.M.E., Saini J.S. and Solanki S.C. "Heat transfer and friction in solar air heater duct with V-shaped rib roughness on absorber plate." **International Journal of Heat and Mass Transfer**., vol. 45, 2002. pp. 3383–3396.
- [20] Bhagoria J.L., Saini J.S. and Solanki S.C. "Heat transfer coefficient and friction factor correlations for rectangular solar air heater duct having transverse wedge shaped rib roughness on the absorber plate." **Renewable Energy**., vol. 25, 2002. pp. 341–369.
- [21] Yang Y.T. and Hwang C.Z. "Calculation of turbulent flow and heat transfer in a porous-baffled channel." **International Journal of Heat and Mass Transfer**. vol. 46, 2003. pp. 771–780.
- [22] Chandra P.R., Alexander C.R., and Han J.C. "Heat transfer and friction behaviors in rectangular channels with varying number of ribbed walls." **International Journal of Heat and Mass Transfer**., vol. 46, 2003. pp. 481–495.
- [23] Lau S.C., Cervantes J., Han J.C., Rudolph R.J. and Flannery K. "Measurements of wall heat (mass) transfer for flow through blockages with round and square

- holes in a wide rectangular channel." **International Journal of Heat and Mass Transfer.**, vol. 46, 2003. pp. 3991–4001.
- [24] Sohankar, A. "Heat transfer augmentation in a rectangular channel with a vee-shaped vortex generator." **International Journal of Heat and Fluid Flow.**, vol. 28, 2007. pp. 306–317.
- [25] Sahu M.M., and Bhagoria J.L. "Augmentation of heat transfer coefficient by using 90° broken transverse ribs on absorber plate of solar air heater." **Renewable Energy.**, vol. 30, 2005. pp. 2057–2073.
- [26] Joardar A. and Jacobi A.M. "Impact of leading edge delta-wing vortex generators on the thermal performance of a flat tube, louvered-fin compact heat exchanger." **International Journal of Heat and Mass Transfer.**, vol. 48, 2005. pp. 1480–1493.
- [27] Chaube A., Sahoo P.K. and Solanki S.C. "Analysis of heat transfer augmentation and flow characteristics due to rib roughness over absorber plate of a solar air heater." **Renewable Energy.**, vol. 31, 2006. pp. 317–331.
- [28] Mousavi S.S. and Hooman K. "Heat and fluid flow in entrance region of a channel with staggered baffles." **Energy Conversion and Management.**, vol. 47, 2006. pp. 2011–2019.
- [29] Karmare S.V. and Tikekar A.N. "Heat transfer and friction factor correlation for artificially roughened duct with metal grit ribs." **International Journal of Heat and Mass Transfer.**, vol. 50, 2007. pp. 4342–4351.
- [30] Wu J.M. and Tao W.Q. "Investigation on laminar convection heat transfer in fin-and-tube heat exchanger in aligned arrangement with longitudinal vortex generator from the viewpoint of field synergy principle." **Applied Thermal Engineering.**, vol. 27, 2007. pp. 2609–2617.
- [31] Layek A., Saini J.S. and Solanki S.C. "Second law optimization of a solar air heater having chamfered rib-groove roughness on absorber plate." **Renewable Energy.**, vol. 32, 2007. pp. 1967–1980.
- [32] Saini S.K. and Saini R.P. "Development of correlations for Nusselt number and friction factor for solar air heater with roughened duct having arc-shaped wire as artificial roughness." **Solar Energy.**, vol. 82, 2008. pp. 1118–1130.
- [33] Aharwal K.R., Gandhi B.K. and Saini J.S. "Experimental investigation on heat-transfer enhancement due to a gap in an inclined continuous rib arrangement in a rectangular duct of solar air heater." **Renewable Energy.**, vol. 33, 2008. pp. 585–596.
- [34] Joardar A. and Jacobi A.M. "Heat transfer enhancement by winglet-type vortex generator arrays in compact plain-fin-and-tube heat exchangers." **International Journal of Refrigeration.**, vol. 31, 2008. pp. 87–97.

- [35] Varun, Saini R.P. and Singal S.K. "Investigation of thermal performance of solar air heater having roughness elements as a combination of inclined and transverse ribs on the absorber plate." **Renewable Energy**, vol. 33, 2008. pp. 1398–1405.
- [36] Wu J.M. and Tao W.Q. "Numerical study on laminar convection heat transfer in a rectangular channel with longitudinal vortex generator. Part A: Verification of field synergy principle." **International Journal of Heat and Mass Transfer**, vol. 51, 2008. pp. 1179–1191.
- [37] Wu J.M. and Tao W.Q. "Numerical study on laminar convection heat transfer in a channel with longitudinal vortex generator. Part B: Parametric study of major influence factors." **International Journal of Heat and Mass Transfer**, vol. 51, 2008. pp. 3683–3692.
- [38] Promvong P. and Thianpong C. "Thermal performance assessment of turbulent channel flows over different shaped ribs." **International Communications in Heat and Mass Transfer**, vol. 35, 2008. pp. 1327–1334.
- [39] Bopche S.B. and Tandale M.S. "Experimental investigations on heat transfer and frictional characteristics of a turbulator roughened solar air heater duct." **International Journal of Heat and Mass Transfer**, vol. 52, 2009. pp. 2834–2848.
- [40] Chu P., He Y.L., Lei Y.G., Tian L.T. and Li R. "Three-dimensional numerical study on fin-and-oval-tube heat exchanger with longitudinal vortex generators." **Applied Thermal Engineering**, vol. 29, 2009. pp. 859–876.
- [41] Yu R., Chaoyi W. and Shusheng Z. "Transitional flow and heat transfer characteristics in a rectangular duct with stagger-arrayed short pin fins." **Chinese Journal of Aeronautics**, vol. 22, 2009. pp. 237–242.
- [42] Promvong P., Chompookham T., Kwankaomeng S. and Thianpong C. "Enhanced heat transfer in a triangular ribbed channel with longitudinal vortex generators." **Energy Conversion and Management**, vol. 51, 2010. pp. 1242–1249.
- [43] Promvong P. "Heat transfer and pressure drop in a channel with multiple 60° V-baffles." **International Communications in Heat and Mass Transfer**, vol. 37, 2010. pp. 835–840.
- [44] Promvong P., Sripattanapipat S., Tamna S., Kwankaomeng S. and Thianpong C. "Numerical investigation of laminar heat transfer in a square channel with 45° inclined baffles." **International Communications in Heat and Mass Transfer**, vol. 37, 2010. pp. 170–177.

- [45] Promvong P., Jedsadaratanachai W. and Kwankaomeng S. "Numerical study of laminar flow and heat transfer in square channel with 30° inline angled baffle turbulators." **Applied Thermal Engineering**., vol. 30, 2010. pp. 1292–1303.
- [46] Promvong P. and Kwankaomeng S. "Periodic laminar flow and heat transfer in a channel with 45° staggered V-baffles." **International Communications in Heat and Mass Transfer**., vol. 37, 2010. pp. 841–849.
- [47] Sriromreun S., Thianpong C. and Promvong P. "Experimental and numerical study on heat transfer enhancement in a channel with Z-shaped baffles." **International Communications in Heat and Mass Transfer**., vol. 39, 2012. pp. 945–952.
- [48] Alam T., Saini R.P. and Saini J.S. "Experimental investigation on heat transfer enhancement due to V-shaped perforated blocks in a rectangular duct of solar air heater." **Energy Conversion and Management**., vol. 81, 2014. pp. 374–383.
- [49] Skullong S. and Promvong P. "Experimental investigation on turbulent convection in solar air heater channel fitted with delta winglet vortex generator." **Chinese Journal of Chemical Engineering**., vol. 22, 2014. pp. 1–10.
- [50] Tamna S., Skullong S., Thianpong C. and Promvong P. "Heat transfer behaviors in a solar air heater channel with multiple V-baffle vortex generators." **Solar Energy**., vol. 110, 2014. pp. 720–735.
- [51] Promvong P. "Thermal performance in circular tube fitted with coiled square wires." **Energy Conversion and Management**., vol. 49, 2008. pp. 980–987.
- [52] Promvong P. "Thermal Enhancement in a Round Tube with Snail Entry and Coiled-wire Inserts." **International Communications in Heat and Mass Transfer**., vol. 35, 2008. pp. 623–629.
- [53] Promvong P. "Thermal augmentation in circular tube with twisted tape and wire coil turbulators." **Energy Conversion and Management**., vol. 49, 2008. pp. 2949–2955.
- [54] Gunes S., Ozceyhan V. and Buyukalaca O. "Heat transfer enhancement in a tube with equilateral triangle cross sectioned coiled wire inserts." **Experimental Thermal and Fluid Science**., vol. 34, 2010. pp. 684–691.
- [55] Gunes S., Ozceyhan V. and Buyukalaca O. "The experimental investigation of heat transfer and pressure drop in a tube with coiled wire inserts placed separately from the tube wall." **Applied Thermal Engineering**., vol. 30, 2010. pp. 1719–1725.
- [56] Eiamsa-ard S., Nivesrangsan P., Chokphoemphun S. and Promvong P. "Influence of combined non-uniform wire coil and twisted tape inserts on thermal performance characteristics." **International Communications in Heat and Mass Transfer**., vol. 37, 2010. pp. 850–856.

- [57] Gunes S., Manay E., Senyigit E. and Ozceyhan V. 2011. "A Taguchi approach for optimization of design parameters in a tube with coiled wire inserts." **Applied Thermal Engineering**, vol. 31, 2011. pp. 2568–2577.
- [58] Nasr M.R.J., Khalaj A.H. and Mozaffari S.H. "Modeling of heat transfer enhancement by wire coil inserts using artificial neural network analysis." **Applied Thermal Engineering**, vol. 30, 2010. pp. 143–151.
- [59] Eiamsa-ard S., Thianpong C., Eiamsa-ard P. and Promvong P. "Convective heat transfer in a circular tube with short-length twisted tape insert." **International Communications in Heat and Mass Transfer**, vol. 36, 2009. pp. 365–371.
- [60] Eiamsa-ard S., Thianpong C., Eiamsa-ard P. and Promvong P. "Thermal characteristics in a heat exchanger tube fitted with dual twisted tape elements in tandem." **International Communications in Heat and Mass Transfer**, vol. 37, 2010. pp. 39–46.
- [61] Bas H. and Ozceyhan V. 2012. "Heat transfer enhancement in a tube with twisted tape inserts placed separately from the tube wall." **Experimental Thermal and Fluid Science**, vol. 41, 2012. pp. 51–58.
- [62] Bhuiya M.M.K., Chowdhury M.S.U., Shahabuddin M., Saha M. and Memon L.A. "Thermal characteristics in a heat exchanger tube fitted with triple twisted tape inserts." **International Communications in Heat and Mass Transfer**, vol. 48, 2013. pp. 124–132
- [63] Bhuiya M.M.K., Sayema A.S.M., Islam M., Chowdhury M.S.U. and Shahabuddin M. "Performance assessment in a heat exchanger tube fitted with double counter twisted tape inserts." **International Communications in Heat and Mass Transfer**, vol. 50, 2014. pp. 25–33.
- [64] Eiamsa-ard S., Thianpong C. and Promvong P. "Experimental investigation of heat transfer and flow friction in a circular tube fitted with regularly spaced twisted tape elements." **International Communications in Heat and Mass Transfer**, vol. 33, 2006. pp. 1225–1233.
- [65] Eiamsa-ard S. and Promvong P. "Thermal characteristics in round tube fitted with serrated twisted tape." **Applied Thermal Engineering**, vol. 30, 2010. pp. 1673–1680.
- [66] Murugesan P., Mayilsamy K. and Suresh S. "Turbulent heat transfer and pressure drop in tube fitted with square-cut twisted tape." **Chinese Journal of Chemical Engineering**, vol. 18(4), 2010. pp. 609–617.
- [67] Murugesan P., Mayilsamy K., Suresh S. and Srinivasan P.S.S. "Heat transfer and pressure drop characteristics in a circular tube fitted with and without V-cut twisted tape insert." **International Communications in Heat and Mass Transfer**, vol. 38, 2011. pp. 329–334.

- [68] Chang S.W., Jan Y.J. and Liou J.S. "Turbulent heat transfer and pressure drop in tube fitted with serrated twisted tape." **International Journal of Thermal Sciences.**, vol. 46, 2007. pp. 506–518.
- [69] Bhuiya M.M.K., Chowdhury M.S.U., Saha M. and Islam M.T. "Heat transfer and friction factor characteristics in turbulent flow through a tube fitted with perforated twisted tape inserts." **International Communications in Heat and Mass Transfer.**, vol. 43, 2013. pp. 49–57.
- [70] Sivashanmugam P. and Suresh S. "Experimental studies on heat transfer and friction factor characteristics of turbulent flow through a circular tube fitted with regularly spaced helical screw-tape inserts." **Applied Thermal Engineering.**, vol. 27, 2007. pp. 1311–1319.
- [71] Sivashanmugam P. and Suresh S. "Experimental studies on heat transfer and friction factor characteristics of turbulent flow through a circular tube fitted with helical screw-tape inserts." **Chemical Engineering and Processing.**, vol. 46, 2007. pp. 1292–1298.
- [72] Ibrahim E.Z. "Augmentation of laminar flow and heat transfer in flat tubes by means of helical screw-tape inserts." **Energy Conversion and Management.**, vol. 52, 2011. pp. 250–257.
- [73] Eiamsa-ard S. and Promvongse P. "Performance assessment in a heat exchanger tube with alternate clockwise and counter-clockwise twisted-tape inserts." **International Journal of Heat and Mass Transfer.**, vol. 52, 2010. pp. 1364–1372.
- [74] Eiamsa-ard S., Somkleang P., Nuntadusit C. and Thianpong C. "Heat transfer enhancement in tube by inserting uniform/non-uniform twisted-tapes with alternate axes: Effect of rotated-axis length." **Applied Thermal Engineering.**, vol. 54, 2013. pp. 289–309.
- [75] Eiamsa-ard S., Wongcharee K., Eiamsa-ard P. and Thianpong C. "Thermohydraulic investigation of turbulent flow through a round tube equipped with twisted tapes consisting of centre wings and alternate-axes." **Experimental Thermal and Fluid Science.**, vol. 34, 2010. pp. 1151–1161.
- [76] Eiamsa-ard S., Wongcharee K., Eiamsa-ard P. and Thianpong C. "Heat transfer enhancement in a tube using delta-winglet twisted tape inserts." **Applied Thermal Engineering.**, vol. 30, pp. 310–318.
- [77] Wongcharee K. and Eiamsa-ard S. "Heat transfer enhancement by twisted tapes with alternate-axes and triangular, rectangular and trapezoidal wings." **Chemical Engineering and Processing.**, vol. 50, 2011. pp. 211–219.
- [78] Guo J., Fan A., Zhang X. and Liu W. "A numerical study on heat transfer and friction factor characteristics of laminar flow in a circular tube fitted with center-cleared

- twisted tape." **International Journal of Thermal Sciences.**, vol. 50, 2011. pp. 1263–1270.
- [79] Li P., Liu Z., Liu W. and Chen G. "Numerical study on heat transfer enhancement characteristics of tube inserted with centrally hollow narrow twisted tapes." **International Journal of Heat and Mass Transfer.**, vol. 88, 2015. pp. 481–491.
- [80] Sivashanmugam P. and Suresh S. "Experimental studies on heat transfer and friction factor characteristics of laminar flow through a circular tube fitted with regularly spaced helical screw-tape inserts." **Experimental Thermal and Fluid Science.**, vol. 31, 2007. pp. 301–308.
- [81] Promvong P., Koolnapadol N., Pimsarn M. and Thianpong C. "Thermal performance enhancement in a heat exchanger tube fitted with inclined vortex rings." **Applied Thermal Engineering.**, vol. 62, 2014. pp. 285–292.
- [82] Promvong P., Tamna S., Pimsarn M. and Thianpong C. "Thermal characterization in a circular tube fitted with inclined horseshoe baffles." **Applied Thermal Engineering.** vol. 75, 2015. pp. 1147–1155.
- [83] Tandiroglu A. "Effect of flow geometry parameters on transient heat transfer for turbulent flow in a circular tube with baffle inserts." **International Journal of Heat and Mass Transfer.**, vol. 49, 2006. pp. 1559–1569.
- [84] Eiamsa-ard S. and Promvong P. "Experimental investigation of heat transfer and friction characteristics in a circular tube fitted with V-nozzle turbulators." **International Communications in Heat and Mass Transfer.**, vol. 33, 2006. pp. 591–600.
- [85] Promvong P. "Heat transfer behaviors in round tube with conical ring inserts." **Energy Conversion and Management.**, vol. 49, 2008. pp. 8–15.
- [86] Eiamsa-ard S., Rattanawong S. and Promvong P. "Turbulent convection in round tube equipped with propeller type swirl generators." **International Communications in Heat and Mass Transfer.**, vol. 36, 2009. pp. 357–364.
- [87] Ferziger J.H., and Peric M. **Computational methods for fluid dynamics.** 3rd ED. Berlin : Springer, 2002. ISBN 3-540-42074-6.
- [88] Suhas V. Patankar. **Numerical Heat Transfer and Fluid Flow.** New York : McGraw-Hill, Inc. 1980.
- [89] Roache P.J. "Perspective: A method for uniform reporting of grid refinement studies." **Transactions of the ASME, Journal of Fluids Engineering.**, vol. 116, 1994. pp. 405–413.
- [90] Roache P.J. "Quantification of uncertainty in computational fluid dynamics." **Annual Review of Fluid Mechanics.**, vol. 29, 1997. pp. 123–160
- [91] Versteeg, H.K. and Malalasekera W. **An Introduction to Computational Fluid Dynamics.** Essex : Pearson Education 2007.

- [92] Incropera F.P., Witt P.D., Bergman T.L. and Lavine A.S. "**Fundamentals of heat and mass transfer.**" John-Wiley & Sons, 2006.
- [93] Winterton R. H. S. "Where did the Dittus and Boelter equation come from?" **International Journal of Heat Mass Transfer.**, vol. 41, no. 4-5, 1998. pp. 809-810.

APPENDIX

AUTHOR PUBLICATION

International journal

- [1] Promvongse P., Tamna S., Pimsarn M., and Thianpong C. “Thermal characterization in a circular tube fitted with inclined horseshoe baffles” **Applied Thermal Engineering**, vol. 75, 2015. pp. 1147-1155
- [2] Tamna S., Skullong S., Thianpong C., and Promvongse P. “Heat transfer behaviors in a solar air heater channel with multiple V-baffle vortex generators” **Solar Energy**, vol. 110, 2014. pp. 720-735

International conference

- [1] Tamna S., Suwannapan S., Skullong S., Promvongse P., and Thianpong C. “Numerical Investigation of Laminar Flow and Heat Transfer in a Square Channel with Oblique Baffles” **2013 International Conference on Engineering, Applied Sciences, and Technology**, Bangkok, Thailand, August, 2013. pp. 320-324
- [2] Tamna S., Wongpueng J., Promvongse P., Eiamsa-ard S., and Thianpong, C., “3D Numerical Simulation of Laminar Flow and Heat Transfer in Square Channel with Inclined Discrete-Baffles”, **The 17th International Annual Symposium on Computational Science and Engineering**, Khon Kaen, Thailand, March, 2013. pp. 166-172
- [3] Suwannapan S., Chompookham T., Tamna S., Skullong S., Thianpong C. and Promvongse P. “Augmented Heat Transfer in Square Channel with 45° Inline Baffles” **International Conference on Green and Sustainable Innovation 2012**, Chiang Mai, Thailand, May, 2012.

AUTHOR BIOGRAPHY

Name	Mr.Sombat Tamna
Date of Birth	7 October 1982
Place of Birth	Roi-et, Thailand
Address	62 Moo 6, Pathumrat district, Roi-et province, 45190 Thailand
Education	2006: B.Eng. in Mechanical Engineering King Mongkut's Institute of Technology Ladkrabang (KMITL), Bangkok, Thailand 2009: M.Eng. in Mechanical Engineering King Mongkut's Institute of Technology Ladkrabang (KMITL), Bangkok, Thailand
Scholarships	2011: The Royal Golden Jubilee Ph.D. program (Grant No. PHD/0218/2552), Thailand Research Fund (TRF)
Experiences	2009: Lecturer Department of Mechanical Engineering Rajamangala University of Technology Suvarnabhumi (RMUTSB) Nonthaburi campus, Nonthaburi, Thailand 2010 - Present: Lecturer Department of Automotive Engineering Thai-Nichi Institute of Technology (TNI), Bangkok, Thailand